Closed-loop Feedback Control of Smart Wells for Production Optimisation using Self-Potential Measurement

by

Amadi Ijioma

DEPARTMENT OF EARTH SCIENCE AND ENGINEERING

Imperial College London SW7 2AZ

United Kingdom

Supervisors

Prof. Matthew D. Jackson and Dr. Jan Vinogradov

Thesis submitted as part of the requirements for the award of the PhD in Petroleum Engineering, Imperial College London.

Declaration of Originality

I declare that this thesis, Closed-loop Feedback Control of Smart Wells for Production Optimisation using Self Potential Measurements, is entirely my own work under the supervision of Prof. Matthew D. Jackson and Dr. Jan Vinogradov. The work was performed in the Department of Earth Science and Engineering at Imperial College London. All published and unpublished material used in the thesis has been given full acknowledgment. This work has not been previously submitted, in whole or in part, to any other academic institution for a degree, diploma, or any other qualification.

Copyright Declaration

The copyright of this thesis rests with the author and is made available under a Creative Commons Attribution Non-Commercial No Derivatives licence. Researchers are free to copy, distribute or transmit the thesis on the condition that they attribute it, that they do not use it for commercial purposes and that they do not alter, transform or build upon it. For any reuse or redistribution, researchers must make clear to others the licence terms of this work.

© 2016 Amadi Adebowale Ijioma

Acknowledgements

The Petroleum Technology Development Fund (PTDF) Nigeria is gratefully acknowledged for the funding of this work. Additional financial support was also provided by the Total Reservoir Physics Laboratory.

I would like to extend my sincere gratitude to my supervisors, Prof. Matthew Jackson for his strong guidance throughout my PhD studies. He offered constant support to ensure that I was on the right path by providing critical feedback and guidance.

I would like to appreciate past and present members of the Smart Wells and Reservoir Monitoring Group (2012 – 2016), Dr. Jan Vinogradov, Dr. Fahad Dilib, Dawoud Al-Mahrouqi, Abdulkareem Alroudhan, Malcolm Graham, Donald John MacAllister and Jiazuo Zhang. I also acknowledge the support of colleagues and friends in Imperial College, Dr. Tomiwa Erinosho and Dr. Joao Nunes who I shared this journey with and provided moral support I needed to go through this PhD.

I would like to thank my wonderful girlfriend & partner Martina Campinoti, who has been patient and took good care of me throughout the PhD programme. I would like to appreciate my Siblings, Nnanna, Nkechi, Oyidia and Moore for their support. Last but not the least, I would like to appreciate my parents R. Admiral and Mrs Ijioma whose constant love and support has seen me throughout my academic career. I love you so much and I am forever grateful.

Abstract

Closed-loop ‘reactive’ feedback control techniques used for smart well optimisation, triggered by changes in flow (such as unwanted water production) measured at the well can increase the net present value (NPV) and mitigate reservoir uncertainty, as opposed to model-based control strategies, which use models that are rarely predictive at their spatial and temporal scales required to identify optimum control actions. However, the drawback faced with closed-loop ‘reactive’ feedback control is that control actions are only taken after adverse changes of flow occur at the well. We present a modified close-loop ‘proactive’ feedback inflow control approach based on near-well, downhole measurements of self-potential (SP) and quantify the potential benefit of this approach in different well and reservoir settings during waterflooding or aquifer support production.

The measurement of SP signals downhole in production wells is an encouraging technique that can be used to image waterfronts and has the potential of detecting water encroachment tens to hundreds of meters away from the well. SP signals arise in order to preserve electrical neutrality when charge separation arises due to gradients in pressure, temperature and chemical concentration of the reservoir brine phase. These gradient effects are commonly encountered during waterflooding processes and can be assessed numerically to predict the SP generated downhole in oil production wells. The numerical modelling of SP can be used as a cheap alternative to carrying out actual field experiments and serve as a proxy for predicting the SP measurements taken during waterflood production. Hence, a closed-loop ‘proactive’ feedback control strategy triggered by downhole SP measurements is developed.

We use the NPV of the production wells to measure and compare the performance of the closed-loop feedback control in two different synthetic production cases; the first production case is a simple thin oil-column reservoir with production enabled by a single long horizontal well, and the second more realistic SPE Brugge field model, with production enabled by 20 production wells. The results observed are promising, and suggest that closed-loop control on the basis performance of downhole SP feedback can yield increased gains in NPV, by delaying the production of unwanted fluids compared with water-cut monitoring. These gains are also observed even if the reservoir lies outside the range predicted by reservoir models. Finally, we investigate the potential utility of SP

monitoring in analogue real field applications. Overall the results are promising and suggest that SP measurements can be useful in making critical decisions in real field exploration and production applications, and other non-oil related fields such as saline intrusion monitoring in coastal aquifers.

Table of Contents

1 Introduction 22

1.1 Aims and Objectives 24

1.2 Outline 24

2 Literature Review 26

2.1 Introduction 26

2.2 Proactive Model-based Control Strategies 28

2.3 Reactive Control Strategies 32

2.4 Proactive Feedback Control 34

2.5 Origin of Self- Potential 37

2.5.1 Electrokinetic Potential 39

2.5.2 Electrochemical and Thermoelectric Potentials 43

2.5.3 Relative Coupling Coefficient 44

2.6 Summary 44

3 Methodology: Numerical Modelling of Self-Potential 49

3.1 Introduction 49

3.2 Discretisation of Variables 50

3.3 Electrical Properties 54

3.4 Self-Potential Solver 55

3.5 Summary 60

4 Closed–Loop Feedback Control using Downhole Measurements of SP: Single Horizontal Well Application 62

4.1 Introduction 62

4.2 Methodology 63

4.2.1 Base case reservoir model 63

4.2.2 Numerical Modelling of Production and SP 65

4.2.3 Objective Function 66

4.2.4 Inflow Control Algorithm 67

4.2.5 Uncertain Reservoir Behaviour 70

4.3 Results 71

4.3.1 Optimisation of the inflow control algorithm using the base case reservoir model 71

4.3.2 Impact of inflow control on the base case reservoir model 71
4.3.3 Impact of Inflow Control on the NPV of the Base Case Model 73
4.3.4 Effect of Unexpected Reservoir Behaviour 75
4.4 Discussion 76
4.5 Conclusions 78
5 Self-Potential Measurements in Multi-Well Developments: Application to the Brugge Field Model 79
5.1 Introduction 79
5.2 Methodology 80
5.2.1 Brugge Field Geological Model 80
5.2.2 Reservoir Simulations 81
5.2.3 Numerical Modelling of SP 84
5.3 Results 89
5.3.1 Production behaviour of the 'base case' model 89
5.3.2 SP signals during production 99
5.3.3 Characteristics of the Change in Self-Potential 104
5.3.4 Impact of varying formation brine salinity and production rate 109
5.4 Discussion 113
5.5 Conclusions 114
6 Closed–Loop Feedback Control using Downhole Measurements of SP: Brugge Field Application 115
6.1 Introduction 115
6.2 Methodology 116
6.2.1 Numerical Modelling of Production and Self-Potential 116
6.2.2 Objective Function 117
6.2.3 Inflow Control Strategies 118
6.2.4 Base case model and uncertain reservoir behaviour 122
6.3 Results 122
6.3.1 Tuning of the inflow control algorithm using the base case models 122
6.3.2 Impact of inflow control on the NPV of the base case model realisation. 123
6.3.3 Impact of inflow control on the base case reservoir realisations 124
6.3.4 Impact of unexpected reservoir behaviour 130
6.4 Discussion 131

6.5 Conclusions 133
7 SP Monitoring in Real Field Applications 134
7.1 Introduction 134
7.2 SP Monitoring in the Field 135
7.2.1 X Field Geological Model and Simulation 135
7.2.2 Numerical modelling of SP 135
7.2.3 SP signals during production 137
7.2.4 Relationship between SP measurements and residual oil saturation 142
7.2.5 Summary 143
7.3 Monitoring Seawater Intrusion in fractured coastal aquifer 144
8 Conclusions & Future Work 151
8.1 Conclusions 153
8.2 Recommendations for future work 153
References 155

List of Figures

Figure 2.1: Schematic of Smart Completion (Gai, 2001) 26

Figure 2.2: Schematic organisation of operating control strategies for intelligent wells (Addiego-Guevara *et al.* 2008)..... 27

Figure 2.3: Model-based, closed-loop control process (Nævdal *et al.*, 2006) 29

Figure 2.4: Permanent monitoring applications for resistivity array (Glandt, 2005)..... 35

Figure 2.5: 3D reservoir model cross-section showing water saturation when water front is (a) 50 m away from the production well, (b) 25 m away from the well and (c) at breakthrough. The vertical dashed line represents the well. Plots (d) to (f) show the correspond 36

Figure 2.6: Illustration of the charge separation at the rock-water interface (with the EDL depicted in a very simplified form) and the origin of (a) EK potential, (b) EC potential, and (c) TE potential (Jackson *et al.*, 2012). 40

Figure 2.7: (a) C_EK vs. Salinity, derived using Eq. 2.9 (b) C_EC vs. salinity, derived using Eq. 2.13, at 293 K (solid line) and 393 K (dashed line). (c) C_TE vs. Salinity derived using Eq. 2.14 at 293 K (solid line) and 393 K (dashed line). (Jackson *et al.*, 2012)..... 42

Figure 3.1: Sample rectilinear mesh zones. Solid lines are the vertices, and black circles are the cell centres 50

Figure 3.2: Cell at the boundary 52

Figure 3.3: Discontinuous variation in σ_{fs} and L_{EK} at the interface between two grid cells 53

Figure 3.4: Two snapshots, of the saturation variation within the reservoir, showing the water (blue) moving towards the well, which is located at (b) 130 m and (c) 40 m from the well. 56

Figure 3.5: 3D reservoir model based on Jackson et al. (2012). (a) Perspective view of the 100 m thick sandstone reservoir, surrounded by shales fully saturated with water. Waterflooding is achieved by injection wells which are placed at the inlet boundary not shown in the figure. (b) Cross-section through the middle of the model, showing the confining shale layers above and below the reservoir. (c) Grid used for modelling.... 58

Figure 3.6: 1D horizontal profile across the centre of the reservoir at five different time steps, of (a) EK potential and the corresponding saturation profile, with the EK potential decaying c. 50-100 m ahead of the waterfront (b) EC potential and the salinity profile and (c) TE potential and temperature profile. The production well is positioned at 0m 60

Figure 3.7: Flow chart describing how previous studies relate to our modified feedback inflow control strategy based on downhole measurements of SP. 61

Figure 4.1: Schematic cross-section of a sandstone reservoir with interbedded shales, bounded by shales above and at the sides; these are cut-away for visualization purposes. The model is modified from Dilib and Jackson (2012). The well is placed 35ft from the top of the reservoir and has two completions (diagram not to scale). 64

Figure 4 2: Variable inflow control strategy of Dilib and Jackson (2012), modified here to use downhole measurement of SP..... 69

Figure 4.3: (a) and (b) Cross-section through the centre of the reservoir model showing snapshots of the oil saturation, before and after control actions are taken respectively; (c) and (d) Corresponding SP measurements along the production well. The well watercut limit in this example is 25%. The dashed line denoted the noise level (assumed from Chen *et al.* 2006). 72

Figure 4.4: (a) and (c) Values of watercut and inflow multiplier against time; (b) and (d) oil production rates against time, for the control strategies based on downhole SP measurements (plots (a) and (b)) and watercut measurements(plots (b) and (d)). Results from the base case model with a 25% well watercut limit. 73

Figure 4.5: Cross-section through the reservoir model showing oil saturation at the end of production for (a) uncontrolled production, (b) feedback control using downhole watercut measurement and (c) feedback control using SP measurements. Results obtained from the base case model with 50% well watercut limit..... 74

Figure 4.6: The performance of each control strategy on the base case reservoir model over a range of well watercut limits. The error bars represent the range of estimated development costs and operational revenue/expenditure from Dilib and Jackson (2012). 74

Figure 4.7: NPV gain for feedback control based on downhole measurements of (a) watercut and (b) SP, and (c) model based optimization, at different well watercut limits. Each point represents the NPV gain for a particular unexpected reservoir behavior. The error bars denote the range of estimated development costs and operational revenue/expenditure from Dilib and Jackson (2012). 75

Figure 5.1: The structure of the Brugge Field showing the depth (m) and the positions of the 20 production (denoted BR-P) and 10 injection (denoted BR-I) wells. The well groups G1 and G2 are separated by an internal fault (modified from Peters *et al*., 2010) 80

Figure 5.2 : (a) Brugge Field water saturation variation showing parent and child grids. (b) Water saturation ($\boldsymbol{x1}$-$\boldsymbol{x2}$) cross-section after 330 days of production showing the NNC across the reservoir fault. (c) Overburden and underburden shale layers place above and below the model; example through LGR15 (cross-section $\boldsymbol{x1}$-$\boldsymbol{x2}$)..... 85

Figure 5.3: Sample 2D mesh zones of parent grid, child model/LGR and ghost cells..... 86

Figure 5.4: (a) Saturation variation within the 10 × 20 grid cells parent grid 2D oil Column, and a 6 × 6 LGR placed within cell 10-12 in the x direction and 5-6 in the y direction of the parent grid cell. (b) The corresponding SP signal along the oil column. The SP signal simulated in the LGR match the SP simulated in the Parent grid. 87

Figure 5.5: Result of the LGR grid refinement study (a) Water saturation cross-section through well P15 after 330 days of production, and (b) the corresponding SP signals along the well: relationship with waterfront shape. (c) Table of the grid size and (d) LGR sensitivity plot. 88

Figure 5.6: (a) Field Cumulative oil production and Field Cumulative water production plotted against time. 89

Figure 5.7: The plan-view (a) Water saturation and (b) concentration cross-sections through the middle of the reservoir after 5 years of production. The waterfront reaches well P15 first across the reservoir, highlighted by the concentration front cross section. 90

Figure 5 8: (a) Completion fluid production rate vs. time; (b) Completion oil production rate vs. time and the higher; (c) Completion water production rate vs. time; (d) Completion watercut vs. time; measured in well P12. Water breakthrough occurs in the Waal & Schie (bottom) completion; at a higher resolution in the completion water production rater vs. time plot, we observe that water breakthrough occurs next in the Schelde (top) completion after approximately 5 years, and occurs last in the Maas (middle) completion after 12 years of production. 91

Figure 5 9: (a) saturation $\boldsymbol{x1-x2}$cross-section, (b) concentration $\boldsymbol{x1-x2}$cross-section and, (c) saturation $\boldsymbol{y1-y2}$cross-section (from Figure 5.7) and (d) the pressure drawdown at well P12 at 360, 2700 and 4700 days into production respectively. The horizontal dashed lines show the different stratigraphic layers. The waterfront in the Schelde (top) and Waal & Schie (bottom) layers flows ahead of the front in the Maas (middle) layer. 93

Figure 5.10: (a) Completion fluid production rate vs. time; (b) Completion oil production rate vs. time; (c) Completion water production rate vs. time; (d) Completion watercut vs. time; measured in well P15. At a higher resolution in the completion water production rate vs. time plot, we observe that water breakthrough occurs first in the Schelde (top) completion after 2.5 years. 94

Figure 5.11: : (a) saturation $x3-x4$cross-section, (b) concentration $x3-x4$cross-section, (c) saturation $y3-y4$cross-section (from Figure 5.7) and (d) the pressure drawdown at well P15, at 330, 660 and 1380 days into production respectively. The horizontal dashed lines show the different stratigraphic layers. The waterfront in the Schelde (top) and Waal & Schie (bottom) layers flows ahead of the front in the Maas (middle) layer. The high pressure drawdown in the Schelde (top) layer creates a vertical potential gradient

which drives reservoir fluid from the underlying Waal and Schie (bottom) layer upwards at t = 660 days, leading to the early water breakthrough in the Maas (middle) layer. . 95

Figure 5.12: (a) Completion liquid production rate vs. time; (b) Completion oil production rate vs. time; (c) Completion water production rate vs. time; (d) Completion watercut vs. time; measured in well P5. Water breakthrough occurs first in the Maas (middle) completion after 5 years. 96

Figure 5.13: (a) saturation $\boldsymbol{x5-x6}$ cross-section, (b) concentration $\boldsymbol{x5-x6}$ cross-section, (c) saturation $\boldsymbol{y5-y6}$ cross-section (from Figure 5.6) and (d) the pressure drawdown at well P5 at 30, 1100 and 2000 days into production respectively. The horizontal dashed lines show the different stratigraphic layers. The high pressure drawdown in the Schelde (top) layer creates a vertical potential gradient which drives reservoir fluid from the underlying Waal and Schie (bottom) layer upwards at t = 1100 days, leading to the early water breakthrough in the Maas (middle) layer. 98

Figure 5 14: Cross-section through well P12 of the reservoir model showing the $\boldsymbol{x1-x2}$ (a) concentration, (b) saturation cross-sections and (c) the SP signals along the well at 360, 2700 and 4700 days into production respectively. The horizontal dashed lines show the different stratigraphic layers. Early SP signals can be measured prior to water breakthrough and reflects the movement of the encroaching waterfront. Note that the scale of the SP plot at t = 360 days is different from the SP plot at t = 2700 and 4700 days..... 101

Figure 5 15: Cross-section through well P5 of the reservoir model showing the $\boldsymbol{x5-x6}$ (a) concentration and (b) saturation cross-sections; and (c) the SP signals along the well at 30, 1100 and 2000 days into production respectively. The horizontal dashed lines show the different stratigraphic layers. Early SP signals can be measured prior to water breakthrough and the EK signal reflects the movement of the encroaching waterfront. 102

Figure 5.16: Cross-section through well P-15 of the reservoir model showing the $\boldsymbol{x3-x4}$ (a) concentration and (b) saturation cross-sections and (c) the SP signals measured along the well at 330, 660 and 1380 days into production respectively. The horizontal dashed lines show the different stratigraphic layers. Early SP (EK) signals can be measured prior to water breakthrough; unlike the previous cases the SP does not reflect the waterfront profile. The mean SP signal is more positive in the layer where the waterfront is closest to the well. The EC potential reflects the concentration front when it reaches the well. 103

Figure 5.17: (a) Plots show (from right to left) (i) mean SP and the (ii) EK and (iii) EC potential measured in the middle of each completion along well P12. (b) Plots show (from right to left) magnitude change in (i) mean SP and the (ii) EK and (iii) EC potential measured in the middle of each completion (c) Plots show the corresponding (i) well completion water production rates, (ii) well completion watercut measurement and (iii)

and salinity. Measurable change in SP signals observed at approximately 200 days prior to water breakthrough in the Waal and Schie (bottom) completion. The horizontal red dotted lines represent the assumed noise level of 0.1mV. 106

Figure 5.18: (a) Plots show (from right to left) the (i) mean SP and the (ii) EK and (iii) EC potential measured in the middle of each completion along well P15. (b) Plots show (from right to left) magnitude change in (i) mean SP and the (ii) EK and (iii) EC potential measured in the middle of each completion (c) Plots show the corresponding well completion water production rates and (iii) and salinity. Measurable change in SP signals is observed at approximately 600 days prior to water breakthrough in the Maas completion and at approximately c. 350 days in the Schelde completion. The horizontal red dotted lines represent the assumed noise level of 0.1mV. 107

Figure 5.19: (a) Plots show (from right to left) the (i) mean SP and the (ii) EK and (iii) EC potential measured in the middle of each completion along well P5. (b) Plots show (from right to left) magnitude change in (i) mean SP and the (ii) EK and (iii) EC potential measured in the middle of each completion (c) Plots show the corresponding well completion water production rates and (iii) and salinity. Measurable change in SP signals is observed at approximately 1000 days prior to water breakthrough in the Maas completion. The horizontal red dotted lines represent the assumed noise level of 0.1mV. 108

Figure 5.20: Magnitude of the maximum SP change measured in each completion along well (a) P12, (b) P15 and (b) P5 as a function of production time at different formation brine salinities. Vertical dashed lines indicate the times water breakthrough occurs. The Magnitude of the change in SP decreases as the formation brine salinity increases.. 110

Figure 5.21: Magnitude of the maximum SP change measured in each completion along well (a) P12, (b) P15 and (c) P5 as a function of production time at different formation brine salinities. Vertical dashed lines indicate the times water breakthrough occurs. The magnitude of the change in SP measurements increases as the production rate increases. 111

Figure 5.22: Impact of formation brine salinity variation on the time before breakthrough at which SP signals > 0.1 mV are measurable in well (a) P12, (b) P15 and (c) P5. .. 112

Figure 5.23: Impact of production rate variation on the time before breakthrough at which SP signals > 0.1 mV are measurable in well (a) P12 and (b) P15. Early SP measurements were not observed in well P5 prior to breakthrough at low production rate (<2000 STB/day). 112

Figure 6.1: Inflow control strategy of Dilib *et al*., (2013), modified here to use downhole measurement of SP for optimisation of a multi-well field. The controller requires the adjustable parameters in equation 6.1. Here they are obtained from the small subset of model realisations representing the base case. The wells and ICVs are initially open, but control actions are taken once completion *j* of well *i* exceed the SP trigger change (ΔV_t).

If the well water exceeds the maximum limit, the well is shut in at surface. Control actions are taken every 30 days until end of field life at year 30. 121

Figure 6.2: Field oil and water production rates of the ensemble of reservoir models used to test the performance of the feedback inflow control strategies when the reservoir behaviour is unexpected. The red line represents the base case models used to optimise the inflow control algorithm parameters. 122

Figure 6.3: The NPV obtained for at different well watercut limit on each of the base case model realisations over 10 – 30 years of production from the Brugge field. Each of the markers represents a different base – case model realisation and the red markers show the average NPV at the different watercut limits. The maximum NPV is obtained at a watercut limit of 0.7. 123

Figure 6.4: The performance of each control strategy on the base case model realisations over 0 – 30 years of production from the Brugge field. Each of the markers represents a different base – case model realisation. 124

Figure 6.5: Field performances of the different inflow control strategies on the base case model realisation, with the highest mean NPV. The watercut feedback control strategy yields the highest field oil production but also produces and injects the most amount of water. The heuristic reactive control strategy produces the least amount of oil but produces and injects the least amount of water. The SP feedback control strategy produces similar quantity of oil as the watercut control strategy, but produces and injects marginally less water. 126

Figure 6.6: Field performances of the different inflow control strategies on the base case model realisation, with the lowest mean NPV. The watercut feedback control strategy yields the highest field oil production but also produces and injects the most amount of water. The heuristic reactive control strategy produces the least amount of oil but produces and injects the least amount of water. The SP feedback control strategy in this case produces similar quantity of oil as the watercut control strategy, but produces and injects significantly less water (similar to the heuristic reactive control). 127

Figure 6.7: Inflow control behaviour (a) and (c) Values of watercut and inflow multiplier against time; (b) and (d) well water and oil production total, for the feedback control strategies based on surface and downhole watercut measurements (plots (a) and (b)) and downhole SP measurements(plots (b) and (d)). Results from the base case model with the highest NPV in Figure 6.4. 128

Figure 6.8: (a) and (c) Values of watercut and inflow multiplier against time; (b) and (d) well water and oil production total, for the feedback control strategies based on surface and downhole watercut measurements (plots (a) and (b)) and downhole SP measurements(plots (b) and (d)). Results from the base case model with the lowest NPV in Figure 6.4. 129

Figure 6.9: Range of NPV obtained from 0– 30 years of production for each of the inflow control strategies. Each point represents the NPV for a particular unexpected reservoir behaviour. The red data point represents the mean NPV for each of the control strategies. The SP control strategy yields the highest mean NPV with 4.5% increase over the heuristic reactive control strategy, while the watercut feedback strategy yields a mean NPV gain of 3.8%. 130

Figure 6.10: Cumulative oil and water produced for each of the inflow control strategies normalised against the heuristic strategy, over the ensemble of reservoir model realisations..... 131

Figure 6.11: Range of NPV obtained for the 0 – 30 year production period for each of the inflow control strategies. Each point represents the NPV for particular unexpected reservoir behaviour. The red data point represents the mean NPV for each of the control strategies. The range of NPV data obtained at water cost = \$5/bbl. is similar to Figure 6.7, compared to NPV obtained at water cost = \$20/bbl..... 132

Figure 7.1: (a) Saturation plan view of the X field highlighting well A and (b) the $x^1 - x^2$ saturation cross-section through well A which only penetrates the reservoir in layer 4 (L4). LGRs are placed around the well A to obtain higher resolution SP simulation results and the inactive cells between the sand layers represent the impermeable shale layers. 136

Figure 7. 2: (a) Saturation plan view of the X field highlighting well B and (b) the $x^3 - x^4$ saturation cross-section showing well B which only penetrates the reservoir in layer 4 (L4). The inactive cells between the sand layers represent the impermeable shale layers. LGRs are also placed around well B1A to obtain higher resolution SP simulation results, but are not shown above..... 136

Figure 7.3: (a) saturation plan-view at the base of the lower L4 layer after 300 days, and the $x^1 - x^2$ saturation cross-section through well A from figure 7.2 and the corresponding SP signal measured along well A after (b) 300 and (c) 450 days of production respectively. The vertical dotted red lines on the SP plot represent the assumed noise level of 0.1 mV. Measurable SP is observed in the lower L4 layer with the waterfront approximately 183 m away from the production well. 137

Figure 7.4: (a) saturation plan-view at the base of the upper L4 layer after 600 days, (b) $x^1 - x^2$ saturation cross-section through well B5 from figure 7.2 and the corresponding SP signal profile measured along well A after 600 days; measurable SP is observed in the upper L4 layer with the waterfront approximately 60 m away from the production well after 600 days of production, (c) $x^1 - x^2$ saturation cross-section and the corresponding SP measured after 750 and (d) 900 days of production. The vertical dashed red lines on the SP plot represent the assumed noise level of 0.1 mV. 138

Figure 7.5: Maximum changes in SP (mV) versus production time plots in the (a) lower L4 and (b) upper L4 layers respectively. Vertical dotted line represents times at which the waterfront reaches well B5 in each layer. 139

Figure 7.6: (a) the $x^3 - x^4$ saturation cross-section through well B from figure 7.2 and the corresponding SP signal measured along well B after 150 days of production, (b) saturation plan-view at the base of the lower L4 layer after 150 days of production, (c) the $x^3 - x^4$ saturation cross-section through well B from figure 7.2 and the corresponding SP signal measured along well B after 300 days. The vertical dashed red lines on the SP plot represent the assumed noise level of 0.1 mV. Measurable SP is observed in the lower L4 with the waterfront approximately 183 m away from the production well. The upper L2 layer is highlighted in red because the well is not completed in this layer..... 140

Figure 7.7: (a) saturation plan-view at the base of the lower B4 layer after 450 days of production, (b) $x^3 - x^4$ saturation cross-section through well B from figure 7.3 and the corresponding SP signal profile measured after 450 days, (c) saturation plan-view at the base of the upper B4 layer after 600 days of production, (d) $x^3 - x^4$ saturation cross-section through well B1A and the corresponding SP signal profile measured after 600 days. The vertical dotted red lines on the SP plot represent the assumed noise levels. Measurable SP signal is observed in the Upper B4 layer prior to water breakthrough with the front approximately 50 m away from the production well. The upper B2 layer is highlighted in red because the well is not completed in this layer. 141

Figure 7.8: Maximum changes in SP (mV) versus production time plots in the (a) lower B4 and (b) the upper B4 layers respectively. Vertical dotted line represents times at which the waterfront reaches the well in each layer. 142

Figure 7.9: Change in SP versus change in water saturation observed in well (a) A and (b) B in the upper and lower L4 layers respectively. The change in the total SP remains constant at each time step regardless of the change in saturation. 143

Figure 7.10: Simplified diagram of a coastal unconfined aquifer setting, showing (a) seawater wedge toe, (b) seawater intrusion at the base of the abstraction borehole and (c) saline coning at the base of the borehole due to prolonged groundwater pumping due to tidal effects, and (d) sea-level fluctuation. 144

Figure 7.11: (a) Location of the NERC field sites affected by seawater intrusion (NERC) highlighting the locations of the inland and coastal boreholes (b) SP versus depth in the inland borehole (c) SP versus depth in the saltsdean coastal borehole (MacAllister *et al*. 2015)..... 146

Figure 7.12: (a) Saltdean borehole with SP tool properties. (b) Field measurements of SP (mV) and the corresponding head versus time (c) SP (mV) and the corresponding fluid conductivity versus time (MacAllister *et al*. 2015)..... 147

Figure 7.13: Simplified hydrodynamic model of a steady state saline wedge developed in a coastal aquifer (MacAllister *et al*. 2015). 148

Figure 7.14: (a) Simulated SP and field SP measurement plotted versus time, (b) electrochemical (EC) potential contribution to the tidal SP (c) electrokinetic (EK) potential contribution to the tidal SP. The EC contributes to most of the SP measured in the borehole (MacAllister *et al*., 2015). 149

Figure 7.15: Comparison of the model borehole gradient against the observed borehole gradient as shown in Figure 7.11 (c). (MacAllister et al., 2015)..... 150

List of Tables

Table 3.1: Properties of the 1D model 56

Table 3.2: Properties of the 3D model 58

Table 4.1: Properties of the 3D model 65

Table 4.2: Uncertain reservoir behaviour 70

Table 4.3: Optimized Inflow Control Parameters 71

Table 5.1: Stratigraphy used in Brugge field with main reservoir characteristics (Peters *et al.*, 2010; *average values for sand only i.e., net porosity and permeability) 81

Table 5.2: Brugge Model Fluid Properties 82

Table 5.3: Well completion and corresponding reservoir zones (Peters *et al.*, 2010) 83

Table 5.4: Rate and pressure constraints for producer and injector wells (Peters *et al.*, 2010) 84

Table 6.1: Summary of the optimised inflow control parameters used in the SP feedback control strategy algorithm 123

Table 7.1: Hydrodynamic and electrodynamic properties of simulated coastal Aquifer MacAllister *et al*. 2015). Note: mAOD denote Meters above Ordnance Datum..... 148

Nomenclature

Symbol	Description	Units
C_{EC}	Electrochemical coupling coefficient	VM^{-1}
C_{EK}	Electrokinetic coupling coefficient	VPa^{-1}
C_f	Brine Salinity	M
C_r	Relative coupling coefficient	[-]
C_{TE}	Thermoelectric coupling coefficient	VK^{-1}
C	Revenue/Cost	US$/BOE or US$/Mscf
D	Diffusion coefficient	m^2s^{-1}
D_c	Initial installation cost of well	US$
G	Percentage gain	%
SP	Self-Potential	mV
V	Volume	STB or Mscf
W	Watercut	[-]
NPV	Net present value	US$
e	Charge on an electron	1.602×10^{-19} C
g	Gravitational acceleration	ms^{-2}
h	Heat flux	Wm^{-2}
j	Charge flux	Am^{-2}
k	Permeability	md
k_B	Boltzmann constant	$= 1.38\times10^{-23}JK^{-1}$
k_{rw}	Water relative permeability	[-]
L_{EC}	Electrochemical coupling term	$AM^{-1}m^{-1}$
L_{EK}	Electrokinetic coupling term	$APa^{-1}m^{-1}$
L_{TE}	Thermoelectric coupling term	$AK^{-1}m^{-1}$
Φ_w	Water potential	Pa
q_w	Flow of water	ms^{-1}
Q	Heat of transport of chloride ions	JM^{-1}
S_i^0	molar partial entropy	$JK^{-1}M^{-1}$
t_i^0	Hittorf transport number	[-]
T	Temperature	K
U	Electrical potential	V

κ	Thermal conductivity	$Wm^{-1}K^{-1}$
σ	Conductivity	Sm^{-1}
S	Saturation	[-]
ϕ	Potential	Pascals (Pa)
Π	Inflow multiplier	[-]
n	total	[-]
t	time	years
k	Annual discount rate	% per annum

Chapter 1

Introduction

"Smart wells" in the broad sense are nonconventional wells equipped with instrumentation along the production tubing, which allows for constant observation and regulation of inflow rates and pressures (Robison, 1997). Over the past decade, the use of smart wells in practical applications has been on the increase due to improvements in reliability of downhole equipment, as well as developments in their functionality. For example, downhole instrumentation can transform a horizontal or deviated monobore well into a smart multi-segmented well, allowing for commingled production. By regulating the flowrate or pressure along the segments of the wellbore in a waterflooded oilfield, sweep efficiency can be improved and production of unwanted fluids can be delayed. These developments, combined with the growing pressure on oil companies to improve controllability of wells to improve safety and recovery of producing fields, have led to a rising interest in the use of smart wells for effective reservoir management and production optimisation (Kleef *et al.,* 2001; Addiego-Guevera *et al.,* 2008; Al-Khelaiwi *et al.,* 2010).

Control of smart well valves can be 'reactive' or 'proactive'. Reactive control strategies are feedback methods, which adjust valve settings based on measurements of adverse fluid changes (such as unwanted water) observed at the well. Proactive control strategies are triggered by variations in fluid flow at some distance away from the well observed by measurements or predicted by a reservoir simulation model (Kharghoria *et al.*, 2002). Various studies have been carried out to show how reactive and proactive control strategies can be used for effective reservoir and well management in different production settings (e.g. Brouwer, 2001; Brouwer *et al.*, 2004; Yeten *et al.*, 2004; Aitokhuehi and Durlofsky, 2005). However, the main issue faced with the control of smart wells is the challenge of trying to incorporate reservoir uncertainty into control decision workflows (Elmsallati *et al.*, 2005; Ebadi and Davies, 2006). Proactive model-based control strategies take control actions using predictive reservoir models, which are usually uncertain and may lack the

required spatial and temporal resolution to make inflow control decisions. Reactive feedback control, on the other hand, can mitigate problems associated with uncertainties but the drawback with this is that control actions are only taken after adverse changes of flow occur at the well (Kharghoria *et al.,* 2002; Elmsallati *et al.,* 2005; Ebadi and Davies, 2006; Addiego-Guevera *et al.,* 2008; Dilib and Jackson, 2012). However, if encroaching unwanted fluids such as water can be sensed and located before the waterfront reaches the production well, proactive feedback control actions can be taken in order to minimise or prevent water production (Jackson *et al.,* 2012).

The use of 4D seismic has been widely embraced in the oil and gas industry and is the only widespread surveillance method currently used in monitoring saturation changes. However, the initial cost of installation can be high, so only economically important assets can justify the use of this in practice. The measurement of self-potential (SP) signals downhole in production wells is an encouraging technique that can be used to image waterfronts and has the potential of detecting water encroachment tens to hundreds of meters away from the well (Jackson *et al.* 2012). SP signals arise in order to preserve electrical neutrality when charge separation arises due to gradients in pressure, temperature and chemical concentration of the reservoir brine phase (Gulamali *et al.* 2011). These gradient effects are commonly encountered during waterflooding processes and can be assessed numerically to predict the SP generated downhole in oil production wells. The numerical modelling of SP can be used as a cheap alternative to carrying out actual field experiments and serve as a proxy for predicting the SP measurements taken during waterflood production. A closed-loop 'proactive' feedback control strategy triggered by downhole SP measurements could then be developed. The aim of this project is to demonstrate whether proactive feedback control using SP measurements can be used to reduce the negative consequences associate with production of unwanted fluids.

1.1 Aims and Objectives

The aim of this project is to develop a closed-loop, 'proactive' feedback inflow control approach based on downhole SP measurements, and to quantify the potential benefit of this approach in different production and reservoir scenarios. An electrodynamic model will be developed using a finite-difference scheme and will incorporate earlier and on-going electrokinetic, thermoelectric and electrochemical experimental measurements being carried out by the Smart Wells and Reservoir Monitoring research group at Imperial College. The electrodynamic model will be interpreted to yield quantitative information to make proactive inflow control decisions. The models will be used to

1. Demonstrate that 'proactive' feedback control can be used to reduce the negative production consequences associated with production of unwanted fluids.
2. Investigate the benefit of saturation monitoring and 'proactive' inflow control, from technically less complex approaches involving single zone downhole monitoring and on/off control valves, to technically more complex approaches involving multi-segment wells and infinitely variable control valves.
3. Quantify the benefit of feedback control in the scenarios tested, using a customized objective function which accounts for the additional installation and operating costs of the monitoring and control technology.
4. Demonstrate that reservoir monitoring using SP measurements can be useful in making critical decisions in oil and gas exploration and production applications and other non-oil related fields.

1.2 Outline

Identifying the additional value generated by the use of proactive feedback control over reactive feedback control and proactive model-based control strategies requires an understanding of recent advances in smart well control technology. Various smart well control strategies are discussed in chapter 2; a brief overview of the origin of self- potential is also discussed.

In Chapter 3, the control volume finite difference (CVFD) SP solver that will be used to numerically model the SP signals generated during water flooding is developed. This allows for data from the ECLIPSE hydrodynamic model, which also uses a CVFD numerical method, to be used directly. The SP solver differs from previous methods used

by Saunders *et al.* (2008) and Jackson *et al.* (2012) which uses a finite element (FE) SP solver. The solver is tested using a simple 1D hydrodynamic model and a similar 3D reservoir model, used by Saunders *et al.* (2008) to verify that the SP solver has been successfully developed.

In Chapter 4, a new closed-loop feedback inflow control strategy, based on downhole measurements of self-potential (SP) is highlighted and the performance is compared against model-based and watercut feedback inflow control strategies. The inflow control strategies are compared by simulating production from a single horizontal well in a thin oil column model and accounting for model uncertainties using an ensemble of reservoir models.

Chapter 5 explores the benefits of monitoring waterfront encroachments at production wells during waterflooding using downhole measurements of SP by numerical modelling using a synthetic Brugge Field multi-well reservoir model. In Chapter 6, the performance of the SP feedback control strategy in the Brugge model is quantified and benchmarked against a heuristic inflow control strategy and watercut based feedback inflow control strategies.

In Chapter 7, we investigate whether SP measurements can be useful in making critical decisions in oil and gas exploration and production applications. The use of SP monitoring is extended to other non-oil related fields, to see whether saline intrusion can be monitored in coastal aquifers.

Chapter 2

Literature Review

2.1 Introduction

In order to realise the full benefits of smart well technology for reservoir management and/or production optimisation, three key components are required: (i) the ability to regulate inflow and outflow of fluids from the reservoir into each segment of the well using adjustable (closed-loop control strategies) or fixed (open-loop control strategies) downhole chokes; (ii) the ability to monitor reservoir and well operating conditions, such as temperature, pressure and phase composition using downhole and/or surface sensors, and (iii) a control algorithm which integrates the available information of the reservoir and well state to determine the best valve settings for optimal oil recovery (Algeroy *et al.,* 1999; Glandt, 2005; Crow *et al.* 2006; Mitchell, 2008). The combination of these three components distinguishes smart completions from conventional completions as they offer the ability to interactively address a situation without carrying out costly workover operations. Figure 2.1 shows a schematic of a smart well completion with multiple ICVs in an extended-reach, multilateral well.

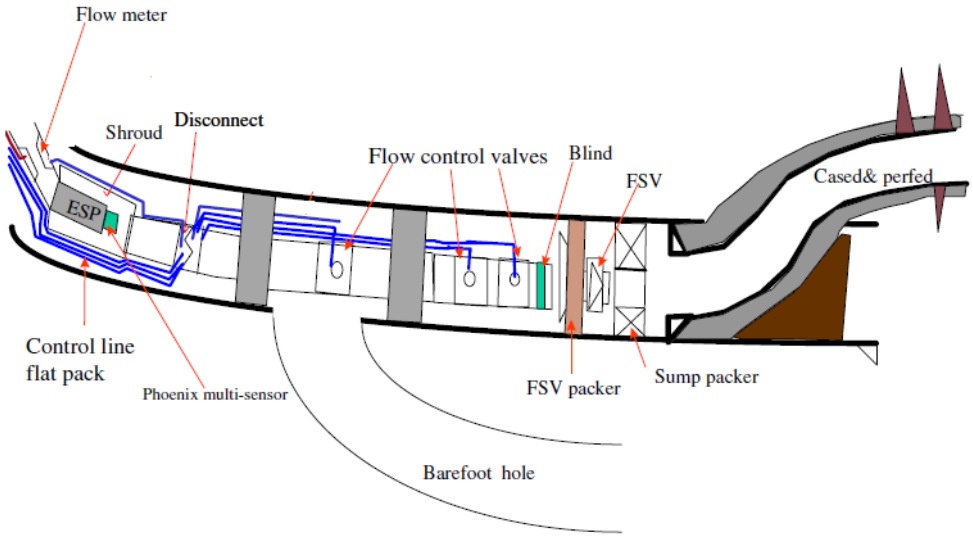


Figure 2.1: Schematic of Smart Completion (Gai, 2001)

Inflow control strategies for smart wells are divided into two main categories which can either be open or closed-loop (Figure 2.2; Addiego-Guevera *et al.,* 2008). Open-loop control is prompted by the use of fixed ICDs, which are sized and configured before installation, based on reservoir conditions and predicted reservoir performance. ICDs are fixed choking devices that can be used to equalise the inflow profile (typically along horizontal wells) by creating a further frictional pressure drop between the well casing and tubing, and are usually used as part of the well completion. For this system to be effective, the uncertainties associated with the reservoir model need to be small, and the model needs to provide high confidence in prediction. However, differences between the real and forecasted fluid inflow could mean that the ICD settings are no longer optimal, and could be unfavourable to the well performance (Algeroy *et al.,* 1999).

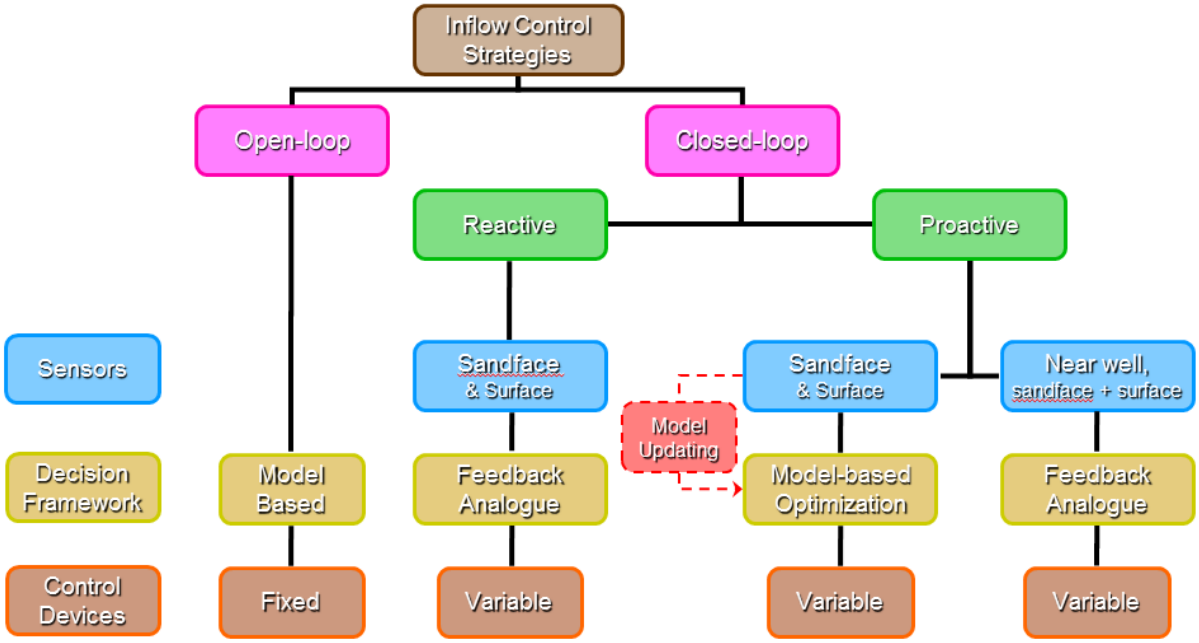


Figure 2.2: Schematic organisation of operating control strategies for intelligent wells (Addiego-Guevara et al. 2008)

Alternatively, closed-loop control is enabled by the use of variable inflow control valves (ICVs), which are fitted across segments of the wells. Unlike open-loop control, this mode of control is particularly beneficial when there are uncertainties associated with the reservoir and/or well models. The valve settings can be adjusted to optimise inflow in reaction to data acquired during production, using downhole sensors, or based on predictive well and reservoir simulation models. Closed-loop 'reactive' control strategies adjust the configuration of ICVs in reaction to the influx of unwanted fluids into production wells or

the adjacent reservoir region (Dilib and Jackson, 2012). Conversely, closed-loop 'proactive' control strategies adjust the configuration of ICVs in reaction to variations in flow measured or forecasted in the reservoir at some distance away from the well (Naus, 2004; Yeten *et al.,* 2004). The benefit of proactive control strategies is that unwanted fluids can be prevented from affecting production at the well (Aitokhuehi and Durlofsky, 2005).

The common challenge faced by both open- and closed-loop control strategies is the task of finding the optimal ICD/ICV settings that maximise an objective function. The exact scope of optimisation can vary depending on many factors such as geological features, well design and operating constraints. The scope could also depend on whether to optimise the production and injection rates on a short term or a long term basis, over the life of the reservoir (Ebadi and Davies, 2006; Almeida *et al.,* 2010). The problem becomes more computationally difficult when the number ICVs increases, or if the number of wells and their location are considered in the optimisation process. In this section, a review of studies carried out to address various optimisation problems using closed-loop proactive (model-based and feedback) and reactive feedback control strategies is presented.

2.2 Proactive Model-based Control Strategies

Proactive model-based control, otherwise known as "defensive control", uses predictive reservoir models to determine the optimal valve settings required to maximise or minimise an objective function. In doing so, valve settings can be adjusted to prevent the occurrence of problems associated with production of unwanted fluids, rather than after breakthrough has occurred. Several studies have demonstrated how model-based control strategies can be used for reservoir management and production optimisation (e.g. Brouwer *et al.*, 2004; Naus *et al.,* 2004; Yeten *et al.*, 2004; Aitokhuehi and Durlofsky, 2005; Elmsallati *et al.*, 2005a; Sarma *et al.*, 2006; Meum *et al.,* 2008; Chen *et al.*, 2010). The general approach of applying proactive model-based control strategies is shown in Figure 2.3 (Nævdal *et al.*, 2006). The optimisation process involves finding the set of control actions such as well rates that optimises the objective function on an approximated system model. The controls are then used to operate the real system over the control step, which affects the production from the reservoir and provides new information on the reservoir state (such as bottomhole pressure and water cuts). Measurements taken during production can be used to update the reservoir model so that uncertainties associated with the model can be reduced.

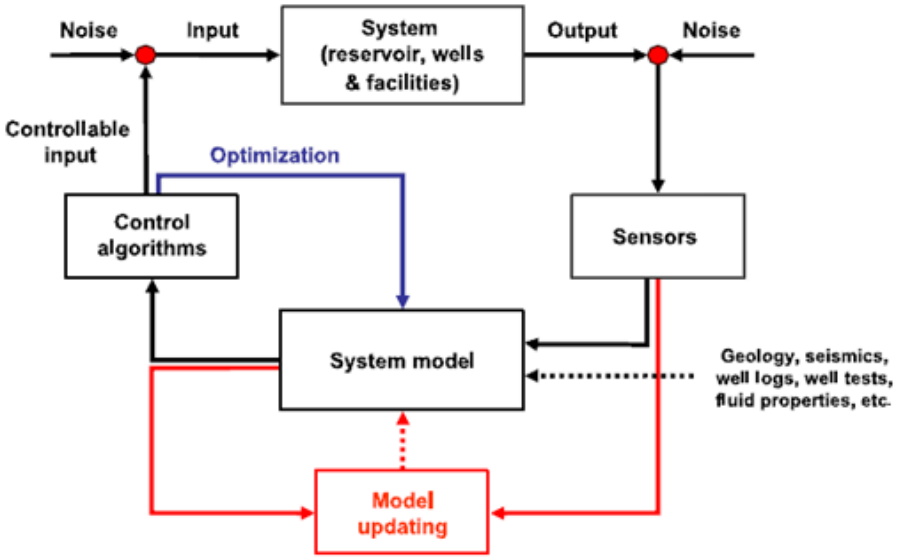


Figure 2.3: Model-based, closed-loop control process (Nævdal *et al.*, 2006)

Early studies of model-based control strategies used gradient-based optimisation algorithms, externally linked to reservoir simulators, in order to determine the ICV configuration which maximises production over the production life of the reservoir (Yeten *et al.*, 2002, 2004; Naus *et al.*, 2004; Elmsallati and Davies, 2005). These gradient-based optimisation methods require derivate information about the change in the objective function due to changes in the valve settings. Gradient-based optimisation was first applied to inflow control by Yeten *et al.* (2002, 2004). They adopted a nonlinear conjugate gradient (CG) optimisation algorithm to determine the reservoir performance for particular valve settings by means of forward simulations. The process is carried out by distributing the total simulation period into several optimisation steps, during which the valve setting is optimal for the entire simulation (the optimisation steps are different from the simulation time steps). The aim of this method is to avoid using valve settings that are optimal during a specific period but will cause harmful effects in the future. The overall optimisation technique was applied to several example problems comprising of different well types and geological models, as well as different geostatistical realisations of a given model, and showed improved performance of up to 65% over conventional production. Naus *et al.* (2004) developed a short term optimisation strategy for commingled operation with variable ICVs using sequential linear programming (SLP) which was tested on two simplified real reservoir models. The entire simulation period is divided into a number of optimisation steps during which the ICV settings are varied to determine the maximum oil production rate achievable. The ICV settings are then updated in the reservoir model and

run until the next optimisation period. In both test cases, the optimisation resulted in accelerated oil production, but the ultimate recovery was reduced.

Practical optimisation problems on real fields usually involve very complex reservoir models, production or facilities-associated constraints, and many unknowns, which can make numerical calculation of gradients using forward simulations for the optimisation process slow, due to the large number of parameters used. In order to circumvent this problem, Brouwer and Jansen (2004) presented early work on the application of optimal control theory for ICV optimisation during waterflooding. This methods allows for the objective function, with all the constraints (e.g. dynamic state equation, well control constraints and initial conditions) to be scripted in an augmented adjoint equation, using a set of Lagrange multipliers, which enables the gradients of the objective function with respect to the controls to be obtained efficiently (Stengel, 1985). A simulator is used to compute the forward model equations for all the time steps using the initial conditions and control strategies. The objective function is calculated with results from the forward simulation and the adjoint equation is solved using the stored dynamic states to determine the objective function gradients for all control steps. An optimisation algorithm is used to choose a new control setting, and the process is repeated till all the gradients are close to zero. The new control settings take the dynamic state from one optimisation step to the next. Brouwer and Jansen (2004) tested the method for wells operating on BHP and flow rate constraints and concluded that wells operating on flow rate constraints have a larger scope for accelerating production and cumulative recovery, while BHP constraints mainly reduce water production. However, coding of the adjoint model can be difficult and time consuming as the method is reliant on access to forward simulation code. Sarma *et al.* (2006) proposed an adjoint-based algorithm which is independent of the forward simulation reservoir model, and incorporates nonlinear constraints which affect the control bounds within the adjoint equation, in order to improve the computational efficiency.

Further development of closed-loop reservoir management techniques aimed to address the impact of model-based reservoir uncertainty, by updating reservoir and well models with real-time production measurements, obtained from downhole in-well sensors. Aitokhuehi and Durlofsky (2005) performed inflow control optimisation using the gradient-based optimisation algorithm of Yeten *et al.* (2002, 2004), in combination with multiple-point geostatistics (MPS) to update the reservoir model at each optimisation step. The MPS method involves gradual alteration of the initial permeability and porosity until the

production data is matched. The combined technique resulted in production closely matched with results attained using optimised valves with known geology, showing the possible benefits of the approach. Nævdal *et al.* (2006) demonstrated how the use of an ensemble Kalman filter technique for updating permeability fields in the reservoir models, in conjunction with an adjoint-based optimisation algorithm, can be used to significantly improve the NPV during a waterflood process. The ensemble Kalman filter is an ensemble of models that are continuously updated as new production data are obtained. The initial pressure and saturation are assumed to be in a known equilibrium state, but static parameters such as the permeability fields for each of the ensemble models are determined using a mixture distribution. The mean of the updated models, which reflects the model that most likely represents the state of the reservoir, are then used with the adjoint model. Sarma *et al.* (2006) used a Bayesian inverse modelling in conjunction with an adjoint solver of the unknown parameter field in terms of a Karhunen-Loeve (K-L) expansion. The representation is used to determine a set of parameters such as permeability, in terms of two-point statistics. This ensures that the permeability values used in the history matched model lie within a range of values that maintains some degree of geological realism.

The optimisation methods previously discussed rely on gradient-based optimisation which tends to find local, rather than global minima. By using stochastic algorithms like genetic algorithm, the convergence problems can be mitigated. Almeida *et al.* (2010) used a genetic algorithm, based on chromosome representation to formulate a valve control strategy. The chromosome representation uses a mutation and evolution process to formulate a control strategy for all the valves, at each optimisation time step. To account for uncertainties in the reservoir model, the NPV is calculated over three Monte-Carlo realisations of 'best-case', 'most-probable' and 'worst-case' models. The genetic algorithm selects the solution, which averagely represents the best solution over the three scenarios. They tested this genetic method on two channelized permeability fields and oil production was shown to be closely matched to the results attained using optimised valves with known geology. However the problem with using genetic algorithms is that they do not guarantee monotonic minimisation/maximisation of the objective function, and therefore would typically require a greater number of function evaluations than gradient-based optimisation methods for a similar case.

Practical optimisation problems typically comprise complex reservoirs with a lot of unknowns and many nonlinear constraints, which might not be captured in the reservoir

model, thus making model-based optimisation impractical. Also, reservoir models are rarely predictive over the spatial and temporal resolution, required to make inflow control decisions (Dilib and Jackson, 2012). Even traditional history matched models might be non-effective as the updated model may replicate the production history, but have no predictive capability because the model might have been over fitted by fine-tuning many unknown parameters using fewer elements (Tavassoli *et al.,* 2004; Nævdal *et al.,* 2006; Carter *et al.,* 2006). There is also a cultural problem in the oil and gas industry associated with the use of reservoir model predictions for making control decisions. Production engineers are usually apprehensive in using control instructions based on reservoir model predictions, especially when the current performance of the reservoir is satisfactory. The combinations of these factors have prevented the use of model-based control strategies in practical optimisation cases.

2.3 Reactive Control Strategies

Reactive control strategies are triggered by measurements of adverse changes in fluid flow moving into and within a well, and could be in the form of rate cut-back at surface (e.g., surface choking) or downhole (e.g., closing segments of the well with high water-cut measurements using discrete or continuous valves) (Kharghoria *et al.*, 2002; Dilib and Jackson, 2012). The advantage of reactive control over model-based control strategies is that they can potentially mitigate problems due to unforeseen events associated with uncertainties in the understanding of the reservoir. The approach is applicable when surface and/or downhole sensors can provide real-time information on the state of the well. The various studies presented in this subsection demonstrate how reactive control strategies can be employed to improve recovery and also account for uncertainties associated with reservoir model prediction.

Brouwer *et al.* (2001) presented an optimisation method that maximises sweep during a waterflood process, using smart horizontal production and injection wells in two dimensional, horizontal reservoir models with simple large-scale heterogeneities. Initially, injection and production rates of the ICVs in the wells were kept constant throughout the displacement process, until a high water-cut value was observed at the producers. The waterflood process was then improved by closing segments of the well with the highest productivity index (PI), and adding the flow rate recorded before shut-in to the segments of the well with the lowest PI. This process allows for water breakthrough at the production

well to be delayed by changing flow paths. Elmsallati *et al.* (2005b) showed how reactive control of ICVs can improve production from horizontal wells in a rich gas-condensate field, where the frictional pressure drop along the wellbore is greater than the producing drawdown. This effect generates a skewed pressure profile along the wellbore, which causes most of the production to occur at the heel of the well instead of being spread over the wellbore length. They were able to improve oil production by choking the segments of the well with the highest gas/oil ratio to maximise oil production whilst meeting the maximum gas production constraints.

Konopczynski and Ajayi (2007) used a nodal analysis technique to obtain the optimal performance of a multi-segment well, by identifying the intersection of the flow performance curve (pressure drop vs. flow rate) of the ICVs with the combined inflow performance for each of the producing segments of the reservoir. By reviewing all the possible ICV configurations, a flow performance map of total production, water cut and net oil production was generated and used to determine the setting of the ICV that optimises oil production. Grebenkin and Davies (2010) analysed the impact of smart well completions on oil production uncertainties. A probabilistic approach that takes into consideration the main uncertainties in the description of the reservoir and production processes (parameters such as the petrophysical properties, fluid contacts, relative permeabilities, faults and aquifer strength), was implemented. For all the reservoir realisations, they simulated production using conventional and smart wells. The smart wells are controlled on an ad-hoc basis by choking intervals with high water cut values. Probability density curves were generated to show the oil production distribution for geological and dynamic uncertainties. The results showed that smart wells gave improved oil production, in addition to a decrease in its variation in all the models.

More recently, Dilib and Jackson (2012) developed a closed-loop, direct feedback control strategy designed to work across a range of reservoir and production settings. Their method differs from previous reactive strategy studies, in which the control actions were carried out on an ad-hoc basis (Brouwer *et al.,* 2001; Elmsallati *et al.,* 2005b; Grebenkin and Davies, 2010). Instead, they use model predictions to determine an optimised direct feedback control relationship between measured data and inflow control settings. They compared the performance of their feedback control methods to a model-based control strategy, which assumes perfect knowledge of the reservoir characteristics. Their results suggest that closed-loop control based on direct feedback between reservoir monitoring

and inflow valve settings can yield close-to-optimal gains in net present value (NPV) compared to uncontrolled production, even when the reservoir does not perform as forecasted. The various reactive feedback control strategies discussed, show how uncertain reservoir behaviour can be mitigated when key properties are not captured within the reservoir model.

2.4 Proactive Feedback Control

Although reactive feedback control strategies may yield improved or accelerated production, control actions are only taken after some adverse flow change is detected at the well, which may not yield optimal inflow control. By contrast, proactive feedback strategies take a pre-emptive control approach; if the encroachment of unwanted fluid such as water can be sensed and located before it reaches the well, inflow might be regulated to mitigate or minimise water production (Kharghoria *et al.,* 2002). The efficiency of these strategies, however, depends on the ability to image the saturation variation within the reservoir, away from the well. Current downhole monitoring sensors measure fluid distribution, pressure and temperature only within the wellbore, so are mostly suitable for reactive control strategies. As a result, there has since been increased research effort to find new monitoring methods that could image reservoir saturation variations at greater distances away from a production well (Glandt, 2005; Miorali *et al.*, 2011).

4D seismic has been widely embraced in the oil and gas industry and is the only widespread surveillance method currently used in monitoring saturation changes. Saturation variation across a reservoir can be imaged using the differences in sub-surface time-lapse seismic images (Glandt, 2005; Watts *et al.,* 2006). With the aid of permanently installed geophones, accurate and frequent seismic surveys can be carried out. Although they deliver poor vertical spatial resolution, they may provide better resolution than simulation model predictions. However, the initial cost of installation can be high, so only economically important assets can justify the use of this in practice (Watts *et al.* 2006). More recently, Miorali *et al.* (2011) considered borehole radar imaging as a technique capable of potentially sensing fluid saturation variations adjacent to production wells and which provides better spatial and temporal resolution than 4D seismic imaging. Borehole radar is a high resolution electromagnetic (EM) sensor for detecting electrical discontinuities in rock formations. Variations in water saturation generate partial EM wave reflections, which can be detected using the radar system. Miorali *et al.* (2011) concluded that a monitoring

depth of only several metres can be realised for relatively low conductivity reservoirs, which makes it applicable particularly in cases where the depth to be investigated suits the possible depth of study for a radar system, such as thin oil rims or steam supported gravity drainage processes.

Time lapse resistivity measurements using permanent downhole arrays can be used to image reservoir saturation adjacent the well (Kleef, 2001; Khargorai *et al.*, 2002; Glandt, 2005; Dutta and Badr, 2008). Time lapse resistivity measurements are obtained by injecting current into the reservoir, to measure resistivity differences between the segments of the well where the electrodes have been fitted and the invading medium to be monitored (Figure 2.4). The use of resistivity arrays for proactive feedback control was successfully applied in a water shutoff operation in a commingled, cased-hole production well, in the Bahariya formation of The Western Desert, Egypt (Dutta and Badr, 2008). Intervals of the well with low values of measured resistivity were shut, allowing production from other well intervals. The corrective water shut-off operation of well intervals improved oil recovery from 540 to 2250 bbl/day with a substantial reduction in water cut from 84% to 0.5%. Nevertheless, the depth of imaging waterfronts from a production well using time lapse resistivity measurements is restricted to only a few meters away from the well, similar to the borehole radar technique.

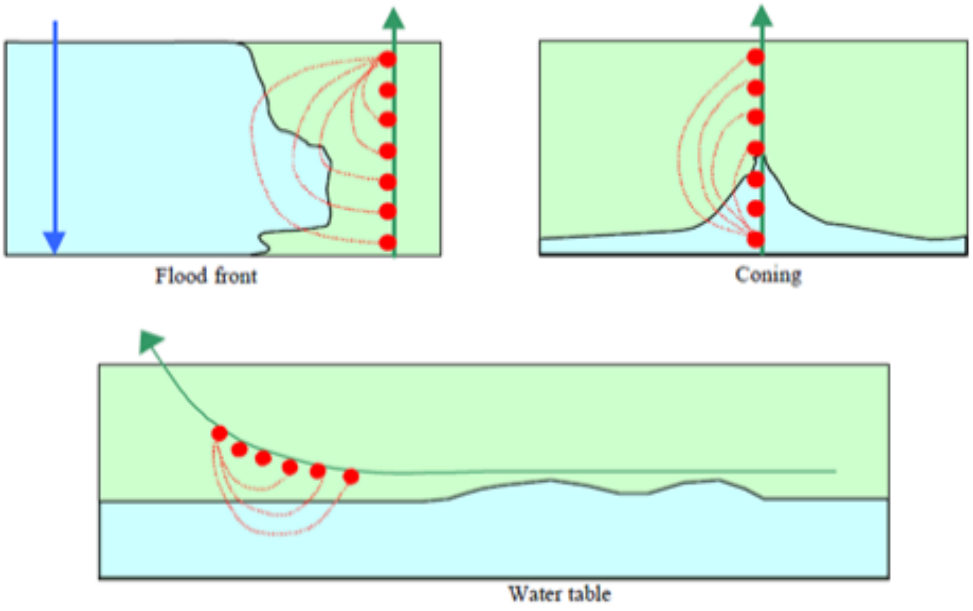


Figure 2.4: Permanent monitoring applications for resistivity array (Glandt, 2005)

SP signals can also be measured using permanent downhole electrode arrays. Various experimental and numerical results suggest that permanent downhole measurement of SP is an encouraging technique used to image encroaching waterfronts across reservoir formations (Saunders *et al.,* 2006, 2008; Chen *et al.,* 2006; Jaafar *et al.,* 2009; Vinogradov *et al.,* 2010; Jackson *et al.,* 2011; Jackson *et al.,* 2012). SP signals are generated due to related reservoir fluid flow. Numerical modelling by Jackson *et al.* (2012) showed that the magnitude of SP produced during a waterflood process within a hydrocarbon reservoir can be measured significantly above background noise (of approximately 0.5 mV) and could potentially be used to sense and characterise an encroaching water front before it arrives at the production well (tens to hundreds of meters away) as opposed to previous imaging techniques discussed. Figure 2.5 shows a cross-section of water saturation within a heterogeneous 3D reservoir model at different time steps, with the corresponding SP signal measurements expected at the production well. The waterfront flows through a high-permeability layer. The SP signal measured along the well increases as the waterfront gets closer to the well and the profile of the SP signal measured across the well mimics the shape of the encroaching waterfront (figure 2.5).

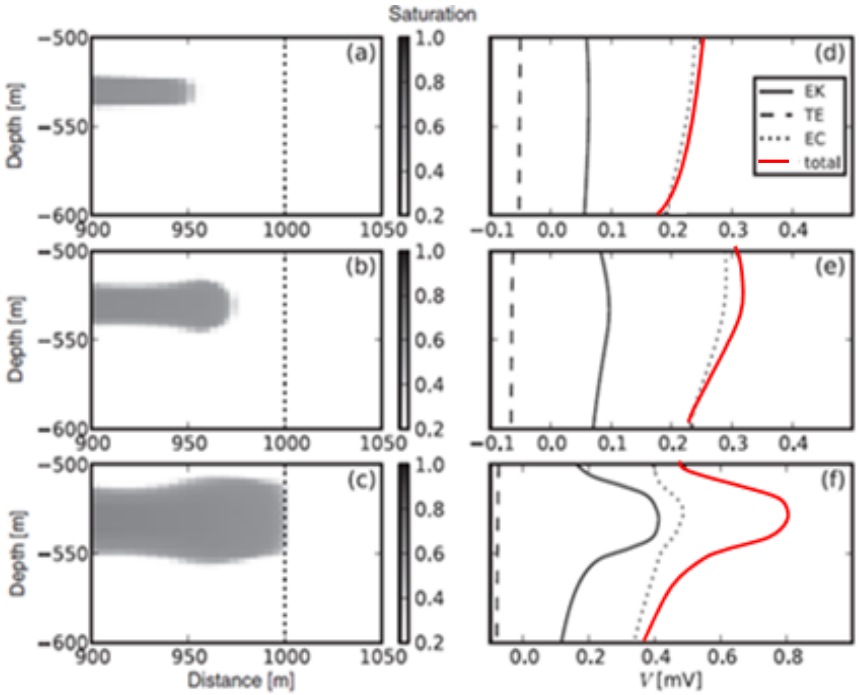


Figure 2.5: 3D reservoir model cross-section showing water saturation when water front is (a) 50 m away from the production well, (b) 25 m away from the well and (c) at breakthrough. The vertical dashed line represents the well. Plots (d) to (f) show the corresponding EK, TE and EC components of the SP signal measured at the production. well.

Two field tests were successfully carried out by Chen *et al.*, (2006) in a shallow oil producing field in Indiana, U.S.A., in order to examine the effectiveness of using electrode arrays to measure SP in response to pressure transients. The first measurements were taken in a vertical oil production and water injection well, while the second set was taken in a horizontal well drilled through a thin oil column. They observed that boreholes are essentially isobaric regions and do not give comprehensive information of the pressure transients within a heterogeneous reservoir formation, making it difficult to obtain SP transient measurements. However, by dividing the wellbore into different hydraulic zones, SP transients measured in both the horizontal and vertical wells were able to deliver comparable information to pressure transient test results, with high spatial resolution. Based on the positive results of both Chen *et al.* (2006) and Jackson *et al,* (2012), measurements of SP signals during production can be considered as a viable option for imaging reservoir saturation at distance from the well during proactive feedback control strategies; this will be the focus of research in this project.

2.5 Origin of Self- Potential

Self-potentials (SP) are naturally occurring electric potential differences generated when separation of charges occurs due to gradients in pressure (electrokinetic or streaming potential), chemical composition (electrochemical potential), and temperature (thermoelectric potential) (Jackson *et al.,* 2012). Between the solid-fluid interface of a water-wet porous reservoir rock system, with brine acting as an electrolyte, charge separation occurs when the charged rock surfaces which are (typically) negatively charged attract positive counter ions from the adjacent brine, leaving an excess of positive charge in the brine. The charge arrangement between the rock and brine interface is referred to as the electrical double layer (EDL) (e.g., Hunter, 1981; Jackson 2012). The EDL is made up of a Stern layer, which holds the fixed positive charge, and a diffuse layer of mobile excess positive charge which can move with the fluid. Also, variations in the ionic concentration and temperature of the brine will lead to salinity and temperature gradients, along which ions can diffuse. Ionic advection due to the relative contribution of pressure, salinity and temperature gradients creates an electrical current which is balanced by a conduction current. The SP is the electrical potential that is required to maintain the overall electrical neutrality (Revil, 1999).

By neglecting the relations between fluxes other than as a result of charge separation, the constituent equations that relate the transport of ions due to pressure, temperature and concentration gradients in the water phase (brine) can be described as (Jackson *et al.,* 2012):

$$\begin{bmatrix} j \\ q_w \\ h \\ v \end{bmatrix} = -\begin{bmatrix} \sigma_{fs}(S_w) & L_{EK}(S_w) & L_{TE}(S_w) & L_{EC}(S_w) \\ L_{EK}(S_w) & \dfrac{kk_{rw}(S_w)}{\mu_w} & 0 & 0 \\ L_{TE}(S_w) & 0 & \kappa(S_w) & 0 \\ L_{EC}(S_w) & 0 & 0 & D(S_w) \end{bmatrix} \begin{bmatrix} \nabla U \\ \nabla(P_w - \rho_w g z) \\ \nabla T \\ \nabla C_f \end{bmatrix} \quad (2.1)$$

here j is the current (A), σ_{fs} is the electrical conductivity of the saturated porous media $(\mathrm{S/m})$, ∇U is the electrical potential (SP) gradient (V/m), q_w is the flow rate $(\mathrm{m/s})$, k is the absolute permeability of the porous media (m^2), k_{rw} is the relative permeability of the water phase, μ_w is the dynamic viscosity of the water phase (Pa.s), $\nabla(P_w - \rho_w g z)$ also represented as $\nabla\Phi$ is the pressure gradient above hydrostatic pressure (Pa), h is heat flux (W/m^2), κ is thermal conductivity (W/m.K), ∇T is the temperature gradient (K/m), v is concentration flux ($M.s^{-1}/m^2$) and D is the diffusion coefficient (m^2/s). The saturation fraction $S_w \in [0,1]$ is the fraction of the pore space occupied by brine, on which the rock properties are dependent. The terms L_{EK}, L_{TE}, and L_{EC} are the electrokinetic (EK), thermoelectric (TE) and electrochemical (EC) coupling terms respectively. The on-diagonal terms represent Ohm's law, Darcy's law, Fourier's law and Fick's law respectively. The non-zero, off-diagonal terms describe the cross-coupling between the constituent equations arising due to the separation of charge. The cross-coupling term for each component of SP is a function of the saturated rock electrical conductivity σ_{fs} and a coupling coefficient C_x and can determined by equation 2.2.

$$L_x = \sigma_{fs} C_x \quad (2.2)$$

Subscript x is EK, EC or TE. The coupling coefficients C_x are key petro-physical properties, which can be used to determine the magnitude of the SP signal generated due to pressure, concentration or temperature gradients and possess units of VPa^{-1}, VM^{-1} and VK^{-1}, respectively. Each of the coupling coefficients are dependent on brine salinity, temperature and the "relative coupling coefficient" C_r, which is a function of the brine saturation and varies (in principle) between zero and one (Jackson 2008, 2010):

$$C_{EK} = C_{EK}|_{S_w=1} C_{r,EK} \quad (2.3a)$$

$$C_{TE} = C_{TE}|_{S_w=1} C_{r,TE} \quad (2.3b)$$

$$C_{EC} = C_{EC}|_{S_w=1} C_{r,EC} \quad (2.3c)$$

where $C_{EK}|_{S_w=1}, C_{TE}|_{S_w=1}$ and $C_{EC}|_{S_w=1}$ represent the EK, TE, and EC coupling coefficients when $S_w = 1$.

2.5.1 Electrokinetic Potential

When brine is made to flow by an external pressure gradient, some of the excess charges within the diffuse part of the EDL are transported along with the flow, resulting in an electrokinetic (EK) or streaming current (figure 2.6(a)). Simultaneously, a conduction current is established in order to balance the electrokinetic current. The associated electrical potential generated to maintain the conduction current is referred to as the EK or streaming potential (Ishido and Mizutani, 1981; Revil *et al.,* 1999). The magnitude of the EK potential generated depends on the electrical conductivity, dielectric constant, viscosity of the fluid, and the zeta potential, which is a measure of the electrical potential of the mineral surface. If the gradient of salinity and temperature are zero ($\nabla C = 0, \nabla T = 0$), equation 2.1 simplifies to

$$q_w = -L_{EK}(S_w)\nabla U - \frac{k k_{rw}(S_w)}{\mu_w}\nabla \Phi \quad (2.4)$$

$$j = -\sigma_{fs}(S_w)\nabla U - L_{EK}(S_w)\nabla \Phi \quad (2.5)$$

where the EK coupling term $L_{EK}(S_w)$ is

$$L_{EK}(S_w) = \frac{\varepsilon_w \zeta}{\mu_w F} \quad (2.6)$$

Here, ε_w is the brine permittivity, ζ is the zeta potential, and $F = \sigma_w/\sigma_{fs}$ is the formation factor, where σ_w is the conductivity of the brine. Equations 2.4 and 2.5 correspond to Darcy's law and Ohm's law respectively, when $L_{EK} = 0$. In a 1D system, the electrical current generated due to the advection of ions (EK current) is balanced at each point by a conduction current at steady state, therefore the current $j = 0$ in equation 2.5. The EK potential coupling coefficient can then be defined as (Saunders *et al.,* 2008):

$$C_{EK}(S_w) = \frac{\Delta U}{\Delta \Phi} = \frac{L_{EK}(S_w)}{\sigma_{fs}} = \frac{\varepsilon_w \zeta}{\mu_w \sigma_{fs} F} \quad (2.7)$$

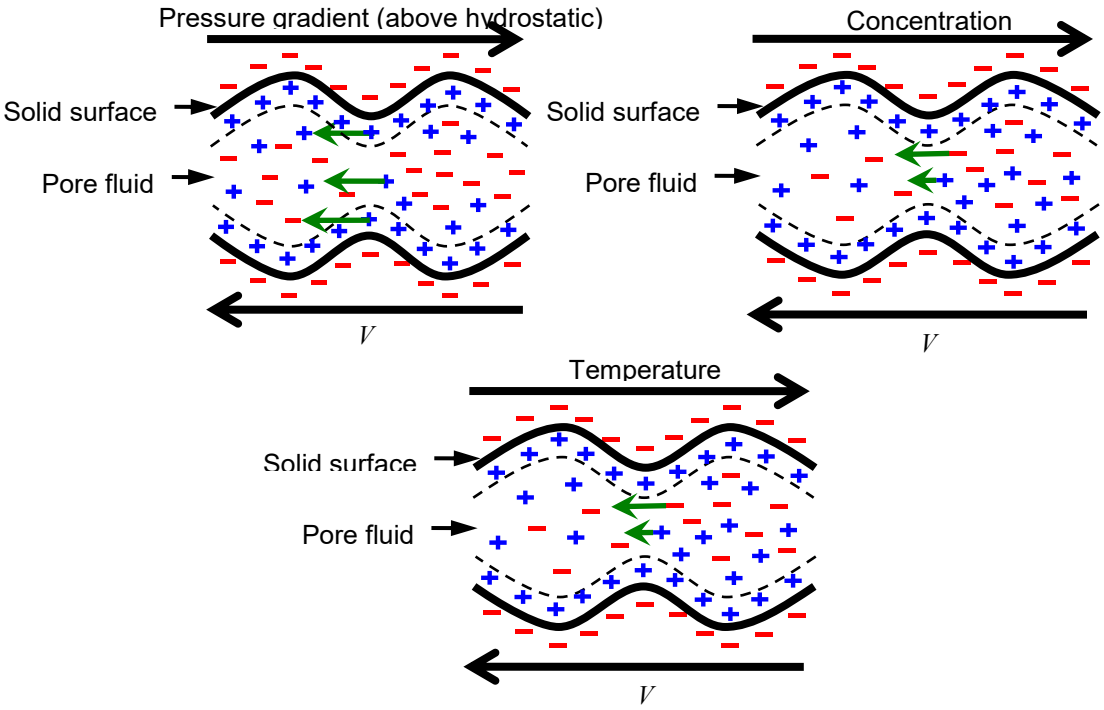


Figure 2.6: Illustration of the charge separation at the rock-water interface (with the EDL depicted in a very simplified form) and the origin of (a) EK potential, (b) EC potential, and (c) TE potential (Jackson et al., 2012).

Jackson *et al.* (2012) modelled the temperature and salinity dependence of EK coupling coefficient based on experimental data. Vinogradov *et al.* (2010) measured the EK coupling coefficient in brine saturated sandstones and investigated the effects of increasing the brine salinity. Their results were explained using the EDL thickness dependence on salinity. They noticed that the zeta potential reduces with increased salinity, which in turn means the EDL thickness reduces with salinity. Therefore, the excess charges transported with the flow will be reduced, and the C_{EK} will in turn be reduced with increasing salinity. However, the magnitude of the C_{EK} will remain more than zero up to the maximum saturated brine salinity. Vinogradov *et al.* (2010) suggested that the counter ions needed to balance the charge on the rock surfaces are not totally confined within the Stern layer. This means that the maximum charge density has been reached and is constrained by the diameter of the hydrated counter ions. As a result, the diffuse layer does not fall to zero. Instead, some of the counter ions within the diffuse layer remain mobile and an EK current can be generated due to the advection of ions; consequentially, C_{EK} can be measured.

Experimental results by Vinogradov and Jackson (2011) show that at the end of drainage with oil displacing brine (i.e., $S_w = S_{wirr}$), a non-zero EK potential can be measured. They hypothesised that the EK potential measurement is as a result of the flow of brine within the wetting layers, initiated by the hydraulic coupling between the non-wetting and wetting (brine) phases. The brine has a very high density of excess positive charge, because it is confined within the diffuse part of the EDL initiated at the rock-brine and oil-brine interfaces, leading to a substantial EK current as a result of the advection of ions, and hence a non-zero C_{EK}. Conversely, at the end of imbibition with brine displacing oil (i.e. $S_w = 1 - S_{or}$), the EK potential measured is greater than the value obtained when the porous media is fully saturated with brine (i.e. $S_w = 1$). Vinogradov and Jackson (2011) hypothesised that the increase in the C_{EK} is due to the higher excess charge transported with the flow of brine, at residual oil saturation. This is as a result of the presence of excess charge in the EDL at the oil-brine interface.

However, given that the pressure gradients observed in an oil reservoir during waterflooding is usually lower than that used during laboratory measurements of C_{EK}, Jackson *et al.,* 2012 modelled the C_{EK} at $S_w = S_{wirr}$ using equation 2.8, assuming the hydraulic coupling between the wetting and non-wetting phase is negligible. The salinity effects on the C_{EK} at $S_w = 1 - S_{or}$ is modelled using equation 2.9. The temperature effects were neglected because experimental results presented by Reppert and Morgan (2003) show that variations in temperature over the range of 20 to 120℃ will have minimal influence on the EK coupling.

$$C_{EK}(S_{wirr}) = 0 \quad (2.8)$$

$$C_{EK}(1 - S_{or}) \approx C_{EK}(S_w = 1) = -1.36 C_f^{-0.9123} \text{mV. MPa}^{-1} \quad (2.9)$$

where the brine salinity C_f is in M (mole/litre).

Ionic species diffuse along salinity gradients caused by variations in chemical composition, in isobaric and isothermal conditions (Figure 2.6(b)). The diffusivity of the ionic species depends on their mobility and the ionic species do not diffuse at similar rates. For instance, sodium ions have mobility of about 70% that of chloride ions at 25℃ (Braun and Weingartner 1985). The resultant separation of the ions produces an electrical field known as the electrochemical (EC) potential to preserve the electrical neutrality (Revil, 1999;

Jackson 2012). The origin of the EC potential can be attributed to two processes involving the diffusion of ions: (i) liquid junction (otherwise known as diffusion potential) and (ii) membrane potential. The liquid junction or diffusion potential arises when two solutions of unequal concentrations are in connection with each other. The more concentrated solution will have a propensity to diffuse into the relatively less concentrated solution. If the EDL is negligible, the total EC potential is only given by the liquid junction potential as charge displacement is mainly through the water outside the double layer. Conversely, the membrane potential is dependent upon the properties of the EDL. The (typically) negatively charged porous rock surface leaves an excess of positive charge which flows down concentration gradient creating a membrane potential. The thicker the EDL relative to the pore radius, the more likely it is that co-ions are excluded from the pore space. When all the co-ions are expelled from the pore-space the medium is termed a perfect membrane. In this case, the total EC potential will be solely given by the membrane potential. However, in natural environments, combinations of the liquid junction and membrane potential are likely to occur, which both contribute to the total electrochemical potential.

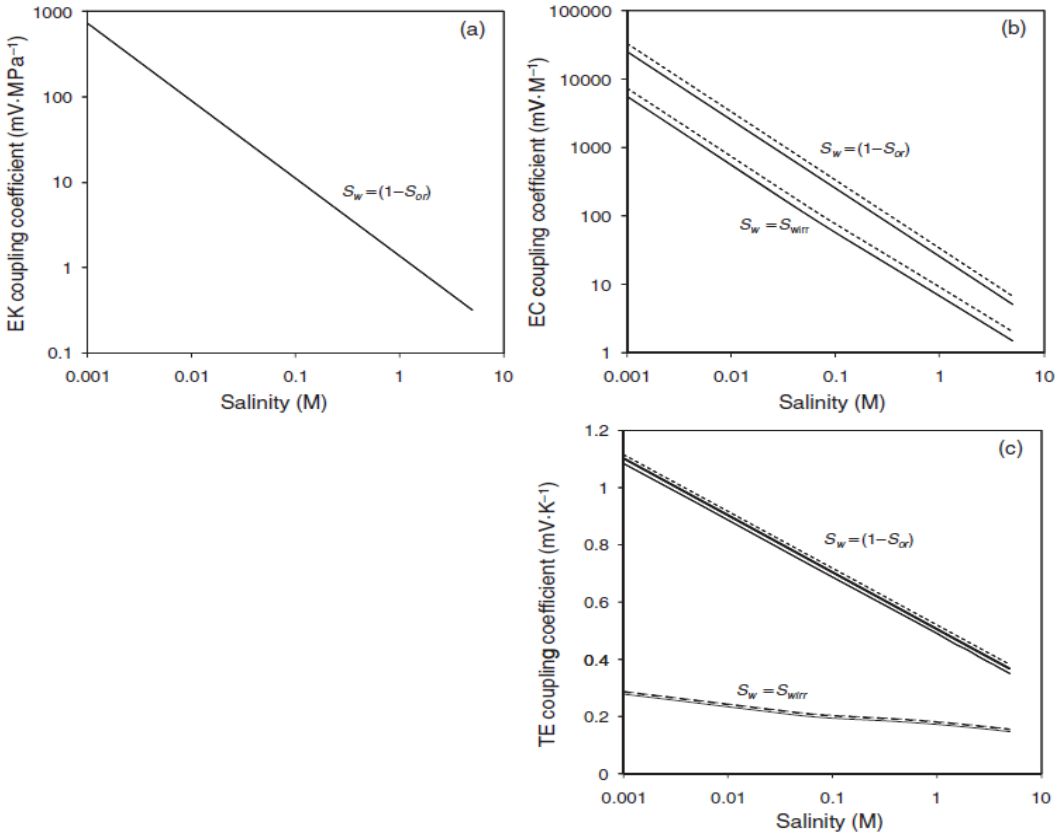


Figure 2.7: (a) C_EK vs. Salinity, derived using Eq. 2.9 (b) C_EC vs. salinity, derived using Eq. 2.13, at 293 K (solid line) and 393 K (dashed line). (c) C_TE vs. Salinity derived using Eq. 2.14 at 293 K (solid line) and 393 K (dashed line). (Jackson et al., 2012)

2.5.2 Electrochemical and Thermoelectric Potentials

The thermoelectric (TE) potential is the electrical field produced by the presence of a macroscopic temperature gradient (Figure 2.6(c); Jackson *et al.*, 2012). Ionic species also migrate down the temperature gradient and the difference in the mobilities of the ionic species in the brine will result in charge separation. This produces a TE potential to maintain electrical neutrality. Leinov *et al.* (2010) measured the salinity dependence of the TE coupling coefficient in brine saturated sandstones. Their results show that the TE coupling coefficient decreases as the salinity increases, reducing to zero at high salinity values (10^{-2} M) and has similar trends to that of an uncharged porous media. However at low salinity (10^{-4} M/litre), the TE coupling coefficient has similar trends to that of a perfect membrane.

Using the applicable formulations of EC and TE coupling coefficients presented in Ortiz *et al.* (1973), Revil *et al.* (1999), Leinov *et al.* (2010), Jackson *et al.* (2012) modelled the saturation, temperature and concentration dependence of C_{EC} and C_{TE} at saturation endpoints. At irreducible water saturation ($S_w = S_{wirr}$), the transport of electrical charge is mainly within the wetting water layers. The (typically) negative ions are mostly expelled from these wetting water layers, making the rock to act like a membrane. However, at irreducible oil saturation ($S_w = 1 - S_{or}$), the EDL thickness is relatively small in relation to the pore radius, which in turn means that ions exclusion is negligible. Therefore transport of electrical charge occurs mainly through the water outside the EDL. Based on these assumptions, the EC and TE coupling coefficients are modelled at the saturation endpoints as

$$C_{EC}(S_w = S_{wirr}) = \frac{k_b T}{e}\frac{1}{C_f} \quad (2.10a)$$

$$C_{EC}(S_w = 1 - S_{or}) = \frac{k_b T}{e}\frac{(2t_{Na} - 1)}{C_f} \quad (2.10b)$$

$$C_{TE}(S_w = S_{wirr}) = \frac{k_b}{e}\ln C_f + \frac{1}{e}\left(S_{Na}^0 - \frac{Q_{Na}^*}{T}\right) \quad (2.11a)$$

$$C_{TE}(S_w = 1 - S_{or}) = \frac{(2t_{Na} - 1)k_B}{e}\ln(C_f) + \frac{t_{Na}}{e}\left(S_{Na}^0 - \frac{Q_{Na}^*}{T}\right) + \frac{t_{Cl}}{e}\left(S_{Cl}^0 - \frac{Q_{Cl}^*}{T}\right) \quad (2.11b)$$

where k_b is the Boltzmann constant (1.381×10^{-23} JK^{-1}), e is the elementary charge of the ions (C), and T is the absolute temperature (K), Q^* represents the ionic heat of transport (J/M), S_i^0 is the molar partial entropy ($JK^{-1}M^{-1}$) and t_i is the Hittorf transport number of the ions. Substituting the values of $Q^*$and S^0 for Na and Cl in equations 10 and 11 (Agar *et al.* 1989) produces the curves presented in Figure 8b and 8c respectively, with t_{Na} and t_{cl} given by

$$t_{Na} = \begin{cases} 0.39 & C_f < 0.09\text{M} \\ 3.66 \times 10^{-1} - 2.12 \times 10^{-2}\left(\log_{10} C_f\right) & C_f > 0.09\text{M} \end{cases} \quad (2.12)$$

where $t_{cl} = 1 - t_{Na}$.

2.5.3 Relative Coupling Coefficient

The relative coupling coefficient C_{rx} (used in equation 2.3) that describes the behaviour of the coupling coefficient at intermediate water saturation values can be described by (Jackson, 2010):

$$C_{rx} = \frac{C_x(S_w) - C_x(S_w = S_{wirr})}{C_x(S_w = 1 - S_{or}) - C_x(S_w = S_{wirr})} \quad (2.13)$$

where the subscript x in equation 2.13 represents the electrokinetic, thermoelectric and electrochemical potential respectively.

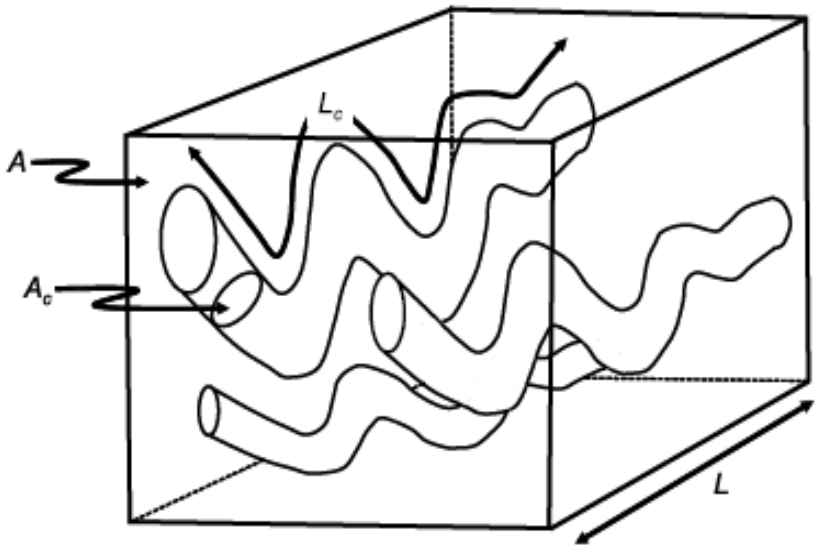


Figure 2.8: The bundle of capillary tube models (Jackson, 2010).

Jackson (2008) used a simple capillary tube model to predict the coupling coefficients at intermediate water saturations. The capillary tube model has been previously used by various researchers (e.g. Ishido and Mizutani, 1981; Jackson and Blunt, 2002) to provide insight into single-phase and multiphase transport in porous media in a variety of geological context. Figure 2.8 shows an example of the bundle of capillary tube model, where A is the area of the model, A_c is the area of the capillary tube, L is the length of the model, and L_c is the lengths of the capillary tubes. Jackson (2008) extended the capillary model to model current flow in a wetting phase *w* flow, with an immiscible non-wetting *nw* phase. The model assumes that each capillary of radius *r* is occupied by a single mobile phase, with capillaries occupied by the non-wetting phase also containing a layer of negligible thin layer of the wetting phase. Jackson (2008) obtained representations of the current *I,* saturation S_w, relative permeability k_{rw}, and electrical conductivity σ of a capillary tube model containing non-wetting and wetting fluids as a function of the number of capillary tubes *n* and radius of the tubes used in the model *r*,

$$I = \frac{Q_w \pi \Delta P_w}{4\mu_w tL} \int_{r_{min}}^{r_{wmax}} r_c^3 n(r_c) dr_c + \frac{Q_{nw} \pi \Delta P_{nw}}{4\mu_{nw} tL} \int_{r_{min}}^{r_{max}} r_c^3 n(r_c) dr_c \quad (2.14)$$

$$S_w = \frac{\int_{r_{min}}^{r_{wmax}} r_c^2 n(r_c) dr_c}{\int_{r_{min}}^{r_{max}} r_c^2 n(r_c) dr_c} \quad (2.15)$$

$$k_{rw} = \frac{\int_{r_{min}}^{r_{wmax}} r_c^4 n(r_c) dr_c}{\int_{r_{min}}^{r_{max}} r_c^4 n(r_c) dr_c} \quad (2.16)$$

$$\sigma = \frac{\phi}{t^2}\left[\sigma_w S_w + 2\sigma_{sw} \frac{\int_{r_{min}}^{r_{wmax}} r_c n(r_c) dr_c}{\int_{r_{min}}^{r_{max}} r_c^2 n(r_c) dr_c} + \sigma_{nw} S_{nw} + 2\sigma_{snw} \frac{\int_{r_{min}}^{r_{wmax}} r_c n(r_c) dr_c}{\int_{r_{min}}^{r_{max}} r_c^2 n(r_c) dr_c}\right] \quad (2.17)$$

where Q is the excess charge density, μ is the viscosity, σ_{sw} is the surface conductivity in the wetting phase, and σ_{snw} is the surface conductivity in the non-wetting phase. Using the definition of the streaming potential coupling coefficient (equation 2.7), saturation (equation 2.15), electrical conductivity (equation 2.17), and imposing a uniform pressure drop across the model for both the wetting and non-wetting phases, Jackson (2008) obtained a general expression for the multiphase electrokinetic coupling coefficient $C(S_w)$

$$C(S_w) = \left[\frac{Q_w}{\mu_w}\int_{r_{min}}^{r_{wmax}} r_c^4 n(r_c)dr_c + \frac{Q_{nw}}{\mu_{nw}}\int_{r_{min}}^{r_{wmax}} r_c^4 n(r_c)dr_c\right].\left\{8\left[\sigma_w\int_{r_{min}}^{r_{wmax}} r_c^2 n(r_c)dr_c + 2\sigma_{sw}\int_{r_{min}}^{r_{wmax}} r_c^2 n(r_c)dr_c + 2\sigma_{nw}\int_{r_{min}}^{r_{wmax}} r_c^2 n(r_c)dr_c + 2\sigma_{snw}\int_{r_{min}}^{r_{wmax}} r_c^2 n(r_c)dr_c\right]\right\}^{-1} \quad (2.18)$$

Jackson (2008) investigated the multiphase flow of an immiscible wetting phase and a non-wetting phase, with the wetting layers assumed to be immobile and volumetrically insignificant. The capillary tubes model assumed that the excess charge transported in a multiphase flow depends on the pore-scale distribution of the fluid phases. For a water-wet case, with water being the wetting phase and a second non polar second phase, Jackson (2008) assumed the charge density and electrical conductivity of the non-wetting to be negligible ($Q_{nw} = \sigma_{nw} = 0$). He also assumed that the wetting layer of water contributes to the surface electrical conductivity even in the capillaries occupied by the non-wetting phase ($\sigma_{snw} = \sigma_{sw}$). Hence at $S_w = 1$ ($r_{wmax} = r_{max}$) equation 2.18 becomes

$$C(S_w = 1) = \frac{\frac{Q_w}{\mu_w}\int_{r_{min}}^{r_{max}} r_c^4 n(r_c)dr_c}{8\left[\sigma_w\int_{r_{min}}^{r_{wmax}} r_c^2 n(r_c)dr_c + 2\sigma_{sw}\int_{r_{min}}^{r_{max}} r_c^2 n(r_c)dr_c\right]} \quad (2.19)$$

Substituting equation (2.14 and 2.17)

$$C(S_w = 1) = \frac{Q_w k}{\mu_w \sigma(S_w = 1)} \quad (2.19)$$

where $\sigma(S_w = 1)$ is the electrical conductivity when the capillaries are fully saturated with water. Therefore the relative electrokinetic potential at intermediate saturation becomes

$$C_r(S_w) = \frac{C(S_w)}{C(S_w = 1)} = \frac{\frac{\int_{r_{min}}^{r_{wmax}} r_c^4 n(r_c)dr_c}{\int_{r_{min}}^{r_{max}} r_c^4 n(r_c)dr_c}}{\frac{\sigma_w\int_{r_{min}}^{r_{wmax}} r_c^2 n(r_c)dr_c + 2\sigma_{sw}\int_{r_{min}}^{r_{max}} r_c^2 n(r_c)dr_c}{\sigma_w\int_{r_{min}}^{r_{max}} r_c^2 n(r_c)dr_c + 2\sigma_{sw}\int_{r_{min}}^{r_{max}} r_c^2 n(r_c)dr_c}} \quad (2.20)$$

The surface conductivity term at partial saturation is integrated over all capillaries to capture the contributions of the global wetting layer. Substituting equation 2.16 and 2.17 to write the relative electrical conductivity $\sigma_r(S_w)$

$$\sigma_r(S_w) = \frac{\sigma(S_w)}{\sigma(S_w = 1)} = \frac{\sigma_w \int_{r_{min}}^{r_{wmax}} r_c^2 n(r_c) dr_c + 2\sigma_{sw} \int_{r_{min}}^{r_{max}} r_c^2 n(r_c) dr_c}{\sigma_w \int_{r_{min}}^{r_{max}} r_c^2 n(r_c) dr_c + 2\sigma_{sw} \int_{r_{min}}^{r_{max}} r_c^2 n(r_c) dr_c} \quad (2.21)$$

Hence, equation 2.20 becomes

$$C_r(S_w) = \frac{k_{rw}(S_w)}{\sigma_r(S_w = 1)} \quad (2.22)$$

In the limit of negligible surface conductivity, the relative electrical conductivity reduces to $\sigma_r = S_w$, which is Archie's law with n = 1. This suggests that the relative streaming coupling coefficient can be described by a simple Corey-type equation, where it is simply a function of the water saturation.

Based on these assumptions, Jackson *et al.* (2012) describe C_{rEK} and C_{rEC} in terms of a normalised water saturation (S_{wn}) as

$$C_{rEK} = S_{wn}^n, \quad (2.23)$$

$$C_{rEC} = (1 - S_{wn})^m \quad (2.24)$$

where

$$S_{wn} = \frac{S_w - S_{wirr}}{1 - S_{or} - S_{wirr}} \quad (2.25)$$

Using $n = 0.6$ and $m = 3$ gave similar results to experimental data reported in Jackson (2010) and Ortiz *et al.* (1973) respectively. For simplicity, Jackson *et al.* (2012) used the same behaviour to describe the saturation dependence of C_{rTE}, due to limited data available. Hence,

$$C_{rTE} = (1 - S_{wn})^m \quad (2.26)$$

2.6 Summary

A review of the different feedback inflow control strategies of smart wells suggest that closed-loop feedback control techniques triggered by in well or reservoir flow measurement (such as watercut) measured at the well can increase NPV and mitigate reservoir uncertainty, as opposed to model-based control strategies, which use models that are rarely predictive at their spatial and temporal scales required to identify optimum control actions. The aim of this project is to develop a close-loop 'proactive' feedback inflow control approach based on near-well reservoir monitoring, using downhole measurements of SP and to quantify the potential benefit of this approach in different well and reservoir settings.

In reference to the above literature review, SP monitoring may prove a useful method for monitoring saturation variation away from a production well. The main attraction over existing monitoring methods is that it responds directly to the movement of water. The SP signal arises in order to maintain overall electrical neutrality when separation of charges occurs due to gradients in pressure, temperature and chemical concentration of the reservoir water-phase during a waterflood or aquifer influx. The origin of SP signals generated during a waterflood or aquifer influx within an oil reservoir is presented and the coupling coefficient (equations 2.9, 2.10 and 2.11) and the relative coupling coefficient terms (equation 2.15 – 2.17) will be used to calculate the coupling terms, which in turn will be used for modelling SP signals generated during the waterflood process, and will be explained further in section 3.

Chapter 3

Methodology: Numerical Modelling of Self-Potential

3.1 Introduction

Various recent studies such as Saunders *et al.* (2008), Gulamali *et al.* (2010) and Jackson *et al.* (2012) have used experimental data in numerical models to predict the SP signals that would be measured at a well during production due to electrokinetic (EK), electrochemical (EC) and thermoelectric (TE) effects, and their results suggest that SP signals can be measurable above background noise. The relative contributions of EK, TC and EC potentials to the overall SP signal generated were numerically assessed. In this project, the approach used by Gulamali *et al.* (2011) and Jackson *et al.*, (2012) to model the SP variation across a waterflooded reservoir will be used. The flow of a brine (subscript *w*) and immiscible non-wetting (oil or gas) phase within a hydrocarbon reservoir will be modelled using the ECLIPSE reservoir simulator (Schlumberger, 2011) to determine the pressures, temperatures and salinities, neglecting the electrodynamic problem. Each grid block in the simulator will hold reservoir fluid properties that will be used to create the electrodynamic model. The electrodynamic problem can be coupled to the hydrodynamic problem via (Gulamali *et al.,* 2011)

$$j = -\sigma_{fs}(S_w)\nabla U - L_{EK}(S_w)\nabla \Phi - L_{TE}(S_w)\nabla T - L_{EC}(S_w)\nabla C_f \quad (3.1)$$

as shown in the on-diagonal term in equation 1, which represents Ohm's law with the EK, TE and EC cross coupling terms. Assuming the model has no external current source or sinks, electrical charge is conserved and the net current flowing across the model boundaries is zero, then

$$\nabla . j = 0. \quad (3.2)$$

Combining equations 3.1 and 3.2 gives

$$\nabla.\left(\sigma_{fs}(S_w)\nabla U\right) = -\nabla.\left(L_{EK}(S_w)\nabla\Phi\right) - \nabla.\left(L_{TE}(S_w)\nabla T\right) - \nabla.\left(L_{EC}(S_w)\nabla C_f\right) \quad (3.3)$$

Thus there are sources (nonzero divergence) of conduction current whenever there are gradients of the cross-coupling coefficient parallel to the primary flow, or externally induced sources of primary flow (Sill 1983). The sources of the conduction current given by the right-hand side of equation (3.3) can then be used to determine the potential difference *U* across the reservoir. Jackson *et al.* (2012) solved the electrodynamic problem using a finite-element scheme, setting the volume-averaged hydrodynamic variables at the centre of the grid cells to the elements sharing that node. However, it would be more suitable to solve the electrodynamic model using a control-volume finite-different (CVFD) scheme, as it will be compatible with the ECLIPSE orthogonal reservoir mesh. Hence the SP at each grid cell can be solved for and stored in the same format as the hydrodynamic variables used by ECLIPSE.

3.2 Discretisation of Variables

To solve equation 3.3 numerically, a control volume finite different (CVFD) method is used (Recktenwald 2012) to write the formulation conveniently in matrix form. For simplicity, a one dimensional domain will be used for explanation. The CVFD method transforms equation 3.3 into a number of discrete equations for the cell centre values of $\sigma_{fs}, U, \Phi, T, C_f$ and L_x in a one dimensional domain depicted in figure 3.1. The one dimensional domain is divided into a mesh of grid cells. Cell centres on the domain are identified by their x_i indices, and the cell faces represented by their $\bar{x}_i$ and $\bar{x}_{i+1}$ grid indices. At each grid cell centre, an electrical conductivity σ_{fs}, pressure Φ, concentration C_f, temperature *T* and a cross-coupling term L_{EK}, L_{EC}, L_{TE} is assigned. The variables are constant in each cell, but can vary from one cell to the next.

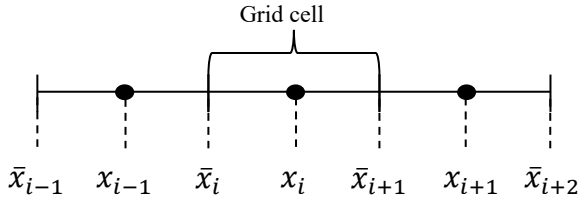


Figure 3.1: Sample rectilinear mesh zones. Solid lines are the vertices, and black circles are the cell centres

Considering only the EK coupling term, for a cell within the boundary of the domain (figure 3.1), equation 3.3 becomes

$$\int_{\bar{x}_i}^{\bar{x}_{i+1}} \frac{d}{dx}\left(\sigma_{fs}\frac{dU}{dx} + L_{EK}\frac{d\Phi}{dx}\right)\mathrm{dx} = 0 \quad (3.4)$$

$$\left[\left(\sigma_{fs_{\bar{x}_{i+1}}}\frac{dU}{dx}\right)_{\bar{x}_{i+1}} - \left(\sigma_{fs_{\bar{x}_i}}\frac{dU}{dx}\right)_{\bar{x}_i}\right] + \left[\left(\sigma_{fs_{\bar{x}_{i+1}}}\frac{d\Phi}{dx}\right)_{\bar{x}_{i+1}} - \left(\sigma_{fs_{\bar{x}_i}}\frac{d\Phi}{dx}\right)_{\bar{x}_i}\right] = 0 \ (3.5)$$

Equation 3.5 is integrated over the grid cell and is reduced to first order derivatives in space. The first derivatives are discretised over the domain using the finite difference (central difference approximation) method. In these expressions U_{x_i} and Φ_{x_i} are cell centre values, while $\sigma_{fs_{\bar{x}_i}}$ and $L_{EK_{\bar{x}_i}}$ are the conductivity and coupling terms at the cell faces. The method used to determine $\sigma_{fs_{\bar{x}_i}}$ and $L_{EK_{\bar{x}_i}}$ (conductivity and coupling terms at the grid interface) is described in using figure 3.3.

$$\left.\frac{dU}{dx}\right|_{\bar{x}_{i+1}} = \frac{U_{x_{i+1}} - U_{x_i}}{x_{i+1} - x_i} \quad (3.6); \quad \left.\frac{d\Phi}{dx}\right|_{\bar{x}_{i+1}} = \frac{\Phi_{x_{i+1}} - \Phi_{x_i}}{x_{i+1} - x_i} \quad (3.7)$$

$$\left.\frac{dU}{dx}\right|_{\bar{x}_i} = \frac{U_{x_i} - U_{x_{i-1}}}{x_i - x_{i-1}} \quad (3.8); \quad \left.\frac{d\Phi}{dx}\right|_{\bar{x}_i} = \frac{\Phi_{x_i} - \Phi_{x_{i-1}}}{x_i - x_{i-1}} \quad (3.9)$$

$$\left[\sigma_{fs_{\bar{x}_{i+1}}}\frac{U_{x_{i+1}} - U_{x_i}}{x_{i+1} - x_i} - \sigma_{fs_{\bar{x}_i}}\frac{U_{x_i} - U_{x_{i-1}}}{x_i - x_{i-1}}\right] + \left[L_{EK_{\bar{x}_{i+1}}}\frac{\Phi_{x_{i+1}} - \Phi_{x_i}}{x_{i+1} - x_i} - L_{EK_{\bar{x}_i}}\frac{\Phi_{x_i} - \Phi_{x_{i-1}}}{x_i - x_{i-1}}\right] = 0 \ (3.10)$$

Equation 3.10 is expanded and simplified to give

$$a_{\bar{x}_{i+1}}U_{x_{i+1}} + a_P U_{x_i} + a_{\bar{x}_{i-1}}U_{x_{i-1}} = b_{\bar{x}_{i+1}}\Phi_{x_{i+1}} + b_P\Phi_{x_i} + b_{\bar{x}_{i-1}}\Phi_{x_{i-1}} \quad (3.11)$$

where

$$a_{\bar{x}_{i+1}} = -\frac{\sigma_{fs_{\bar{x}_{i+1}}}}{x_i - x_{i-1}} \ (3.12); \ a_{\bar{x}_{i-1}} = -\frac{\sigma_{fs_{\bar{x}_{i-1}}}}{x_i - x_{i-1}} \ (3.13)$$

$$a_P = a_{\bar{x}_{i+1}} + a_{\bar{x}_{i-1}} \ (3.14)$$

$$b_{\bar{x}_{i+1}} = -\frac{L_{EK\,\bar{x}_{i+1}}}{x_i - x_{i-1}} \quad (3.15);\; b_{\bar{x}_{i-1}} = -\frac{L_{EK\,\bar{x}_{i-1}}}{x_i - x_{i-1}} \quad (3.16)$$

$$b_P = b_{\bar{x}_{i+1}} + b_{\bar{x}_{i-1}} \quad (3.17)$$

For a cell positioned at the boundary of the domain (figure 3.1), $\nabla U = 0$ will be set to ensure no current enters or leaves the domain. Considering only the EK coupling term, equation 3.3 becomes

$$\int_{\bar{x}_n}^{\bar{x}_{n+1}} \frac{d}{dx}\left(\sigma_{fs}\frac{dU}{dx} + L_{EK}\frac{d\Phi}{dx}\right)\mathrm{dx} = 0 \quad (3.18)$$

$$\left.\frac{dU}{dx}\right|_{\bar{x}_{n+1}} = 0 \quad (3.19)$$

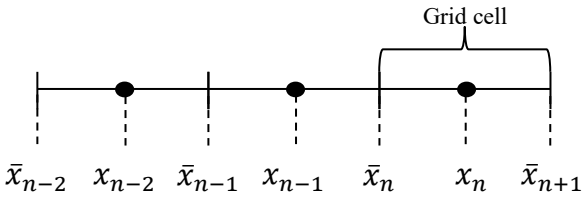


Figure 3.2: Cell at the boundary

$\nabla\Phi = 0$ is also set on the boundaries of the domain $\left(\Phi_{\bar{x}_{n+1}} = \Phi_{\bar{x}_n}\right)$, and equation 3.18 becomes

$$\left[\sigma_{fs_{\bar{x}_n}}\frac{U_{\bar{x}_n} - U_{\bar{x}_{n-1}}}{\Delta x}\right] + \left[L_{EK\,\bar{x}_n}\frac{\Phi_n - \Phi_{n-1}}{\Delta x}\right] = 0 \quad (3.20)$$

$$a_{\bar{x}_n}U_{x_n} + a_{\bar{x}_{n-1}}U_{x_{n-1}} = b_{\bar{x}_n}\Phi_{x_n} + b_{\bar{x}_{n-1}}\Phi_{x_{n-1}} \quad (3.21)$$

$$a_{\bar{x}_n} = -\frac{\sigma_{fs_{\bar{x}_n}}}{\Delta x} \quad (3.22);\; a_{\bar{x}_{n-1}} = -\frac{\sigma_{fs_{\bar{x}_{n-1}}}}{\Delta x} \quad (3.23)$$

$$b_{\bar{x}_n} = -\frac{L_{EK\,\bar{x}_n}}{\Delta x} \quad (3.24);\; b_{\bar{x}_{n-1}} = -\frac{L_{EK\,\bar{x}_{n-1}}}{\Delta x} \quad (3.25)$$

This same formulation can be used for a grid cell located on the left hand side of the 1D domain. Calculation of the coefficients in equation 28 and 38 requires values of $L_{EK\,\bar{x}_{i+1}}$ and

$\sigma_{fs_{\bar{x}_{i+1}}}$ at the interface between cell 1 and 2 (Figure 3.3). Instead of using an interpolation scheme, the values of L_{EK} and σ_{fs} at the interface can be determined by assuming the current at the interfaces of the cells is continuous.

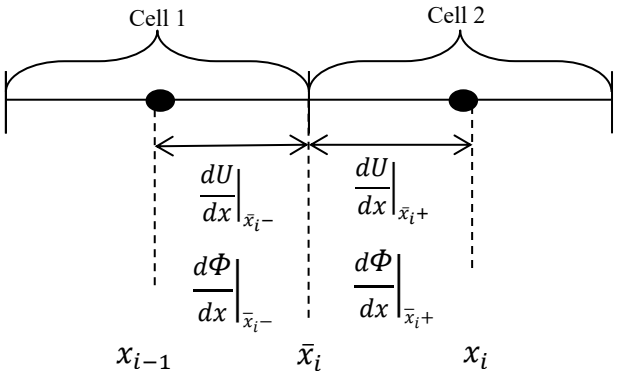


Figure 3.3: Discontinuous variation in σ_{fs} and L_{EK} at the interface between two grid cells

$$\sigma_{fs_{x_{i-1}}} \frac{dU}{dx}\Big|_{-} = \sigma_{fs_{x_i}} \frac{dU}{dx}\Big|_{+} = \sigma_{fs_{\bar{x}_i}} \frac{dU}{dx}\Big| \quad (3.26)$$

$$L_{EK_{x_{i-1}}} \frac{d\Phi}{dx}\Big|_{-} = L_{EK_{x_i}} \frac{d\Phi}{dx}\Big|_{+} = L_{EK_{\bar{x}_i}} \frac{d\Phi}{dx}\Big| \quad (3.27)$$

Equation 3.26 and 3.27 are approximations of the current flowing into the left (minus) and right (plus) sides of the grid cell interface in figure 3.3. Equations 3.26 and 3.27 define $\sigma_{fs_{\bar{x}_i}}$ and $L_{EK_{\bar{x}_i}}$ respectively, and can be determined by assuming the fluxes $\sigma_{fs_{\bar{x}_i}} \frac{dU}{dx}$ and $L_{EK_{\bar{x}_i}} \frac{d\Phi}{dx}$ are continuous. Equation 3.26 becomes

$$\sigma_{fs_i} \frac{U_{x_i} - U_{x_{i-1}}}{x_i - x_{i-1}} = \sigma_{fs_{i-1}} \frac{U_{\bar{x}_i} - U_{x_{i-1}}}{\bar{x}_i - x_{i-1}} \quad (3.28)$$

$$U_{\bar{x}_i} - U_{x_{i-1}} = \frac{\sigma_{fs_{\bar{x}_i}}}{\sigma_{fs_{x_{i-1}}}} \left(\frac{\bar{x}_i - x_{i-1}}{x_i - x_{i-1}}\right) U_{x_i} - U_{x_{i-1}} \quad (3.29)$$

$$\sigma_{fs_i} \frac{U_{x_i} - U_{x_{i-1}}}{x_i - x_{i-1}} = \sigma_{fs_{i-1}} \frac{U_{x_i} - U_{\bar{x}_i}}{x_i - \bar{x}_i} \quad (3.30)$$

$$U_{x_i} - U_{\bar{x}_i} = \frac{\sigma_{fs_{x_i}}}{\sigma_{fs_{x_{i-1}}}} \left(\frac{x_i - \bar{x}_i}{x_i - x_{i-1}}\right) U_{x_i} - U_{i-1} \quad (3.31)$$

Adding 3.29 and 3.31 yields

$$U_i - U_{i-1} = \left(\frac{U_{x_i} - U_{x_{i-1}}}{x_i - x_{i-1}}\right)\left(\frac{\bar{x}_i - x_{i-1}}{\sigma_{fs_{x_{i-1}}}} + \frac{x_i - \bar{x}_i}{\sigma_{fs_{x_i}}}\right)\sigma_{fs_{\bar{x}_i}} \quad (3.32)$$

Hence the conductivity $\sigma_{fs_{\bar{x}_i}}$ approximation at the cell interface becomes

$$\sigma_{fs_{\bar{x}_i}} = \frac{\sigma_{fs_{x_i}}\sigma_{fs_{x_{i-1}}}(x_i - x_{i-1})}{\sigma_{fs_{x_i}}(\bar{x}_i - x_{i-1}) + \sigma_{fs_{x_{i-1}}}(x_i - \bar{x}_i)} \quad (3.33)$$

Similarly the coupling term $L_{EK_{\bar{x}_i}}$ is

$$L_{EK_{\bar{x}_i}} = \frac{L_{EK_{x_i}}L_{EK_{x_{i-1}}}(x_i - x_{i-1})}{L_{EK_{x_i}}(\bar{x}_i - x_{i-1}) + L_{EK_{x_{i-1}}}(x_i - \bar{x}_i)} \quad (3.34)$$

Equation 3.11 and 3.21 will be used to write the formulation in matrix form, to conveniently solve for the potential (U) at each cell, given the Φ, T, C_f and σ_{fs} at each cell.

3.3 Electrical Properties

Variations in water saturation, salinity and temperature are observed when injecting less saline water at a lower temperature into a reservoir that contains irreducible oil and water with higher salinity and temperature. These variations affect the electrical properties of the reservoir, and therefore needs to be described in order to solve the electrodynamic model. The cross-coupling term is a function of the rock electrical conductivity and coupling coefficient. Moreover, the coupling coefficients dependency on salinity and temperature at the saturation endpoints ($S_w = 1 - S_{or}$ and $S_w = S_{wirr}$) need to be identified, after which the coupling coefficient of intermediate saturation values will be considered (Jackson *et al.* 2012).

The EK, EC and TE coupling coefficient in each grid cell can be approximated using equations 2.9, 2.10 and 2.11 at the saturation endpoints. At intermediate values of saturation, the coupling coefficient can be determined using equation 2.3. The relative coupling coefficient required to solve equation 2.3 will be approximated using equation 2.14, 2.15 and 2.17 to determine the electrokinetic, electrochemical and thermoelectric coupling coefficient respectively.

At intermediate saturation values, the electrical conductivity of the porous medium can be determined by Archie's law (Telford *et al.* 1990)

$$\sigma_{fs} = \phi^m \sigma_w S_w^n \quad (3.35)$$

where ϕ is the porosity of the porous medium, m is the cementation exponent of the rock, n is the saturation exponent, and σ_w is the electrical conductivity of brine (S/m), which is dependent on the brine salinity and approximated by (Worthington *et al.* 1990)

$$\log_{10} C_f = -1.03024 + 1.06627(\log_{10} \sigma_w) + 2.41239 \times 10^{-2}(\log_{10} \sigma_w)^2 + 3.68102 \times 10^{-3}(\log_{10} \sigma_w)^3 + 1.46369 \times 10^{-4}(\log_{10} \sigma_w)^4. \quad (3.36)$$

3.4 Self-Potential Solver

A self-potential (SP) solver has been developed to numerically solve equation 3.4, neglecting the electrochemical and thermoelectric cross coupling terms. The SP solver is tested using a simple 1D sandstone oil column model. The model measures 100 × 50 × 200 m and has 40 active grid blocks divided evenly in the vertical plane (Figure 3.4). The sandstone column contains undersaturated oil and connate water with an aquifer connected to the bottom of the oil column to support production. For simplicity, capillary pressure effects are not considered in the model. The OWC is at a depth of 1900 m with a reference pressure of 500 bars.

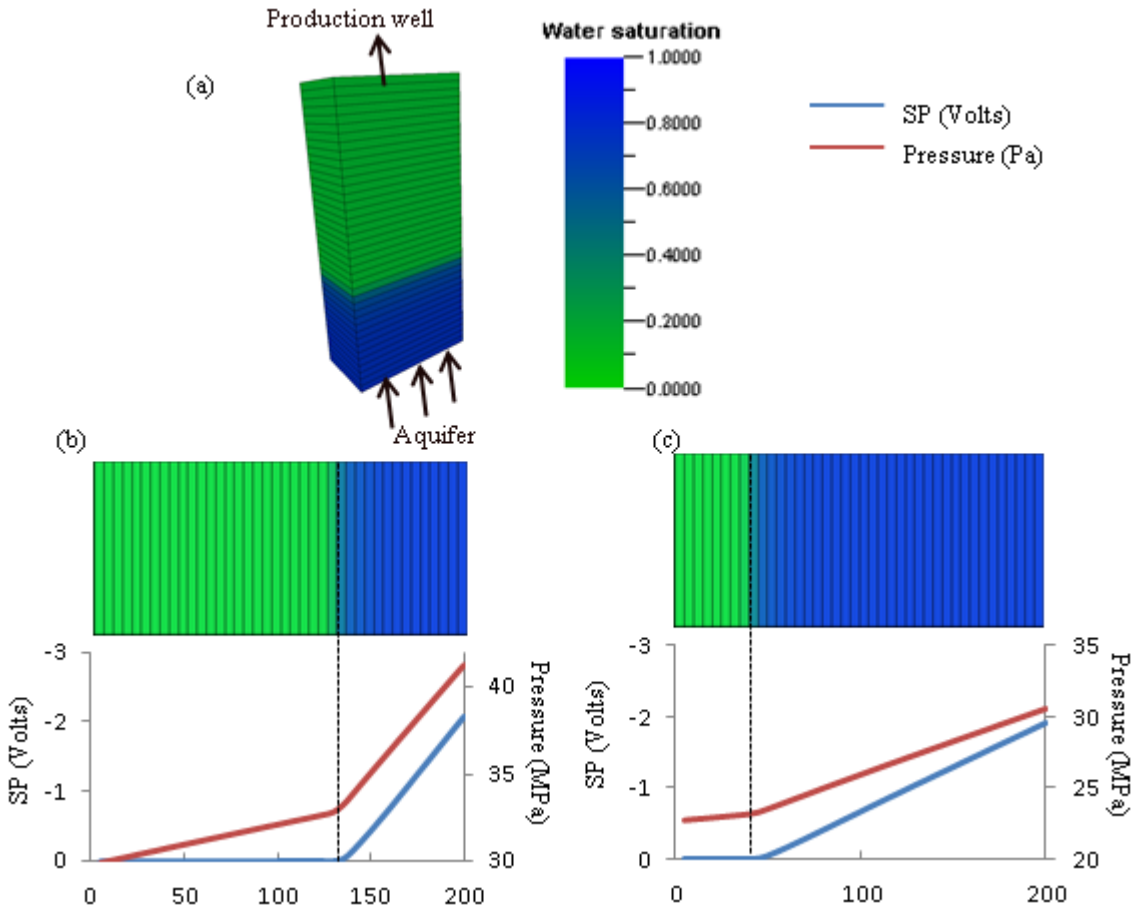


Figure 3.4: Two snapshots, of the saturation variation within the reservoir, showing the water (blue) moving towards the well, which is located at (b) 130 m and (c) 40 m from the well;and the corresponding SP signal across the oil column

Property (Unit)	Notation	Value
Coupling coefficient (V/MPa)	C_{EK}	-27
Brine conductivity (S/m)	σ_w	0.1183
C_{rEK} exponent (equation 8)	n	1
Oil density (kg/m^3)	ρ_o	883.0
Water density (kg/m^3)	ρ_w	1038.8

Table 3.1: Properties of the 1D model

The 'ECLIPSE' reservoir simulator is used to model water displacing oil through the 1D reservoir. The oil viscosity is set to be very low (0.1 cp) to allow for a piston-like displacement in the sense that a sharp interface (front) exists between the oil and water and is also stabilised by gravity, on either side of which only one of the fluids is mobile (water viscosity set to 1 cp). Ahead of the waterfront, the water saturation is the connate water or irreducible water saturation $S_w = 0.2$, which will not flow. Consequently there will be no transport of charge and EK potential will be zero. The water saturation behind the waterfront is $S_w = 1 - S_{or}, S_{or} = 0.2$ as a result electrokinetic potential generated is associated with only the water phase (relative coupling coefficient C_{rEK} = 1). Figure 3.4(b) and (c) shows the EK potential generated due to flow with the magnitude increasing with depth. The change in EK associated with the pressure gradient (above hydrostatic) behind the waterfront returns the coupling coefficient used in the solver which implies the EK solver is accurate ($C_{EK} = \frac{\Delta U}{\Delta \Phi} = -27\ \mathrm{V/MPa}$).

The SP solver is also tested using a 3D reservoir model which is based on that described in Jackson *et al.* (2012), this time taking the electrochemical and thermoelectric contribution to the total SP into consideration. The horizontal sandstone reservoir layer is 1150 × 500 × 100 m thick and lies at a depth of 500 m (Figure 3.5). The reservoir is bounded by water saturated, low permeable shale conductive layers, serving as the reservoir seals. The shales allows for the potential at the outer boundary to serve as a reference; however in reality, the reference point would be located in a rock fomation close to the surface. The reservoir contains understaturated oil and connate water. Pressure support is provided by injection wells placed at the left face of the reservoir model, which injects fresh seawater into the reservoir containing connate brine. The shale layers are impermeable and fully saturated with water. The grid cells that represent the shale layers in the hydrodynamic model are inactive. In the electrodynamic model, the shale layers are treated as active grid cells that are assumed to be fully saturated with water. The electrical conductivity in the shale layers are determined using Archie's law (equation 3.35), with the saturation and porosity set to 1 and 0.3 respectively. The salinity of the water in the shale porespace are also set to the initial formation water salinity. The reservoir fluid properties are summarised in Table 3.2.

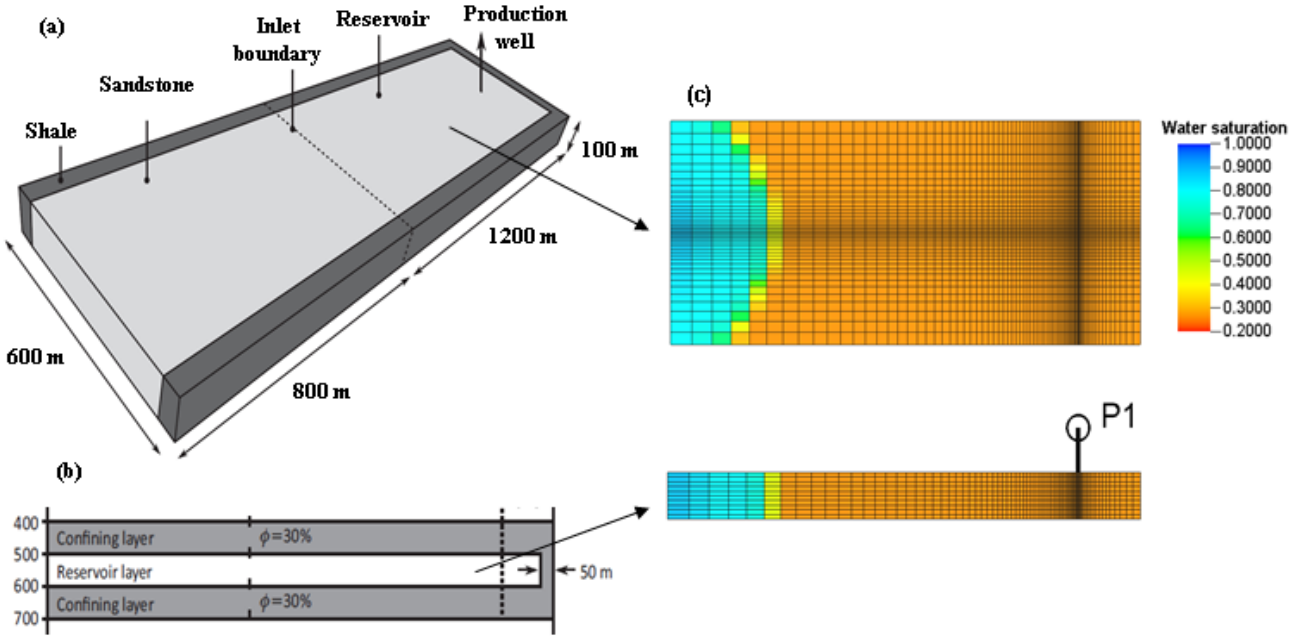


Figure 3.5: 3D reservoir model based on Jackson et al. (2012). (a) Perspective view of the 100 m thick sandstone reservoir, surrounded by shales fully saturated with water. Waterflooding is achieved by injection wells which are placed at the inlet boundary not shown in the figure. (b) Cross-section through the middle of the model, showing the confining shale layers above and below the reservoir. (c) Grid used for modelling.

Property (Unit)	Rock	Oil	Water
Viscosity (cp)	-	1	1
Density (kgm^{-3})	2100	1000	1000
Formation (initial) –salinity (M)	-	-	5
Injection salinity (M)	-	-	0.5 (seawater)
Formation (initial) – temperature ($°C$)	30-130	30-130	30-130
Injection temperature ($°C$)	-	-	30
Porosity	0.25	-	-
Permeability (md)	75-1500	-	-
Irreducible water saturation	0.2	-	-
Residual oil saturation	0.2	-	-
Endpoint water relative permeability	0.3	-	-
Endpoint oil relative permeability	0.8	-	-

Table 3.2: Properties of the 3D model

Similar EK potential trends are observed when compared to the results in Saunders *et al.,* (2008) and Jackson *et al.* (2012). The oil production results in a shock-front dominated displacement by seawater injection. The waterfront approaches the well as oil is being produced from the reservoir and, associated with the displacement of oil by water is the EK potential as shown in Figure 3.6 (a). The peak of the EK potential coincides with the location of the waterfront because the equation 3.3 becomes nonzero due to abrupt change in saturation at the water front. The waterfront therefore acts as a current source (Saunders *et al.,* 2008). Figure 3.7 shows the simulation of the EK, EC and TE potential profiles generated across the middle of the reservoir. The EK signal decays at approximately 100 m behind and ahead of the front, with measurable signals above assumed noise level of 0.1 mV observed at the production well approximately 250 days prior to water breakthrough, with the front 50 m away from the well. Implying that it can be possible to sense or monitor waterfront encroachment before the front reaches the production well. Moreover, the high EK potential (1.5 mV) observed when the water front reaches the well is as a result of the grid refinement placed around the well which results in higher simulation resolutions.

The salinity and temperature gradients also give rise to EC and TE potentials. The EC potential is zero ahead of the saline front, but becomes positive behind the leading edge of the front, as the saline front flows in phase with the waterfront. The EC potential peaks at some distance behind the trailing end of the saline front. The TE potential is also zero ahead of the temperature front but negative behind the leading edge of the front reaching a maximum magnitude at the tail of the front. The temperature front significantly lags behind the waterfront due to the low rate of heat transfer as a result of the low thermal conductivity of reservoir formation. Moreover, a simple sensitivity analysis by Jackson *et al.* (2012) varying production rate, permeability, temperature and formation brine salinity of reservoir properties suggests that EC potential can contribute to SP signals measured at a production well during waterflooding prior to water breakthrough. Whereas, they observed that the TE potentials have negligible contribution to the SP signals measured at the well before water breakthrough as temperature fronts associated with the injected water lags significantly behind the saturation front. Therefore, throughout this study the TE contributions towards the total simulated SP would be neglected for all the SP analysis carried out.

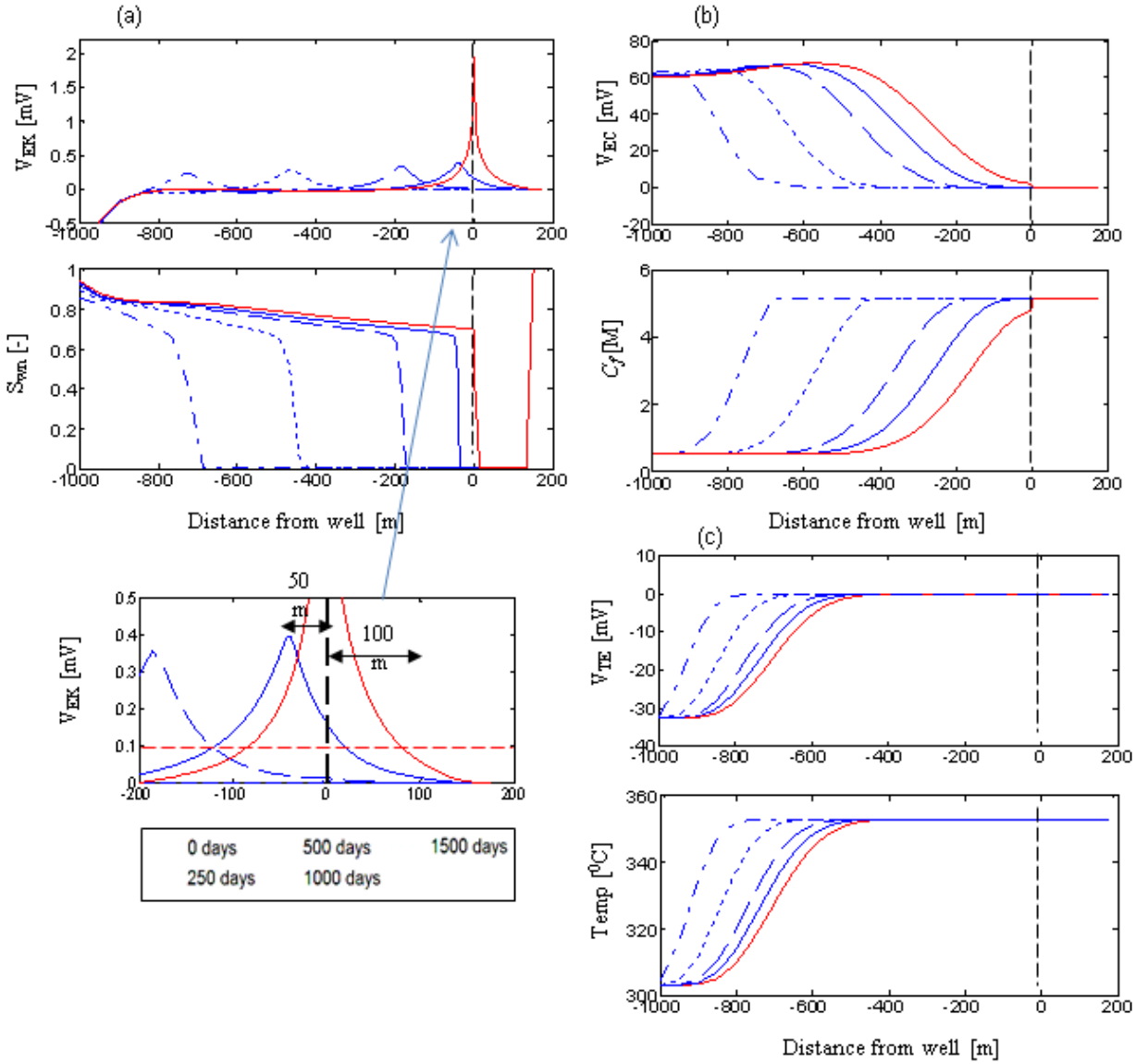


Figure 3.6: 1D horizontal profile across the centre of the reservoir at five different time steps, of (a) EK potential and the corresponding saturation profile, with the EK potential decaying c. 50-100 m ahead of the waterfront (b) EC potential and the salinity profile and (c) TE potential and temperature profile. The production well is positioned at 0m

3.5 Summary

Results of the 1D and 3D electrodynamic problem verify that a SP solver has been successfully developed. The 3D numerical-modelling results show that the magnitude of the SP generated during water flooding of a hydrocarbon reservoir can be measured above assumed downhole electrode noise level of 0.1 mV, with the peak coinciding with the waterfront. The SP solver is successfully extended to accommodate electrochemical and thermoelectric terms. This solver developed based on work carried out by Jackson and coworkers is designed to form part of a closed-loop feedback control workflow investigated

by Dilib and Jackson (2012 and 2013) and will be used to determine whether proactive feedback control using SP measurements can reduce the negative consequences associated with production of unwanted fluids.

This research therefore builds on two sets of earlier studies to investigate a new inflow control strategy (Fig. 3.7): the reservoir model and feedback control approach are modified from Dilib and Jackson (2013), and the numerical modelling of SP is based on Jackson *et al.* (2012). A closed-loop, feedback control strategy in which ICV settings are directly related to downhole measurements of SP is developed and used to quantify the benefits of this in terms of well NPV. In common with most studies, the impact of the streaming current on fluid flow as described by Darcy's Law is neglected; hence a commercial simulator, ECLIPSE (Schlumberger 2012) is used to solve the hydrodynamic flow equations and the SP problem can be treated as a post-processing step, using values of brine phase potential, saturation, temperature and concentration (salinity) determined from the reservoir simulator at a given time step.

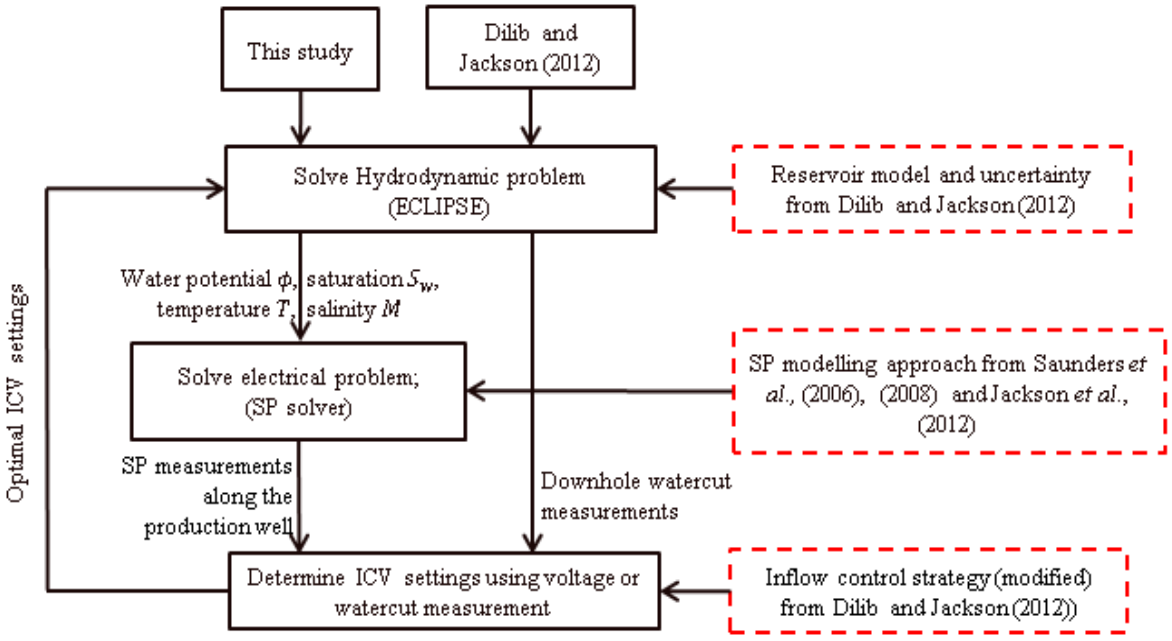


Figure 3.7: Flow chart describing how previous studies relate to our modified feedback inflow control strategy based on downhole measurements of SP.

Chapter 4

Closed–Loop Feedback Control using Downhole Measurements of SP: Single Horizontal Well Application

4.1 Introduction

Numerous studies have demonstrated that closed-loop feedback control, facilitated by smart (or intelligent/advanced) wells equipped with downhole monitoring technology and inflow control valves (ICV), can be used for production optimization during waterflooding (e.g. Brouwer *et al.*, 2004; Naus *et al.,* 2004; Yeten *et al.*, 2004; Aitokhuehi and Durlofsky, 2005; Elmsallati *et al.*, 2005; Sarma *et al.*, 2006; Meum *et al.,* 2008; Chen *et al.*, 2010). However, identifying the optimal ICV settings that maximize an objective function remains challenging, especially when the reservoir behaviour is uncertain. Model-based control strategies allow control actions to be taken at any time during production and can, in principle, identify the optimal solution. However, they require predictive reservoir models which are rarely available at the spatial and temporal resolution necessary to make inflow control decisions; moreover, model-based techniques may suggest control actions that are counter-intuitive and are therefore unlikely to be implemented in practice (e.g. Dilib and Jackson, 2012).

Direct feedback strategies, in which control actions are taken based on (often heuristic or ad-hoc) rules relating monitoring data to ICV settings avoid the problems associated with uncertain reservoir model predictions, but control actions are taken only after some adverse change in flow or related reservoir properties (such as temperature or pressure) is measured at the well; moreover, control actions may be far from optimal (e.g. Kharghoria *et al.,* 2002; Elmsallati *et al.,* 2005; Ebadi and Davies, 2006; Dilib and Jackson, 2012). As yet, no study has investigated the use of reservoir monitoring technology, in which adverse changes in flow are detected or monitored at some distance from the well, for inflow control in smart wells. Yet the potential benefits of such an approach are clear: control actions can be taken

before adverse changes in flow are detected at the well, but do not depend upon the predictions of an uncertain reservoir model. For example, if unwanted fluids such as water encroaching on a production well can be monitored before they reach the well, control actions can be taken in order to minimize or prevent water production (Jackson *et al.,* 2012).

We investigate the benefit of closed-loop feedback control using SP data acquired along a horizontal well equipped with two ICVs, producing from a high-productivity, thin oil column with uncertain reservoir properties. This is the same production scenario investigated by Dilib and Jackson (2012), and we compare feedback control using SP data to their approach based on watercut measurements. In this chapter, we therefore build on two earlier studies to investigate a new inflow control strategy: the reservoir model and feedback control approach are modified from Dilib and Jackson (2012), and the numerical modelling of SP is based on Jackson *et al.* (2012). Numerical modelling of SP developed in Chapter 3 is used as a cheap alternative to field experiments, to develop a closed-loop feedback control strategy triggered by downhole measurements of SP at a production well and compare the performance in terms of NPV, against inflow control based on conventional in-well data in a single smart horizontal well.

4.2 Methodology

4.2.1 Base case reservoir model

The base case reservoir model is modified from that presented by Dilib and Jackson (2012). The model comprises a sandstone reservoir containing laterally discontinuous shales that reduce the effective vertical permeability; a locally shale-free region is represented by a column of high effective vertical permeability (Figure 4.1). The reservoir measures 1830 × 945 × 30 m; the reservoir top is at a depth of 1830 m. and the oil/water contact (OWC) at 1860 m. The reservoir contains water and undersaturated oil; no gas-cap is present. The reservoir rock and fluid properties are summarized in Table 4.1. The model is modified here to include electrically conductive, water saturated shales that bound the reservoir above and at the sides; these are required for the SP modelling as electrical currents may exploit these shale layers. The high electrical conductivity of the shales means that the net current flow through the boundaries of the model is zero. The base of the reservoir is

connected to a large aquifer (represented by the Fetkovich model; Fetkovich, 1971) and water influx supports oil production.

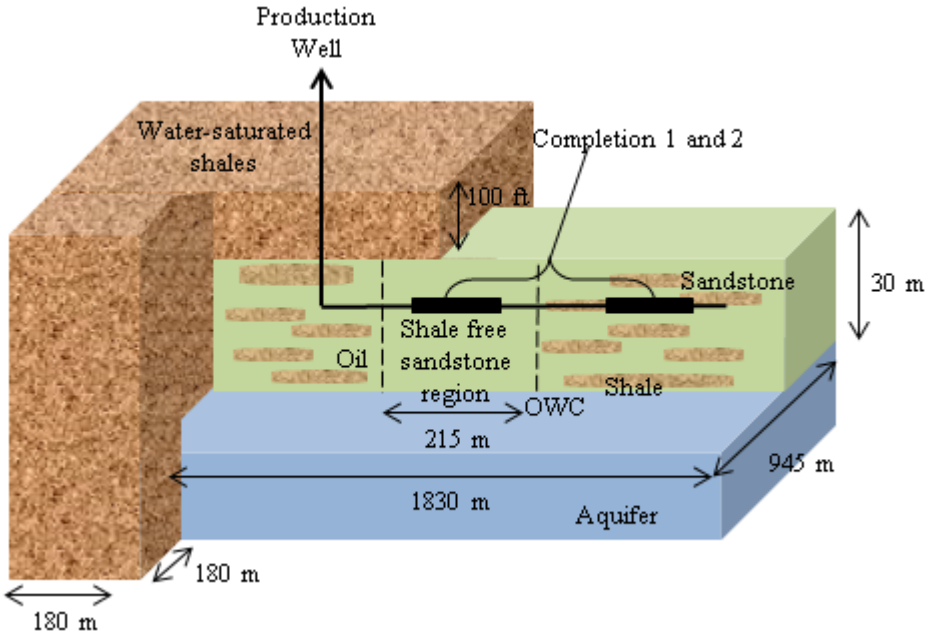


Figure 4 1: Schematic cross-section of a sandstone reservoir with interbedded shales, bounded by shales above and at the sides; these are cut-away for visualization purposes. The model is modified from Dilib and Jackson (2012). The well is placed 35ft from the top of the reservoir and has two completions (diagram not to scale).

Property (Unit)	Rock	Oil	Water
Viscosity (cp)	-	0.34	0.5
Density (kgm^{-3})	2100	800	1000
Formation (initial) –salinity (M)	-	-	0.5
Injection salinity (M)	-	-	0.5 (seawater)
Porosity	0.25	-	-
Low vertical Permeability (md)	50	-	-
High vertical Permeability (md)	500	-	-
Horizontal Permeability (md)	500		
Irreducible water saturation	0.2	-	-
Residual oil saturation	0.2	-	-
Endpoint water relative permeability	0.2	-	-
Endpoint oil relative permeability	0.8	-	-

Table 4.1: Properties of the 3D model

4.2.2 Numerical Modelling of Production and SP

The ECLIPSE reservoir simulator (Schlumberger, 2012) is used to model oil production from an 880-m-long horizontal well, which is located along the centre of the reservoir and 10 m from the top of the oil column. The water saturated shales that bound the reservoir are made to be inactive in the hydrodynamic model, because they do not contribute to flow. The base-case model predicts that early water breakthrough will occur at the heel of the well, due to the higher pressure drawdown and higher vertical permeability. As a result, ICVs are placed at the heel and toe of the well, modelled using a multi-segment well model. An inflow control multiplier Π, which varies from zero (valve completely shut) to one (valve completely opened) ($0 \leq \Pi_i \leq 1$), is assigned to the flow rate Q from each completion i (van Essen *et al.* 2009; 2010). Production is constrained at 10,000 STB/D with a minimum bottomhole-pressure of 1,450 psia (allowing a pressure drawdown of 1150 psia from the initial reservoir pressure of 3600 psia). Dilib and Jackson (2012) showed that the benefits offered by inflow control depend on well life, and can be unrealistically high if determined over a short, fixed well life; following their approach, the operational life of the well here is not fixed *a-priori*. Rather, well life depends upon watercut measurements at the wellhead; the well is shut-in if the well watercut W_w exceeds a maximum value W_l. In practice, a maximum watercut limit can be imposed by surface production equipment, well lift or tubing constraints, or an economic limit based on oil rate (Turner *et al.* 1969; Pucknell *et al.* 2003; Van Essen *et al.* 2009). We examine well watercut limits over the range of 5 to 90%, with well life varying from 900 – 7300 days as a result.

The modelling of SP signals in the reservoir during production follows the approach of Jackson *et al.* (2012) as shown in chapter 3. The water saturated shale layers that bound the reservoir are included in the electrodynamic model to ensure that electrical neutrality is maintained within the reservoir. Just like the 3D example in Chapter 3, the shale layers are treated as active grid cells which are assumed to be fully saturated with water. The electrical conductivity in the shale layers are determined using Archie's law (equation 3.35 in Chapter 3), with the water saturation set to 1 and the porosity set to 0.3. The salinity of the water in the shale pore space are also set to the initial formation water salinity. We assume that the aquifer and formation brine have the same salinity C_f (0.5M, approximately equivalent to seawater) so concentration gradients are zero; we also assume that temperature differences across the 100 ft. oil column can be neglected. Thus SP signals

arise only in response to pressure gradients in the brine; the SP is dominated by the electrokinetic or streaming potential. Here, concentration and temperature are assumed constant but their values are still required to determine (i) the electrical conductivity of the brine (0.1183 Sm^{-1} in this study), and (ii) a material property termed the streaming potential coupling coefficient (measured in VPa^{-1}) which relates the local gradient in streaming potential to the local gradient in brine phase potential. The value of the coupling coefficient depends upon brine salinity and saturation, and the value used here for fully brine saturated rock is taken from the regression using in equation 2.9 (Vinogradov *et al.*, 2010), yielding a value of 2.56 $mV.MPa^{-1}$. Following Jackson *et al.* (2012), we use Archie's Law with a saturation exponent *n* of 2 to describe the saturation dependence of the rock electrical conductivity, and an Archie-type expression with a saturation exponent of 0.6 to describe the saturation dependence of the coupling coefficient.

4.2.3 Objective Function

We compare the performance of each control strategy using the net present value (NPV) of the well, accounting for the hardware cost of each control strategy, the revenues from gas and oil production, the costs of water production, and the time value of money (van der Poel and Jansen 2004; Dilib and Jackson, 2012)

$$NPV = \frac{1}{C_{oil}}\left[\sum_{t=1}^{n}\frac{\left(C_{oil}\Delta V_{oil} + C_{gas}\Delta V_{gas} - C_{wat}\Delta V_{wat}\right)}{(1+k)^t} - D_c\right] \quad (4.1)$$

where *t* represents time in years, *k* is the annual discount rate, ΔV_{oil} represents the volume of oil produced during time *t*, C_{oil} is the price of oil per barrel in US$/BOE, C_{gas} is the gas price (US$/Mscf), ΔV_{gas} is the volume of gas produced, C_{wat} is the cost associated with water production in USD/bbl., ΔV_{wat} is the volume of water produced, and D_c represents the initial installation cost of the well for each monitoring and control strategy. The resulting unit of NPV is the equivalent barrels of oil at surface conditons (BOE). Dilib and Jackson (2012) used a range of values for each economic parameter to calculate NPV for a given control method, and we use the same approach and range here (see their Figure 2).

The inflow-control performance is measured in terms of the percentage gain (*G*) in well NPV over uncontrolled production

$$G = \frac{NPV_c - NPV_u}{NPV_u} \times 100 \quad (4.2)$$

where the subscripts *c* and *u* denote controlled and uncontrolled production, respectively. We take the cost of inflow control strategy based on SP and watercut measurement to be the same (US$ 13.3M), as both strategies could be implemented using a similar configuration of downhole monitoring sensors and variable inflow control technology.

4.2.4 Inflow Control Algorithm

We evaluate the closed-loop, feedback control strategy based on measurements of SP downhole in the production well. The inflow control strategy uses continuously variable ICVs (Williamson *et al.* 2000) and electrodes placed along the well that provide continuous measurements of SP at each completion (e.g. Chen *et al.*, 2006). Dilib and Jackson (2012) used a simple feedback relationship that adjusts the settings of each ICV in completion *i* based on downhole watercut measurements

$$\Pi_i = MAX\left[A - \left(\frac{W_i - W_m}{W_l - W_m}\right)^c, B\right] \quad (4.3)$$

where Π_i is the value of the inflow multiplier, W_i is the watercut for a given completion *i*, W_m is the completion with the smallest watercut, W_l is the well watercut limit, and *A*, *B* and *c* are constants with $c \geq 0$, $A \leq \Pi_i \leq B$. The values of *A*, *B* and *c* are identified using the base case reservoir model and a gradient based optimization algorithm to maximize the well NPV over the (variable) well life (see Dilib and Jackson, 2012). Here we modify equation (4.3) to use measured values of SP (V) in each completion *i* such that

$$\Pi_i = MAX\left[D - E\left(\frac{V_m}{V_i}\right)^f, G\right] \quad (4.4)$$

where V_i is the average change in SP measured by the electrodes located along completion *i*, compared to a base-case value measured prior to production, V_{im} is the voltage at the completion with the lowest average SP measurement, and *D*, *E*, *f* and G are constants with $0 \leq E \leq 1$, $f \geq 0$ and $G \leq \Pi_i \leq D$. As above, the values of *D, E, f* and *G* are identified using the base case reservoir model. Equation (4.4) is applied in the control workflow shown in Figure 4.2. The first step is to identify a minimum voltage change V_t above which control actions are triggered; this avoids spurious actions being triggered by noisy data.

The segment with the smallest average SP measurement V_{im} is identified, and the ICV in this segment remains fully open until the well watercut limit is reached. The other ICVs in each completion i are proportionally choked according to equation 4.4. Downhole SP measurements in each completion prompt the controller to update the ICV settings every 30 days, and the cycle is repeated until the well watercut limit W_l is reached.

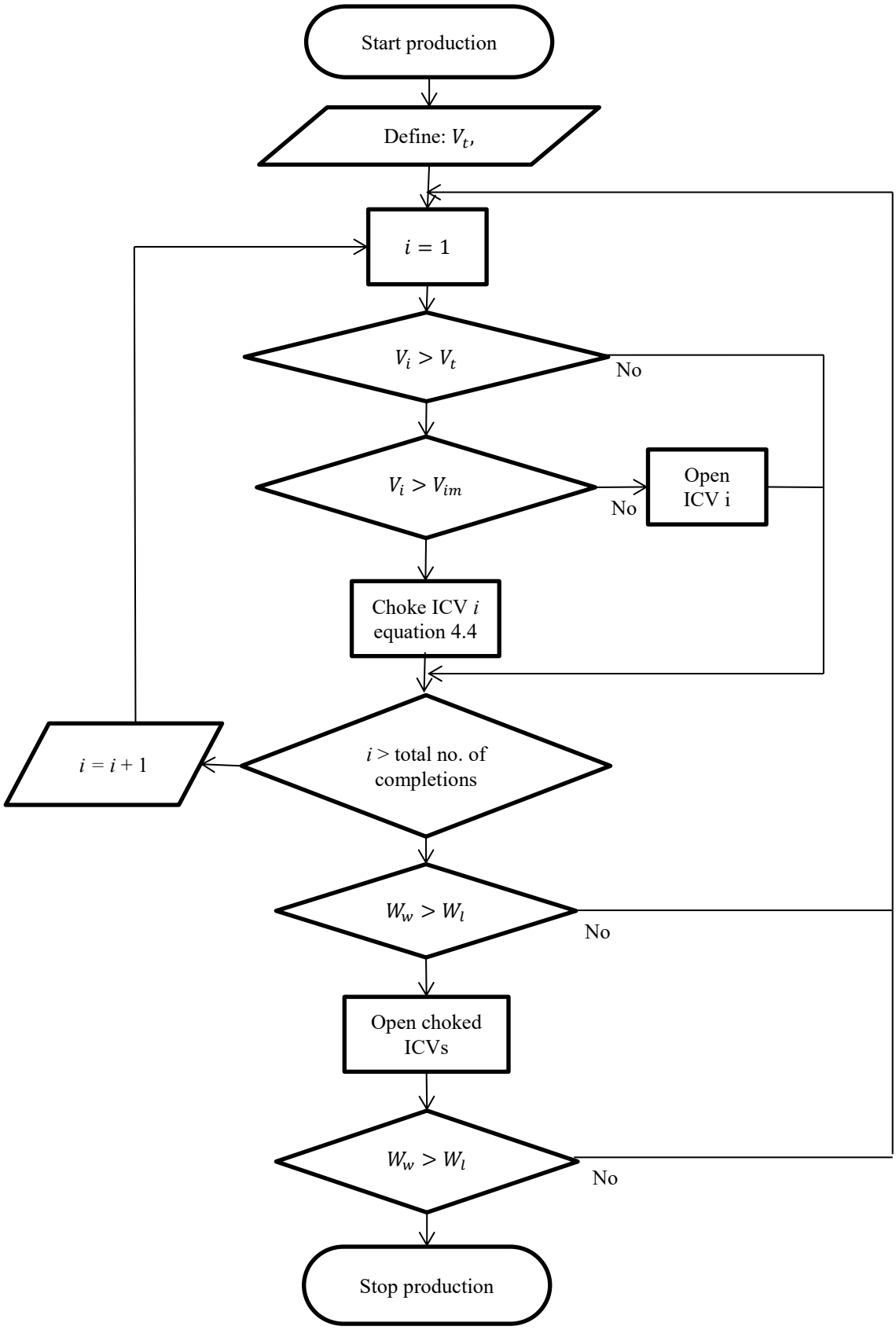


Figure 4.2: Variable inflow control strategy of Dilib and Jackson (2012), modified here to use downhole measurement of SP. The inflow control requires the control trigger value V_t to be defined, and completion i is choked subsequently using equation 4.4; W_l represents the well watercut limit and W_w is the measured well watercut at surface.

4.2.5 Uncertain Reservoir Behaviour

A key aspect of this study is to test the performance of the feedback control strategy against unexpected reservoir behaviour, captured here using a range of model realisations. We investigate the same uncertainties as Dilib and Jackson (2012) and use the same experimental design methodology, so our results can be directly compared against theirs. The uncertainties are (i) the sandstone horizontal permeability with the vertical permeability fixed, (ii) the width of the shale-free, high vertical permeability column, (iii) the aquifer strength, and (iv) the shapes of the oil and water relative permeability curves shown in Table 4.2. Note that the constants in the closed-loop feedback control algorithm (equation 4.4) are optimised once on the base-case model and are not re-optimised for the other reservoir model realisations: these realisations represent unexpected reservoir behaviour that was not predicted by the base-case model. We will determine here whether inflow control based on downhole SP measurements can mitigate the negative production consequences of such unexpected reservoir behaviour.

	Shale free width, ft	**Kh, mD**	**Aquifer Strength, stb/d/psia**	**Relative Permeability**
Low	300	50	1000	$k_{rw}^{max} = 0.2; b = 3$
Base case	700	500	4500	$k_{rw}^{max} = 0.3; b = 4$
High	1100	2500	8000	$k_{rw}^{max} = 0.4; b = 5$

Table 4.2: Uncertain reservoir behaviour

4.3 Results

4.3.1 Optimisation of the inflow control algorithm using the base case reservoir model

We begin by presenting the optimization of the parameters in the inflow control workflow over the range of well watercut limits investigated, before reporting the impact of inflow control in the base-case model. We set the minimum voltage change V_t at which control actions are triggered to be 0.1mV, which is the noise level estimated from the downhole SP data reported by Chen *et al.* (2006). We also set $G = 0$ and $D = 1$, to allow the ICVs to be operated at maximum open and closed positions. The results in Table 4.2 show that the optimal settings of E and f vary depending on the well watercut limit. At high and low well watercut limits (0.05 and 0.75 – 0.9), the well NPV is maximized when the value of f is low (0.01 – 0.2), which means the ICV settings change gradually in response to changes in SP. However, at the mid-range well watercut limits (0.25 - 0.75), the optimal value of f is high, which means the ICV settings change considerably in response to changes in SP; indeed, the variable ICVs behave like on-off valves, shutting off flow when the SP changes by only a small amount.

Parameters	$V_t\ (mV)$	f	E
Constraints	$0.1 \leq V_t$	$f \geq 0$	$0 \leq E \leq 1$
initial	0.1	0.01	0.1
0.05	0.1	0.2	1
0.25	0.1	10	0.1
0.5	0.1	10	0.1
0.75	0.1	0.2	1
0.9	0.1	0.1	0.2

Table 4.3: Optimized Inflow Control Parameters

4.3.2 Impact of inflow control on the base case reservoir model

Figure 4.3 shows snapshots of the saturation within the reservoir, and the corresponding SP profile along the production well, before and after control actions are taken. It is clear that the SP measured along the well is highest in segments where the encroaching water front is closer; to first order, a higher value of SP corresponds to a closer waterfront. Similar results have been reported previously (Jackson *et al.*, 2012; Saunders *et al.*, 2012). Control actions are not taken until the SP exceeds the trigger value of 0.1mV, which causes

the ICV at the heel of the well to close (Fig. 4.3c), yielding an increased oil production rate from the toe (Fig. 4.4b) and causing the water front to approach the toe. However, once the well is about to shut in, the valve at the heel is fully opened, reducing water production from the toe. Consequently, the waterfront accelerates towards the heel of the well and the measured SP increases, resulting in choking of the heel ICV and opening of the toe ICV (Fig. 4.4a). This control strategy improves the well NPV by redirecting water flow paths to create a more even reservoir sweep (Fig. 4.6); it also ensures that production is maintained below the well watercut limit for as long as possible (Fig. 4.4a). The watercut-based inflow control strategy of Dilib and Jackson (2012) yields different inflow control behaviour (Fig. 4.4 c,d). Fewer control actions are taken, starting later in well life, and well life is shorter (compare Fig. 4.4a and 4.4c); moreover, flow through each completion remains similar until late in well life (compare Fig. 4.4b and 4.4d). The result is lower sweep efficiency compared to the SP-based control strategy developed here (compare Fig. 4.5b and 4.5c).

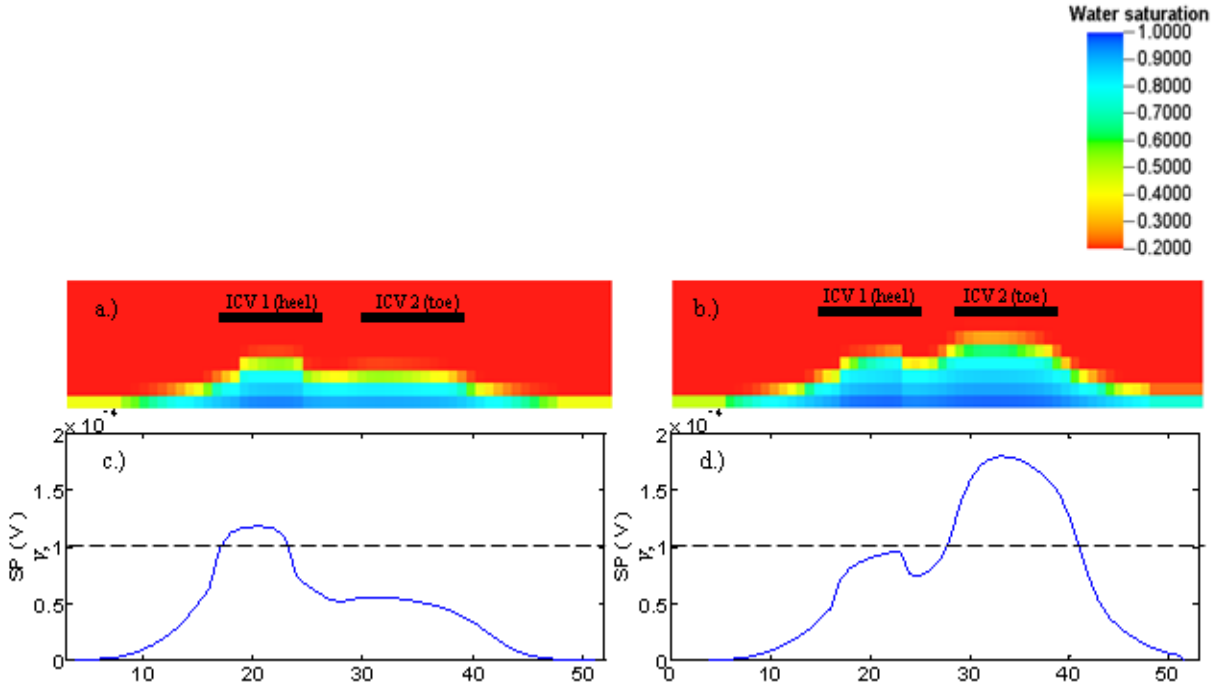


Figure 4.3: (a) and (b) Cross-section through the centre of the reservoir model showing snapshots of the oil saturation, before and after control actions are taken respectively; (c) and (d) Corresponding SP measurements along the production well. The well watercut limit in this example is 25%. The dashed line denoted the noise level (assumed from Chen et al. 2006).

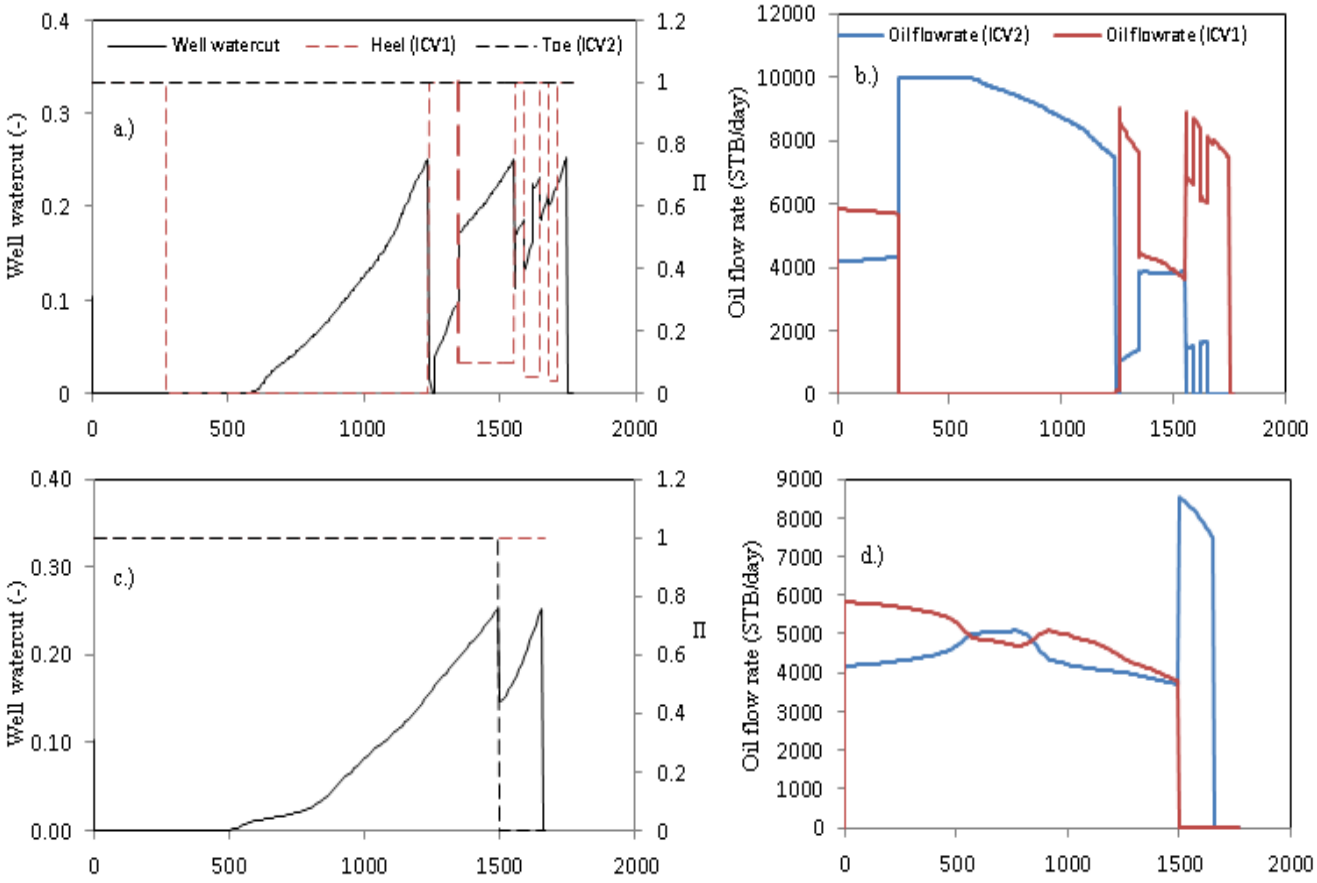


Figure 4.4: (a) and (c) Values of watercut and inflow multiplier against time; (b) and (d) oil production rates against time, for the control strategies based on downhole SP measurements (plots (a) and (b)) and watercut measurements(plots (b) and (d)). Results from the base case model with a 25% well watercut limit.

4.3.3 Impact of Inflow Control on the NPV of the Base Case Model

We now apply the SP-based optimized inflow control strategy on the base case reservoir model to determine the change in well NPV relative to uncontrolled production, and benchmark the results against (i) feedback control based on downhole watercut measurements, and (ii) model-based optimization assuming a perfectly predictive reservoir model, both originally presented in Dilib and Jackson (2012). Figure 4.5 shows the NPV gain for each production strategy as a function of the well watercut limit. The highest gains in NPV are observed at low well watercut limits and decrease as the well watercut limit increases, irrespective of the control mode. At high well watercut limits (> 0.75), inflow control yields no substantial increase in NPV because water production does not incur a significant penalty, and because the discount factor plays a larger role over the longer production timescale. However, even at these high watercut limits, both feedback control

strategies are able to recover the installation costs, so there are no negative NPV gains. At lower well watercut limits (< 0.75), the SP-based feedback control strategy performs better than the watercut-based strategy, particularly at midrange well watercut limits (0.25 – 0.5) where SP-based inflow control yields significant and close to optimal NPV gains.

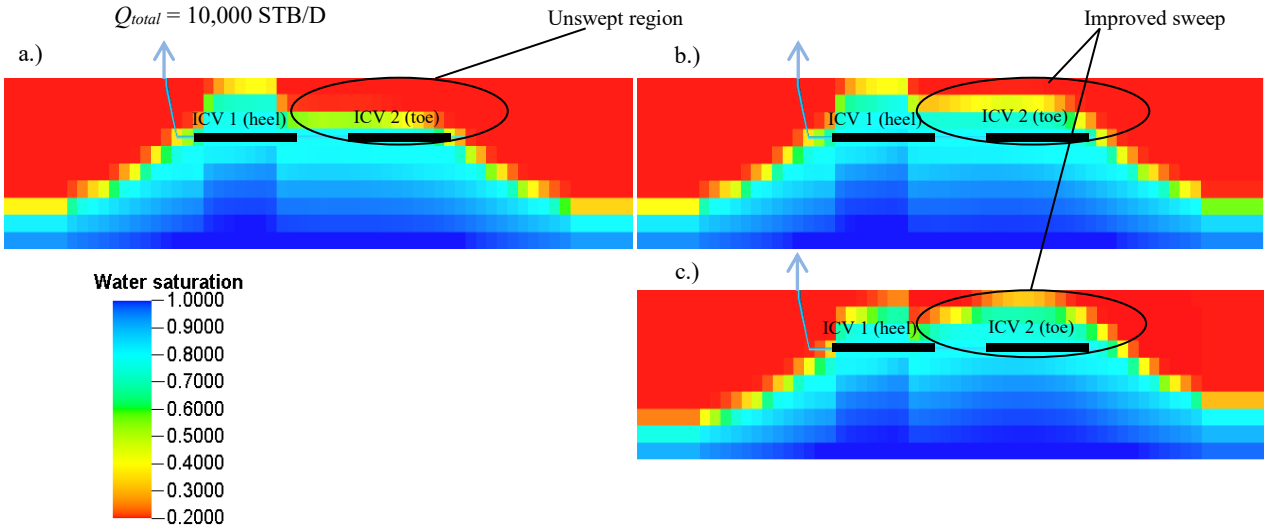


Figure 4.5: Cross-section through the reservoir model showing oil saturation at the end of production for (a) uncontrolled production, (b) feedback control using downhole watercut measurement and (c) feedback control using SP measurements. Results obtained from the base case model with 50% well watercut limit

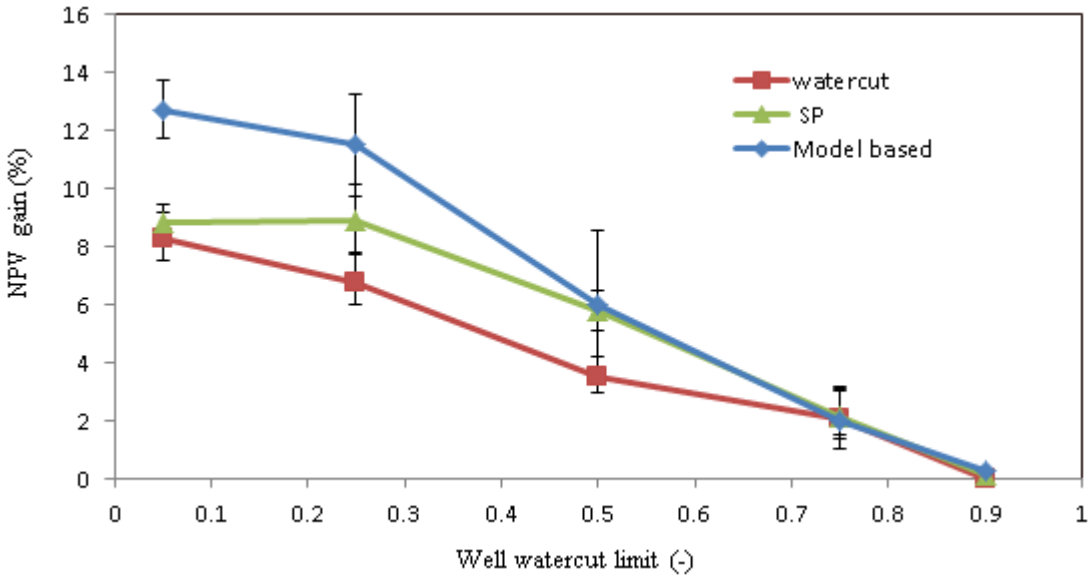


Figure 4.6: The performance of each control strategy on the base case reservoir model over a range of well watercut limits. The error bars represent the range of estimated development costs and operational revenue/expenditure from Dilib and Jackson (2012).

4.3.4 Effect of Unexpected Reservoir Behaviour

We finish by investigating the effect of unexpected reservoir behaviour on the NPV gains for each control strategy as a function of the well watercut limit (Figure 4.7). Each datapoint indicates the NPV gain for a particular uncertain reservoir behavior. The range of NPV gains is higher at the lower well watercut limits regardless of the control approach, ranging from +31% to -2% depending on the reservoir behavior; overall, the gains reduce as the well watercut limit increases. The highest NPV gains are observed when the reservoir anisotropy (k_v/k_h ratio) is high, leading to low sweep efficiency by the aquifer, and are further increased when the aquifer strength is very high. Conversely, the losses in NPV are restricted to one specific reservoir behavior, in which the aquifer strength is very low. Watercut-based feedback control yields a larger range of NPV gains than SP-based control at low well watercut limits, although the average gains over the ensemble of uncertainty are similar. However, as the well watercut limit increases, the benefits of using downhole SP measurements for feedback control become more pronounced, showing higher NPV gains. At higher well watercut limits, inflow control yields negligible NPV gains; even the optimal, model-based strategy adds little value for the reasons discussed previously.

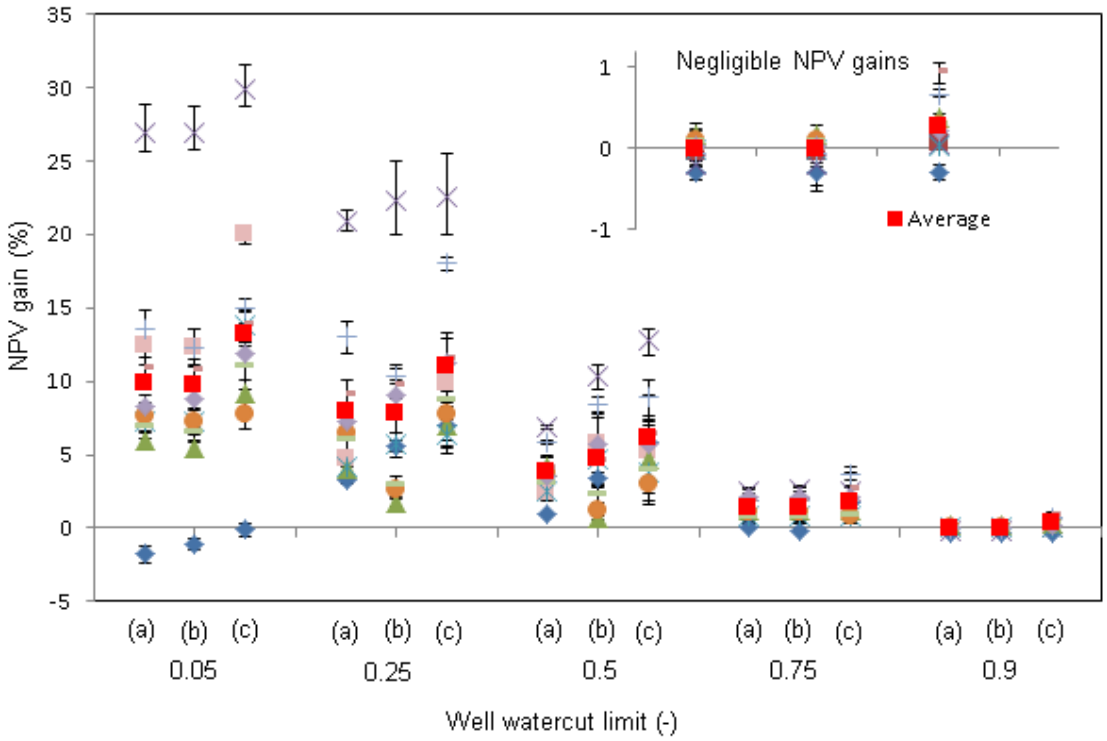


Figure 4.7: NPV gain for feedback control based on downhole measurements of (a) watercut and (b) SP, and (c) model based optimization, at different well watercut limits. Each point represents the NPV gain for a particular unexpected reservoir behavior. The error bars denote the range of estimated development costs and operational revenue/expenditure from Dilib and Jackson (2012).

Reservoir behaviours that show the highest gains from inflow control are those in which the waterfront deviates most significantly from planar. For example, if the permeability is lower than predicted by the base case model, then inflow control yields significant gains in NPV, because this scenario exaggerates the uneven waterfront encroachment towards the heel of the well. At low well watercut limits, watercut-based feedback inflow control shows marginally higher NPV gains compared to SP-based inflow control, because both control methods produce similar volumes of oil, but watercut-control yields shorter production timescales so the discount factor impacts less on well NPV. However, at intermediate well watercut limits, SP-based inflow control yields marginally higher gains that watercut-based control for two reasons. Firstly, there are gains resulting from improved sweep efficiency as a result of early control actions facilitated by SP monitoring; secondly, reduced water production extends well life. Together, these gains outweigh the relative losses resulting from lower initial production rates. Overall, both feedback inflow control methods show similar performance in this production scenario, as indicated by the average points in Figure 4.7.

4.4 Discussion

The NPV gains reported here for inflow control based on downhole measurements of SP are similar to those obtained by Dilib and Jackson (2012) for inflow control based on downhole measurements of phase flow rates (watercut), despite the differences in control actions that result from the different reservoir monitoring strategies. Dilib and Jackson (2012) showed that direct feedback control based on in-well measurements can yield close to optimal NPV gains, but found the optimal strategy was to delay control actions until the well was about to be shut-in because the well watercut had reached the maximum allowed value. They argued that late control is favoured in a direct feedback strategy because the only available control action is to reduce production from one or more completions, and this can result in lower oil production as well as reduced watercut. Optimal strategies, based on perfect model predictions, may take different control actions, but these are often highly non-intuitive and are unlikely to be implemented in practice; for example, in the model studied here, model-based control often found optimal solutions in which the toe completion is initially closed and production is only via the heel, bringing water rapidly to the well before switching production to the toe (Dilib and Jackson, 2012). Such a strategy is unlikely to be adopted in practice. However, here we find SP-based control yields similar

gains to the watercut-based strategy of Dilib and Jackson (2012), even though the SP-based strategy prompts control actions much earlier in well life. This is because SP-based feedback control delays water production by choking the segment of the well with the highest SP, thereby allowing for a more even reservoir sweep. The gains we observe here were not anticipated and are encouraging. Dilib *et al.* (2012) used the base case model to optimise the parameters of the model based and watercut inflow control algorithms. Here, we used the same model to determine the parameters of the SP control strategy to get a fair comparison with both the model based and watercut inflow control strategies. However, using only one model to determine the control parameters of the feedback control strategies could fail to be optimal for reservoir models with intrinsically different behaviour from the base case. For example, the SP feedback control strategy resulted in the lowest NPV (see Figure 4.7 at 0.05 watercut limit) in the reservoir model that showed an almost even waterfront encroachment profile across the axis of the well, compared with the reservoir model that yields the highest NPV which has a significantly higher vertical permeability in the shale free zone than the rest of the reservoir. The control actions are triggered when the change in SP measurements (V_t) exceeds the assumed noise level (0.1 mV). This means that even though there is only a marginally higher effective vertical permeability in the shale free zone, an aggressive control action will be taken by shutting the ICV located at the heel of the well; reducing the well oil production rate. By using an ensemble of reservoir models to determine the constants of the control algorithm, we could improve the performance of the feedback inflow control strategies, allowing for the value of V_t to be optimised for a range of reservoir behaviours. We expect that SP monitoring and inflow control in multi-well developments will yield more significant NPV gains, because inflow control can divert oil towards other nearby producers, so reduced water production need not be associated with reduced oil production. Such multi-well cases are the focus of current research.

4.5 Conclusions

Downhole SP measurements is a promising reservoir monitoring technology that can be used to detect and image waterfronts whilst they are several tens to hundreds of meters away from an instrumented production well. Here we show that closed-loop inflow control based on such measurements can yield gains in well NPV when compared to inflow control based on conventional in-well data in a single smart horizontal well. Moreover, SP-based feedback control can be used to improve well NPV over uncontrolled production when the reservoir does not behave as predicted. Gains in NPV are close to optimal. These results are significant because they suggest a new reservoir technology that can provide a simple but effective approach to production optimization using smart wells. Further studies will examine how the use of an ensemble of models to determine the constants of the feedback control algorithm, can improve the performance of the feedback control strategy. The SP based feedback control strategy will also be tested on a wider range of reservoir and well scenarios, including multi-well developments.

Chapter 5

Self-Potential Measurements in Multi-Well Developments: Application to the Brugge Field Model

5.1 Introduction

In Chapter 4, we demonstrated that closed-loop feedback control of smart wells, facilitated by the use of downhole measurements of self-potential (SP) and inflow control valves (ICVs), can be used for production optimization during waterflooding. An inflow control strategy based on downhole SP measurements can be used to prevent or minimise water production by monitoring waterfront encroachment prior to water breakthrough at the well. In this section, we extend the work done in Chapter 4 for the first time in a realistic multi-well development by means of numerical simulation using the synthetic Brugge field case study (Peters *et al.* 2010). The Brugge case study presents a more realistic reservoir model than that used in Chapter 4, consisting of a heterogeneous Brent-type reservoir with faults and an underlying active aquifer. Understanding the SP signals generated during waterflooding in the type of reservoir represented by the Brugge field model is an important step to demonstrate the technical case for a field trial of the SP monitoring technology.

The objectives are therefore twofold. First, we investigate whether measurements of SP signals along instrumented production wells could provide useful information to monitor waterfronts moving in the vicinity of a well. Second, we determine whether, and under what reservoir and production conditions, the resulting SP signals would be large enough to be measured and interpreted. We compare the relative contributions of the EK and EC potentials to the SP signals generated in the Brugge reservoir model during production. We want to understand how these contributions may vary with respect to the properties of the injected and formation brine and, subsequently, to determine whether SP measurements in instrumented production wells can be useful in making inflow control decisions.

5.2 Methodology

5.2.1 Brugge Field Geological Model

The Brugge field case is a synthetic model that was developed for a comparative study to assess and benchmark a range of history matching and production optimisation algorithms as part of an SPE Advanced Technology Workshop (Peters *et al.*, 2010). The geological characteristics of the Brugge Field comprise a half dome structure separated into an east and west region by a vertical fault, oriented 20° N and positioned at the northern edge (Figure 5.1; Peters *et al.*, 2010). The reservoir is approximately 10×3 km in plan-view and has an average thickness of 60 m. The properties of the reservoir are based on a North Sea Brent-type North Sea field, following the general Brent stratigraphy which consists of the Broom, Rannoch, Etive, Ness and Tarbert formations (Morris *et al.*, 2003). In the Brugge field model, the Tarbert formation was omitted and the remaining stratigraphic layers were termed the Schie, Waal, Maas and Schelde from bottom to top respectively (Table 5.1). Note that Peters *et al.* (2010) swapped the sequence of the Rannoch and Etive formations of the Brent stratigraphy in the brugge model; hence the Maas and Waal stratigraphic layers are based on the Rannoch and Etive formation properties respectively. They claimed that this improved the attractiveness of the exercise.

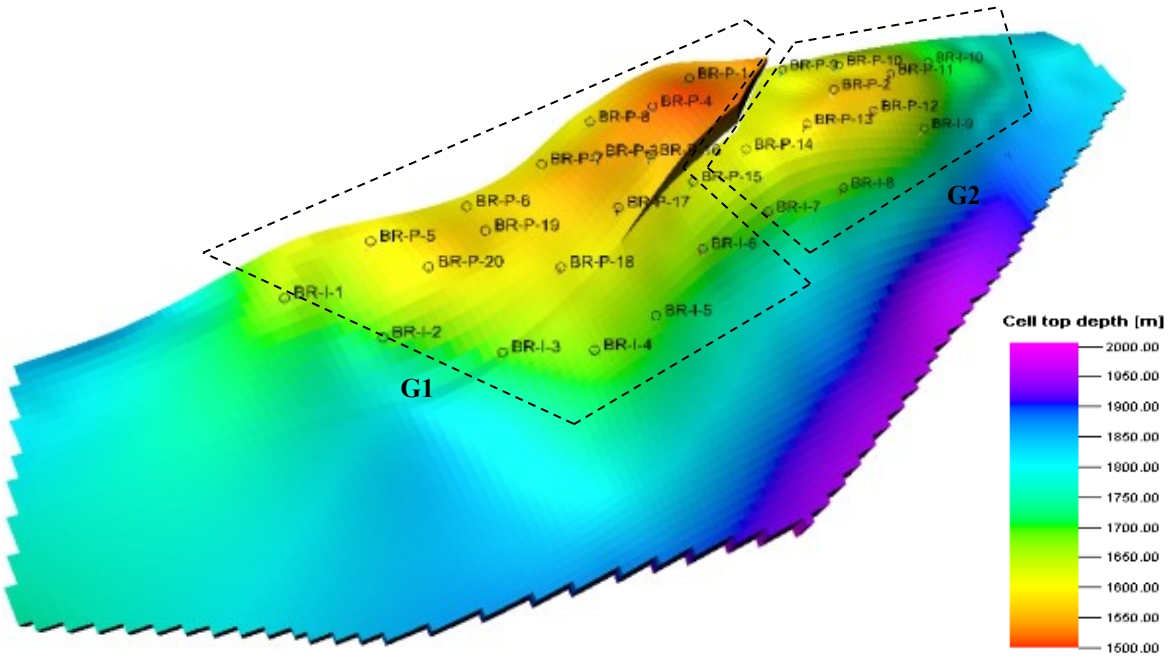


Figure 5.1: The structure of the Brugge Field showing the depth (m) and the positions of the 20 production (denoted BR-P) and 10 injection (denoted BR-I) wells. The well groups G1 and G2 are separated by an internal fault (modified from Peters *et al.*, 2010)

Reservoir formation	Average thickness (m)	Average Porosity* (%)	Average Permeability* (md)	Average NTG (%)	Depositional environment	Brent Analogue
Schelde	10	20.7	1105	60	Fluvial	N
Maas	20	19.0	90	88	Lower Shoreface	R
Waal	26	24.1	814	97	Upper Shoreface	E
Schie	5	19.4	36	77	Sandy shelf	B

Table 5.1: Stratigraphy used in Brugge field with main reservoir characteristics (Peters *et al.*, 2010; *average values for sand only i.e., net porosity and permeability)

5.2.2 Reservoir Simulations

The simulation model used by Peters *et al.* (2010) was derived from a high resolution geological model comprising 20 million grid cells, upscaled to a 450,000 grid cell model to yield the 'truth' case for reservoir simulation purposes. The reservoir contains under-saturated oil underlain by an active aquifer. There are no continuous flow barriers between the stratigraphic layers and the estimated oil in place is 756 MM STB (Peters *et al.* 2010). An ensemble of 104 upscaled (60,000 grid cells) reservoir model realisations with 139 rows, 48 columns and 9 layers varying in permeability, porosity and NTG were created for the comparative history matching study. Production was simulated via 20 production wells and 10 injection wells completed in the reservoir zones listed in Table 5.2. The comparative study assumed a 30 year production period with production and injection constraints given in Table 5.3. The first 10 years of production simulation was used for the history matching exercise and the 10 – 30 year production period for the production optimisation exercise. The 'truth' model was run for the first 10 years to generate observations of a synthetic production and injection 'history data'. This synthetic history data was then used to produce an updated, history matched upscaled model from the ensemble that behaved closest to the truth case model. The updated model from the history matching exercise was used to carry out the comparative production optimisation exercise for the 10 – 30 year period.

In this chapter, we randomly selected a reservoir model from the ensemble of 104 upscaled realisations to represent a stochastic realisation of a 'base case' reservoir model. Note that the 'truth' model used by Peters *et al.* (2010) was not made available. In Chapter 6 we use the remaining 103 model realisations to test the performance of different feedback control strategies against unexpected reservoir behaviour. Production was simulated using ECLIPSE 100 (Schlumberger, 2012) for 30 years to determine the key reservoir parameters (such as the water phase potential, saturation and salinity) required to simulate the SP. The selected reservoir model was simulated for the 0 – 30 years period using the production and injection constraints of the 10 – 30 years period in Table 5.3. Thus the maximum production rate was 3,000 STB/day at all the production wells and the maximum water injection rate was 4,000 STB/day at all the injection wells. Production was also maintained at a minimum bottomhole pressure (BHP) of 725 psi and a maximum watercut of 0.90, while the injection wells were maintained at a maximum BHP of 2,611 psi for the duration of the simulation. Note that we did not constrain production during the first 10 years using the synthetic 'history data' generated from the truth model.

Well	Top Completion	Middle Completion	Bottom Completion
All injectors (I1 – I10)	Layer 1-2 (Schelde)	Layer 3-5 (Maas)	Layer 6-9 (Waal and Schie)
All Producers, except P5, P9, P10, P14 and P15	Layer 1-2 (Schelde)	Layer 3-5 (Maas)	Layer 6-8 (Waal)
P5, P10, P14 and P15	Layer 1-2 (Schelde)	Layer 3-5 (Maas)	
P9	Layer 1-2 (Schelde)		

Table 5.2: Well completion and corresponding reservoir zones (Peters *et al.*, 2010)

We set the initial temperature and formation brine salinity at 80 ^{0}C and 2.5 M respectively, and injected brine of 0.5 M and a temperature of 30 ^{0}C. The chosen parameters represent waterflooding where seawater is injected into a reservoir containing typically more saline formation brine. The reservoir fluid properties are summarised in Table 5.4. We also investigated the impact of varying the production rate and formation brine salinity on the

SP signal. We varied the production rates between 500 and 3000 STB/D, which is the range of production rates observed in the synthetic production history data available for the first 10 years of production in Peters *et al.* (2010), and the formation brine salinity between 0.5 and 3 M. For the salinity variation cases, we assumed that the formation brine has the same salinity as the injected water. Hence, the EK potential contributes to the total SP signal measured at the production well, with the EC potential being zero because there is no concentration gradient.

	Well constraints	**0 – 10 years**	**10 – 30 years**	**Units**
Producer	Maximum liquid rate	2,000	3,000	STB/day
	Minimum BHP	725	725	psi
	Maximum watercut	0.90	-	(-)
Injector	Maximum liquid rate	-	4000	STB/day
	Maximum BHP	2611	2611	psi

Table 5.3: Base case rate and pressure constraints for producer and injector wells (Peters *et al.*, 2010). Simulation was constrained for this study using the producer and injector constraints between 10 – 30 years (highlighted by the dashed rectangle).

Property (Unit)	Rock	Oil	Water
Viscosity (cp)	-	1.294	0.32
Density (kgm^{-3})	-	62.6	56
Formation (initial) –salinity (M)	-	-	2.5
Injection salinity (M)	-	-	0.5 (seawater)
Formation (initial) – temperature ($°C$)	80	80	80
Injection temperature ($°C$)	-	-	30

Table 5. 4: Base case fluid and rock properties.

5.2.3 Numerical Modelling of SP

The SP signal was simulated using the post-processor developed in Chapter 3 that uses values of water phase potential (Φ), saturation (S_w), salinity (C_f) and temperature (T) obtained from the Eclipse 100 simulation as shown in Chapter 4. The electrokinetic (C_{EK}) and electrochemical (C_{EC}) coupling coefficients, and the conductivity terms used in the SP solver are dependent on the water salinity, temperature and the "relative coupling coefficient" C_r, determined using the equation in Chapter 3.3. We also observed that the thermoelectric potential contribution to the SP signals measured at a production well prior water breakthrough is negligible, as temperature fronts associated with the injected water lags significantly behind the saturation front. Thus we simulate the SP signals in response to only the pressure and concentration gradients in the brine; with the SP dominated by the electrokinetic and electrochemical potential. The average grid size of the base case model is 120m×120m×10m, which is approximately the average distance at which measurable SP signals can be measured at an instrumented production well as shown in Jackson *et al.* (2012) and Chapter 4. Thus, local grid refinements (LGRs) were placed around each of the production wells to simulate high resolution reservoir fluid flow using a refined/local grid (child model) within a coarser (parent grid) model. This method was also extended to the SP solver to generate higher resolution SP simulation results around the wells.

Figure 5.2 (a) shows an example of the child model/LGRs with cells of 10m×10m×2.5m (determined based on grid refinement study described later in Figure 5.4), located within the coarser parent grid of the upscaled Brugge model. The NNC keyword in the ECLIPSE 100 software was used to identify the non-neighbour connections between cells across the fault (Figure 5.2 (b)) and these were incorporated into the SP solver to allow for the flow of charge across the fault. Electrically conductive, water saturated shale layers of 20m (thickness) were also placed on the sides of the Brugge model and overburden and underburden shale layers of 60m (thickness) were placed above and below the Brugge model (as shown in Figure 5.2 (c)); these are required for the SP modelling as electrical currents may exploit these shale layers (as in the base case model use in Chapter 4.2.1). We developed a MATLAB script to identify the non-neighbour connections across the fault between these overburden and underburden shale layers and the reservoir model; these were also incorporated into the SP solver to allow for the flow of charge across the fault between the shale layer and reservoir.

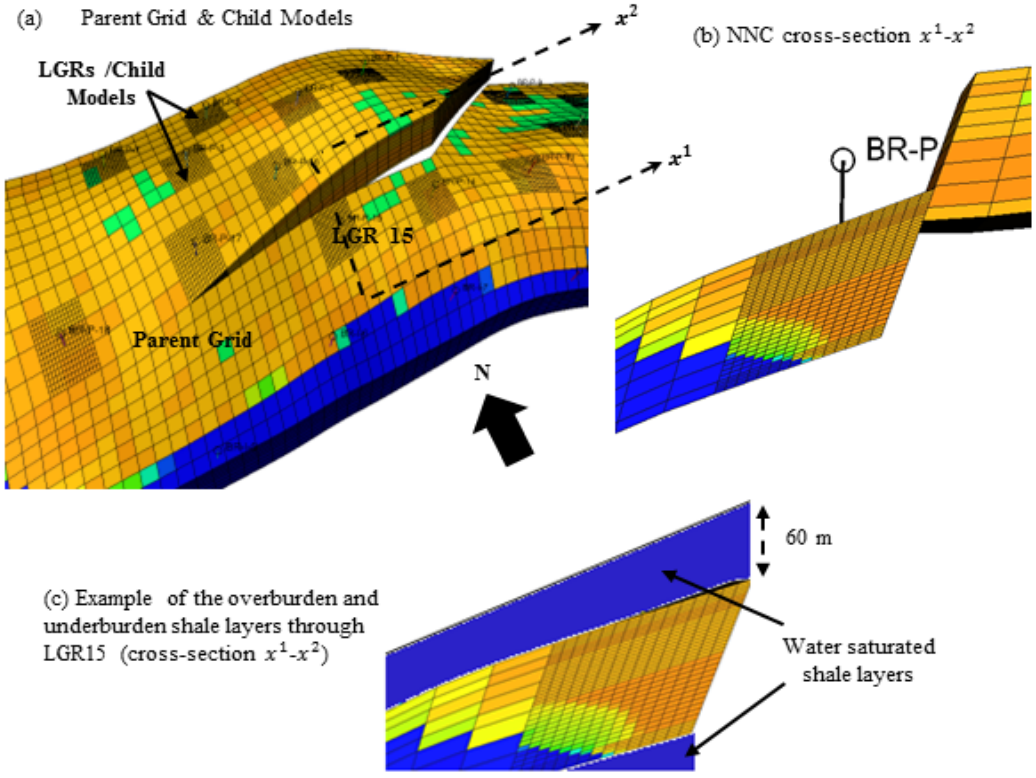


Figure 5.2 : (a) Brugge Field water saturation variation showing parent and child grids. (b) Water saturation (x^1-x^2) cross-section after 330 days of production showing the NNC across the reservoir fault. (c) Overburden and underburden shale layers place above and below the model; example through LGR15 (cross-section x^1-x^2)

A coupled shared node method (James *et al.,* 2006) was adopted to solve the electrodynamic model. Figure 5.3 shows an example of a 2D parent grid and a LGR. The cell centres of the parent grid are identified by their x_i, y_j indices. At each grid cell centre, an electrical conductivity σ_{fs}, potential Φ, concentration C_f, temperature T and a cross-coupling term L_{EK}, L_{EC} is assigned. The SP is simulated independently on the parent grid and child models (i.e. the LGRs) using the SP solver developed in Chapter 3. The electrodynamic model is first solved on the parent grid to allow for the SP on the child models to be simulated, imposing the boundary conditions of the voltage calculated on the coarse cells/parent grid which border the LGR in the parent grid. Ghost cells similar in dimension to the LGR cells, identified by their x_i^p, y_j^p indices are placed in the parent cells on the boundary of the LGR, and the values of the voltage and pressure are set to that of the parent cells. The electrodynamic model is then solved on the child models/LGRs subject to the boundary values defined in the ghost cells.

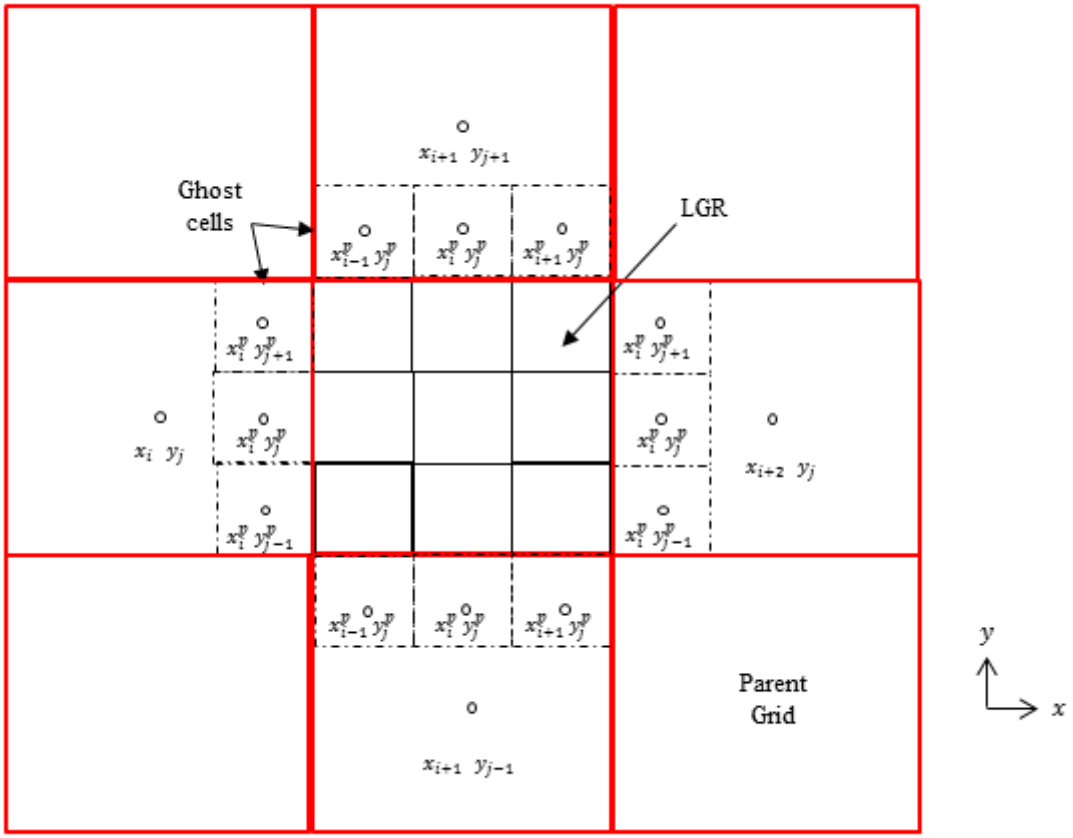


Figure 5.3: Sample 2D mesh zones of parent grid, child model/LGR and ghost cells

We tested the updated SP solver on a simple 2D sandstone oil column model (Figure 5.4), which measures 10×20 m and has 10 × 20 active parent grid cells, divided evenly across the model. A local grid refinement of 6 × 6 grid cells was confined within the parent grid in cell 10 – 12 in the x direction and 5 – 6 in the y direction. The sandstone contains undersaturated oil and connate water, with water injected into the far right of the model to displace the oil, which creates a pressure gradient of 20 MPa across the boundary. For simplicity, capillary pressure effects were not considered in the model. The oil viscosity and water viscosity were set to be 0.1 and 1 cp respectively to allow for a piston-like displacement in the sense that a sharp interface (front) exists between the oil and water. We used the same petrophysical properties of the electrokinetic coupling coefficient, brine conductivity, oil density and water density presented in chapter 3 to simulate the SP obtained in the parent grid and the LGR. The result of the SP simulated on the LGR matched that of the parent grid.

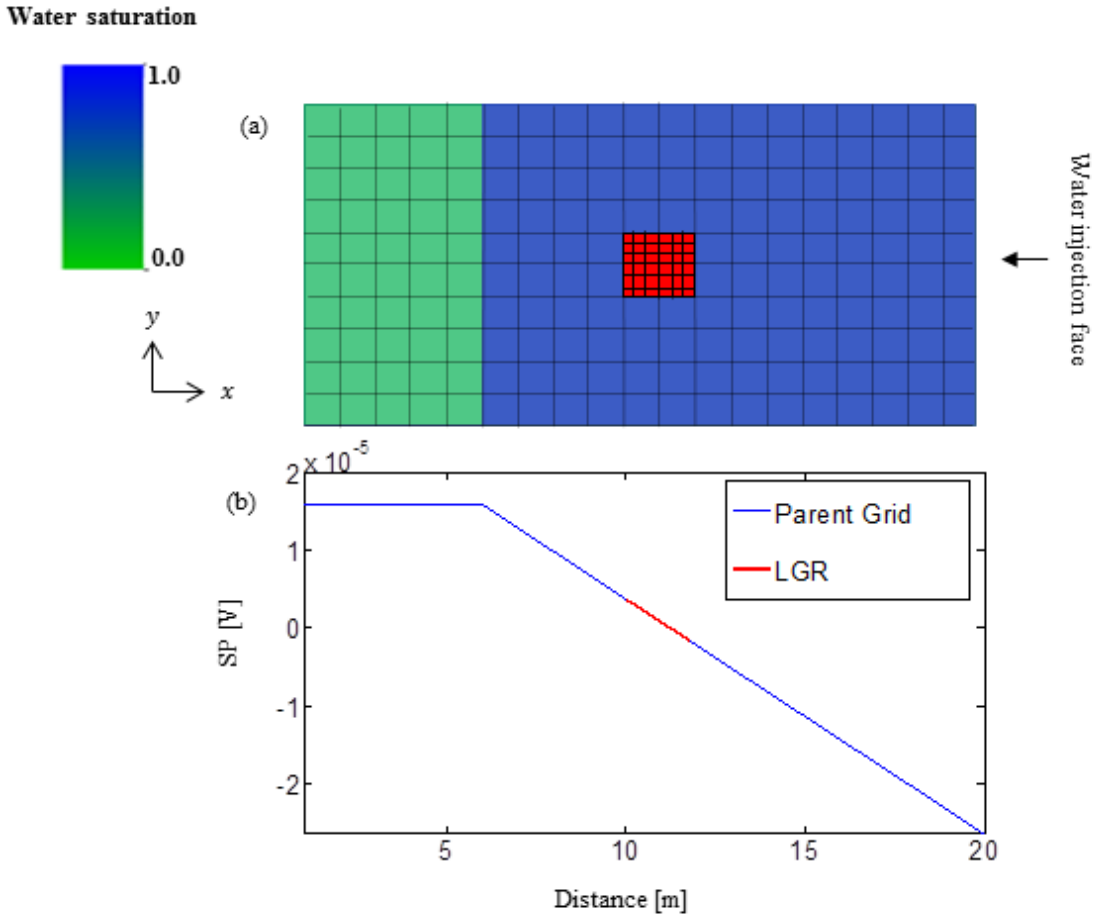
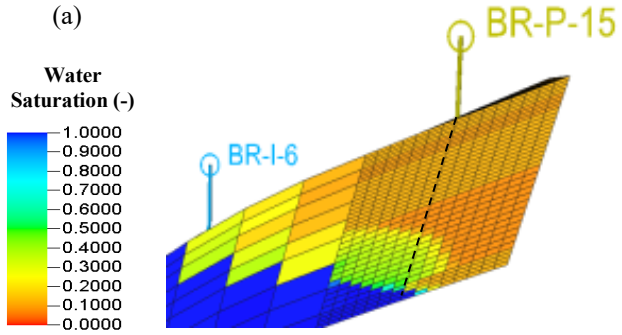


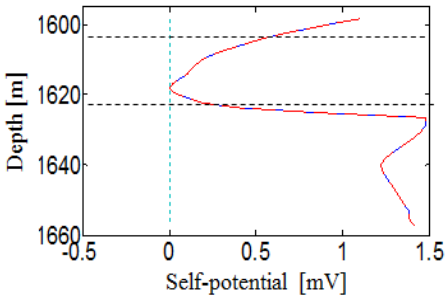
Figure 5.4: (a) Saturation variation within the 10 × 20 grid cells parent grid 2D oil Column, and a 6 × 6 LGR placed within cell 10-12 in the x direction and 5-6 in the y direction of the parent grid cell. (b) The corresponding SP signal along the oil column. The SP signal simulated in the LGR match the SP simulated in the Parent grid.

The LGRs defined in the Brugge model were confined within one coarse parent grid cell around each of the production wells. This is because the ECLIPSE 100 simulator does not run if an LGR overlaps with the LGRs around other wells and/or faults in the model. The coupled, shared-node method of LGR provides a less computationally expensive approach to obtaining higher resolution SP simulation results than refining the entire parent grid. The solution accuracy was controlled by the number of grid cells used in the LGR, determined by a grid refinement study. Figure 5.4 shows a cross-section of the water saturation through well P15 after 300 days of production and the corresponding simulated SP signals measured along well P15 taken with reference to a distance electrode in the shale layer. The magnitude of the maximum SP signal measured along well P15 varies with the grid size in the LGR (Figure 5.4 (c)), which plots the magnitude of the SP signal against the grid size. Figure 5.5 shows that the magnitude peaks and stabilises when the grid size is 10×10×2.5 m, and will be used in this study.

(a)



(b)



(c)

Num	Grid size [m]	Max SP [mV]
1	4×4×0.625	1.4981
2	6×6×1.25	1.4989
3	8×8×1.875	1.4991
4	10×10×2.5	1.4992
5	12×12×3.25	1.4992

(d)

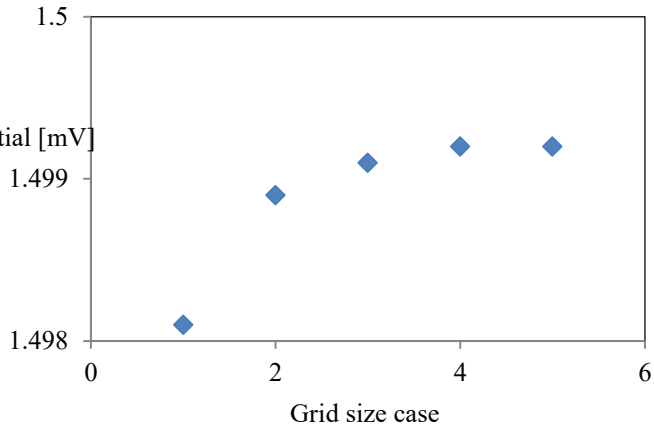


Figure 5.5: Result of the LGR grid refinement study (a) Water saturation cross-section through well P15 after 330 days of production, and (b) the corresponding SP signals along the well: relationship with waterfront shape. (c) Table of the grid size and (d) LGR sensitivity plot.

5.3 Results

5.3.1 Production behaviour of the 'base case' model

The simulated field cumulative oil and water production versus time, and the field oil and water production rates versus time are plotted in Figure 5.6, with water breakthrough observed after approximately 1 year of production. Figure 5.7 shows a plan view of the saturation and concentration through the middle of the reservoir after 5 years of production. The saturation front moves towards the production wells and, ahead of the saturation front, oil flows in the presence of irreducible water; behind the front, water flows in the presence of residual oil. The concentration front associated with the injection of lower salinity seawater into the higher salinity formation brine also moves towards the production wells but lags behind the saturation front due to mixing of the injected and formation brine. The saturation and concentration fronts reach well P15 first (Figure 5.6).

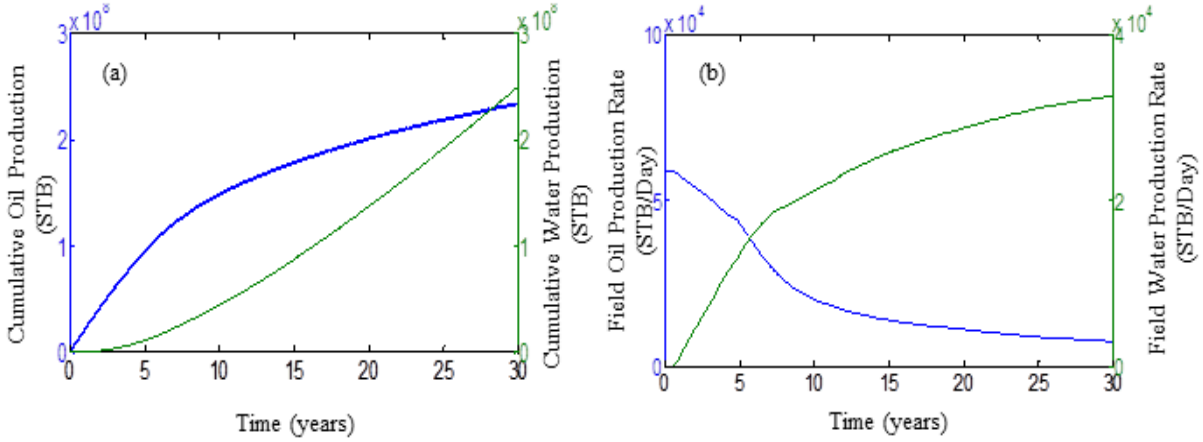


Figure 5.6: (a) Field Cumulative oil production and Field Cumulative water production plotted against time.

We analyse production from wells P12, P15 and P5 (highlighted in Figure 5.7 (a)), to understand the reservoir flow dynamics in the vicinity of wells with different completion configurations, at different locations in the field. Figure 5.8 shows plots of the completion liquid production rates, oil production rates, water production rates and watercut versus production time measured in well P12. The well is completed in the Schelde (top), Maas (middle) and Waal & Schie (bottom) stratigraphic layers. As expected, the highest liquid (oil and water) production rate is observed from the completion located in the highest permeability layer, which is the Waal & Schie (bottom) completion in this case, followed by the Schelde (top) completion and the Maas (middle) completion respectively. Water

breakthrough occurs first in the Waal and Schie (bottom) completion at approximately 2 years as shown in Figure 5.8 (c), suggesting that the saturation front has reached the base of the well.

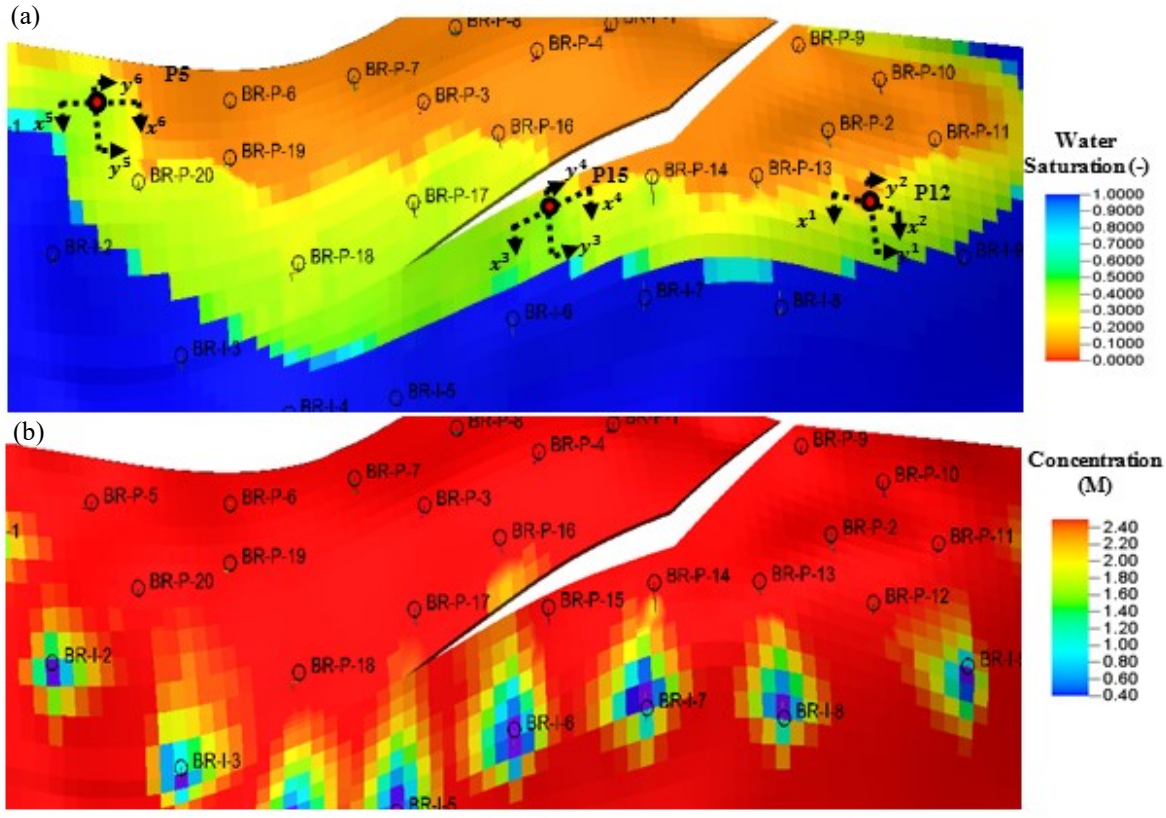


Figure 5.7: The plan-view (a) Water saturation and (b) concentration cross-sections through the middle of the reservoir after 5 years of production. The waterfront reaches well P15 first across the reservoir, highlighted by the concentration front cross section.

After water breakthrough, the oil production rate in the Waal & Schie (bottom) completion reduces significantly, with the Schelde (top) completion yielding the highest oil production rate (see Figure 5.8 (b)). Water breakthrough occurs next in the Schelde (top) completion at approximately 5 years, with a relatively low water production rate compared to the oil rate; hence, the watercut measurement in the Schelde completion is negligible. Water breakthrough occurs last in the Maas (middle) completion at approximately 12 years, but has a higher post-breakthrough watercut than the Schelde (top) completion (Figure 5.8 (d)). The water production rate in the Schelde completion eventually becomes higher than the Maas completion before the end of production.

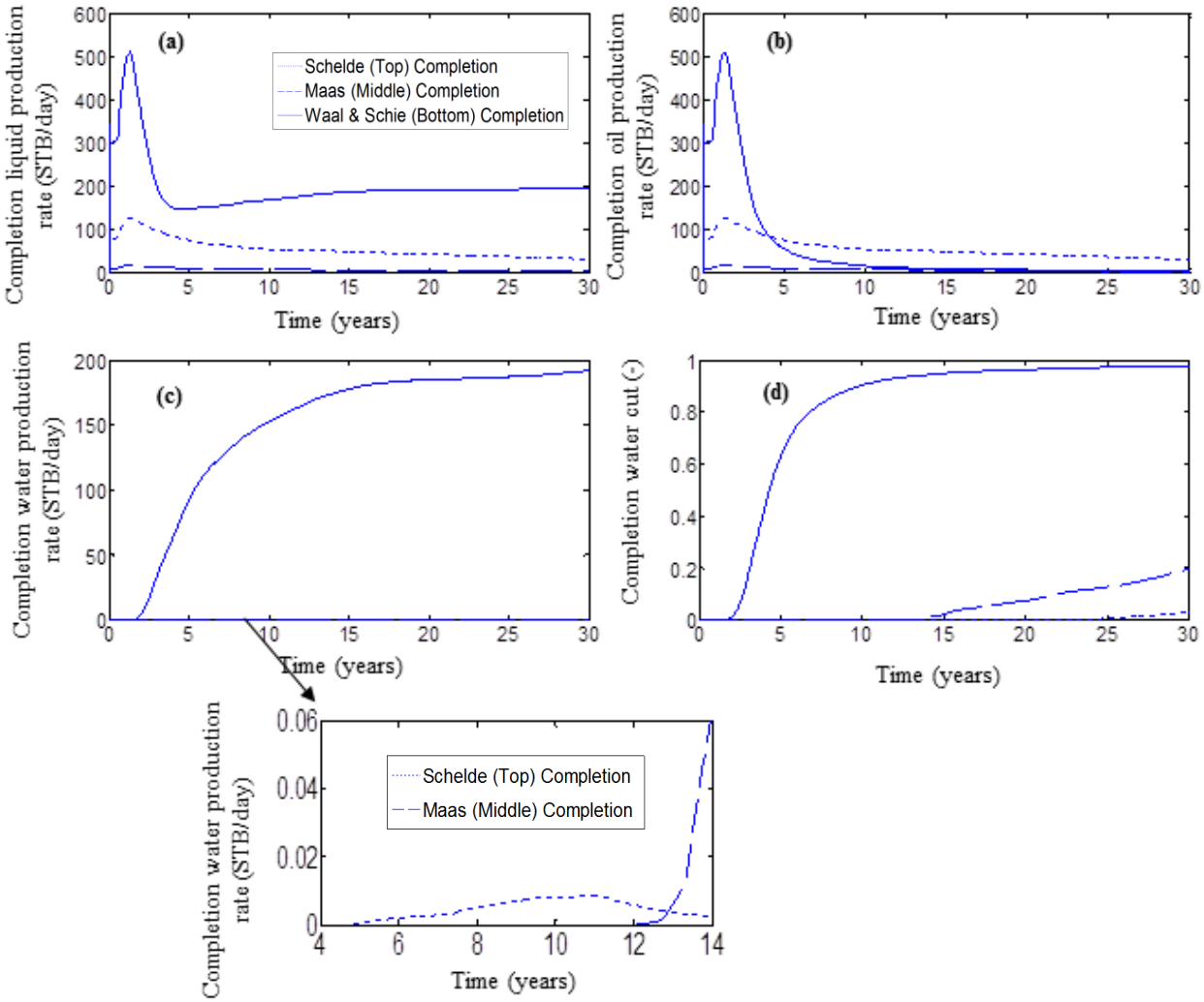


Figure 5.8: (a) Completion fluid production rate vs. time; (b) Completion oil production rate vs. time; (c) Completion water production rate vs. time; (d) Completion watercut vs. time; measured in well P12. Water breakthrough occurs in the Waal & Schie (bottom) completion; at a higher resolution in the completion water production rater vs. time plot, we observe that water breakthrough occurs next in the Schelde (top) completion after approximately 5 years, and occurs last in the Maas (middle) completion after 12 years of production.

Figure 5.9 shows the $(x^1 - x^2)$ saturation and concentration cross-sections and the $(y^1 - y^2)$ saturation cross-sections (see Figure 5.7 (a) for the location of the section), through well P12 after 360, 2700 and 4700 days of production respectively; also shown are plots of the pressure drawdown along the well. Because the well is completed in all three stratigraphic layers, the pressure drawdown profile along the well is approximately constant; hence, the waterfront flows towards the well laterally along each of the stratigraphic layers. The waterfront reaches the well first in the highest permeability layer i.e. the Waal & Schie (bottom) layer which is closest to the oil water contact (OWC). Due to the higher permeability of the Schelde (top) layer than the Maas (middle) layer, the waterfront in Schelde layer flows ahead of the front in the Maas (middle) layer, and reaches the well at a later time (not shown in Figure 5.9). The waterfront in the Schelde (top) layer has to travel a longer distance laterally to reach the well due to the dome-like structure of the reservoir; which explains the significantly lower water production rate when water breakthrough occurs. Furthermore, gravity slumping of the injected water is dominant as a result of the constant pressure drawdown profile along the well and is channelled towards the bottom of the well. Hence, the concentration front reaches the well first in the Waal & Schie (bottom) layer.

Plots of the completion liquid production rates, oil production rates, water production rates and watercut versus production time measured in well P15, which is only completed in the Schelde (top) and Maas (middle) stratigraphic layers are shown in Figure 5.10. As expected, a higher liquid (oil and water) production rate is observed from the completion in the Schelde (top) layer which has a higher permeability than the Maas (middle) layer. Water breakthrough occurs first in the higher permeability Schelde (top) completion after approximately 2.5 years of production and 90 days later in the Maas (middle) completion (see Figure 5.10 (c)). At this time, the water production rate starts increasing and oil production rate reduces. A higher water production rate is observed from the Schelde (top) completion, suggesting that the waterfront in the Schelde (top) layer is flowing ahead of the front in the Maas (middle) layer. However, because the water production rate relative to the total liquid production rate measured in the Maas completion is higher than the Schelde completion, a higher watercut measurement is observed in the Maas (middle) completion (Figure 5.10 (d)).

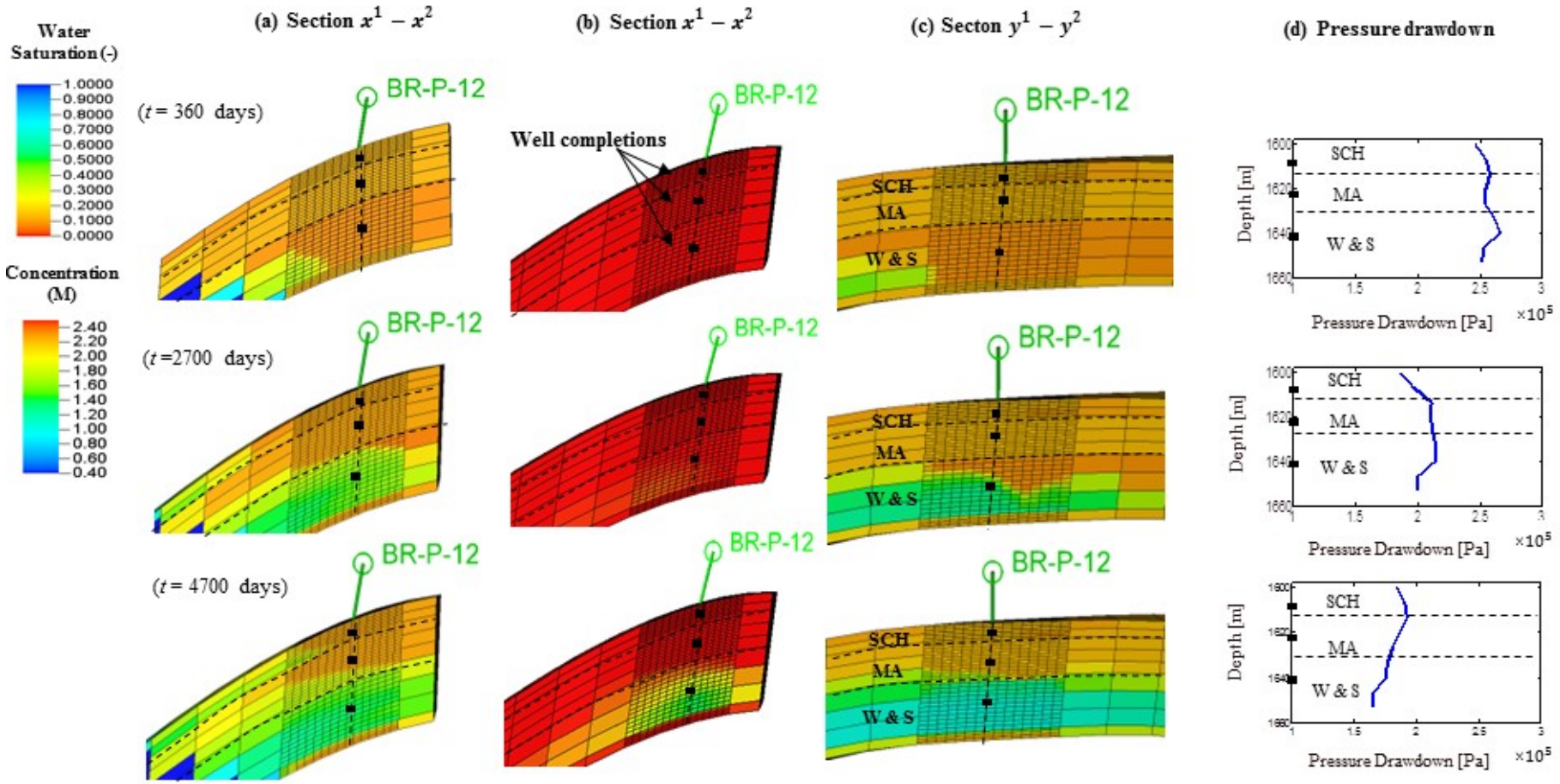


Figure 5.9: (a) saturation $x^1 - x^2$cross-section, (b) concentration $x^1 - x^2$cross-section and, (c) saturation $y^1 - y^2$cross-section (from Figure 5.7) and (d) the pressure drawdown at well P12 at 360, 2700 and 4700 days into production respectively. The horizontal dashed lines show the different stratigraphic layers. The waterfront in the Schelde (top) and Waal & Schie (bottom) layers flows ahead of the front in the Maas (middle) layer.

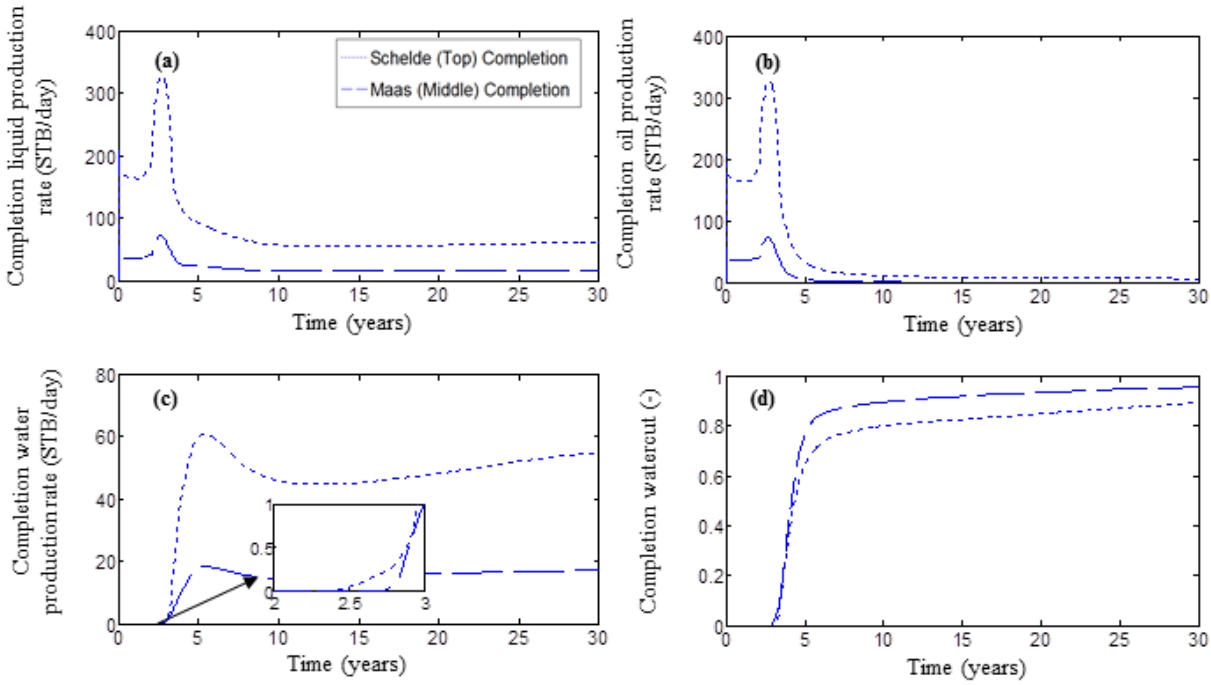


Figure 5.10: (a) Completion fluid production rate vs. time; (b) Completion oil production rate vs. time; (c) Completion water production rate vs. time; (d) Completion watercut vs. time; measured in well P15. At a higher resolution in the completion water production rate vs. time plot, we observe that water breakthrough occurs first in the Schelde (top) completion after 2.5 years.

Figure 5.11 shows the $(x^3 - x^4)$ saturation and concentration cross-sections and the $(y^3 - y^4)$ saturation cross-section in Figure 5.7 (a), through well P15 at 330, 660 and 1380 days of production respectively; along with the corresponding pressure drawdown profile along the well. Unlike well P12, the drawdown decreases from top to bottom, with the Waal & Schie layer having the smallest drawdown as the well is not completed in this layer. This leads to a vertical potential gradient that channels reservoir fluid towards the top of the reservoir. Hence, water from the Waal & Schie layer (bottom) layer flows upwards into the Maas (middle) layer completion and the waterfront front flows laterally into the Schelde (top) layer completion. The waterfront reaches the well first in the highest permeability Waal & Schie (bottom) layer after 330 days of production, followed by water breakthrough in the Schelde (top) layer completion and shortly afterwards in the Maas (middle) completion. The concentration fronts in the Schelde (top) and Waal & Schie (bottom) layer both flow ahead of the concentration front in the Maas (middle) layer, and reaches the well first in the Schelde (top) completion which has the higher liquid production rate after approximately 1380 days of production.

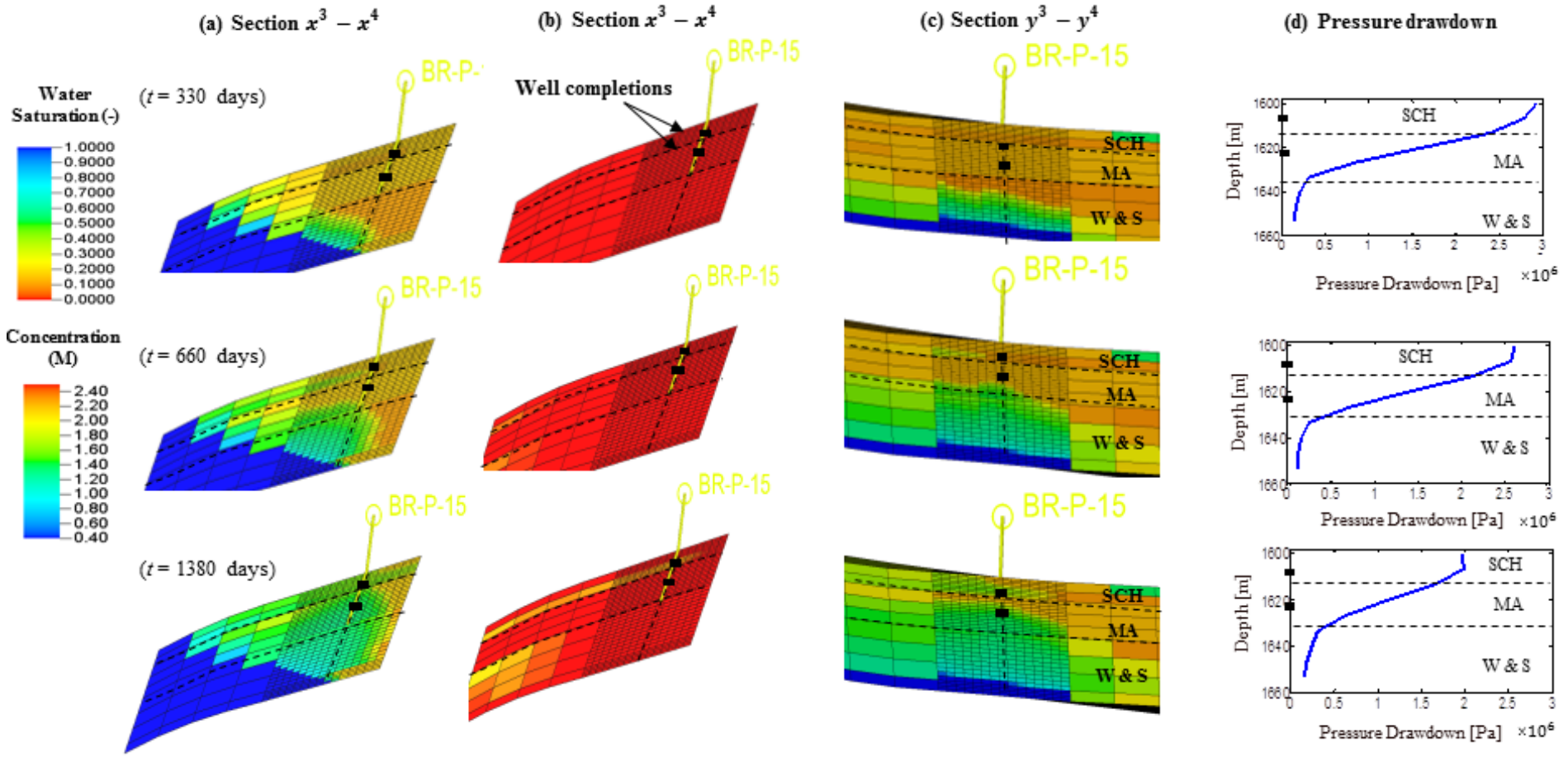


Figure 5.11: (a) saturation $x^3 - x^4$cross-section, (b) concentration $x^3 - x^4$cross-section, (c) saturation $y^3 - y^4$cross-section (from Figure 5.7) and (d) the pressure drawdown at well P15, at 330, 660 and 1380 days into production respectively. The horizontal dashed lines show the different stratigraphic layers. The waterfront in the Schelde (top) and Waal & Schie (bottom) layers flows ahead of the front in the Maas (middle) layer. The high pressure drawdown in the Schelde (top) layer creates a vertical potential gradient which drives reservoir fluid from the underlying Waal and Schie (bottom) layer upwards at t = 660 days, leading to the early water breakthrough in the Maas (middle) layer.

We now investigate the production behaviour of well P5. Figure 5.12 shows plots of the completion liquid production rates, oil production rates, water production rates and watercut versus production time measured in well P5. Just like the well completed in all 3 layers where the Waal & Schie has the highest liquid (oil and water) production rate, significantly higher liquid production rate is observed from the completion in the Schelde (top) layer which has a higher permeability than the Maas layer. However, water breakthrough occurs first in the Maas (middle) completion at approximately 5 years, with a simultaneous decrease in oil production. Water breakthrough occurs later in the Schelde (top) completion at approximately 5.5 years as shown in Figure 5.12 (c). Higher water production rate is also observed in the Schelde completion after water breakthrough, although a higher watercut measurement is observed in the Maas (middle) completion.

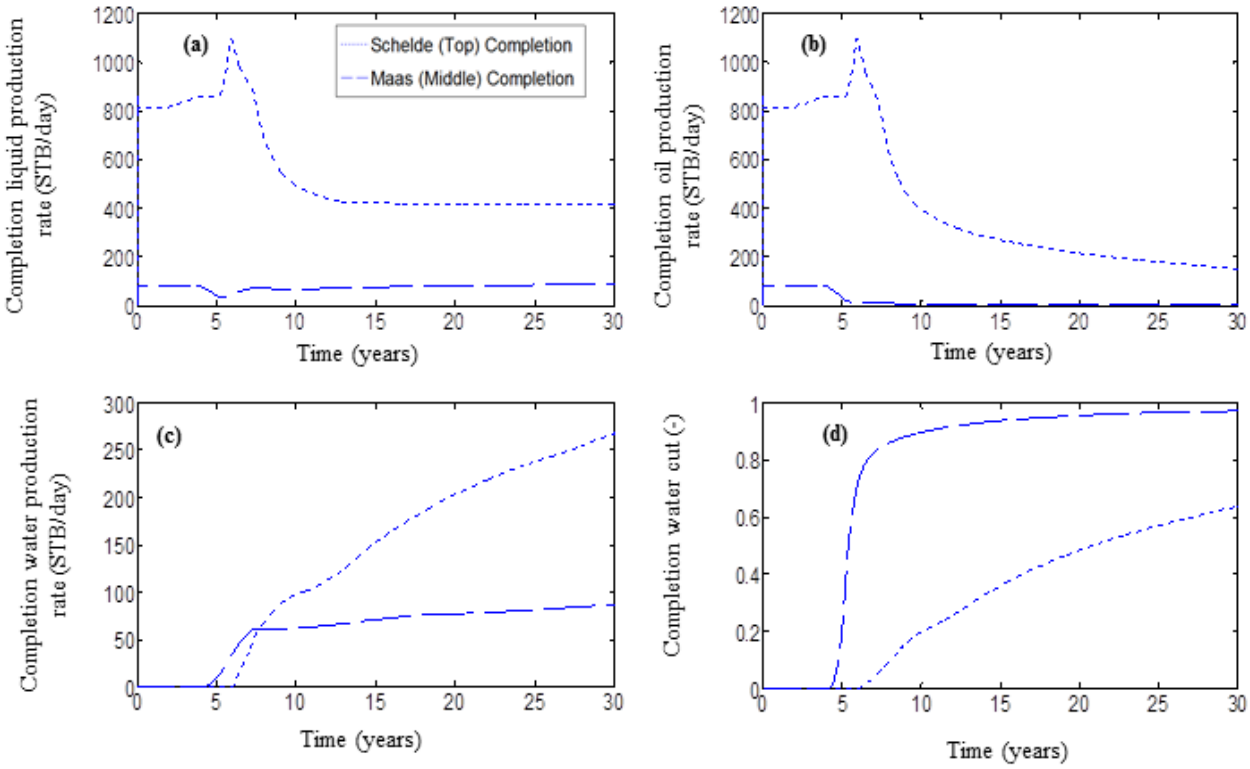


Figure 5.12: (a) Completion liquid production rate vs. time; (b) Completion oil production rate vs. time; (c) Completion water production rate vs. time; (d) Completion watercut vs. time; measured in well P5. Water breakthrough occurs first in the Maas (middle) completion after 5 years.

In well P5, the saturation and concentration fronts flow towards the well in a similar manner to well P15. Figure 5.13 shows the $(x^5 - x^6)$ saturation and concentration cross-sections and the $(y^5 - y^6)$ saturation cross-section (location in Figure 5.7 (a)), through well P5 at 30, 1100 and 2000 days of production respectively; along with the pressure drawdown measured along the well. Similar to well P15, the drawdown increases from top to bottom, with the Waal & Schie layer having the smallest drawdown, leading to a vertical potential gradient that channels reservoir fluid towards the top of the reservoir. Thus, water from the Waal & Schie layer (bottom) layer again flows upwards into the Maas (middle) layer completion, but water flows laterally into the Schelde (top) layer completion. The vertical potential gradient allows for a more rapid upward flow of the water from the Waal & Schie (bottom) layer into the Maas (layer) than well P15, leading to the earlier water breakthrough in the Maas (middle) completion after approximately 2000 days of production and this upward flow creates a region of bypassed oil in the Mass layer. The waterfront reaches the Schelde (top) completion later. The concentration front in the Schelde (top) and Waal & Schie (bottom) layer both flow ahead of the concentration front in the Maas (middle) layer but significantly lags behind the saturation front and does not breakthrough in well P5 after the simulation production time.

Overall, production simulation observed in the three wells (P12, P15 and P5) show similar trends. In well P12 and P15, water breakthrough occurs first in the completions placed in the high permeability stratigraphic layers i.e. the Waal & Schie (bottom) completions and the Schelde (top) completions, with water breakthrough occurring latest in the Maas (middle) completion. In well P5, water breakthrough occurs in the Maas (middle) completion first, due to the flow of water from the bottom Waal & Schie layer; after breakthrough occurs in the higher permeability Schelde (top) layer, the water production rate subsequently becomes higher than the water production rate in the Maas (middle) completion. However, in the three wells, higher watercut measurements were observed in the Maas (middle) completion than the Schelde (top) layer.

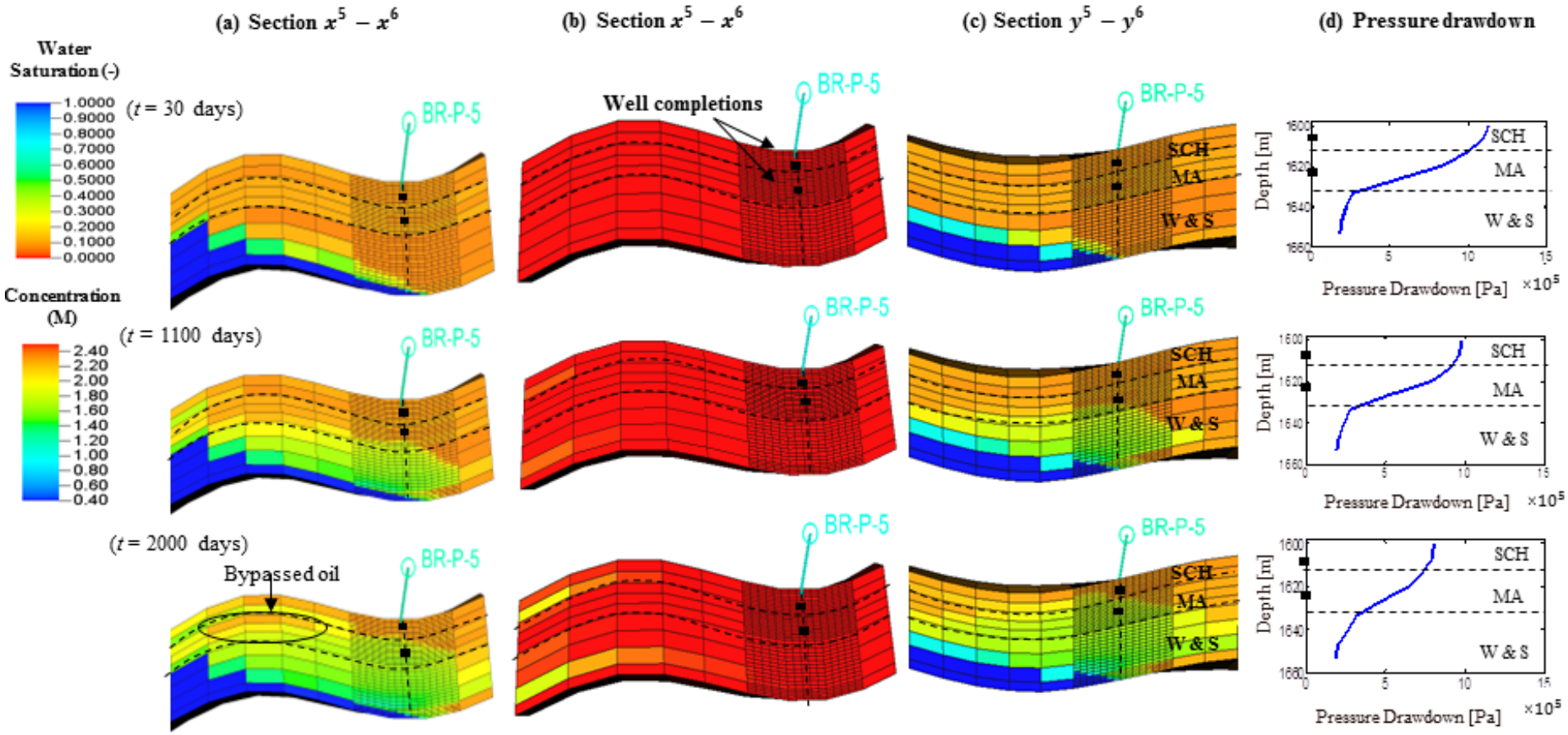


Figure 5.13: (a) saturation $x^5 - x^6$ cross-section, (b) concentration $x^5 - x^6$ cross-section, (c) saturation $y^5 - y^6$ cross-section (from Figure 5.6) and (d) the pressure drawdown at well P5 at 30, 1100 and 2000 days into production respectively. The horizontal dashed lines show the different stratigraphic layers. The high pressure drawdown in the Schelde (top) layer creates a vertical potential gradient which drives reservoir fluid from the underlying Waal and Schie (bottom) layer upwards at t = 1100 days, leading to the early water breakthrough in the Maas (middle) layer.

5.3.2 SP signals during production

We analyse first the SP signal generated in well P12 where water breakthrough occurs first, and then wells P5 and P12 (highlighted in Figure 5.7 (a)) to understand the SP response in different well completion configurations. Figure 5.14 shows the $(x^1 - x^2)$ concentration and saturation cross-sections at well P12 after 360 days, 2700 days and 4700 days of production respectively (i.e. at similar times to Figure 5.8), and also shows the corresponding SP (V_{SP}) that would be measured along the well with reference to a distant electrode in the overlying shale layer

$$V_{SP} = V_i - V_{ref} \quad (5.1)$$

where V_{ref} is the voltage measured in the electrode placed in the overlying shale layer and V_i is the voltage measured in each electrode. The electrokinetic (V_{EK}) and electrochemical (V_{EC}) components of the total SP are also shown. The electrokinetic (EK) potential dominates the SP signal measured along well P12 prior to water breakthrough and reflects the movement of the encroaching waterfront. Measurable SP are observed in the Waal & Schie (bottom) layer with the waterfront approximately 100 m away from the well (see Figure 5.14, t = 360 days). The assumed downhole electrode noise level (0.1 mV) is represented by the vertical red dashed line and is consistent with downhole SP measurements in deep boreholes (Chen *et al.*, 2006), also assumed in Chapter 4. The SP measured after 2700 days of production reflects the movement of the encroaching waterfront in the Schelde (top) layer, which flows ahead of the front in the Maas (middle) layer, with the waterfront 300 m away from the well. The electrochemical (EC) potential dominates the total SP measured after water breakthrough occurs in the Waal & Schie (bottom) layer; this is due to the vertical concentration gradient between the injected lower salinity seawater in the Waal & Schie (bottom) layer and high salinity formation brine in the Schelde (top) layer (see Figure 5.14, t = 4700 days).

However, the SP measurements taken in well P5 and P15 which are completed only in the Schelde (top) and Maas (middle) layers exhibit different behaviour to well P12, particularly with respect to the EK component. Figure 5.16 (a) and (b) show the $(x^5 - x^6)$ concentration and saturation cross-sections at well P5 after 30 days, 1100 days and 2200 days of production respectively, and the corresponding SP measurements taken along the

well. Measurable SP is observed in both the Schelde (top) and Maas completion after only 30 days of production. As the waterfront approaches the production well, the magnitude of the SP signal increases and reflects the movement of the encroaching waterfront; note that the negative EK potential measured relative to the distant reference electrode is due to the high drawdown at the top of the well, which allows for the upward flow of the reservoir fluid as discussed in section 5.3.1. After 1100 days of production, the most positive SP measurement is observed in the high permeability Waal & Schie (bottom) completion, followed by the Schelde (top) layer; with the most negative SP measurement observed in the Maas (middle) layer where the waterfront is farthest away from the well. However, after water breakthrough occurs in the Maas (middle) layer, the voltage measured in the Maas (middle) completion increases and becomes higher than the SP measured in the Schelde (top) layer (Figure 5.16 (c), t = 2000 days).

Figure 5.15 (a) and (b) show the $(x^3 - x^4)$ concentration and saturation variation cross-sections (from Figure 5.7) at well P15 after 330 days, 660 days and 1380 days of production respectively Similar to well P5, P15 is only completed in the Schelde and Maas completion. The waterfront reaches well P15 earliest in the Waal & Schie (bottom) layer, followed by breakthrough in the Schelde (top) completion. The EK potential dominates the measurable SP signals observed prior to water breakthrough after 330 days of production, with the waterfront approximately 200m away from the well in both the Schelde and Maas layers. The magnitude of the SP measurement increases as the waterfront gets closer to the well but does not reflect the encroaching waterfront profile within the Schelde (top) layer in this case. However, the mean SP measured is more positive in the completion where the waterfront is closest to the well and more negative where the front is farthest away. For example, the SP measurement observed in the Waal & Schie (bottom) completion where the encroaching waterfront is closest to the well is the most positive, and is more negative in the Maas (middle) layer where the waterfront is farthest away from the well. The concentration gradient also gives rise to EC potentials but remains zero until the leading edge of the concentration front reaches the well in the Schelde (top) completion; and reflects the concentration front profile after water breakthrough occurs in the Schelde layer.

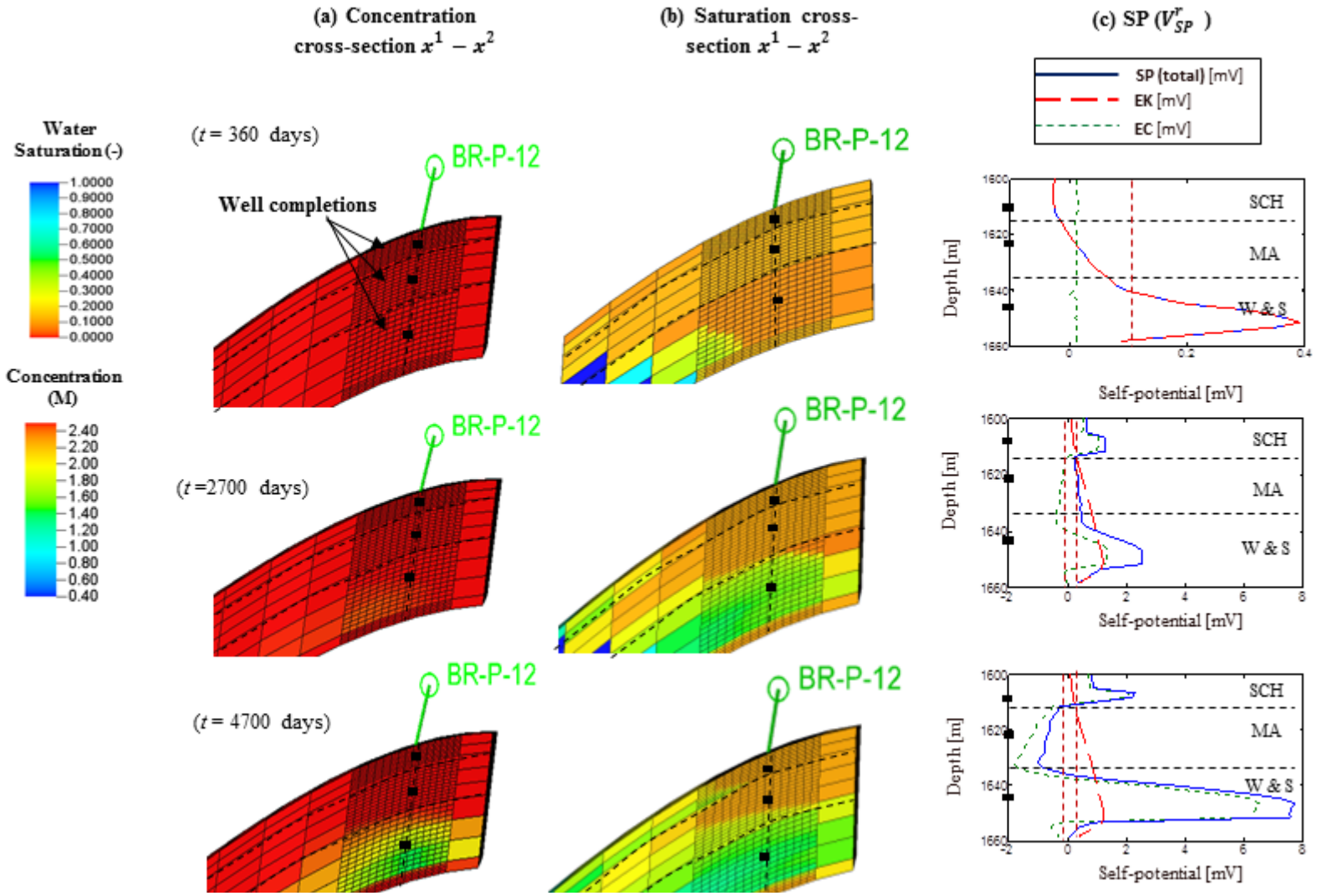


Figure 5.14: Cross-section through well P12 of the reservoir model showing the $x^1 - x^2$ (a) concentration, (b) saturation cross-sections and (c) the SP signals along the well at 360, 2700 and 4700 days into production respectively. The horizontal dashed lines show the different stratigraphic layers. Early SP signals can be measured prior to water breakthrough and reflects the movement of the encroaching waterfront. Note that the scale of the SP plot at *t* = 360 days is different from the SP plot at *t* = 2700 and 4700 days.

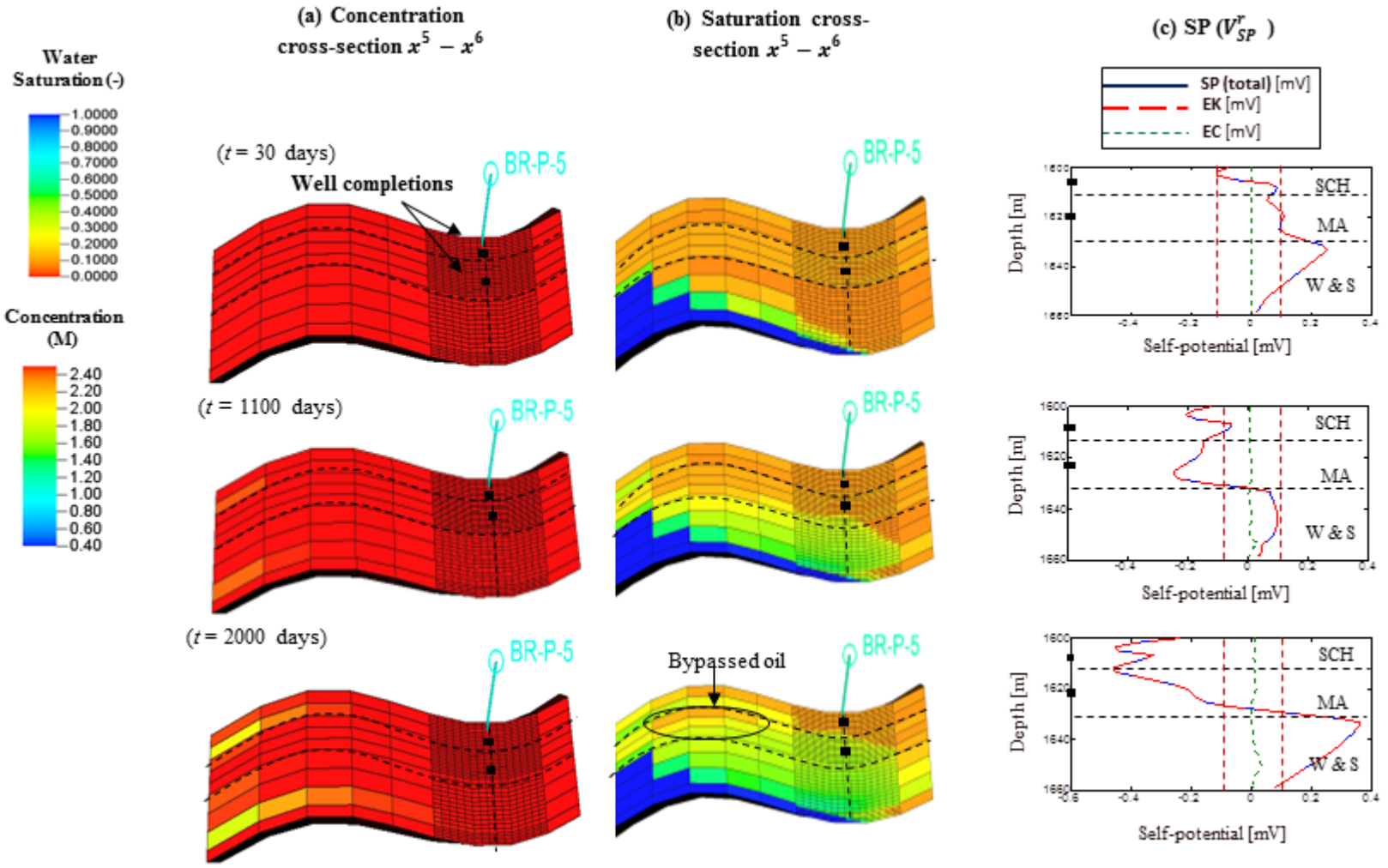


Figure 5.15: Cross-section through well P5 of the reservoir model showing the $x^5 - x^6$ (a) concentration and (b) saturation cross-sections; and (c) the SP signals along the well at 30, 1100 and 2000 days into production respectively. The horizontal dashed lines show the different stratigraphic layers. Early SP signals can be measured prior to water breakthrough and the EK signal reflects the movement of the encroaching waterfront.

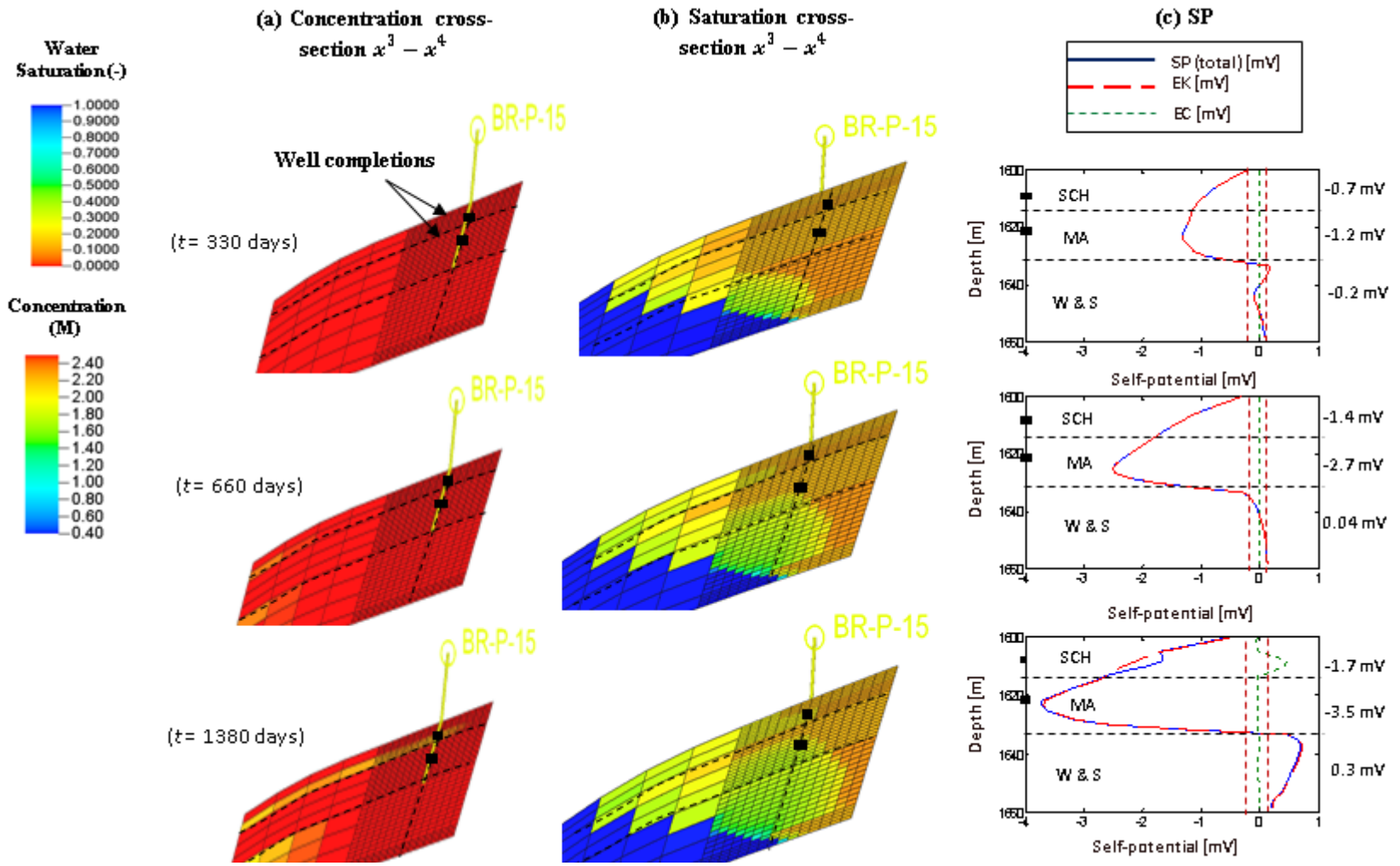


Figure 5.16: Cross-section through well P-15 of the reservoir model showing the $x^3 - x^4$ (a) concentration and (b) saturation cross-sections and (c) the SP signals measured along the well at 330, 660 and 1380 days into production respectively. The horizontal dashed lines show the different stratigraphic layers. Early SP (EK) signals can be measured prior to water breakthrough; unlike the previous cases the SP does not reflect the waterfront profile. The mean SP signal is more positive in the layer where the waterfront is closest to the well. The EC potential reflects the concentration front when it reaches the well.

5.3.3 Characteristics of the Change in Self-Potential

In this section, we show the plots of the change in mean SP measurement ($\Delta\bar{V}_{SP}$) taken in each of the completions of the production wells (P12, P15 and P5) with respect to the initial SP measurements taken at the first day of production (t = 0 days); and the corresponding magnitude of the change in mean SP $|\Delta\bar{V}_{SP}|$ with respect to the initial SP measurement, to determine how the SP measurement can be used in making inflow control decisions. Where

$$\Delta\bar{V}_{SP} = \bar{V}_{SP}(t) - \bar{V}_{SP}(t = 0) \qquad (5.2)$$

$$|\Delta\bar{V}_{SP}| = |\bar{V}_{SP}(t) - \bar{V}_{SP}(t = 0)| \qquad (5.3)$$

Figure 5.17 shows the plots of the change in mean SP ($\Delta\bar{V}_{SP}$) and the magnitude of the change in mean SP $|\Delta\bar{V}_{SP}|$, along with the corresponding well completion water production rate, watercut and salinity measurements in well P12. The magnitude of the change in mean SP measured in the Waal & Schie (bottom) completion exceeds the noise level approximately 200 days prior to water breakthrough (see figure 5.17 (b)); suggesting that the waterfront encroaching well P12 can be monitored more than half a year prior to water breakthrough. As shown in figure 5.14, the waterfront reaches the well P12 first in the Waal & Schie layer and the change in mean SP measurement plot (figure 5.17 (a)) shows that the most positive change in mean SP measurement is observed in the Waal & Schie completion prior to water breakthrough. The change in the mean EK potential contributes to the total change in mean SP measured prior to water breakthrough in the Waal & Schie (bottom) layer, while the change in the mean EC potential contributes to most of the change in mean SP observed in the Schelde layer prior to water breakthrough.

The plots of the change in mean SP ($\Delta\bar{V}_{SP}$) and the magnitude of the change in mean SP $|\Delta\bar{V}_{SP}|$ measured in well P15 are shown in figure 5.18. The magnitude of the change in the mean SP observed in the Schelde (top) completion exceeds the assumed noise level approximately 600 days prior to water breakthrough, suggesting that the waterfront movement can be tracked almost two years prior to water breakthrough (see figure 5.18 (b)). As shown in figure 5.16, water breakthrough occurs in the Schelde layer first and figures 5.18 (a) shows that the Schelde (top) completion has the most positive change in mean SP prior to water breakthrough. The change in mean EK potential also dominates the change in mean SP measured prior to breakthrough in well P15 and the magnitude of the change in mean EK potential reaches the maximum value when water breakthrough occurs

in both completions; after which the magnitude of the change in mean EK potential decreases in both completions. The change in the mean EC potential is zero until water breakthrough occurs in the Schelde (top) layer and leads to an increase in the total SP measurement. The SP measurements observed in well P5 are consistent with SP measurements in well P15. Figure 5.19 shows the change in mean SP measured in well P5, with measurable change in mean SP observed in the Maas (middle) and Schelde (top) layer at approximately 1000 and 600 days prior to water breakthrough respectively. The magnitude of the change in mean EK potential measured in both completions reach the maximum values when water breakthrough occurs, and starts decreasing after breakthrough (Figure 5.19 (b)). The change in mean SP measured in the Schelde (top) layer is initially more positive, but the change in the mean SP in the Maas (middle) layer becomes more positive after water breakthrough occurs in the Maas completion (See Figure 5.19 (a)).

In all three wells, we observe that water breakthrough occurs in the completion with the most positive change in mean SP measurement. Therefore, the SP measurements taken in each of the completion *j* of well *i* can be used to shut in/choke a particular completion in order to stop or reduce water production. The control action can be initiated once the difference between the most positive change in mean SP ($\Delta\bar{V}_{i,max}$) and the minimum change in mean SP measurement ($\Delta\bar{V}_{i,min}$) is greater than a threshold value greater than the noise level associated with electrode ($\Delta\bar{V}_t \geq 0.1$), using the simple algorithm shown below.

$\Delta\bar{V}_{i,j} = \Delta\bar{V}_{i,max}$ Shut in/choke completion *j*

$\Delta\bar{V}_{i,j} - \Delta\bar{V}_{i,min} > \Delta\bar{V}_t$ Shut in/choke completion *j*

$\Delta\bar{V}_{i,j} = \Delta\bar{V}_{i,min}$ Open completion *j*

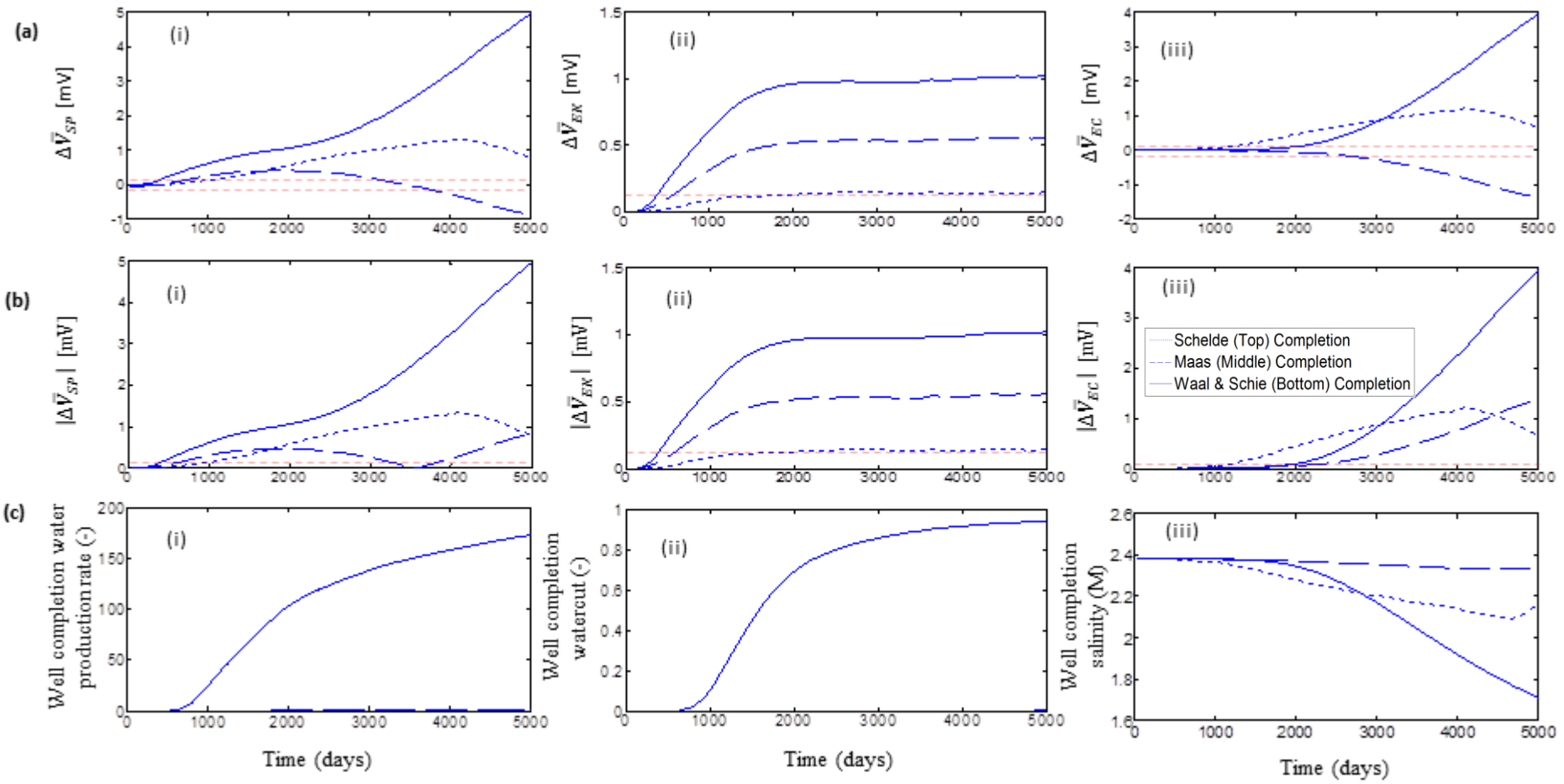


Figure 5.17: (a) Plots show (from left to right) (i) mean SP and the (ii) EK and (iii) EC potential measured in the middle of each completion along well P12. (b) Plots show (from right to left) magnitude change in (i) mean SP and the (ii) EK and (iii) EC potential measured in the middle of each completion (c) Plots show the corresponding (i) well completion water production rates, (ii) well completion watercut measurement and (iii) and salinity. Measurable change in SP signals observed at approximately 200 days prior to water breakthrough in the Waal and Schie (bottom) completion. The horizontal red dotted lines represent the assumed noise level of 0.1mV.

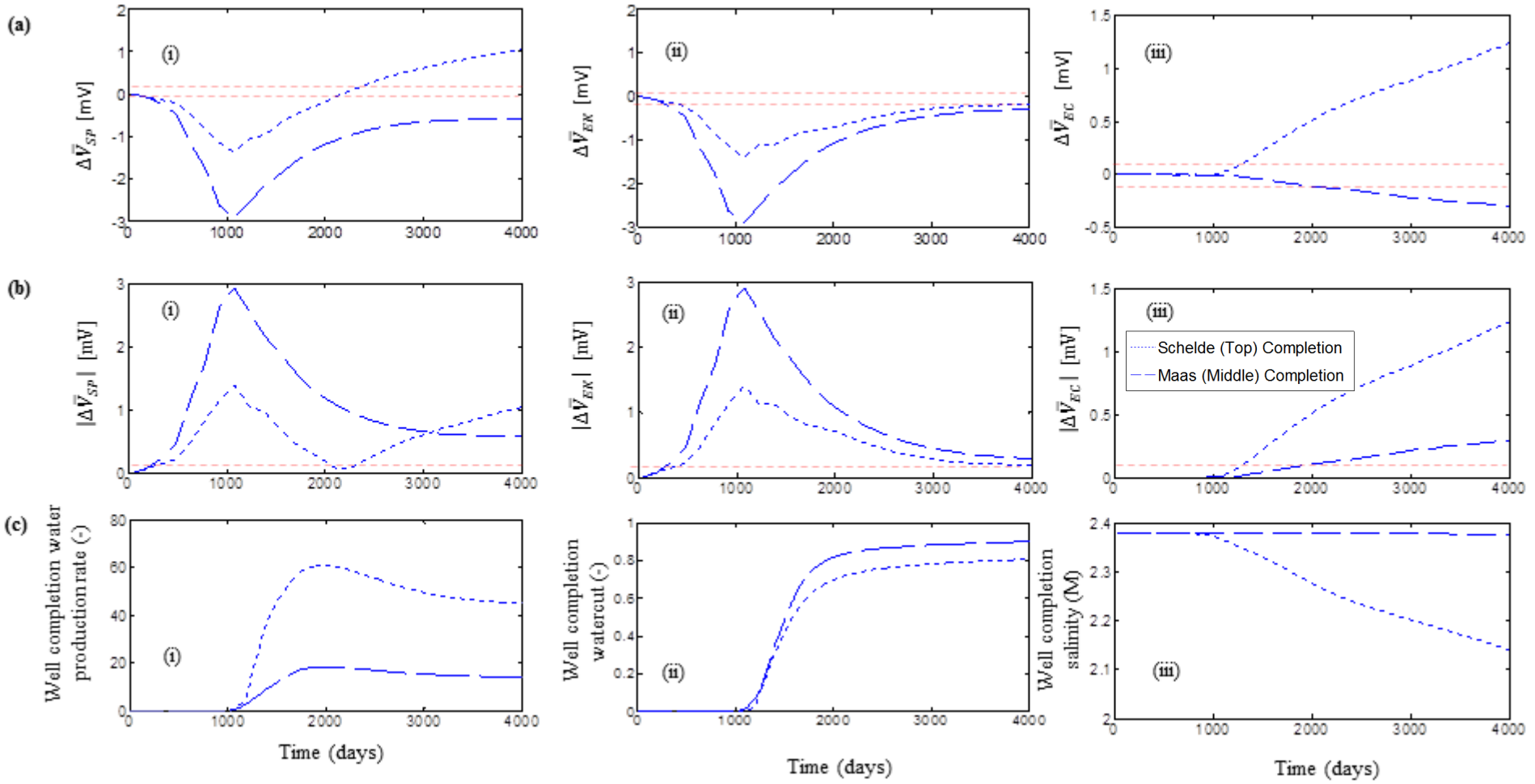


Figure 5.18: (a) Plots show (from left to righ) the (i) mean SP and the (ii) EK and (iii) EC potential measured in the middle of each completion along well P15. (b) Plots show (from right to left) magnitude change in (i) mean SP and the (ii) EK and (iii) EC potential measured in the middle of each completion (c) Plots show the corresponding well completion water production rates and (iii) and salinity. Measurable change in SP signals is observed at approximately 600 days prior to water breakthrough in the Maas completion and at approximately c. 350 days in the Schelde completion. The horizontal red dotted lines represent the assumed noise level of 0.1mV.

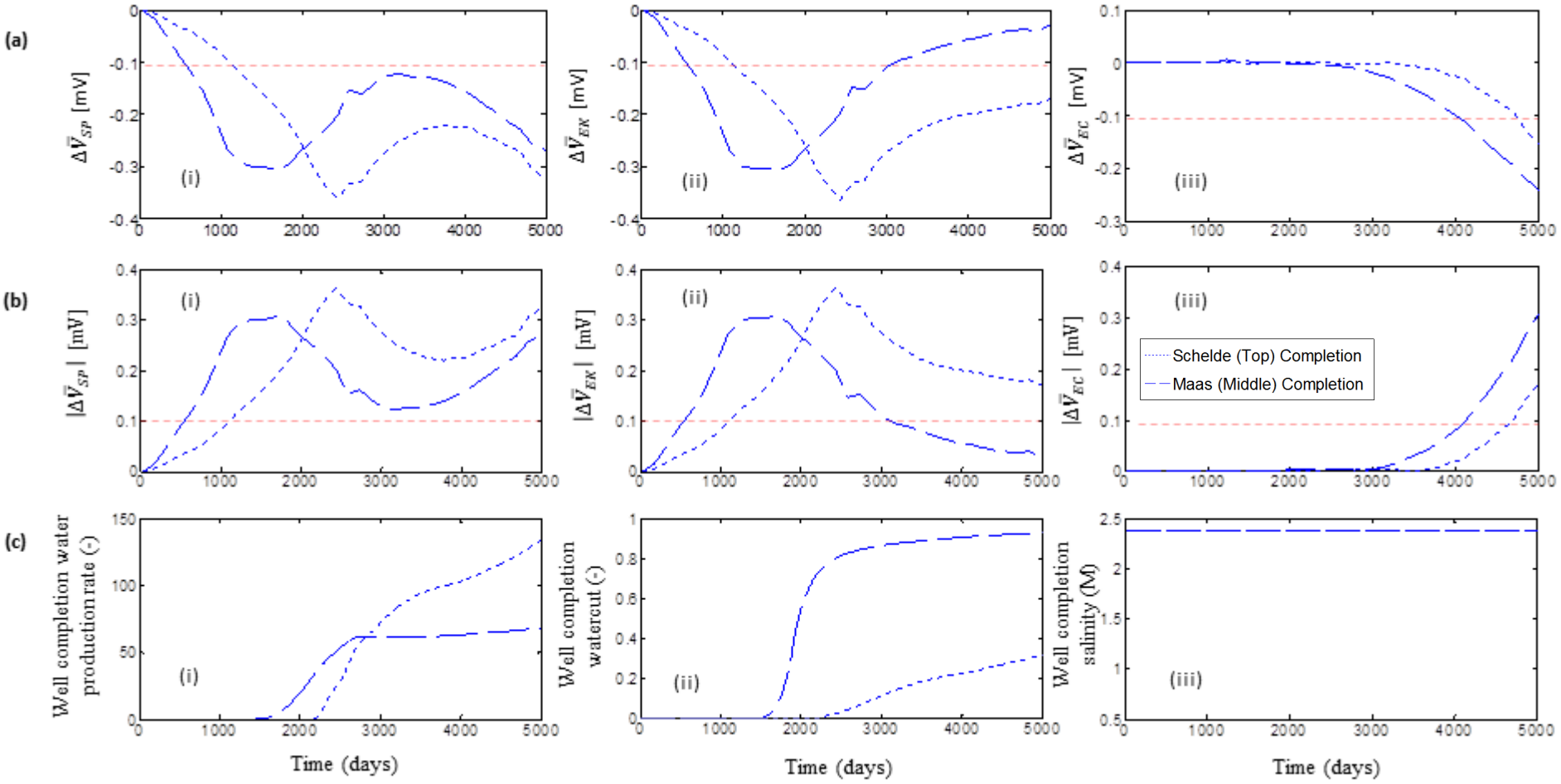


Figure 5.19: (a) Plots show (from left to right) the (i) mean SP and the (ii) EK and (iii) EC potential measured in the middle of each completion along well P5. (b) Plots show (from right to left) magnitude change in (i) mean SP and the (ii) EK and (iii) EC potential measured in the middle of each completion (c) Plots show the corresponding well completion water production rates and (iii) and salinity. Measurable change in SP signals is observed at approximately 1000 days prior to water breakthrough in the Maas completion. The horizontal red dotted lines represent the assumed noise level of 0.1mV.

5.3.4 Impact of varying formation brine salinity and production rate

In this section, we investigate the impact of varying production rates and formation brine salinity, both of which will affect the magnitude of the change in maximum SP that can be measurable in well P12, P15 and P5. We begin by investigating the case in which the formation brine has the same salinity as the injected water. In this case, only the EK potential contributes to the total SP signal measured at the production well, with the EC potential being zero because there is no concentration gradient. Figure 5.20 shows how the change in formation brine salinity affects the magnitude of the change in maximum SP measured in each of the completions of wells P12, P15 and P5 respectively. The vertical dashed line highlights the time at which water breakthrough occurs at each well. In all three wells the effect of varying the formation and injected brine salinity is clear; as the formation brine salinity increases the maximum change in SP at the production wells decreases, and the time at which water encroachment can be detected prior to breakthrough is delayed. This is because the signal measured at the well is dominated by the EK potential which is approximately inversely proportional to the salinity (Gulamali *et al.*, 2011). Figure 5.22 shows the impact of formation brine salinity on the time before breakthrough at which SP signals can be measured in well P12, P15 and P5 respectively. As the formation salinity increases, the signal measured at the well decreases and the time prior to breakthrough at which the signal exceeds the noise level is later.

Figure 5.21 shows how varying the production rates in well P12, P15 and P5 affects the change in mean SP measured in each of the well completions. In all three wells, the effect of varying the production rate is similar. As the production rate increases the maximum change in SP at the production wells also increases; measurable SP signals were not attainable in well P5 at low production rates. This is because, as production rate is increased, the pressure drawdown at the well, which is proportional to the EK potential, also increases (Saunders *et al.*, 2008). However, the time prior to breakthrough at which the signal exceeds the noise level is later in relation to the time of water breakthrough, because increase in production rate means that earlier water breakthrough occurs at the wells. Figure 5.23 shows the impact of production rate on the time before breakthrough at which SP signals can be measured in well P15 and P12. As the production rate increases, the signal measured at the well increases and the time prior to breakthrough at which the signal exceeds the noise level is later.

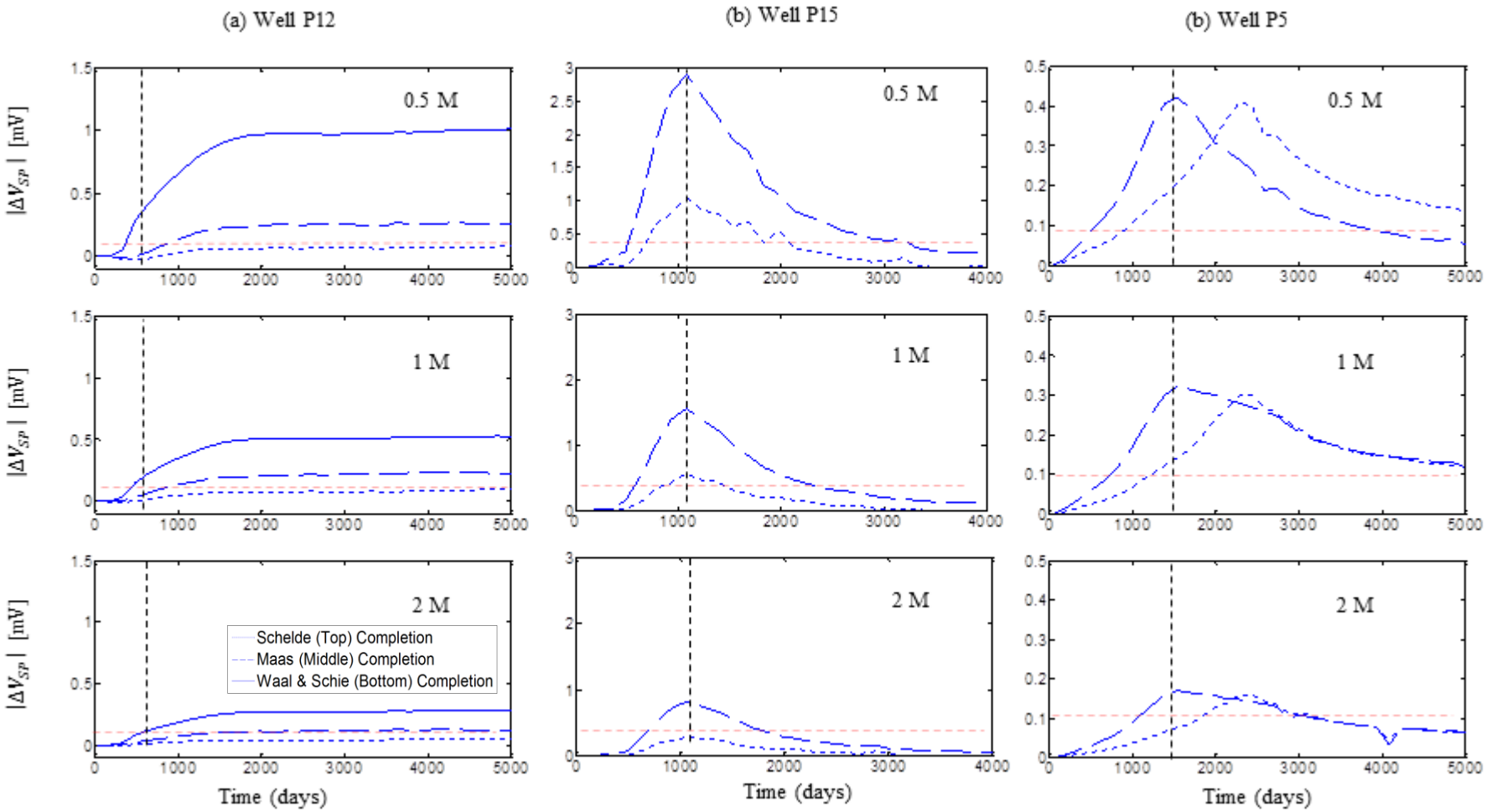


Figure 5.20: Magnitude of the maximum SP change measured in each completion along well (a) P12, (b) P15 and (b) P5 as a function of production time at different formation brine salinities. Vertical dashed lines indicate the times water breakthrough occurs. The Magnitude of the change in SP decreases as the formation brine salinity increases.

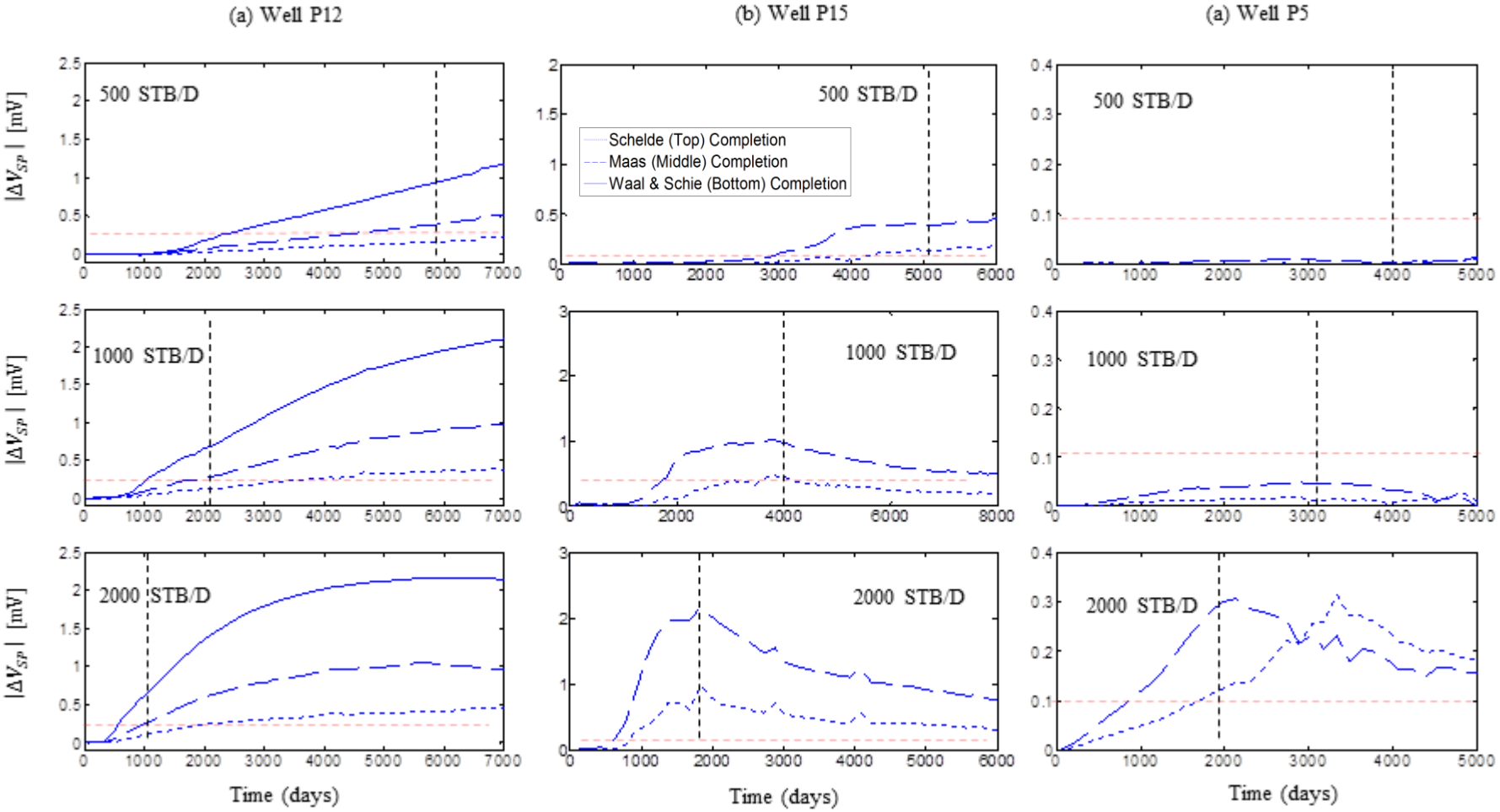


Figure 5.21: Magnitude of the maximum SP change measured in each completion along well (a) P12, (b) P15 and (c) P5 as a function of production time at different formation brine salinities. Vertical dashed lines indicate the times water breakthrough occurs. The magnitude of the change in SP measurements increases as the production rate increases.

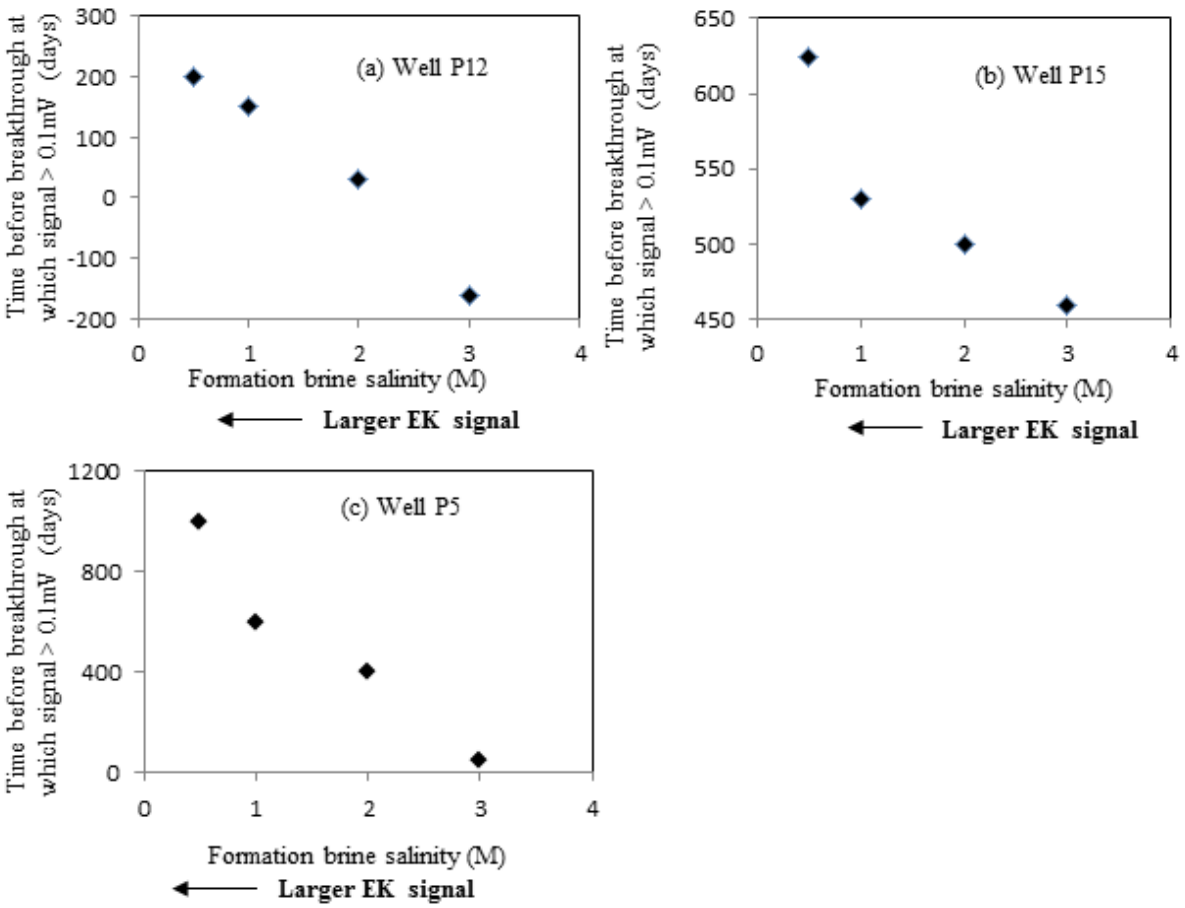


Figure 5.22: Impact of formation brine salinity variation on the time before breakthrough at which SP signals > 0.1 mV are measurable in well (a) P12, (b) P15 and (c) P5.

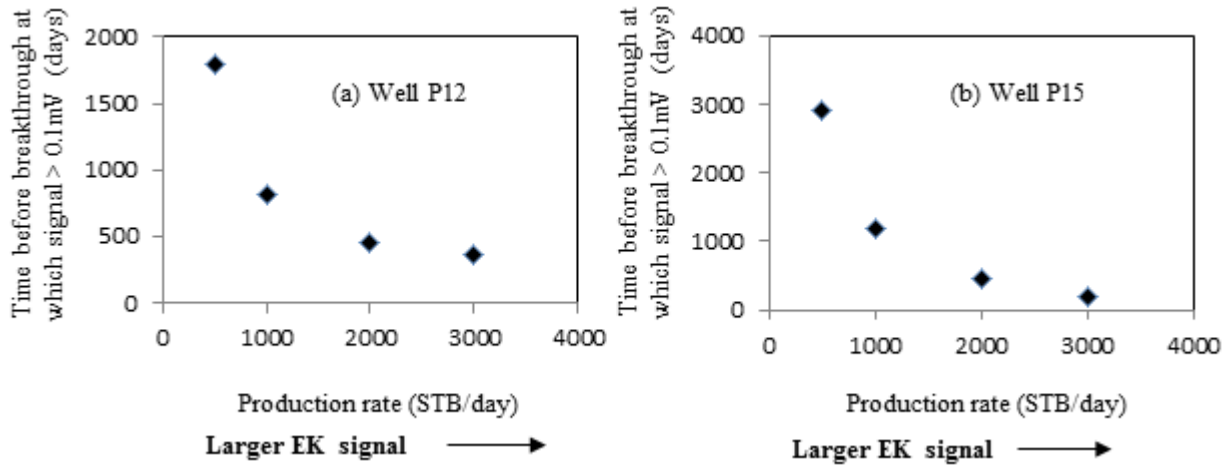


Figure 5.23: Impact of production rate variation on the time before breakthrough at which SP signals > 0.1 mV are measurable in well (a) P12 and (b) P15. Early SP measurements were not observed in well P5 prior to breakthrough at low production rate (<2000 STB/day).

5.4 Discussion

The numerical modelling results of the Brugge Field model suggest that the SP signals generated during waterflooding can be measured at magnitudes above the assumed noise level associated with downhole electrodes used to acquire the data. The model demonstrates that SP measurements taken along the production wells (with reference to a distance electrode) can be used to track the movement of the waterfronts in each of the stratigraphic layers prior to water breakthrough. Furthermore, the simulations also show that both the electrokinetic (EK) and electrochemical (EC) potentials contribute to the total SP signals measured prior to water breakthrough depending on the reservoir fluid dynamics. The EK potential typically dominates the measurable SP signals observed at the production wells prior to water breakthrough; however, the EC potential can also contribute to the SP signal measured prior to breakthrough but depends on the interaction between the injected low concentration seawater and the higher concentration formation brine. The sensitivity analysis suggests that the EK potential component of the SP signals generated at the production wells prior to water breakthrough will be highly dependent on the reservoir formation salinity and production rates, with higher magnitudes of change in SP measurements observed at higher production rates and lower formation salinity.

Furthermore, the use of multiple SP sensors placed along the well in each of the stratigraphic layers could be used to prevent spurious control actions from occurring. For example, if the Brugge model was a steeply dipping reservoir with similar vertical wells completed across the field, water encroachment in the top Schelde layer may be sensed by the SP sensors located in the Maas (middle) or Waal & Schie (bottom) layers, leading to the ICVs in the layer not affected by early water influx being shut off or choked. However, by using the SP measurements obtained from the SP sensors located in each of the stratigraphic layers, a mean SP measurements can be obtained in each layer when the measurements exceed the assumed noise level (0.1 mV). This will enable the ICV in a particular layer to be shut/choked, if the difference between the SP measurement in the layer and the most negative mean SP measurement exceeds a minimum threshold trigger value is exceeded. The layer with the most negative mean SP measurement remains fully opened. These results therefore suggest that SP measurements could be used to balance the waterflood front advance and manage voidage within the field.

5.5 Conclusions

The results presented in this chapter suggest SP measurements taken in multi-well field developments can be used to add value and aid reservoir management, by allowing monitoring of waterfront encroachment towards production wells prior to water breakthrough. SP measurements taken along an instrumented well can be used to identify completions/segments of the well where the waterfront is closest. Furthermore, both electrokinetic and electrochemical potentials contribute towards the SP signals measured at a production well, and signals can be resolved above equipment noise level at up to 200-1000 days prior to water breakthrough, with interpretable signals obtained earlier in wells with higher production rates and lower formation salinity. There is an intricate relation between the dominance of the electrokinetic (EK) and electrochemical (EC) components of SP, which depends on the well completion configuration and the dynamics between injected freshwater and formation brine. Generally the results are encouraging and the signals can be used for effective smart well control for production optimisation and management. This is investigated in the next chapter.

Chapter 6

Closed–Loop Feedback Control using Downhole Measurements of SP: Brugge Field Application

6.1 Introduction

In Chapter 4, we presented a new proactive closed-loop feedback inflow control strategy, using downhole measurements of self-potential (SP) and quantified the benefit of this approach in preventing or minimizing water production from a simple reservoir model containing a single horizontal well. Unlike model-based inflow control methods (highlighted in Chapter 2.2), we used model predictions only to determine an optimised direct feedback control relationship between downhole measurements of SP and inflow control settings on a base case model. The SP-based feedback control was then tested on an ensemble of reservoir model realisations to mimic cases when the reservoir does not behave as predicted. The results showed that closed-loop feedback control using downhole SP measurement could yield gains in NPV when compared to inflow control based on surface and downhole watercut measurements. Moreover, higher gains in SP over feedback control based on watercut measurements were observed when there were high penalties associated with the production of water, and in cases with high reservoir heterogeneity.

However, it is still not clear whether feedback inflow control based on downhole SP measurements is applicable in other reservoir types, production mechanisms and to multiple wells. We therefore extend this work to ascertain how feedback control based on SP measurements performs in a multi-well development using the synthetic SPE Brugge field model. This is a more realistic reservoir model than that used in Chapter 4. Peters *et al*. (2010) used the Brugge field model in a comparative case study to assess and benchmark a range of history matching and production optimisation control strategies as part of an SPE Advanced Technology Workshop. In Chapter 5, numerical modelling of SP in the Brugge model was carried out to determine the likely SP signal that would be measured at

production wells. The results suggest that SP measurements could be used to track the movement of an encroaching waterfront prior to water breakthrough.

In this chapter, we compare the performance of the closed-loop feedback control approach based on downhole SP measurements developed in Chapter 4 against surface and downhole feedback control based on surface and downhole watercut measurement (Dilib *et al*., 2013), and also the heuristic reactive control strategy presented in Peters *et al.* (2010). The closed-loop feedback control strategies are developed on a small subset of the published Brugge model realisations (Peters *et al*., 2010), which we assume to represent a range of stochastic realisations of a base case reservoir model. We then test the closed-loop control strategies on an ensemble of reservoir models to ascertain whether well NPV can be improved over the heuristic control strategy when the reservoir does not behave as predicted.

6.2 Methodology

6.2.1 Numerical Modelling of Production and Self-Potential

A summary of the synthetic 3D Brugge field model used in this study is presented in Chapter 5. The model is based on that developed by Peters *et al.*, (2010), derived from a high resolution Brent-type geological model comprising of 20 million grid cells, upscaled to a 450,000 grid cell model to yield the 'truth' case for reservoir simulation purposes. An ensemble of 104 upscaled (60,000 grid cells) reservoir model realisations varying in permeability, porosity and NTG were created for the comparative history matching study. Here, we use the 104 model realisations to test the performance of the different feedback control strategies against unexpected reservoir behaviours. The models were run for 30 years, with production enabled by 20 production wells and 10 injection wells. The LGRs placed around the production wells in chapter 5 are retained to allow for higher resolution SP simulation results. From years 0 - 10, the production and injection wells were operated and limited by the maximum liquid rate and watercut limit, and the minimum and maximum bottom-hole pressure (BHP) of the synthetic production and injection 'history data' of the truth model. From years 10 – 30, the production wells were operated at a maximum well liquid production of 3,000 STB/day, and the well watercut limit of 90% was also removed (see Table 5.3 in chapter 5). The BHP limit of 2611 psi at the production wells are maintained and, the injection wells rates are switched to a voidage replacement strategy for pressure support, with a maximum well injection of 4000 STB/day per well.

Although the life of the field is fixed, the life of each production well is determined by the chosen production strategy.

The SP signals generated during production from the Brugge field model were simulated using the updated SP solver developed in Chapter 5. We set the initial temperature and formation brine salinity at 80^0C and 2.5 M respectively, and inject brine of 0.5 M at a temperature of 30^0C. The chosen parameters represent waterflooding where seawater is injected into a reservoir containing more saline formation brine. However, Gulamali *et al*. (2011) observed that the thermoelectric potential contribution to the SP signals measured at a production well prior water breakthrough is negligible, as temperature fronts associated with the injected water lags significantly behind the saturation front. Thus we simulate the SP signals in response to only the pressure and concentration gradients in the brine; with the SP dominated by the electrokinetic and electrochemical potential.

6.2.2 Objective Function

We evaluate the performance of each inflow control strategy using the net present value (NPV) presented Peters *et al.* (2010), accounting for the revenues from oil production, the cost of producing and injecting water, and the time value of money. The objective function is given by

$$NPV = \sum_{t=1}^{n} \frac{\left(C_o \Delta V_o - C_w \Delta V_{w,prod} - C_{w,inj} \Delta V_{w,inj}\right)_t}{(1+k)^t} \quad (6.1)$$

where t is the time in years, k is the annual discount rate (10%), ΔV_o represents the incremental oil volume produced during time t, C_o is the oil price (80 US$/STB), C_w is the cost associated with producing water (5 US$/bbl water), $C_{w,inj}$ is the cost associated with injecting water (5 US$/bbl water), and $\Delta V_{w,prod}$ and $\Delta V_{w,inj}$ are the incremental water produced and injected, respectively. Unlike the objective function used in chapter 4, we do not take the cost associated with installation into consideration when calculating the NPV. The inflow-control performance is measured in terms of the percentage gain (G) in well NPV over the heuristic inflow control strategy

$$G = \frac{NPV_c - NPV_h}{NPV_h} \times 100 \quad (6.2)$$

where the subscripts *c* and *h* denote controlled and heuristic production, respectively.

6.2.3 Inflow Control Strategies

We assess two closed-loop feedback inflow control strategies based on (i) surface and downhole measurement of watercut presented in Dilib *et al.* (2013) and (ii) the self-potential (SP) feedback inflow control strategy developed in chapter 4, modified here to account for multiple wells and well completions. The closed-loop feedback control strategies are benchmarked against the heuristic reactive strategy presented in Peters *et al.* (2010). For the three inflow control strategies, all the ICVs are initially open at the beginning of production. Because production is limited by the synthetic production data between the 0 – 10 year period, Dilib *et al.* (2013) and Peters *et al*. (2010) suggested that the watercut based feedback control strategy and heuristic strategy were optimised when initiated after year 10 to the end of field life. Here, the SP control strategy is triggered after all the production wells in the field where in operation, which is at the end of the second year of production. This ensures that inflow control actions are taken prior to when water breakthrough occurs at the production wells. After the initial SP control actions are taken, each of the ICV setting can only be updated when the watercut limit is reached (see Figure 6.1). Because none of the production wells reaches the well watercut limits (0.9) during the first 10 years of production, the ICV settings could only be updated once. However, for the three control strategies after year 10 when the production constrains are lifted, the ICV settings were updated based on monitoring and control actions taken every 30 days until the end of the life of the field is reached. Dilib *et al.* (2013) used a subset of 4 of the 104 reservoir model realisations, randomly selected to represent stochastic realisations of base case reservoir models, to optimise the adjustable parameters of the watercut based feedback control strategy that maximises the average NPV. We used the same 4 reservoir model realisations to determine the adjustable parameters used in the SP based feedback control strategy.

6.2.3.1 Watercut based feedback inflow control strategy

The watercut based feedback control strategy assumes a two-level feedback controller which uses surface on/off valves and multiphase flow meters, and downhole inflow control valves (ICVs) and multiphase flow meters. The downhole ICVs and multiphase flow meters are placed in each of the production well completions to control inflow of reservoir fluids into the borehole and provide continuous measurements of watercut at each

completion. Control actions are initiated when the surface watercut W_i of well *i* exceeds a threshold trigger value W_t. The ICV in the completion with the minimum watercut in well *i* ($W_{i,min}$) remains fully open and the ICVs in other completions *j* in well *i* are proportionally choked by

$$\Pi_{i,j} = MAX\left[A\left(\frac{W_{i,min}}{W_{l,j}}\right)^{c}, B\right] \quad (6.3)$$

where *A*, *B* and *c* are constants with $A \leq \Pi_i \leq B$, $c \geq 0$, Π_i is the value of the inflow control multiplier of the ICV *j* in well *i*, $W_{i,j}$ is the watercut for a given completion *j* in well *i*. A minimum threshold value δW which is the difference in watercut measurement between a completion *j* and $W_{i,min}$, is used to prevent fluctuations in the control actions over well completions with similar watercut measurements. The surface on/off valves of well *i* are shut once the watercut W_i exceeds the watercut limit W_l. Dilib *et al.* (2013) used a gradient-based optimization method to determine the adjustable parameters *c*, W_t, W_l *and* δW that maximized the average NPV of the base case models. They set *A* = 1 and *B* = 0 to allow the ICVs to operate up to the maximum open and closed position; they found the NPV was maximised when W_l=0.73, W_t = 0.65, δW = 0.05, and *c* = 21 which is a large value and consequently means the ICVs are operated between the fully opened and closed positions.

6.2.3.2 Self-potential based feedback control strategy

The self-potential (SP) feedback control strategy developed in chapter 4 is modified here to account for multiple wells and completions. The SP based feedback control strategy assumes that ICVs are placed in each of the well completions and downhole electrodes provide continuous measurements of SP with reference to a distance electrode. On/off well head valves are also placed in each well and are shut once the measured surface watercut of a well W_i exceeds the watercut limit W_l. As highlighted in chapter 5.3.2, the mean SP measurements taken in each well completion, with reference to a distance electrode placed in the overlying shale layer, can be used to track the movement of the encroaching waterfront; the waterfront closest to the completion records the most positive SP measurement. The work-flow of the multi-well feedback inflow control strategy using downhole SP measurements and surface watercut measurement is shown in Figure 6.1. Inflow control actions are initiated in a particular well *i,* when the difference between the

mean SP measurement in completion j ($V_{i,j}$) and the most negative mean SP measurement of the well completions ($V_{i,min}$) is greater than a threshold value $\Delta V_t > 0.1$ mV, which is the assumed noise level associated with the downhole electrodes. The completion j of well i with the most negative SP measurement $V_{i,min}$ remains fully open, while the other completions are proportionally choked using

$$\Pi_{i,j} = MAX\left[A\left(1 - \frac{V_{i,j} - V_{i,min}}{V_{i,max} - V_{i,min}}\right)^{c}, B\right] \quad (6.4)$$

where $\Pi_{i,j}$ is the value of the inflow multiplier of completion j of well i, $V_{i,max}$ is the completions with the most positive mean SP measurement, and A, B, and c are constants with $0 \leq A \leq 1$, $A \leq \Pi_i \leq B$ and $c \geq 0$. The surface on/off valves of a particular well are shut once the watercut W_i exceeds the watercut limit W_l. Just like Dilib *et al.* (2013), we set $A = 1$ and $B = 0$ to allow the ICVs operate up to the maximum open and closed position; and we set c to be a large value so that the ICVs operated between the fully opened and closed positions. However, we used a simple forward simulation method to determine the value of ΔV_t and W_l that maximises the average NPV of the 4 base case model realisations. Each of the base case models were run over a ΔV_t range value of 0.1 – 1 and watercut limit W_l range values of 0.1 – 1, and identify the value that maximises the NPV.

6.2.3.3 Heuristic 'reactive' strategy

Peters *et al.* (2010) presented a heuristic reactive strategy to obtain a benchmark on the truth reservoir model, which was used to compare a range of model-based control strategies developed on an ensemble of history matched reservoir models but assessed on the 'truth' model. We implemented the heuristic strategy to benchmark the performance of the closed-loop feedback control strategies. The heuristic reactive strategy makes use of surface and downhole on/off control valves in each of the production wells. The control philosophy is based on a set of production and injection strategies to obtain a uniform sweep from the bottom to the top of the truth reservoir model. This was achieved by producing from the Schelde (top) and Maas (middle) formations only (open completion 1 and 2, and shut completion 3) and injecting in only the Maas (middle), Waal, and Schie (bottom) formations (completion 1 shut, injection into completions 2 and 3). The completions in the Schelde (top) formation are shut once the well watercut exceeds 0.92 and the well is shut once the well watercut limit reaches 0.94.

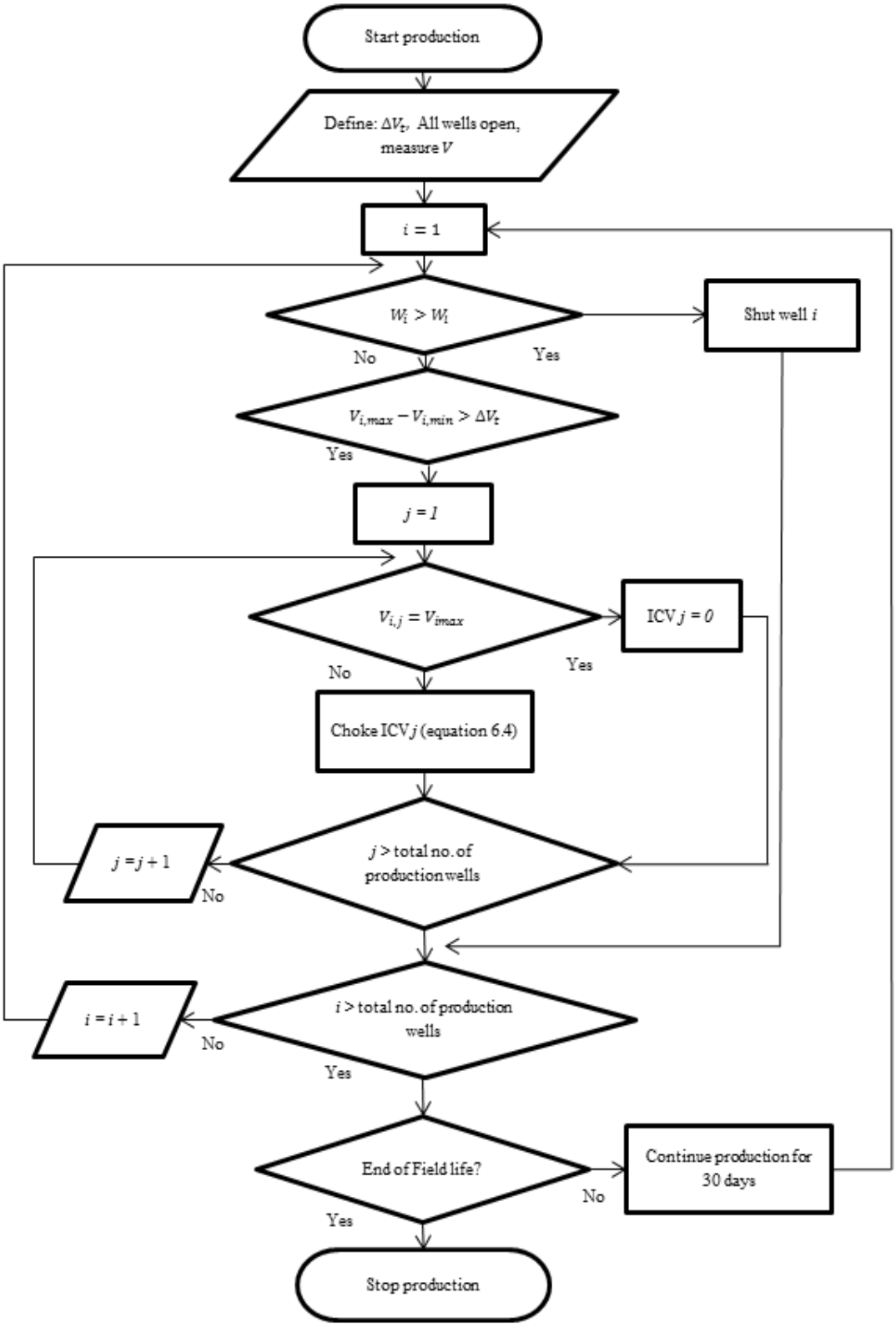


Figure 6.1: Inflow control strategy of Dilib *et al.*, (2013), modified here to use downhole measurement of SP for optimisation of a multi-well field. The controller requires the adjustable parameters in equation 6.1. Here they are obtained from the small subset of model realisations representing the base case. The wells and ICVs are initially open, but control actions are taken once completion *j* of well *i* exceed the SP trigger change (ΔV_t). If the well water exceeds the maximum limit, the well is shut in at surface. Control actions are taken every 30 days until end of field life at year 30.

6.2.4 Base case model and uncertain reservoir behaviour

The range of reservoir behaviours captured by the ensemble of 104 models provided with the Brugge case study is shown in Figure 6.2. The 4 realizations randomly selected to represent the base case models are shown in red and the remaining 100 realizations in blue represent uncertain reservoir behaviour. Unlike Chapter 4 where a single base case model was selected to determine the constants used in the inflow control algorithm, we used the subset of 4 models randomly selected by Dilib and Jackson (2013) for a more robust parameter set. Peters *et al.* (2010) suggests that the spread observed in Figure 5.3 is smaller than will be observed in a typical Brent field case, as the structure of the field, the initial water/oil contact, and the oil PVT data are known perfectly in this case.

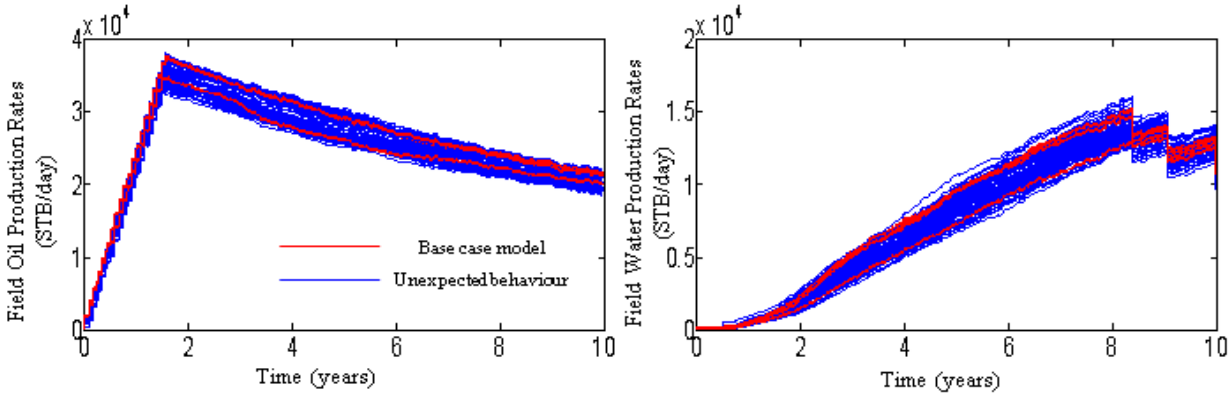


Figure 6.2: Field oil and water production rates of the ensemble of reservoir models used to test the performance of the feedback inflow control strategies when the reservoir behaviour is unexpected. The red line represents the base case models used to optimise the inflow control algorithm parameters.

6.3 Results

6.3.1 Tuning of the inflow control algorithm using the base case models

Table 6.1 shows the values of the tuning parameters used in the SP feedback inflow control workflow on a subset of four base case reservoir model realisations, which were randomly selected by Dilib *et al.* (2013) to represent stochastic realisation of a base case reservoir model. It is important to note that because production was constrained between years 0 – 10 by the synthetic historical data, the NPV was only optimised for years 11 – 30. The values of A and B are set to 0 and 1 respectively, to allow the ICVs to be operated at maximum open and close positions. The minimum change in SP, ΔV_t at which control actions can be triggered, is set to 0.1 mV, which is the noise level estimated from the downhole SP data as discussed in Chapter 2. However, the optimal trigger value is found

to be 0.5 mV. The maximum NPV observed in each of the base case realisations was observed at $W_l = 0.7$ as shown in Figure 6.3.

SP feedback inflow control			
Parameters	ΔV_t [mV]	c	W_l
Constraints	$\Delta V_t \geq 0.1$	$c \geq 0$	$0 \leq W_l \leq 1$
Value	0.5	10	0.7

Table 6.1: Summary of the optimised inflow control parameters used in the SP feedback control strategy algorithm

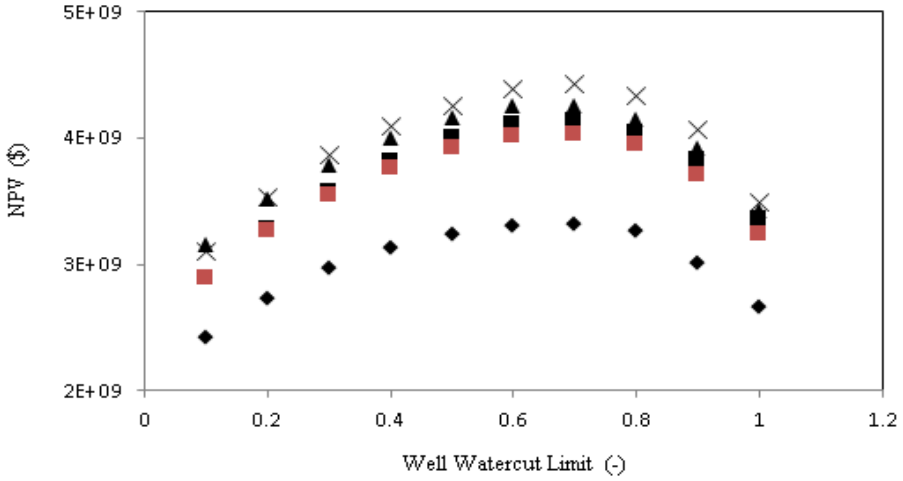


Figure 6.3: The NPV obtained for at different well watercut limit on each of the base case model realisations over 10 – 30 years of production from the Brugge field. Each of the markers represents a different base – case model realisation and the red markers show the average NPV at the different watercut limits. The maximum NPV is obtained at a watercut limit of 0.7.

6.3.2 Impact of inflow control on the NPV of the base case model realisation

Figure 6.4 shows the NPV obtained for years 0 - 30 for each of the different inflow control strategies on the 4 base case model realisations. The closed-loop feedback control strategy based on downhole measurements of SP is compared with the feedback control strategy using surface and downhole watercut measurement presented in Dilib *et al.* (2013). The performance of both feedback control strategies are benchmarked using the heuristic reactive strategy presented in the Brugge case study by Peters *et al.*, (2010). The SP based feedback control strategy yields a mean NPV of US$ 5.95×10^9 and the watercut feedback control strategy yields a lower mean NPV of US$ 5.9×10^9. However, both feedback inflow control strategies outperformed the heuristic reactive control strategy, which yields a mean NPV of US$ 5.86×10^9.

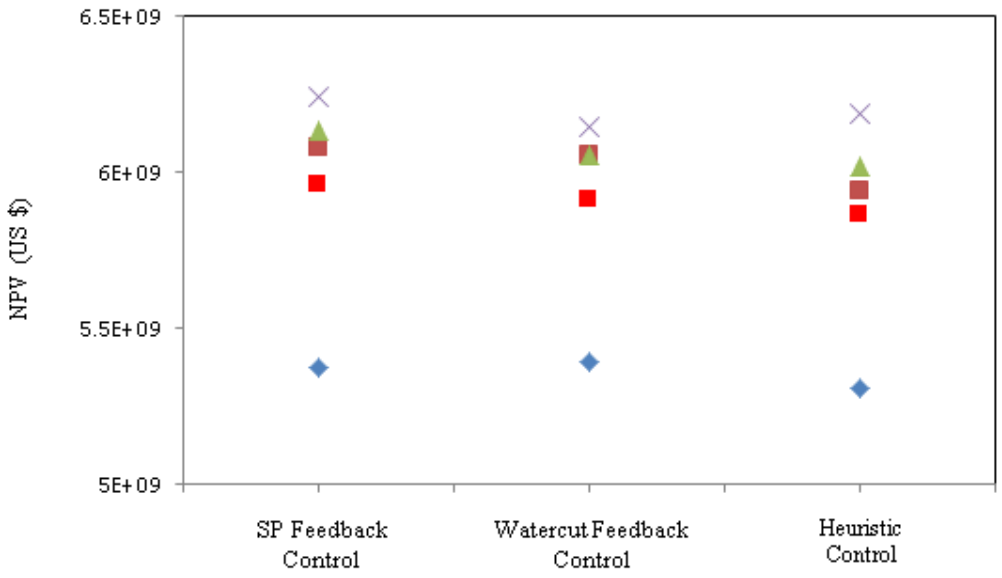


Figure 6.4: The performance of each control strategy on the base case model realisations over 0 – 30 years of production from the Brugge field. Each of the markers represents a different base – case model realisation. The red marker represents the mean NPV for each of the control strategies.

6.3.3 Impact of inflow control on the base case reservoir realisations

We compare the reservoir performance between each of the inflow control strategies on the base case model realisations in Figure 6.5 and 6.6, using the realisations that yield the highest and lowest NPVs in Figure 6.4. In Figures 6.5 and 6.6, the field oil and water production rates are shown in plot (a) and (b), and the water injection rates and total volumes of reservoir fluids produced and injected are shown in (c) and (d) respectively. In the example of the base case model realisation with the highest NPV (Figure 6.5), the heuristic reactive control strategy yields the lowest cumulative oil production of approximately 2.05×10^8 STB, but produces and injects significantly less water, with cumulative water production and injection of 8.5×10^7 and 3.05×10^8 STB respectively. The SP feedback control strategy yields similar cumulative oil production as the watercut feedback control strategy of approximately 2.1×10^8 STB, but produces and injects slightly less water than the watercut feedback control strategy. However, in the example of the base case model with the lowest NPV (Figure 6.6), the SP control strategy yields an intermediate cumulative oil production of approximately 1.7×10^8 STB, less than the watercut feedback control strategy of 1.8×10^8 STB but more than the heuristic reactive control strategy of 1.6×10^8 STB. The SP feedback strategy also produces and injects significantly less water than the watercut feedback control, similar to that of the heuristic reactive control strategy.

Figure 6.7 and 6.8 highlights the control actions observed in well P12, for the watercut and SP based feedback control strategies in the base case model realisation that yields the highest NPV. As shown in Figure 5.14 (Chapter 5), well P12 is completed in the Schelde (top), Maas (middle) and the Waal & Schie (bottom) layers. Figure 6.7 (a) shows the inflow control multiplier of the ICVs, along with the corresponding well completion watercut measurement, and Figure 6.7 (b) shows the water and oil production total. In the watercut feedback control strategy, the ICV in the Waal & Schie (bottom) completion is shut first, followed by the ICV in the Maas (middle) completion. The Schelde (top) completion ICV is shut last when the well watercut limit is reached. The SP based feedback control strategy yields different inflow control behaviour (Figure 6.7 (c)), with the ICVs in the Schelde (top) and Waal & Schie (bottom) completions initial choked, even though water breakthrough had not occurred in the Schelde layer. Consequently, this resulted in a reduction in the well water production total and a marginal increase in the well oil production total when compared to the watercut feedback strategy (see Figure 6.7 (d)). Similar inflow control actions were observed in the base case model with the lowest NPV, with the SP based feedback control also resulting in a reduction in the well water production total (see Figure 6.8).

Overall the heuristic reactive approach yields the lowest cumulative oil over the 30 year production period but produces and injects the lowest amount of water. In contrast, the SP feedback control strategy is able to produce significantly larger volumes of oil than the heuristic strategy, whilst reducing the cumulative water production and injection volumes significantly below the watercut feedback control strategy. However, the results presented here are specific to the base case models and, as consistently mentioned over the course of this research, reservoir models are rarely predictive at the temporal and spatial resolution required to make inflow control decisions. The inflow control strategies are therefore tested on the remaining 100 reservoir models shown in Figure 6.2 to assess how the individual control strategies perform when the reservoir fails to perform as predicted. Consistent with chapter 4, we do not adjust the parameters in the feedback control algorithm determined using the base-case model realisations.

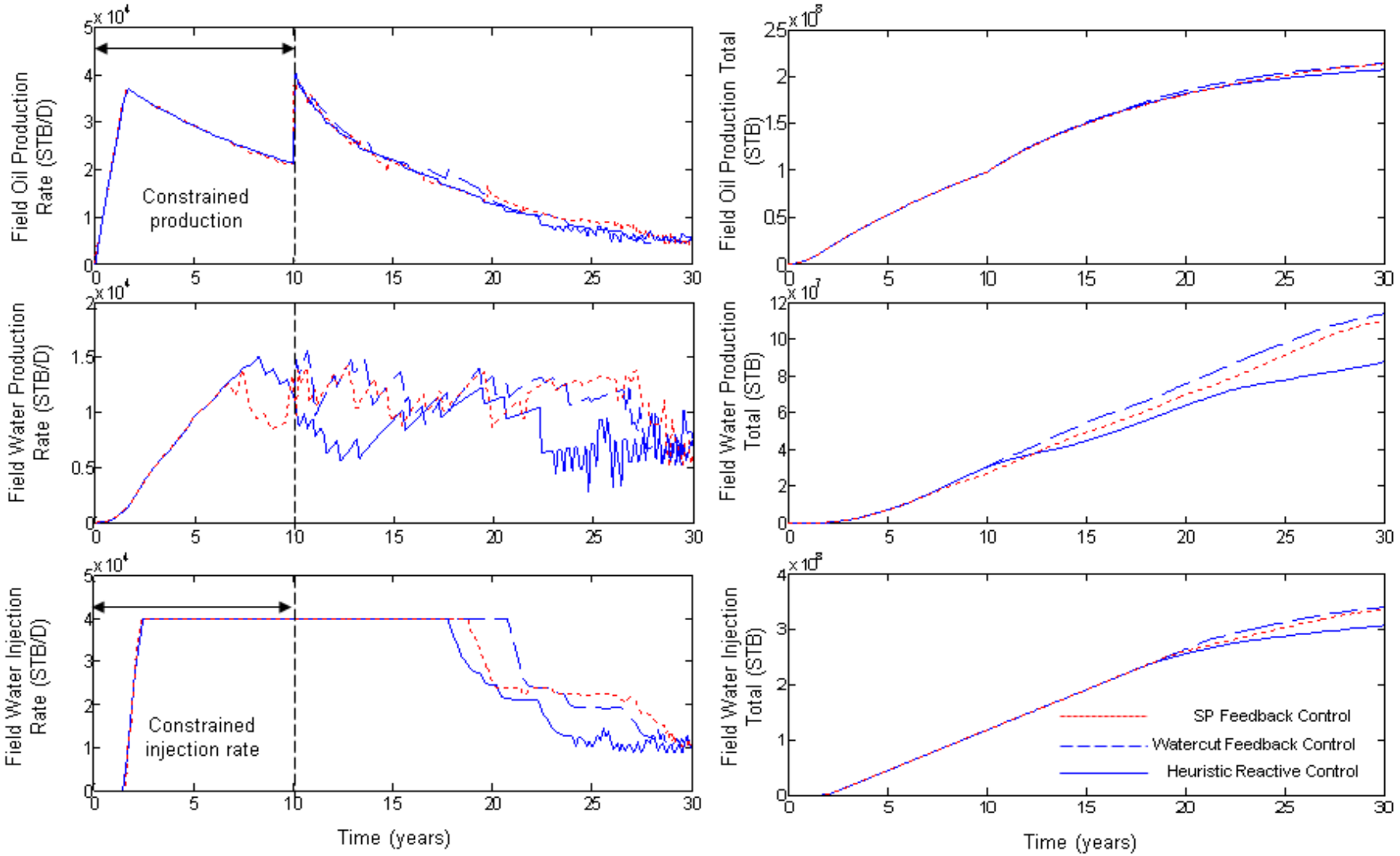


Figure 6.5: Field performances of the different inflow control strategies on the base case model realisation, with the highest mean NPV. The watercut feedback control strategy yields the highest field oil production but also produces and injects the most amount of water. The heuristic reactive control strategy produces the least amount of oil but produces and injects the least amount of water. The SP feedback control strategy produces similar quantity of oil as the watercut control strategy, but produces and injects marginally less water.

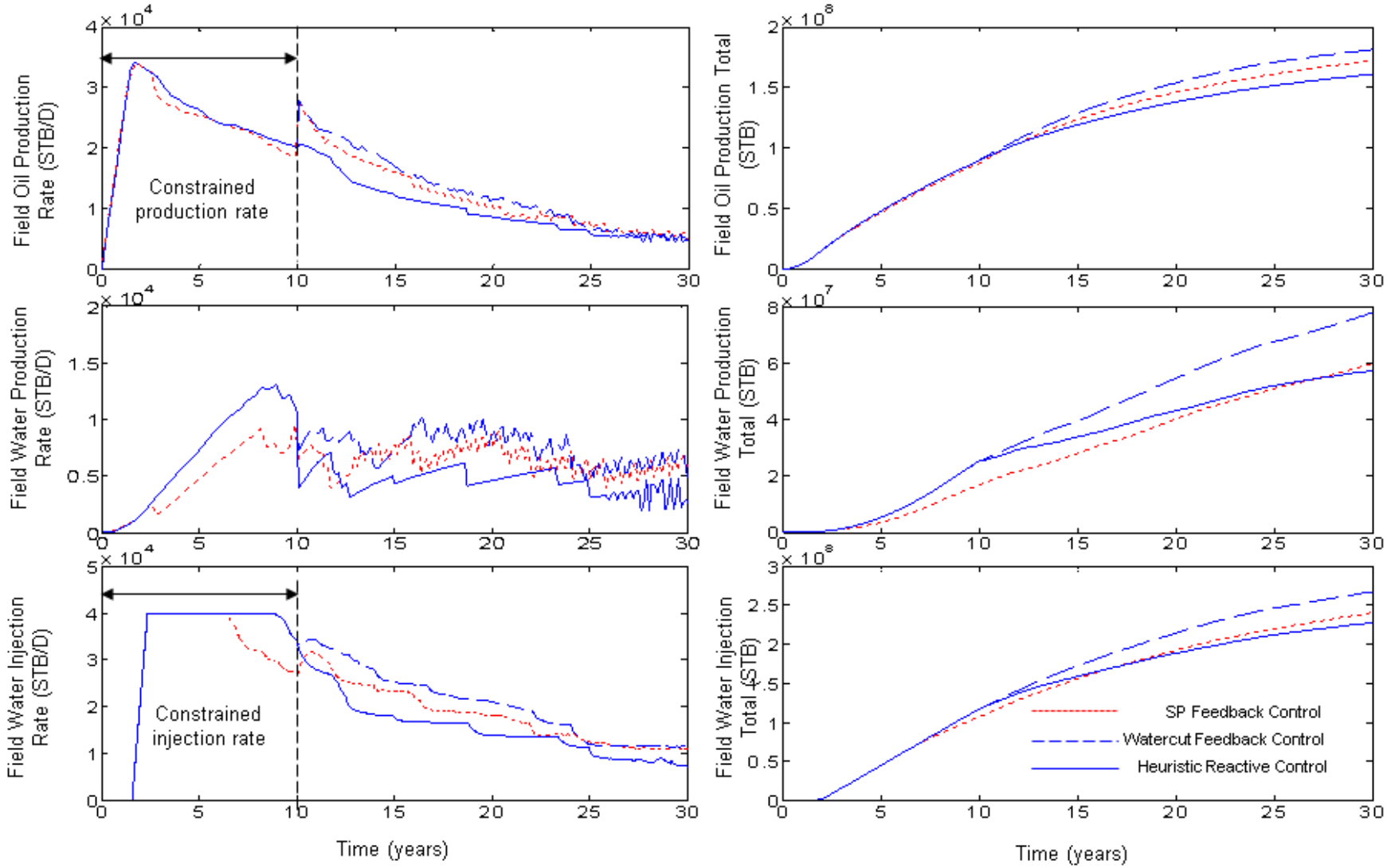


Figure 6.6: Field performances of the different inflow control strategies on the base case model realisation, with the lowest mean NPV. The watercut feedback control strategy yields the highest field oil production but also produces and injects the most amount of water. The heuristic reactive control strategy produces the least amount of oil but produces and injects the least amount of water. The SP feedback control strategy in this case produces similar quantity of oil as the watercut control strategy, but produces and injects significantly less water (similar to the heuristic reactive control).

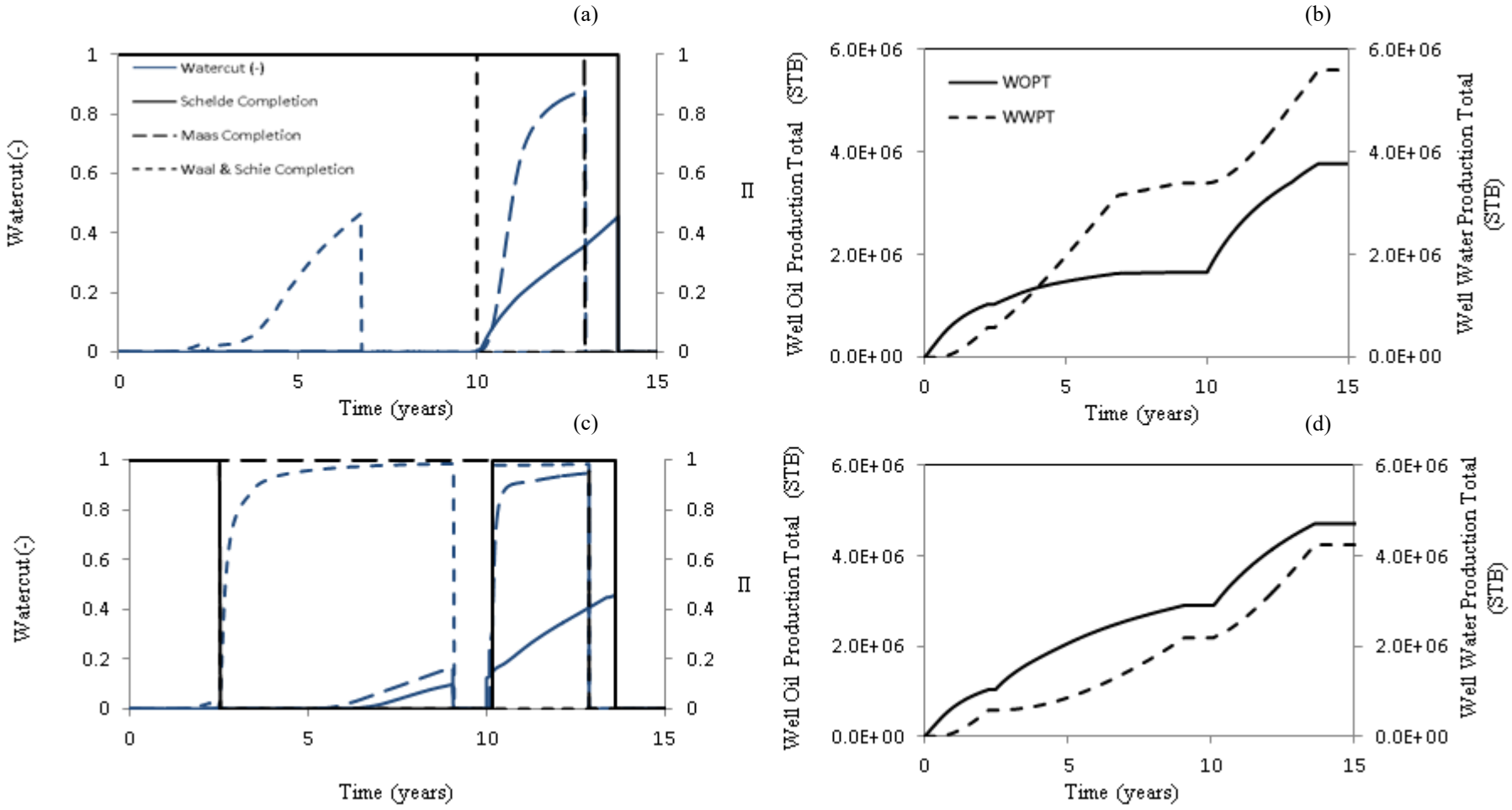


Figure 6.7: Inflow control behaviour (a) and (c) Values of watercut and inflow multiplier against time; (b) and (d) well water and oil production total, for the feedback control strategies based on surface and downhole watercut measurements (plots (a) and (b)) and downhole SP measurements(plots (b) and (d)). Results from the base case model with the highest NPV in Figure 6.4.

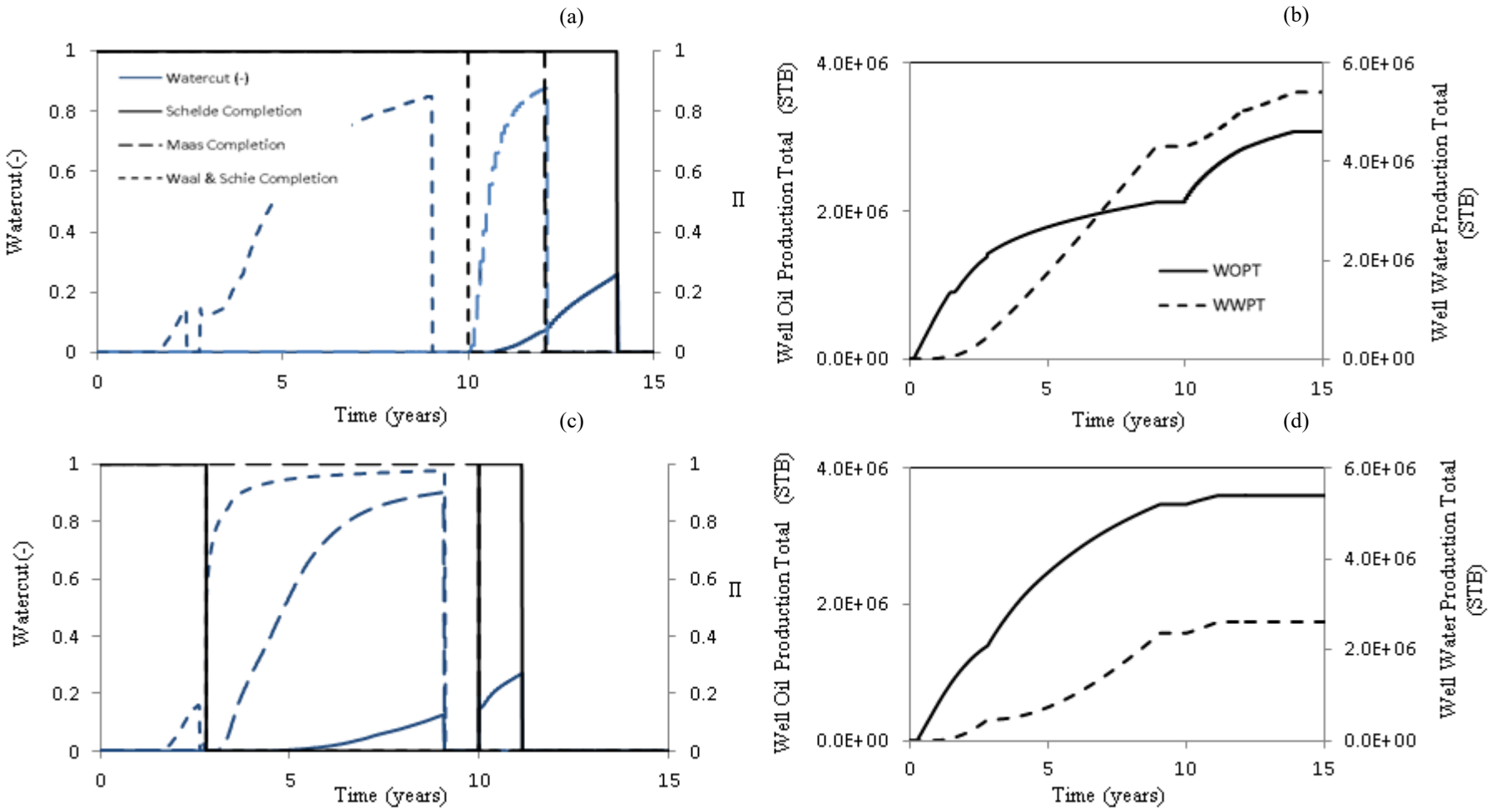


Figure 6.8: Inflow control behaviour (a) and (c) Values of watercut and inflow multiplier against time; (b) and (d) well water and oil production total, for the feedback control strategies based on surface and downhole watercut measurements (plots (a) and (b)) and downhole SP measurements(plots (b) and (d)). Results from the base case model with the lowest NPV in Figure 6.4.

6.3.4 Impact of unexpected reservoir behaviour

We now investigate the impact of unexpected reservoir behaviour on the NPV gains for each control strategy. Figure 6.9 shows the NPV obtained on the remaining 100 reservoir model realisations using the SP and watercut feedback control strategies compared to the heuristic reactive strategy; each data point indicates the NPV gain for a particular uncertain reservoir behaviour. The SP based feedback control strategy yields the highest mean NPV of US$ 5.78 ± 0.36×10^9 with a gain in mean NPV over the heuristic method of 4.5 %. The surface and downhole watercut based feedback control strategy yields a mean NPV and NPV gains of US$ 5.54 ± 0.43×10^9 and 3.8% respectively. The higher NPV variations obtained when using the SP based feedback control strategy suggests that the control strategy might underperform the surface and dowhnhole watercut feedback strategies in some cases, when the reservoir model deviates from the base case models. However, higher NPVs are observed when the reservoir models are highly heterogeneous.

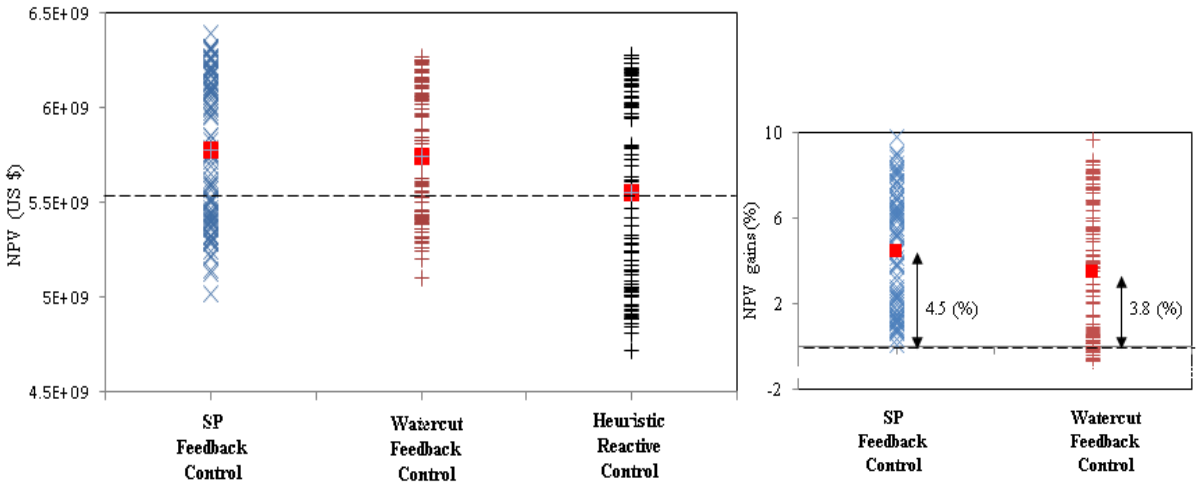


Figure 6.9: Range of NPV obtained from 0– 30 years of production for each of the inflow control strategies. Each point represents the NPV for a particular unexpected reservoir behaviour. The red data point represents the mean NPV for each of the control strategies. The SP control strategy yields the highest mean NPV with 4.5% increase over the heuristic reactive control strategy, while the watercut feedback strategy yields a mean NPV gain of 3.8%.

6.4 Discussion

The results show that closed-loop feedback inflow control based on downhole measurements of SP, which allows control actions to be made prior to water breakthrough, can yield significant gains in NPV when compared to both watercut-based feedback control and heuristic reactive control strategies, even when the reservoir does not behave as expected. The total oil and water volume produced over the 30 year production period of the ensemble of Brugge reservoir models, for each closed-loop feedback control strategy normalised against the heuristic reactive strategy, are shown in Figure 6.10. The SP feedback control strategy produced more oil that the heuristic strategy in all but a very few of the ensemble of model realisations tested and depending upon the reservoir behaviour, the strategy can result in higher or lower total produced water volumes than the heuristic reactive strategy. In contrast, the watercut control strategy produced more cumulative oil in all of the ensemble of model realisations tested. On average however, the SP feedback control strategy produces significantly less water than that watercut feedback control strategy.

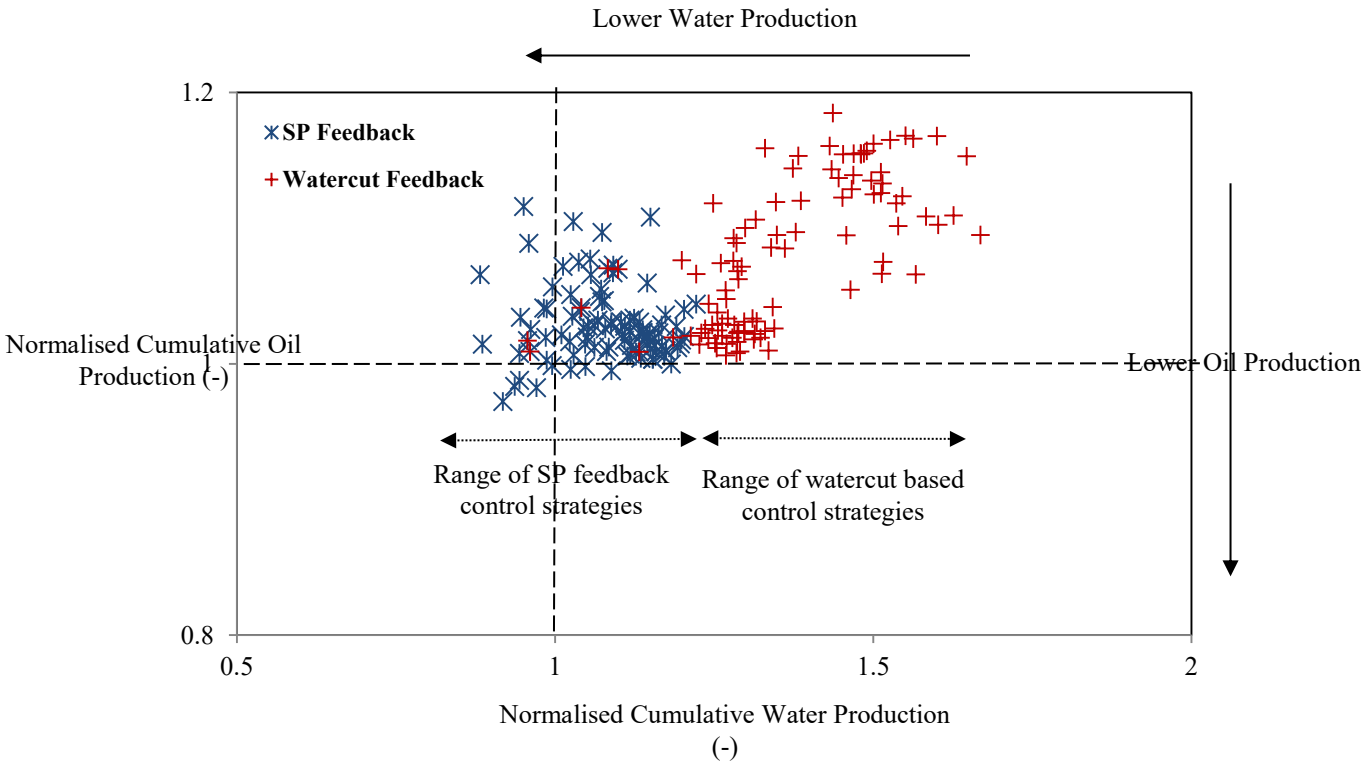


Figure 6.10: Cumulative oil and water produced for each of the inflow control strategies normalised against the heuristic strategy, over the ensemble of reservoir model realisations.

Figure 6.11 shows how the cost associated with the production and injection of water affects the NPV obtained at \$5 (similar to Figure 6.9) and \$20 per barrel of water (bbl), using the different control strategies over 30 years of production. As shown in Figure 6.9, the SP feedback control strategy yields the highest mean NPV of all the control methods and a mean NPV gain of 4.5% over the heuristic model at \$5/bbl of injected or produced water, while the watercut feedback control yields a mean NPV gain of 3.8% over the heuristic model. However, the mean NPV gains for the watercut feedback control strategy decreases to 2.5% at production/injected cost of water at \$20/bbl, with the SP feedback control strategy maintaining a 4.4% gain over the heuristic control strategy, demonstrating that the SP feedback control strategy can be used to reduce the negative production consequences associated with production of water.

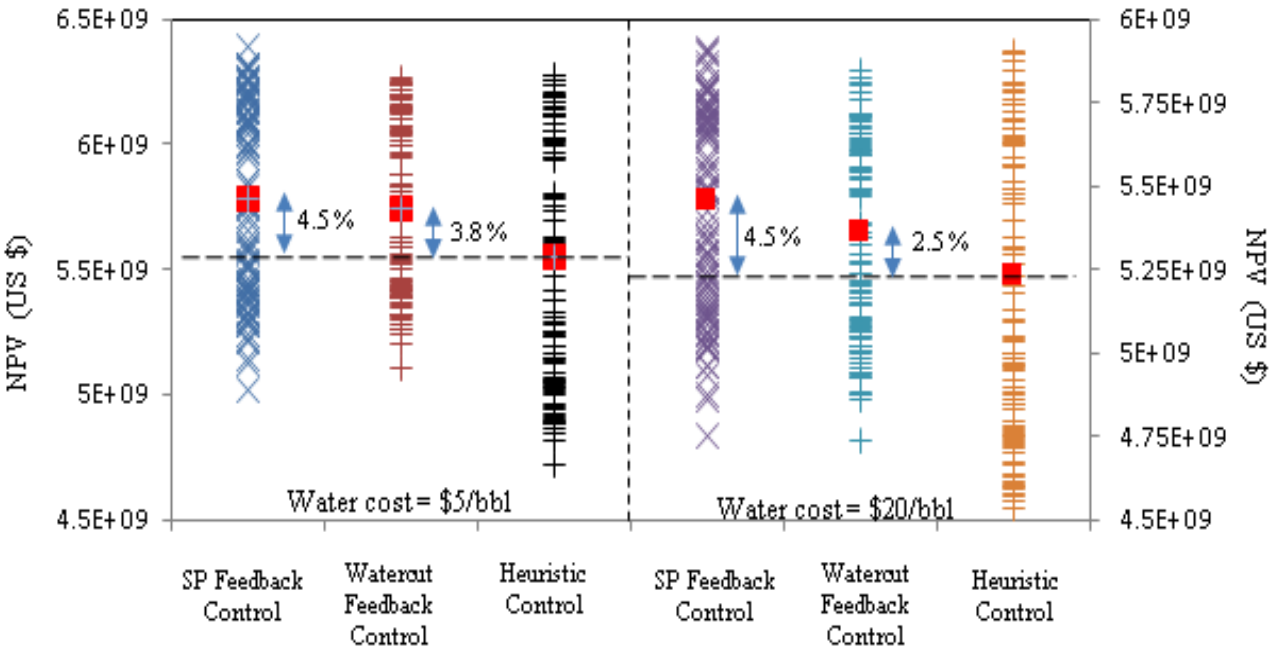


Figure 6.11: Range of NPV obtained for the 0 – 30 year production period for each of the inflow control strategies. Each point represents the NPV for particular unexpected reservoir behaviour. The red data point represents the mean NPV for each of the control strategies. The range of NPV data obtained at water cost = \$5/bbl. is similar to Figure 6.7, compared to NPV obtained at water cost = \$20/bbl.

Overall, the results reveal that the closed-loop feedback control study based on downhole measurements of SP, which was initially implemented in Chapter 4 for single well inflow control, can also be implemented in a multi-well development and yields significant gains in NPV when compared to watercut feedback control strategies and heuristic reactive

control strategies. The results over the ensemble of unexpected reservoir behaviour suggest that the SP-based feedback control can be used to improve well NPV over a feedback inflow control strategy based on watercut measurement by significantly reducing the costs associated with water production, whilst maintaining significant volumes of oil production.

6.5 Conclusions

We have demonstrated that closed-loop feedback inflow control based on downhole measurement of SP can be used for production optimisation in the synthetic multi-well Brugge Field model. The results show that the SP based inflow control strategy can yield significant NPV gains over heuristic reactive control and water based feedback control strategies even when the reservoir does not behave as predicted. We observed that by using a subset of reservoir models to determine the parameters used in the control algorithm, the overall performance of the SP feedback control strategy can be improved. For all the cases tested, the feedback control strategies outperformed the heuristic control strategies. The SP based feedback control strategy presents an alternative to closed-loop feedback control strategies based on surface and downhole watercut measurements, by significantly reducing the expenditure costs associated with water production whilst maintaining significant oil revenues. These results are important because they confirm that the use of downhole SP measurements, based on currently available oilfield technology, can be used as a simple but effective approach to production optimization and reservoir management using smart wells.

Chapter 7

SP Monitoring in Real Field Applications

7.1 Introduction

So far, we have highlighted the benefits of the use of self-potential (SP) measurements in synthetic oil field applications for effective well and reservoir management. In Chapters 4, 5 and 6, we demonstrated how SP measurements taken along horizontal and vertical production wells, in simple and complex synthetic reservoir models, could be used to monitor waterfront encroachment prior to water breakthrough and provide useful information for production optimisation. In this chapter, we investigate the potential utility of SP monitoring for effective reservoir management in two real field analogue applications. First, the simulation of a North Sea reservoir model termed here as the "X-field" is used to determine whether SP monitoring could be used to image moving waterfronts prior to breakthrough, and estimate the time prior to water breakthrough the encroaching waterfront can be sensed. The X Field model presents a more complex reservoir model than that used in Chapter 5 and 6, and consists of multiple faults zones with complex deformation fault planes; as opposed to the Brugge model which consist of a single clean fault fracture. We also investigate whether SP measurements taken at the production wells can be used to determine the residual water saturation in swept zones, and determine the lateral extend of bypassed zones; this could be useful in making future well planning and perforation decisions. Second, we investigate the prospects of using SP measurements in freshwater boreholes for monitoring seawater intrusion into coastal freshwater aquifers. The SP solver developed for this study was adopted by MacAllister *et al.* (2015) to ascertain whether saline intrusion can be monitored in fractured coastal freshwater aquifers.

7.2 SP Monitoring in the Field

7.2.1 X Field Geological Model and Simulation

Due to the commercial sensitivity of the North Sea model termed here as the X Field model, we cannot give a full description of the reservoir model. The field was rapidly appraised following drilling, and a high net-to-gross reservoir was initially mapped out, with the intermittent shale layers thought unlikely to affect flow vertically through the reservoir. However, a recent stratigraphic review showed that field-wide the shale layers served as significant barriers to vertical flow. The current model supports excellent field-wide history match of the field production data despite the presence of laterally extensive shale layers to sand connection across non-sealing faults. The reservoir is composed of NTG and permeability properties of the channel axis faces similar to that of clastic reservoir rock type, with fluid flow through the reservoir governed by Darcy's law.

Figure 7.1 and 7.2 shows a section of plan-view of the current X Field simulation model, highlighting two production wells of interest, A and B which experienced early water breakthrough. The model comprises of intermittent sandstone layers labelled here L1 – L5 from bottom to top varying in thickness, separated by shale layers which are inactive in the reservoir model. The reservoir is a high pressure, high temperature reservoir and contains undersaturated oil with no gas cap, with an underlying aquifer. For SP simulation purposes, the porosity of the inactive alternating shale layers are set to 10% and the pore-space is assumed to be saturated with formation brine. Hence, the shale layers do not contribute to flow but are electrically conductive.

7.2.2 Numerical modelling of SP

The SP solver developed in chapter 5 was updated to account for the flow of charge across the more complex fault zones of the X field reservoir model, making the solver more robust and was used to simulate the SP signals observed in wells A and B. The salinity of the injected seawater during waterflooding is similar to that of the formation brine. Therefore, the concentration gradient across the reservoir is negligible and the electrochemical potential is contribution to the total SP measured is zero. Moreover, in Chapter 3 we observed that the thermoelectric potential contribution to the SP signals measured at a

production well prior water breakthrough is negligible. Hence, the SP signals generated during production in the X Field are dominated by the electrokinetic potential. LGRs of 30×30×360 cells, limited by the ECLIPSE software memory, are placed around each well to obtain higher resolution SP results (see Figure 7.1). Underburden and overburden electrically conductive, water-saturated shale layers of 50m are placed above and below the reservoir (not shown in Figure 7.1 and 7.2) and on the sides of the model; these are required for the SP modelling as electrical currents may exploit these shale layers.

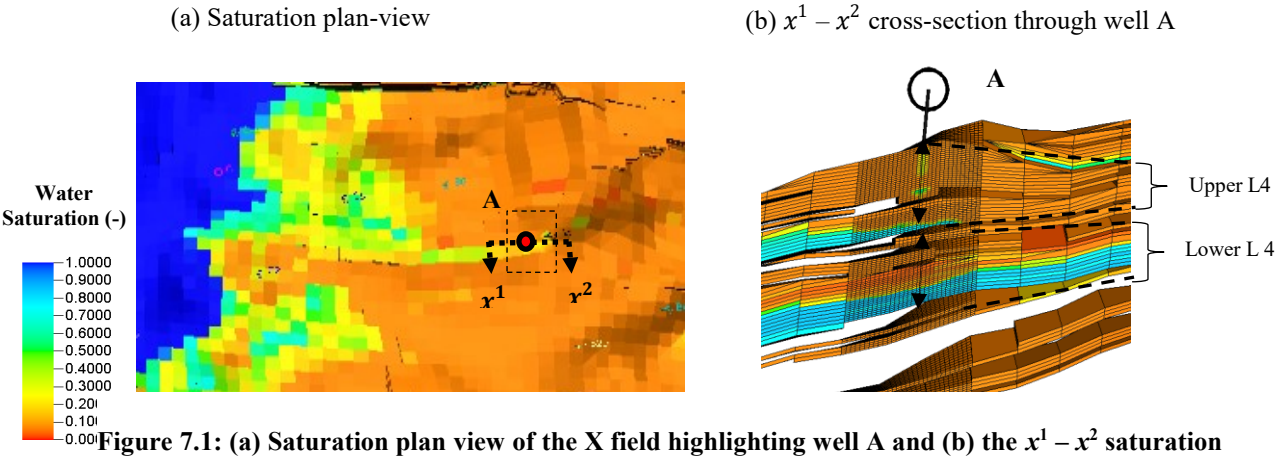


Figure 7.1: (a) Saturation plan view of the X field highlighting well A and (b) the $x^1 - x^2$ saturation cross-section through well A which only penetrates the reservoir in layer 4 (L4). LGRs are placed around the well A to obtain higher resolution SP simulation results and the inactive cells between the sand layers represent the impermeable shale layers.

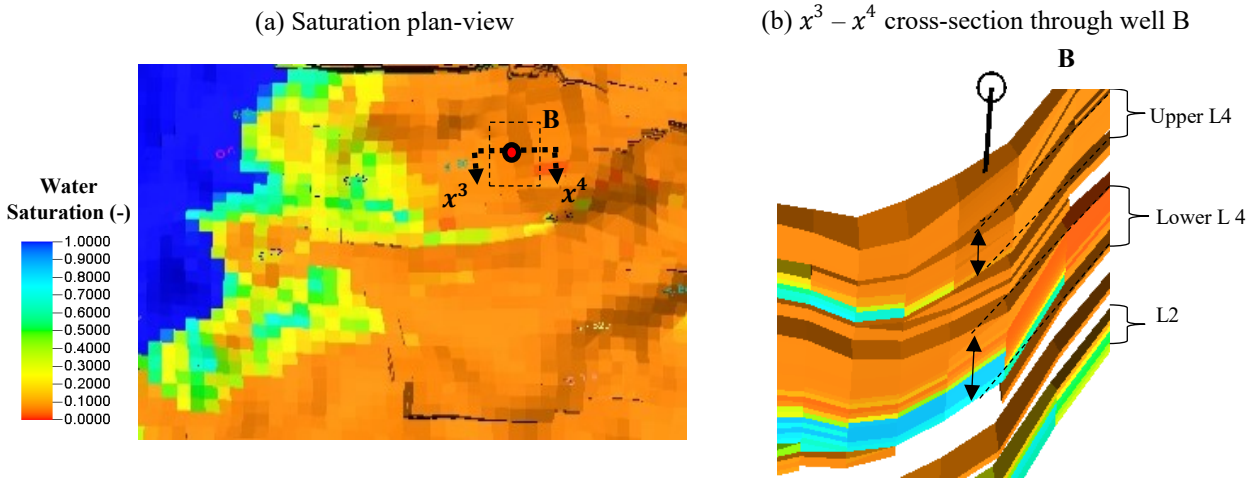


Figure 7.2: (a) Saturation plan view of the X field highlighting well B and (b) the $x^3 - x^4$ saturation cross-section showing well B which only penetrates the reservoir in layer 4 (L4). The inactive cells between the sand layers represent the impermeable shale layers. LGRs are also placed around well B to obtain higher resolution SP simulation results, but are not shown above.

7.2.3 SP signals during production

We begin by showing the SP signals generated during production in well A, which is completed in the upper and lower L4 stratigraphic layer. Figure 7.3 and 7.4 shows the saturation cross-section through well A and the corresponding SP signals measured along the production well with reference to a distance electrode placed in the overlying shale layer. The figures highlights the SP in the upper and lower L4 layers where the well is completed.

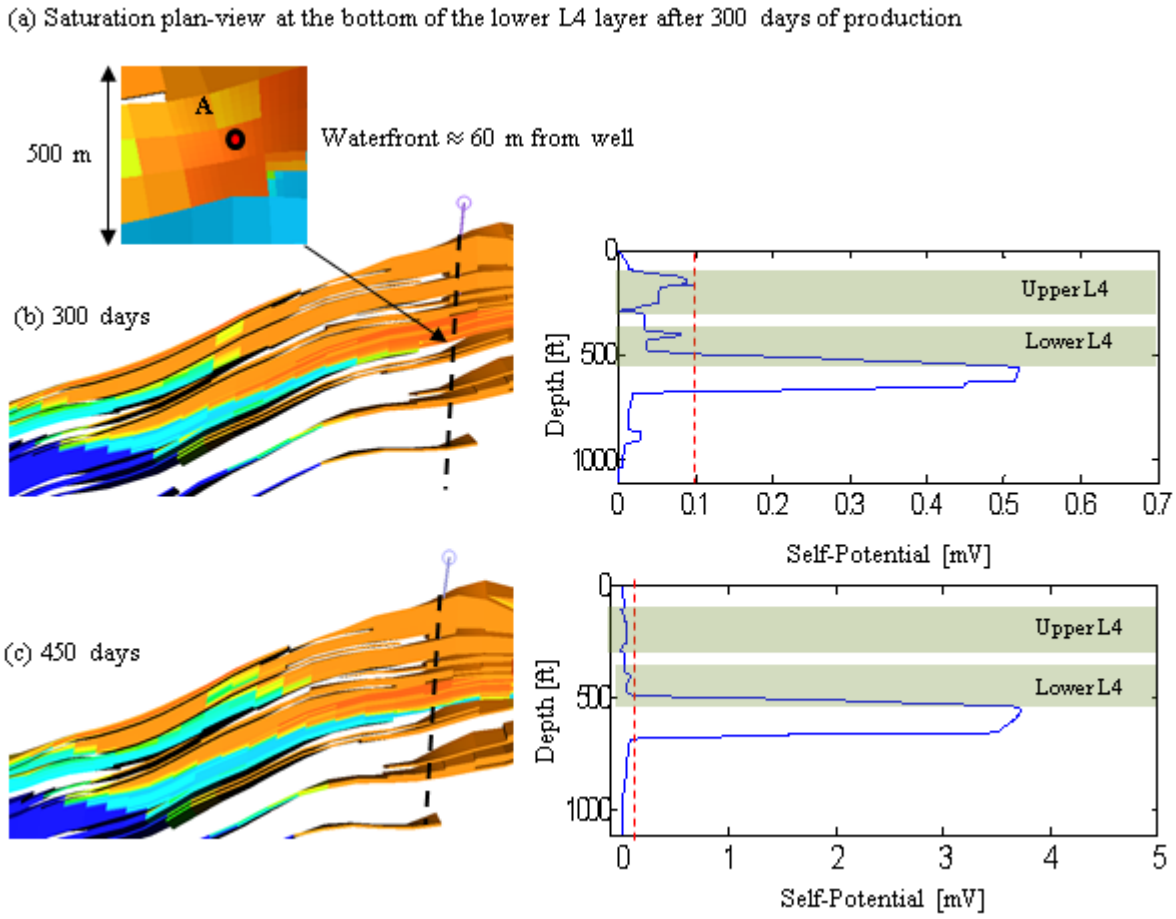


Figure 7.3: (a) saturation plan-view at the base of the lower L4 layer after 300 days, and the $x^1 - x^2$ saturation cross-section through well A from figure 7.2 and the corresponding SP signal measured along well A after (b) 300 and (c) 450 days of production respectively. The vertical dotted red lines on the SP plot represent the assumed noise level of 0.1 mV. Measurable SP is observed in the lower L4 layer with the waterfront approximately 183 m away from the production well.

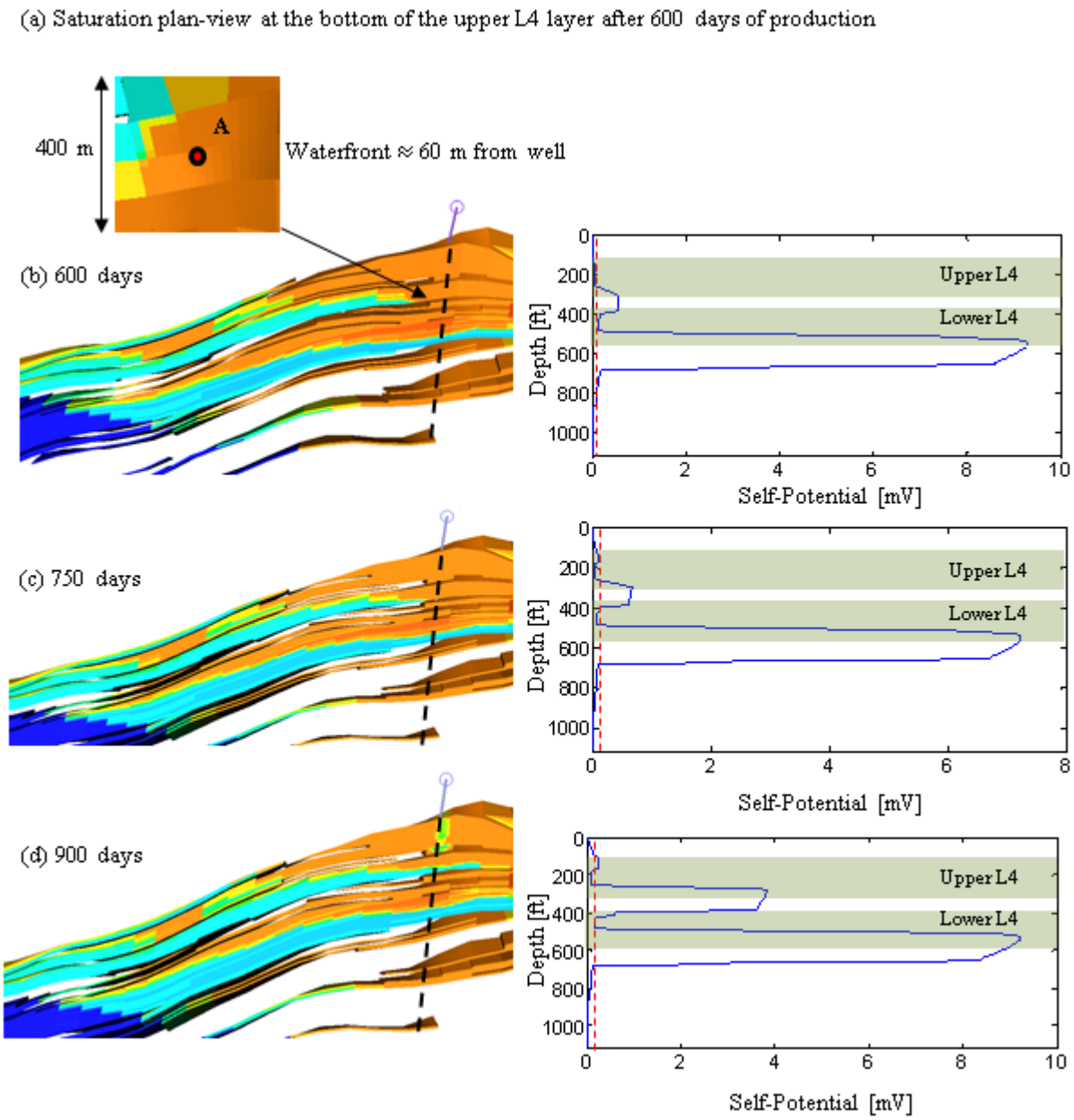


Figure 7.4: (a) saturation plan-view at the base of the upper L4 layer after 600 days, (b) $x^1 - x^2$ saturation cross-section through well A from figure 7.2 and the corresponding SP signal profile measured along well A after 600 days; measurable SP is observed in the upper L4 layer with the waterfront approximately 60 m away from the production well after 600 days of production, (c) $x^1 - x^2$ saturation cross-section and the corresponding SP measured after 750 and (d) 900 days of production. The vertical dashed red lines on the SP plot represent the assumed noise level of 0.1 mV.

The simulations show that measurable SP above the assumed electrode noise level of 0.1 mV is observed in the lower L4 layer with the encroaching waterfront approximately 183m away from the well. The SP signal also reflects the shape of the encroaching waterfront, with the most positive SP observed at the base of the lower L4 stratigraphic layers, where

the waterfront initially reaches the well due to the influence of gravity which directs water to the base of the reservoir layers. Similar observations are made in the upper L4 layer of well A in Figure 7.4. The simulations show that measurable SP above the assumed electrode noised level can also be observed in the upper L4 layer when the encroaching waterfront is approximately 60 m away from the well and reflects the shape of the encroaching waterfront. The most positive SP is also observed at the base of the upper L4 stratigraphic layers, where the waterfront initially reaches the well. However, there seems to be no interference in the SP signals generated in the upper L4 and lower L4 layers, because the water saturated shale layers are electrically conductive and prevent the spread of current between the layers. The change in the maximum SP (ΔV) measured in well A relative to the initial measurement taken at the start of production, in the lower and upper L4 layers respectively is shown in Figure 7.5. The horizontal dashed lines show the assumed noise level of 0.1 mV. The change in the maximum SP measured in both layers exceeds 0.1 mV at approximately 150 days prior to water breakthrough, suggesting that the encroaching water movement can be monitored almost half a year prior to breakthrough in well A.

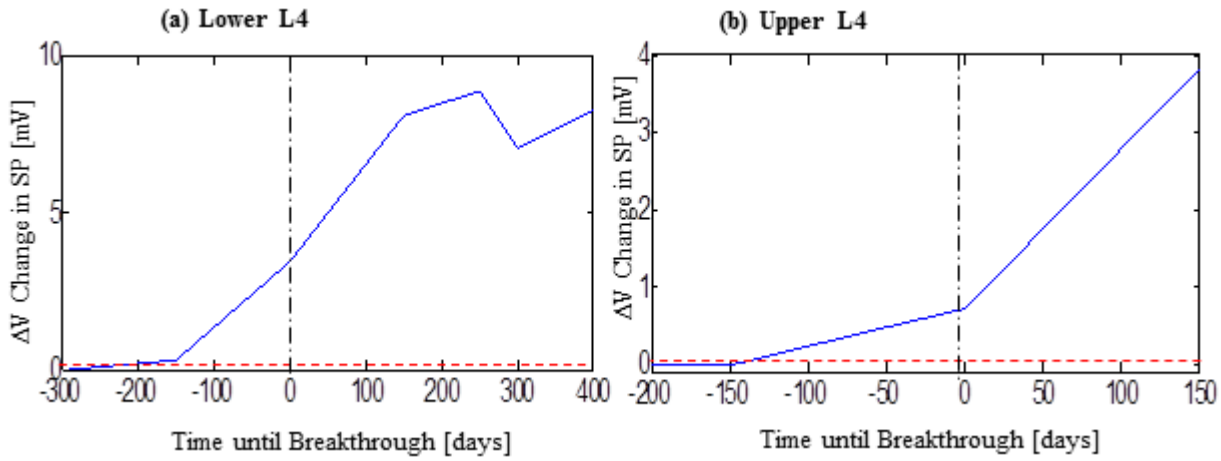


Figure 7.5: Maximum changes in SP (mV) versus production time plots in the (a) lower L4 and (b) upper L4 layers respectively. Vertical dotted line represents times at which the waterfront reaches well A in each layer.

Similar SP results are obtained in well B which is also completed the reservoir in the upper and lower L4 stratigraphic layers (see Figure 7.2). Figures 7.6 and 7.7 show the saturation cross-sections and the corresponding SP measured in well B at different time-steps. Although well B is not completed in the upper L2 stratigraphic layer, the SP measured after

150 days of production reflects the high water saturation in the L2 layer. Measurable SP signal is observed in the lower L4 layer prior to water breakthrough after 300 days of production, with the waterfront approximately 150 m away from the well (see Figure 7.6, b). A measurable SP signal is also observed in the upper L4 layer prior to water breakthrough after 750 days of production, with the waterfront approximately and 50 m away from the well (see Figure 7.7, b).

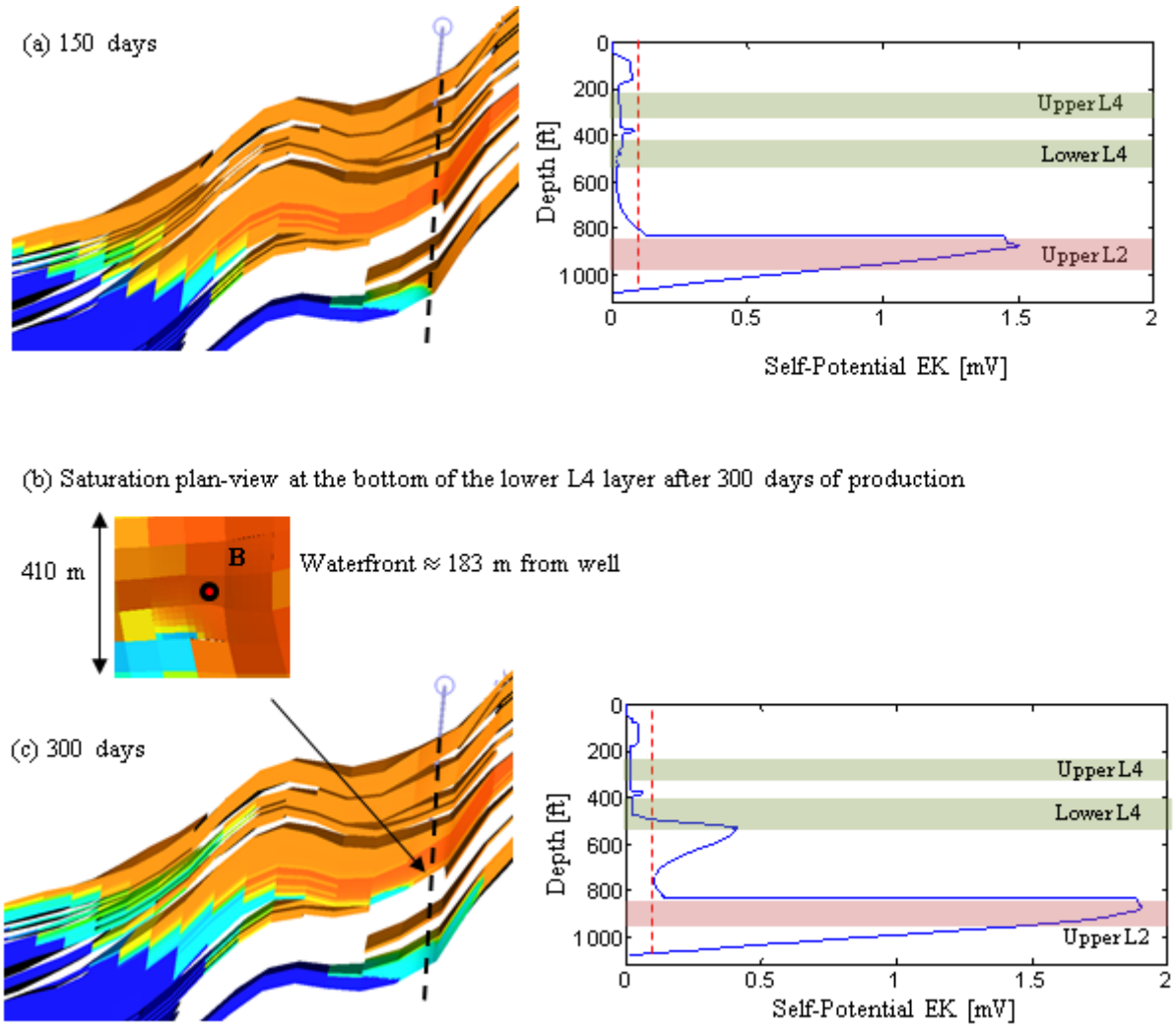


Figure 7.6: (a) the $x^3 - x^4$ saturation cross-section through well B from figure 7.2 and the corresponding SP signal measured along well B after 150 days of production, (b) saturation plan-view at the base of the lower L4 layer after 150 days of production, (c) the $x^3 - x^4$ saturation cross-section through well B from figure 7.2 and the corresponding SP signal measured along well B after 300 days. The vertical dashed red lines on the SP plot represent the assumed noise level of 0.1 mV. Measurable SP is observed in the lower L4 with the waterfront approximately 183 m away from the production well. The upper L2 layer is highlighted in red because the well is not completed in this layer.

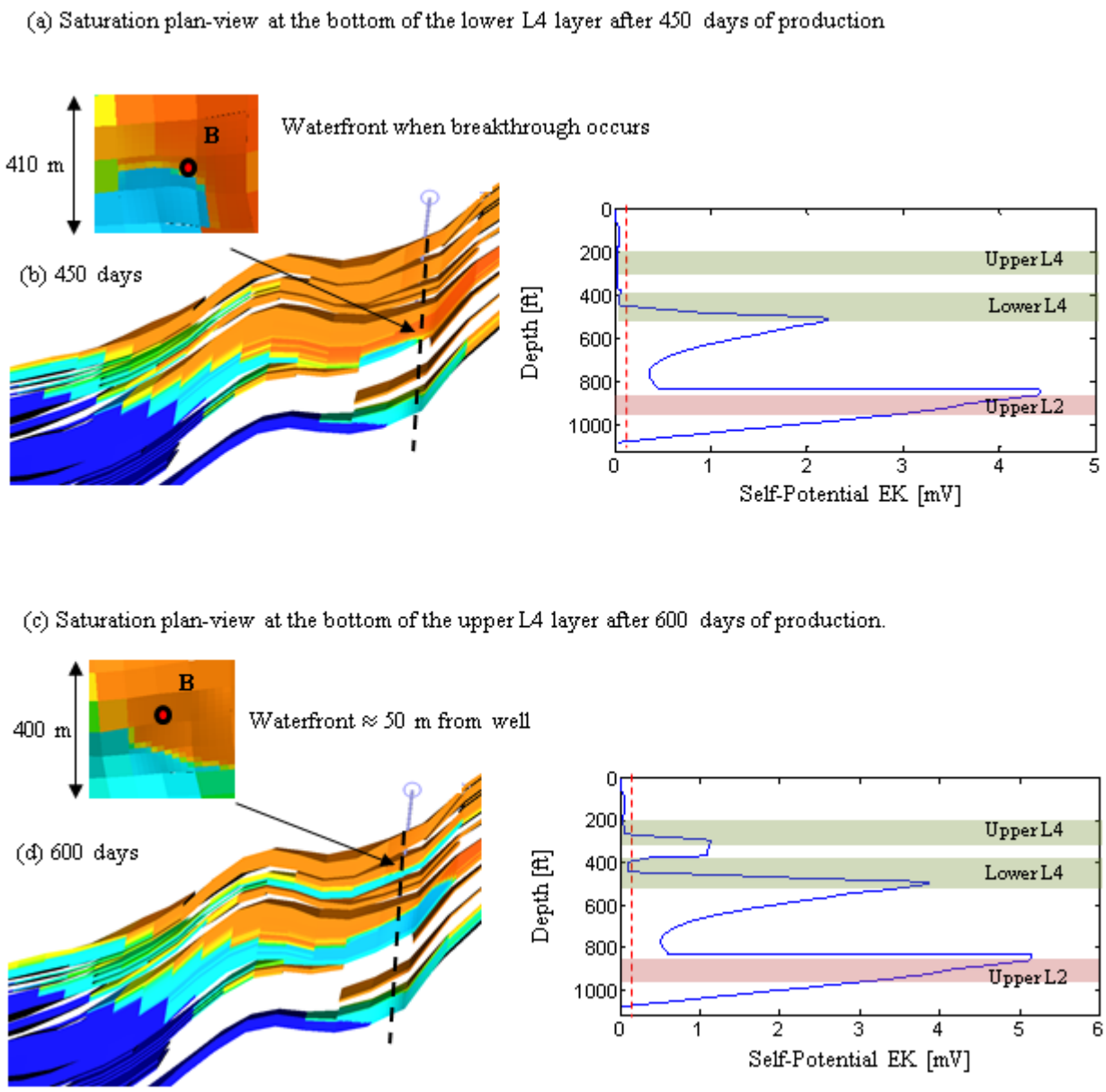


Figure 7.7: (a) saturation plan-view at the base of the lower L4 layer after 450 days of production, (b) $x^3 - x^4$ saturation cross-section through well B from figure 7.3 and the corresponding SP signal profile measured after 450 days, (c) saturation plan-view at the base of the upper L4 layer after 600 days of production, (d) $x^3 - x^4$ saturation cross-section through well B and the corresponding SP signal profile measured after 600 days. The vertical dotted red lines on the SP plot represent the assumed noise levels. Measurable SP signal is observed in the upper L4 layer prior to water breakthrough with the front approximately 50 m away from the production well. The upper L2 layer is highlighted in red because the well is not completed in this layer.

The change in the maximum SP (ΔV) measured in well B, relative to the initial value at the start of production in the lower and upper L4 layers respectively is shown in Figure 7.8. The horizontal dashed lines show the assumed noise level of 0.1 mV. The change in the maximum SP measured in both layers exceeds 0.1 mV at approximately 200 and 300 days prior to water breakthrough in the lower and upper L4 layers respectively. This suggests that the encroaching water movement can be monitored almost a year prior to breakthrough in well B.

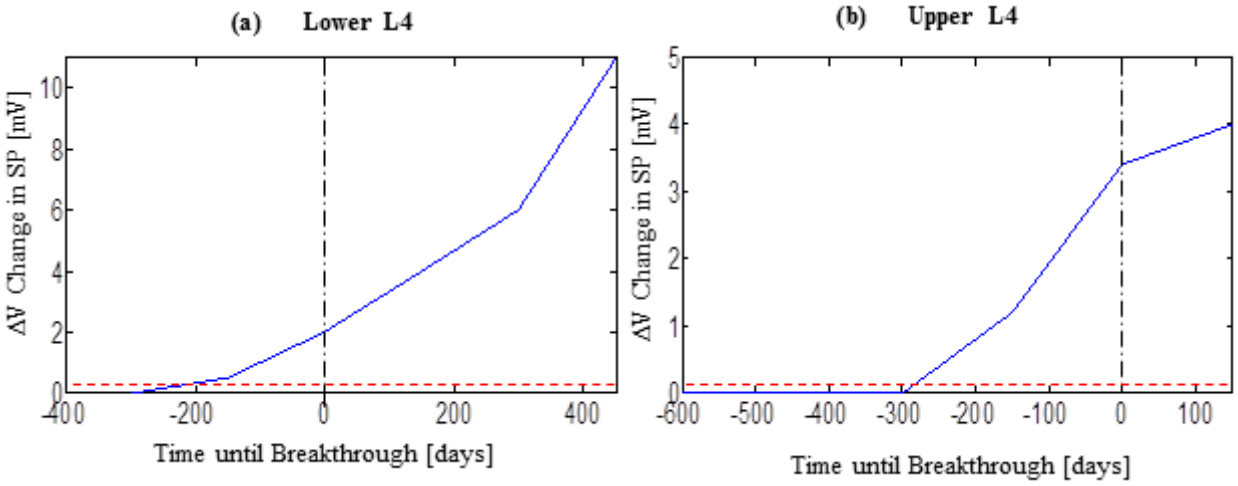


Figure 7.8: Maximum changes in SP (mV) versus production time plots in the (a) lower B4 and (b) the upper B4 layers respectively. Vertical dotted line represents times at which the waterfront reaches the well in each layer.

7.2.4 Relationship between SP measurements and residual oil saturation

In order to ascertain whether SP measurements can be used to determine the residual oil saturation in the reservoir swept zones, the change in the total SP (ΔV) measured with respect to initial measurements is plotted against the change in saturation (ΔSw) in Figure 7.9. The figure shows the measurements taken along the well A and B, in the upper and lower L4 stratigraphic layers at different time steps. In both of the stratigraphic layers, the change in the total SP initially increases due to the encroachment of the waterfront prior to water breakthrough (i.e. $\Delta Sw = 0$). However, once the water saturation changes (i.e. after water breakthrough occurs $\Delta Sw > 0$), the change in the total SP remains constant at each time step regardless of the change in saturation. This suggests that the SP measurements post-breakthrough is insensitive to water saturation.

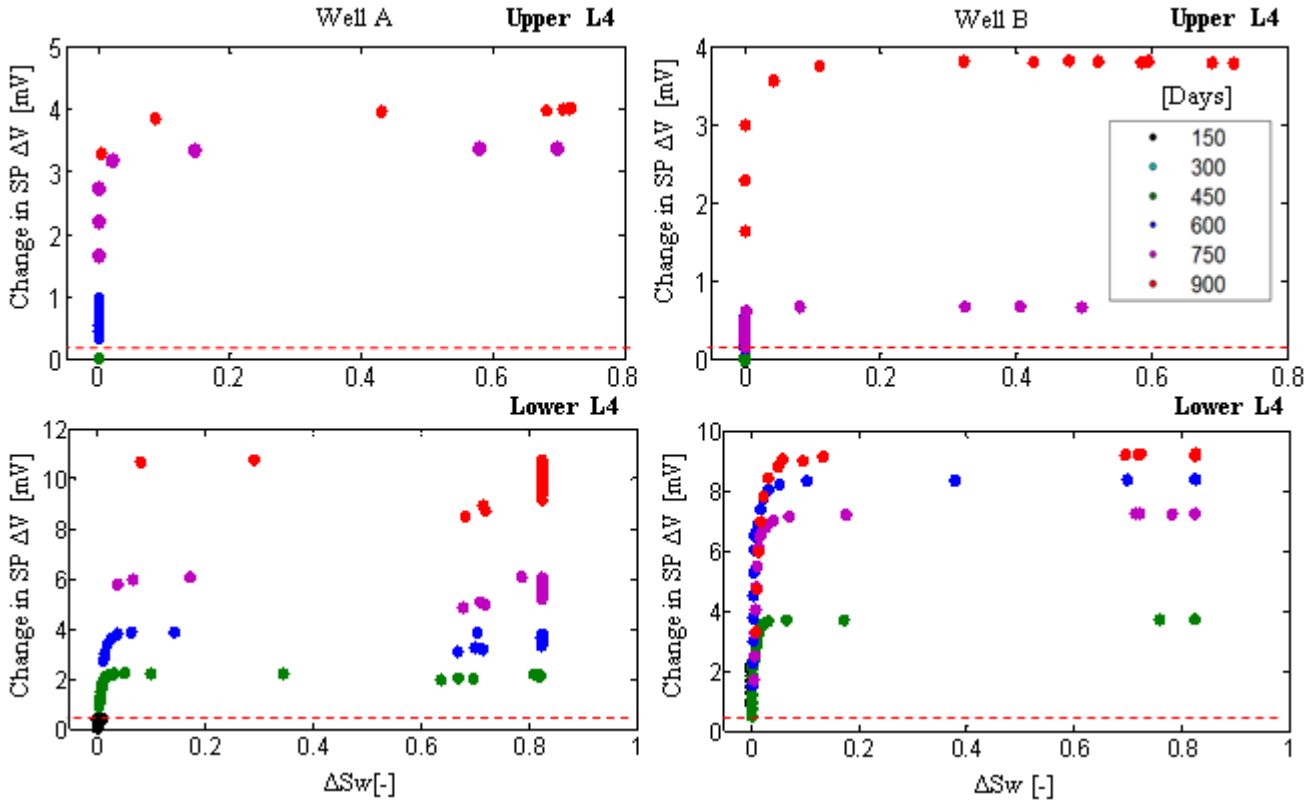


Figure 7.9: Change in SP versus change in water saturation observed in well (a) A and (b) B in the upper and lower L4 layers respectively. The change in the total SP remains constant at each time step regardless of the change in saturation.

7.2.5 Summary

The SP simulation of the X Field model advocates for the use of SP measurements in real clastic reservoir field applications. The results of the SP simulations suggest that SP can be measured using electrodes permanently installed downhole as the signals are measurable above the assumed electrode signal noise level. The simulation also shows that the SP signals can be used to image moving waterfronts up to 200m away from an instrumented production well, 150 – 300 days prior to breakthrough. However, the SP measurements post breakthrough are insensitive to the change in water saturation. The lateral extent of bypassed oil zones could be determined if SP monitoring is carried out in multiple wells simultaneously; this could be used in making future well planning and perforation strategy in production and injection wells to balance the waterflood front advance and manage voidage within the field.

7.3 Monitoring Seawater Intrusion in fractured coastal aquifer

Seawater intrusion is a global phenomenon that affects coastal freshwater aquifers, which provide large volumes of portable water sources (Nowroozi *et al.* 1999; Choudary *et al.* 2001; Essink 2001; Warner *et al.* 2012). Pollution of freshwater aquifers by less than 1% of seawater (~0.25 g/l of chloride or ~0.005M) renders freshwater unhealthy for ingestion. Various studies have been carried out to understand the processes that affect seawater movement in freshwater aquifers (Huyakorn *et al.*, 1987, Werner *et al.* 2012). Figure 7.10 shows an example of a simple coastal aquifer highlighting a selection of the hydrogeological processes of relevance to saline intrusion. In natural conditions, a seawater wedge develops as less dense freshwater overlies more dense seawater. However, seawater intrusion due to prolonged groundwater pumping (water production), and sea-level fluctuation due to tidal effects which impose dynamic hydrologic conditions lead to distribution of dissolved salts, creating saline fingering which may cause contamination of the abstraction boreholes.

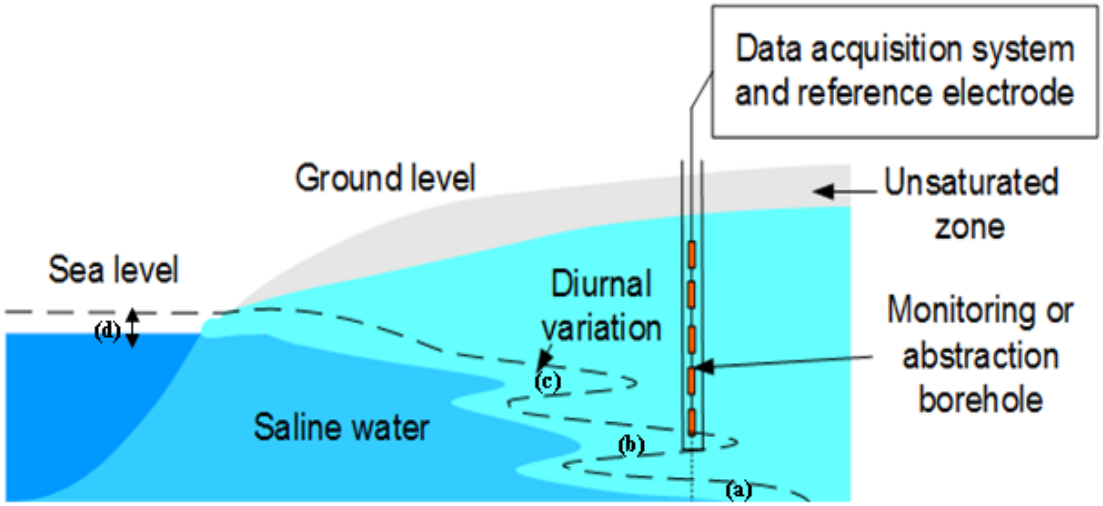


Figure 7.10: Simplified diagram of a coastal unconfined aquifer setting, showing (a) seawater wedge toe, (b) seawater intrusion at the base of the abstraction borehole and (c) saline fingering at the base of the borehole due to prolonged groundwater pumping due to tidal effects, and (d) sea-level fluctuation (MacAllister *et al.* 2015).

The conditions created by seawater intrusion generate electrochemical and electrokinetic potentials, the sum of which will be observed as the overall SP, suggesting that borehole measurements of SP can be used to remotely monitor seawater intrusion into coastal aquifers and detect saline water movement towards an abstraction well. Field measurements of SP were taken in two boreholes in order to compare the difference in borehole SP measurement between an inland site and a coastal site at risk of seawater intrusion as shown in figure 7.11(a). Figure 7.11(c) plots the SP versus borehole depth, which shows a persistent and clear gradient not present at the inland site in Figure 7.11(b). The SP measurements taken in the coastal borehole exhibit oscillations of approximately 0.4 mV in amplitude, that are in phase and anti-correlated with the head fluctuations in the borehole (see Figure 7.12). Moreover, the SP oscillations were also observed before and after saline water entered the borehole, identified using downhole conductivity measurements in Figure 7.12 (c), which shows an increase in conductivity. MacAllister *et al.* (2015) hypothesized that the SP signals generated at the borehole were due to (i) electrokinetic processes local to the borehole associated with the tidally driven head variations and/or (ii) electrochemical (exclusion-diffusion) processes associated with salinity gradients remote from the borehole, and tidally driven lateral variations in the location of the saline front within a fracture zone which intersects the borehole.

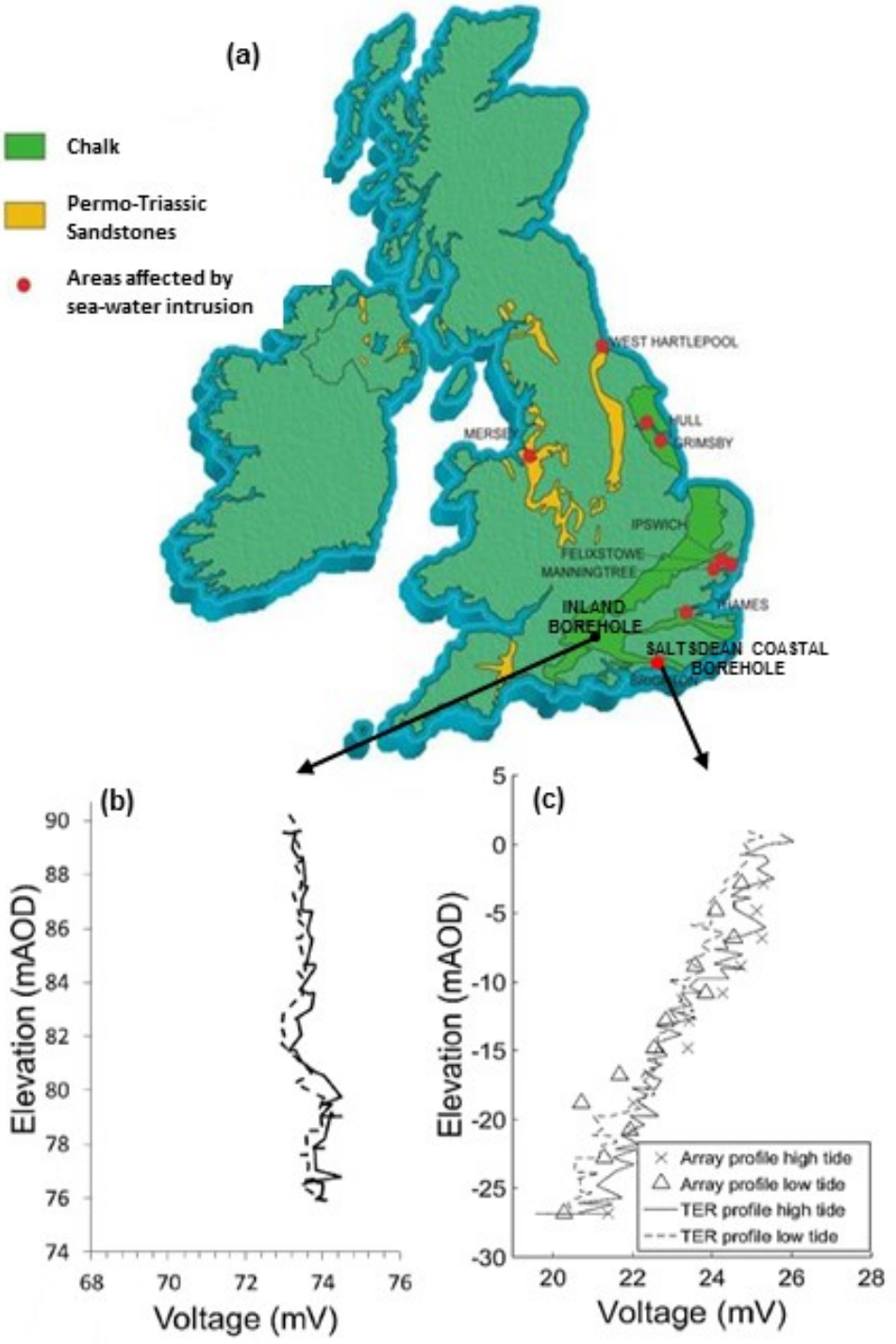


Figure 7.11: (a) Location of the NERC field sites affected by seawater intrusion (NERC) highlighting the locations of the inland and coastal boreholes (b) SP versus depth in the inland borehole (c) SP versus depth in the saltsdean coastal borehole (MacAllister *et al*. 2015).

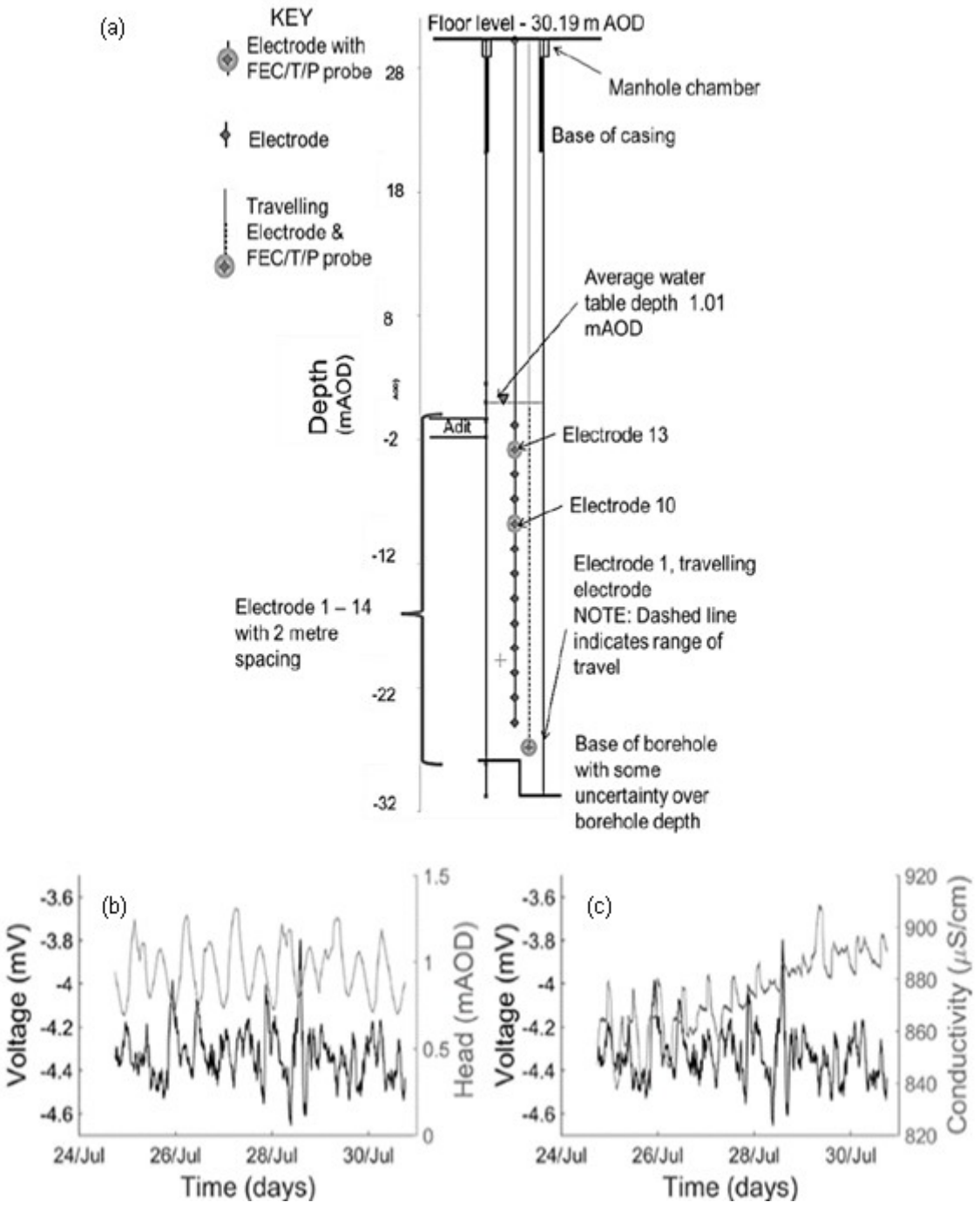


Figure 7.12: (a) Saltsdean borehole with SP tool properties. (b) Field measurements of SP (mV) and the corresponding head versus time (c) SP (mV) and the corresponding fluid conductivity versus time (MacAllister *et al.* 2015).

A simple hydrodynamic model that mimics a naturally occurring steady state saline wedge was developed as shown in Figure 7.13, with the key hydrodynamic and electrodynamic properties summarised in Table 7.2. The seaward boundary is at seawater salinity and the head varies over a tidal cycle consistent with the observed field tidal data. The inland boundary is at groundwater salinity and has a constant head 1m above mean sea-level. A fracture zone is modelled 80m below the top of the model that intersects the borehole, consistent with borehole geophysical data.

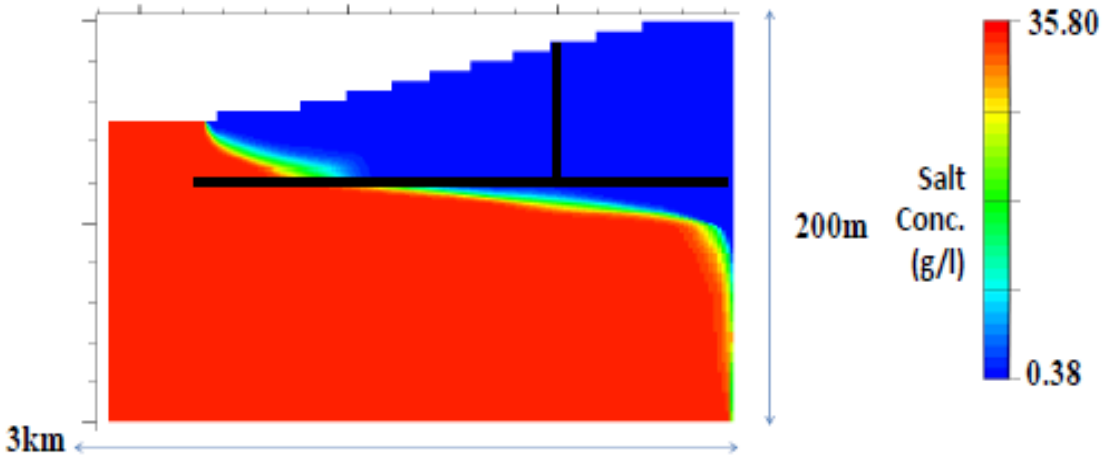


Figure 7.13: Simplified hydrodynamic model of a steady state saline wedge developed in a coastal aquifer (MacAllister *et al.* 2015).

Aquifer Properties		**Tidal Simulation boundaries**
Bulk rock permeability (top 50m): 15D		Pressure Spring:
Exponential perm decrease to base: 2mD		-3.5mAOD to +3.5mAOD
Fracture Permeability: 2500D		Pressure neap:
Bulk rock porosity: 1%		-1.5mAOD to +1.5mAOD
Fracture Porosity: 2%		Constant inland head: 0.5mAOD
Electrodynamic Properties (from laboratory experiments)		
EK	Ground water Coupling Coefficient:	Sea water Coupling Coefficient
	-0.575±0.08 mV/mH2O	-0.0101±0.02 mV/mH2O
EC	19.30±7.3 mV across the saline front	

Table 7.1: Hydrodynamic and electrodynamic properties of simulated coastal Aquifer MacAllister *et al.* 2015). Note: mAOD denote Meters above Ordnance Datum.

The SP solver developed in chapter 3 was used to simulate the SP response to the tidal cycle of the hydrodynamic model. Figure 7.14(a) shows the model SP versus time plot compared to field observation and provides a reasonable match; the model properties were varied iteratively to obtain this match. However, most numerical models have failed to match the field data. Figure 7.14 (b) and (c) show the EC and EK potentials against time plots and the corresponding head (pressure) measurements. The plots suggests that the EC potential is the dominant SP source in the model and is in phase and anti-correlated with the change in head. The EC and EK potential are one time step out of phase, suggesting that the EC potential is solely responsible for the SP measurements taken in the well.

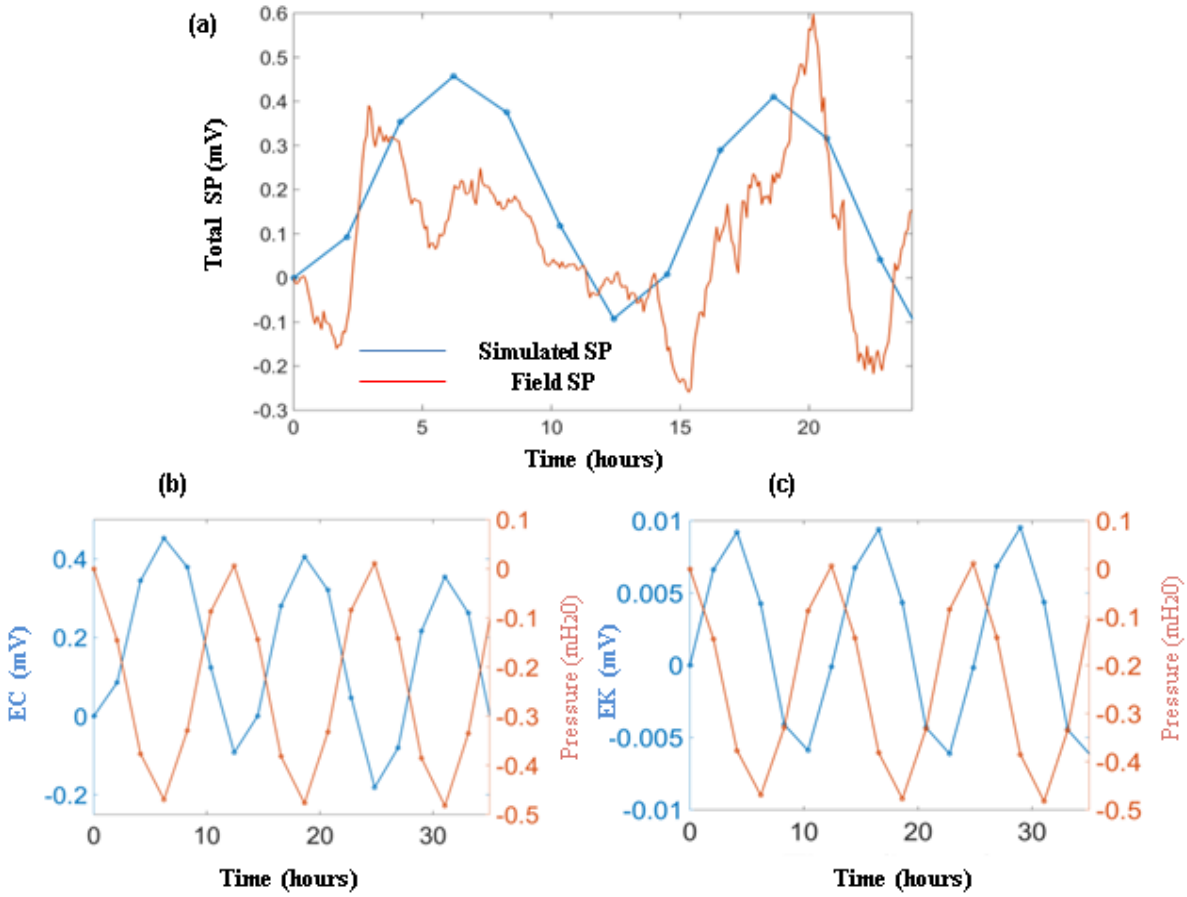


Figure 7.14: (a) Simulated SP and field SP measurement plotted versus time, (b) electrochemical (EC) potential contribution to the tidal SP (c) electrokinetic (EK) potential contribution to the tidal SP. The EC contributes to most of the SP measured in the borehole (MacAllister *et al.*, 2015).

Figure 7.15 shows the plot of the model borehole gradient compared to the observed borehole gradient. The model results suggest that the borehole SP gradient is caused by the proximity of the saline front to the base of the borehole; 4m away as shown in the model (see Figure 7.13). In summary, the numerical modelling suggests that the borehole SP response in the coastal aquifer is dominated by the electrochemical potential generated across a saline front that does not intersect the borehole. Moreover, the tidal SP response is primarily caused by tidal driven variations in the location of the saline front within the sub-horizontal fracture zone. Hence, the SP simulation successfully demonstrates that the borehole SP monitoring can be used to monitor the location of a remote saline front in a coastal aquifer.

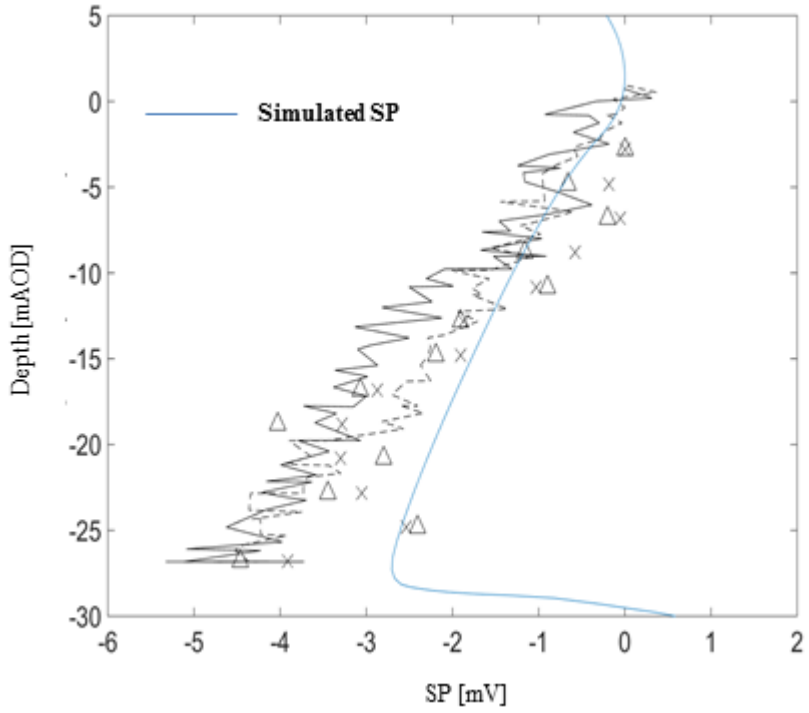


Figure 7.15: Comparison of the model borehole gradient against the observed borehole gradient as shown in Figure 7.11 (c). (MacAllister et al., 2015)

Chapter 8

Conclusions & Future Work

The management of produced water brought to the surface with reservoir oil during production is vital as it plays an important role in the profitability of a hydrocarbon reservoir/field. Moreover, there is an increasing burden to contain the environmental impact associated with the production of contaminated water as environmental limitations in some parts of the world are constantly insistent on the treatment and reinjection of produced water. This is even more critical in deeper waters where water treatment processes can be tremendously expensive due to platform weight limitations and logistic difficulties. Because the economic life of a reservoir depends on the cost associated with the production, treatment, and disposal/reinjection of the produced water, being able to anticipate the arrival of water at production wells is essential to enable operators make adequate plans for water breakthrough and/or water treatment. In other words, if the arrival time of produced water is known, well completions of interest can be shut-in prior to water breakthrough. This thesis investigated a novel closed-loop feedback inflow control strategy, based on downhole measurements of self-potential (SP), and quantified the benefit of this approach in preventing or minimizing water production.

A control volume finite difference (CVFD) numerical SP solver was developed in Chapter 3 based on previous studies by Jackson and co-workers (Saunders *et al.* 2008; Gulamali *et al.* 2010; and Jackson *et al.,* 2012) to simulate the electrokinetic (EK), electrochemical (EC) and thermoelectric (TE) components of the SP generated in a simple sandstone reservoir during waterflooding. The SP solver was used to simulate SP signals generated in two synthetic hydrocarbon reservoir applications: (1) a thin oil column in Chapter 4 and (2) the SPE Brugge field model in Chapter 5. The results in Chapter 4 indicate that SP measurements at a production well can improve reservoir management by monitoring waterfront encroachment towards production wells prior to water breakthrough.

Furthermore, SP measurements can be used to identify completion segments of the well where the waterfront is closest. In Chapter 5, it was observed that there is an intricate relationship between the dominance of the EK and EC contribution to the SP, which depends on the well completion configuration and the dynamics between injected freshwater and formation brine. The results of the SP simulation observed in the analogue hydrocarbon reservoir (Chapter 7) agree with the results of Chapters 4 and 5 where SP signals provide advance warning of water breakthrough in a given stratigraphic layer. In addition, the results in Chapter 7 showed that intermittent water-saturated shale layers which are electrically conductive prevent the spread of electrical current between the stratigraphic layers.

The SP numerical solver, a cheap alternative to hydrocarbon field experiments, was used to develop a closed-loop feedback control strategy triggered by downhole SP measurements at a production well, with inflow control facilitated by inflow control valves (ICVs). The results in Chapters 4 and 6 shows that closed-loop, feedback control using downhole SP measurements can yield gains in well NPV when compared to inflow control based on conventional surface and downhole watercut measurements. This is because by using a dynamic feedback mechanism, water production control using SP measurements significantly reduces the expenditure associated with water production. The economic benefits were observed in both the single smart horizontal well case in Chapter 4 and the multi-well development in Chapter 6. The results in Chapters 4 and 6 also showed that when the reservoir does not behave as predicted, the application of SP-based feedback control can be used to improve well NPV compared to watercut based or heuristic control strategies. In addition, it was observed that for a multi-well development in a situation where the reservoir does not behave as predicted, the SP-based feedback control strategy showed higher gains in NPV than the watercut-based feedback control strategy. However, the NPV gains for the SP-based feedback control strategy and the water-cut based feedback control strategy were similar for a single horizontal well case because watercut-control yields shorter production timescales so the discount factor impacts less on well NPV.

Finally, the prospects of using SP measurements in freshwater boreholes for monitoring seawater intrusion into coastal freshwater aquifers were investigated in Chapter 7. The results suggest that the borehole SP response in the coastal aquifer is dominated by the

electrochemical potential across a saline front that does not intersect the borehole. Moreover, the SP gradient with depth observed in the borehole is caused by the close proximity of the saline front to the base of the borehole.

8.1 Conclusions

The key outcomes of this thesis are as follows:

(i) SP measurements taken along horizontal and vertical production wells, in simple and complex synthetic reservoir models can be used to monitor waterfront encroachment prior to water breakthrough.

(ii) For a single smart horizontal well, closed-loop inflow control based on downhole SP measurements can yield gains in well NPV compared to inflow control based on downhole watercut measurements.

(iii) In multi-well developments, closed-loop feedback control based on downhole SP measurements can be used to reduce the negative production consequences associated with production of water in multi-well developments.

(iv) The forward models presented in this thesis demonstrate that SP signals at production wells are remarkably sensitive to the location of encroaching waterfront, especially if both EK and EC contribute. Therefore, SP measurements can be useful in making critical decisions in real field exploration and production applications, and other non-oil related fields such as saline intrusion monitoring in coastal aquifers.

8.2 Recommendations for future work

In this thesis, the technical feasibility of closed-loop inflow control based on downhole SP measurements was evaluated for single horizontal well and multi-well hydrocarbon field development using a control volume finite difference (CVFD) numerical SP solver. The findings from this study suggest potential paths for future work. The following key issues should be considered to improve upon the research presented here:

1. In this thesis, SP simulation was only investigated in clastic reservoir types. The workflow presented in this thesis should be tested on a carbonate reservoir to identify the impact of the increased heterogeneity inherent to carbonate reservoirs on the conclusions of this study. However, it is still unclear if the SP signals in carbonate reservoirs will be measurable above downhole electrode noise level.

2. In all the numerical simulations conducted in this research, it was assumed that the downhole electrodes were successfully installed in the production wells without the well structure contributing to the electrical conductivity. However, in reality the steel components of the well completion could act as current sink sources that need to be electrically isolated from the formation. Future studies need to account for the contribution of well completions to the electrical signals evaluated in SP-based feedback analysis.

3. Further laboratory work is required to generate a wide range of SP cross-coupling terms for different sedimentary rock types and various oilfield conditions.

4. Development of hardware required to acquire SP measurements downhole and transmit these data to the surface.

5. New methods should be developed to determine waterfront location and geometry from measured SP signals in conjunction with other reservoir data such as 4D seismic imaging.

6. A reservoir screening tool should be developed to identify potential first adopters, completion of interpretation methods, including forward and inverse numerical modelling of the data, to identify and map moving waterfronts and/or water flow.

7. The workflow presented in this study should be applied to a real hydrocarbon field to show the operational benefits of closed-loop SP-based feedback control strategy for improving produced water control and management.

References

Aitokhuehi, I. and Durlofsky, L.J. 2005. Optimizing the performance of smart wells in complex reservoirs using continuously updated geological models. *Journal of Petroleum Science and Engineering*. [Online] 48 (3-4), 254–264.

Agar, J.N., Mou, C.Y., Lin, J.L. 1989. Single-ion heat of transport in electrolyte solutions: a hydrodynamic theory. *J. Phys. Chem.* 93 (5): 2079 - 2082.

Algeroy, J., Morris, A. J., Stracke, M., Auzerais, F., Bryant, I., Raghuraman, B., 1999. Controlling Reservoirs from Afar. *Oilfield Review* 11 (3): 18–29.

Almeida, L.F., Vellasco, M.M.B.R. and Pacheco, M. a. C. 2010. Optimization system for valve control in intelligent wells under uncertainties. *Journal of Petroleum Science and Engineering*. [Online] 73 (1-2), 129–140.

Al-Khelaiwi, F.T., Birchenko, V.M., Konopczynski, M.R., and Davies, D.R. 2010. Advanced Wells : A Comprehensive Approach to the Selection Between Passive and Active Inflow-Control Completions. *SPE Prod & Oper* 25(3): 305 - 326.

Barlow, P.M., Reichard, E.G. 2010. Saltwater Intrusion in Coastal Regions of North America. Hydrogeology Journal 18: 247-260.

Blonk, B., Calvert, R.W., E, S.I., Bv, P., *et al.* (2000) Assessing the Feasibility of a Time-Lapse Seismic Reservoir Monitoring Project. *SPE Reservoir Evaluation Engineering* 3 (1): 80 - 87.

Brouwer, D.R., Jansen, J.D., S. van, D., Kruijsdijk, C.P.J.W., 2001. Recovery Increase through Water Flooding with Smart Well Technology. *Proceedings of SPE European Formation Damage Conference*, The Hague, Netherlands, 21-22 May. doi:10.2523/68979-MS.

Brouwer, D.R., Delft, U., Dut, T., Jansen, J., 2004. Dynamic Optimization of Waterflooding With Smart Wells Using Optimal Control Theory. *SPE Journal* 9(4): 29–31.

Brouwer, D.R., E, S.I., Siep, P., Nævdal, G., *et al.* 2004. Improved Reservoir Management Through Optimal Control and Continuous Model Updating. *SPE Annual Technical Conference and Exhibition,* Houston, Texas, 26 - 29 September.

Bryant, I.D., Chen, M.Y., Raghuranman, B., Raw, I., Delhomme, J. P., Chouzenoux, C. 2002. An Application of Cemented Resistivity Array to Monitor Waterflooding of the

Mansfield Sandstone, Indiana, U.S.A. *SPE Reservoir Evaluation Engineering* 5 (6): 447 - 454.

Carter, J.N., Ballester, P.J., Tavassoli, Z. and King, P.R. 2006. Our calibrated model has poor predictive value: An example from the petroleum industry. *Reliability Engineering & System Safety*. [Online] 91 (10-11), 1373–1381. Available from: doi:10.1016/j.ress.2005.11.033.

Chen, C., Wang, Y., Li, G. & Reynolds, A.C. 2010. Closed-loop reservoir management on the Brugge test case. *Computational Geosciences*. [Online] 14 (4), 691–703. Available from: doi:10.1007/s10596-010-9181-7.

Chen, M.-Y., Raghuraman, B., Supp, M., 2006. Streaming Potential Application in Oil Fields. *SPE Annual Technical Conference and Exhibition, San Antonio, Texas,* U.S.A. 24 - 27 September.

Choudary, K., Saha., D., Chakaraborty, P. 2001. Geophysical Study for Saline Water Intrusion in a Coastal Alluvial Terrain. Journal of Applied Geophysics. 46: 189 - 200.

Crow, S.L., Coronado, M.P., Mody, R.K. 2006. Means for Passive Inflow Control Upon Gas Breakthrough. *SPE Annual Technical Conference and Exhibition*, San Antonio, Texas, 24 - 27 September.

Dilib, F.A. and Jackson, M.D. 2012. Closed-loop Feedback Control for Production Optimization of Intelligent Wells under Uncertainty. *SPE Intelligent Energy Conference*, Utrecht, The Netherlands, 27–29 March.

Dilib, F.A., Jackson, M.D., Khairullin, A.Y. 2013. Field Production Optimization Using Closed-Loop Direct Feedback Control of Intelligent Wells: Application to the Brugge Model. *SPE Annual Technical Conference and Exhibition*, New Orleans, Louisiana, 30 September - 2 October.

Ebadi, F., Davies, D.R. 2006. Should "Proactive" or "Reactive" Control be Chosen for Intelligent Well Management? *SPE Intelligent Energy Conference and Exhibition*, Amsterdam, The Netherlands, 11 - 13 April.

Ekins, P., Vanner, R., Firebrace J., 2005. Management of Produced Water on Offshore Oil Installations: A comparative Assement using Well Flow Analysis. Policy Studies Institute, Final Report, March.

Elmsallati, S.M., Davies, D.R., Erlandsen, S.M. 2005a. A Case Study of Value Generation with Intelligent Well Technology in a High Productivity , Thin Oil Rim Reservoir. *SPE Middle East Oil and Gas Show and Conference,* Bahrain, 12 - 15, March.

Elmsallati, S.M. and Davies, D.R. 2005b. Automatic Optimisation of Infinite Variable Control Valves. *International Petroleum Technology Conference,* Doha, Qatar, 21 - 23 November.

Essink, G.H.P.O. 2001. Saltwater Intrusion in 3D Large-Scale Aquifers: A Dutch Case. Phys. Chem. Earth (B), Vol. 26, No. 4, pp. 337 - 344.

Fetkovich, M.J. 1971. A Simplified Approach to Water Influx Calculations-Finite Aquifer Systems. Journal of Petroleum Technology 23 (7): 814-828.

Gai, H. 2001. Downhole Flow Control Optimization in the Worlds 1st Extended Reach Multilateral Well at Wytch Farm. *Proceedings of SPE/IADC Drilling Conference*. [Online] 1–6. Available from: doi:10.2523/67728-MS.

Glandt, C.A. 2005. Reservoir Management Employing Smart Wells : A Review. *SPE Latin American and Caribbean Petroleum Engineering Conference,* Port-of-Spain, Trinidad, 27–30 December.

Grebenkin, I. and Davies, D. 2010. Analysis of the Impact of an Intelligent Well Completion on the Oil Production Uncertainty (Russian). *Proceedings of SPE Russian Oil and Gas Conference and Exhibition*. [Online] Available from: doi:10.2118/136335-RU.

Gulamali, M.Y., Leinov, E. & Jackson, M.D. 2011. Self-potential anomalies induced by water injection into hydrocarbon reservoirs. *Geophysics*. [Online] 76 (4), F283–F292. Available from: doi:10.1190/1.3596010.

Guerra, K., Dahm, K., Dundorf, S., 2011. Oil and Gas Produced Water Management and Beneficial Use in the Western United States [Online]. US Department of Interior: Science and Technology Program Report No. 157 Available: http://www.usbr.gov/research/AWT/reportpdfs/report157.pdf [Accessed 15/01/2016 2016].

Huyakorn, P.S., Andersen, P.F., Mercer, J.W., White, H.O. 1987. Saltwater Intrusion in Aquifers: Development and Testing of a Three-Dimensional Finite Element Model. *AGU Journal,* Vol 23 (80), 1763–1775.

Ishido, T. & Mizutani, H. 1981. Experimental and Theoretical Basis of Electrokinetic Phenomena in Rock-Water Systems and Its Applications to Geophysics. *Journal of Geophyscal Research,* 86 (2), 293–312.

Jaafar, M.Z., Vinogradov, J. & Jackson, M.D. 2009. Measurement of streaming potential coupling coefficient in sandstones saturated with high salinity NaCl brine. *Geophysical Research Letters*. [Online] 36 (21), L21306. Available from: doi:10.1029/2009GL040549.

Jackson, M.D. 2008. Characterization of multiphase electrokinetic coupling using a bundle of capillary tubes model. *Journal of Geophysical Research*. [Online] 113 (B4), B04201. Available from: doi:10.1029/2007JB005490.

Jackson, M.D. 2010. Multiphase electrokinetic coupling: Insights into the impact of fluid and charge distribution at the pore scale from a bundle of capillary tubes model. *Journal of Geophysical Research*. [Online] 115 (B7), B07206. Available from: doi:10.1029/2009JB007092.

Jackson, M.D., Vinogradov, J., Saunders, J.H., Jaafar, M.Z. 2011. Laboratory Measurements and Numerical Modeling of Streaming Potential for Downhole Monitoring in Intelligent Wells. *SPE Journal* 16 (3): 625 - 636.

Jackson, M.D., Gulamali, M.Y., Leinov, E., Saunders, J.H. 2012. Self Potentials in Hydrocarbon Reservoirs During Waterflooding : Application to Water-Front Monitoring. *SPE Annual Technical Conference and Exhibition*. Florence, Italy, 20–22, September.

Jackson, M.D. & Vinogradov, J. 2012. Impact of wettability on laboratory measurements of streaming potential in carbonates. *Colloids and Surfaces A: Physicochemical and Engineering Aspects*. [Online] 39386–95. Available from: doi:10.1016/j.colsurfa.2011.11.005.

James, S.C., Dickinson, J.E., Mehl, S.W., Hill, M.C., Leake, S.A., Zyvoloski, G.A., Eddebbarh, A.A. 2006. New ghost-node method for linking different models with varied grid refinement: Proceedings of the 11th International High Level Radioactive Waste Management Conference, IHLRWM. 30 April – 4 May.

Jansen, J.D., Douma, S.D., Brouwer, D.R., Van den Hof, P.M.J., Bosgra, O.H., Heemink, A.W. 2009. Closed-Loop Reservoir Management. *SPE Reservoir Simulation Symposium.* The Woodlands, Texas, U.S.A

Kharghoria, A., Zhang, F., Jalali, Y., 2002. Application of Distributed Electrical Measurements and Inflow Control in Horizontal Wells under Bottom-Water Drive. *SPE European Petroleum Coference,* Aberdeen, United Kingdom, 29-31 October.

Kleef, R., Hakvoort, R., Bhushan, V., Al-Khodhori, S. 2001. Water Flood Monitoring in an Oman Carbonate Reservoir Using a Downhole Permanent Electrode Array. *Proceedings of SPE Middle East Oil Show*. Bahrain, 17-20 March. [Online] Available from: doi:10.2523/68078-MS.

Konopczynski, M. & Ajayi, A. 2007. Control of Multiple Zone Intelligent Well To Meet Production-Optimization Requirements. *SPE Production and Operation Symposium,* Okhlahoma, U.S.A., 31 March - 3 April.

Leinov, E., Vinogradov, J., Jackson, M.D. 2010. Salinity dependence of the thermoelectric coupling coefficient in brine-saturated sandstones. *Geophysical Research Letters*. [Online] 37 (23). Available from: doi:10.1029/2010GL045379.

Lucas, C., Duffy, P., Randall, E. & Jalali, Y. 2001. Near-Wellbore Modeling to Assist Operation of an Intelligent Multilateral Well in the Sherwood Formation. *Paper SPE 71828 presented at the Offshore Europe Conference,* Aberdeen, Scotland, 4-7 September.

MacAllister, D.J., Jackson, M.D., Butler, A.P., Vinogradov, J., Ijioma, A. 2015. Self-potential Monitoring of Seawater Intrusion in a Fractured Coastal Aquifer. AGU Fall Meeting, San Francisco, U.S.A, 14-18 December.

Miorali, M., Slob, E. & Arts, R. 2011. A feasibility study of borehole radar as a permanent downhole sensor. *Geophysical Prospecting*. [Online] 59 (1), 120–131. Available from: doi:10.1111/j.1365-2478.2010.00904.x.

Mitchell, A.F., Skarsholt, L.T. 2008. Advanced Wells : How are they Being Used and are they Creating Value ? Paper *SPE 113142 presented at Improved Oil Recovery Symposium*, Tulsa, Oklahoma, U.S.A., 19–23 April.

Meum, P., Tondel, P., Godhavn, J., Aamo, O.M. 2008. Optimization of Smart Well Production Through Nonlinear Model Predictive Control. *SPE Intelligent Energy Conference,* Amsterdam, The Netherlands, 25–27, February.

Morris, J., Hampson, G.J., Maxwell, G. 2003. Controls on facies architecture in the Brent Group, strathspey field, UK North Sea: implications for reservoir characterization. doi: 10.1144/1354-079302-504July 2003 Petroleum Geoscience, 9, 209-220.

Nævdal, G., Brouwer, D.R., Jansen, J.-D. 2006. Waterflooding using closed-loop control. *Computational Geosciences*. [Online] 10 (1), 37–60. Available from: doi:10.1007/s10596-005-9010-6.

Naus, M.M.J.J., Dolle, N., Jansen, J.D., 2004. Optimization of Commingled Production using Infinitely Variable Inflow Control Valves. *SPE Annual Technical Conference and Exhibition.* Houston, Texas, U.S.A., 26-29 September, *SPE 90959.*

Nowroozi, A.A., Horrocks, S.B., Henderson, P., 1999. Saltwater Intrusion into The Freshwater Aquifer in The Easter Shore of Virginia. Journal of Applied Geophysics, 42, 1 - 22.

Ortiz Jr., I., Osoba, J.S., and von Gonten, W.D. 1973. Relationship of the electrochemical potential of porous meda with hydrocarbon saturation. *The Log Analyst* 14 (2): 25 - 32. SPWLA.

Peters, E., Arts, R.J., Brouwer, G.K., Geel, C.R., Cullick, S., Lorentzen, R.J., Chen, Y., Dunlop, K.N.B., Vossepoel., Xu, R., Sarma, P., Alhutali, A.H., Reynolds, A.C. 2010. Results of the Brugge benchmark study for flooding optimisation and history matching. SPE Reservoir Simulation Symposium, The Woodlands, Texas, USA, 2 – 4, February.

Pucknell, J., Holder, G., and Seeahai, T. 2003. Amherstia Field, Trinidad: Breaking Barriers in the New Millennium. SPE paper 81012 presented at the SPE Latin American and Carribean Petroleum Engineering Conference, 27-30 April 2003, Port -of-Spainm Trinidad and Tobago.

Ray, F.M., Pinnock, S.J., Katamish, H., Turnbull, B. 2016. The Buzzard Field: anatomy of the reservoir from appraisal to production. Proceedings of the 7th Petroleum Geology Conference. 369 - 386. DOI: 10.1144/0070369

Reppert, P.M. 2003. Temperature-dependent streaming potentials: 1. Theory. *Journal of Geophysical Research*. [Online] 108 (B11), 2546. Available from: doi:10.1029/2002JB001754.

Revil, A. 1999. Ionic Diffusivity, Electrical Conductivity, Membrane and Thermoelectric Potentials in Colloids and Granular Porous Media: A Unified Model. *Journal of colloid and interface science*. [Online] 212 (2), 503–522. Available from: doi:10.1006/jcis.1998.6077.

Revil, A., Pezard, P.A., Glover, P.W.J. 1999. Streaming potential in porous media: 1. Theory of the zeta potential. *Journal of Geophysical Research*. [Online] 104 (B9), 20021. Available from: doi:10.1029/1999JB900089.

Robison, C.E., 1997. Overcoming the Challenges Associated With the Life-Cycle Management of Multilateral Wells: Assessing Moves Towards the "Intelligent Completion". *Paper SPE 38497 presented at the Offshore European Conference*, Aberdeen, Scotland, 9-12 September.

Sarma, P., Durlofsky, L.J., Aziz, K., Chen, W.H. 2006. Efficient real-time reservoir management using adjoint-based optimal control and model updating. *Computational Geosciences*. [Online] 10 (1), 3–36. Available from: doi:10.1007/s10596-005-9009-z.

Saunders, J.H., Jackson, M.D., Pain, C.C. 2006. A new numerical model of electrokinetic potential response during hydrocarbon recovery. *Geophysical Research Letters*. [Online] 33 (15), L15316. Available from: doi:10.1029/2006GL026835.

Saunders, J.H., Jackson, M.D., Pain, C.C. 2008. Fluid flow monitoring in oil fields using downhole measurements of electrokinetic potential. *Geophysics*. [Online] 73 (5), E165–E180. Available from: doi:10.1190/1.2959139.

Sill, W.R. 1983. Self-potential modeling from primary flows. *Geophysics*. [Online] 48 (1), 76–86. Available from: doi:10.1190/1.1441409.

Stengel, R.F. 1985. Optimal Control and Estimation. *Dover Books on Advanced Mathematics*.

Tavassoli, Z., Carter, J.N., King, P.R. 2004. Errors in History Matching. *SPE Journal* SPE 86883.

Turner, R. J., Hubbard, M.G., and Dukler, A.E. 1969. Analysis and Prediction of Minimum Flow Rate for the Continuous Removal of Liquids from Gas Wells. Journal of Petroleum Technology 21 (11): 1475-1482.

Van der Poel, R., Jansen, J.D. 2004. Probabilistic analysis of the value of a smart well for sequential production of a stacked reservoir. *Journal of Petroleum Science and Engineering*. [Online] 44 (1-2), 155–172. Available from: doi:10.1016/j.petrol.2004.02.012.

van Essen, G.M., Zandvliet, M.J., Van den Hof, P.M.J., Bosgra, O.H., and Jansen, J.D. 2009. Robust Waterflooding Optimization of Multiple Geological Scenarios. *SPE J.* 14 (1): 202-210. SPE-102913-PA.

van Essen, G.M., Jansen, J.D., Brouwer, D.R. Douma, S.G., Zandvliet, M.J., Rollett, K.I. and Harris, D.P., 2010. *SPE Reservoir Evaluation and Engineering* 13 (4) 588-595. DOI: 10.2118/123563-PA.

Vinogradov, J., Jaafar, M.Z., Jackson, M.D. 2010. Measurement of streaming potential coupling coefficient in sandstones saturated with natural and artificial brines at high salinity. *Journal of Geophysical Research*. [Online] 115 (B12), B12204. Available from: doi:10.1029/2010JB007593.

Vinogradov, J., Jackson, M.D. 2011. Multiphase streaming potential in sandstones saturated with gas/brine and oil/brine during drainage and imbibition. *Geophysical Research Letters*. [Online] 38 (1), L01301. Available from: doi:10.1029/2010GL045726.

Watts, G., Barkved, O., Norge, B.P. & Dickens, J. (2006) *SPE 99827 Seismic Surveillance in the Field of the Future*.

Wardle, C. 2011. *Sea-water intrusion* [Online]. UK Groundwater Forum: NERC/British Geological Survey. Available: http://www.groundwateruk.org/downloads/sea_water_intrusion.pdf [Accessed 15/01/2016 2016].

Warner, N.R., Jackson, R.B., Darrah, T.H., Osborn, S.G., Down, A., Zhao, K., White, A., Vengosh, A. 2012. Geochemical Evidence for Possible Natural Migration of Marcellus Formation Brine to Shallow Aquifers in Pennyslvania. Proc. Natl. Acad. Sci., 109, pp. 11961 - 11966.

Worthington, P.F., Evans, R.J., Klien, J.D., Walls, J.D., White, G. 1990. SCA Guidelines for Sample Preparation and Porosity Measurement of Electrical Resistivity Samples Part III -The Mechanics of Electrical Resistivity Measurement on Rock Samples. SCA Guidelines March-April

Yeten, B., Brouwer, D.R., Durlofsky, L.J., Aziz, K. 2004. Decision Analysis under Uncertainty for Smart Well Deployment. *Journal of Petroleum Science and Engineering* 43, 183–199.

Yeten, B., Durlofsky, L.J., Aziz, K. & Eptc, C. 2002. Optimization of Smart Well Control. *SPE International Thermal Operations and Heavy Oil Symposim and International Horizontal Well Technology Conference,* Calgary, Alberta, Canada, 4 - 7 November.

Yildiz, T. 2003. Long-Term Performance of Multilaterals in Commingled Reservoirs. *SPE International Thermal Operations and Heavy Oil Symposim and International Horizontal Well Technology Conference,* Calgary, Alberta, Canada, 4 - 7 November.